Freie Universität Berlin

Coherence in a thermal ensemble: Creation and decay of laser-induced alignment in nitrogen

Nina Katrin Owschimikow

Fachbereich Physik
Freie Universität Berlin

Dissertation
2011

erster Gutachter: Prof. Dr. Nikolaus Schwentner
zweiter Gutachter: Prof. Dr. Ludger Wöste
Disputation: 04. Mai 2011

Abbreviations

BBO	beta-Barium borate
CCD	Charge-coupled device
cw	continuous wave
FROG	Frequency resolved optical gating
FWHM	Full width at half maximum
GCD	greatest common divider
HWHM	Half width at half maximum
ODE	Ordinary differential equation
OKE	Optically induced Kerr effect
OMA	Optical multichannel analyzer
PG	Polarization gating
RCS	Rotational coherence spectroscopy
RIPS	Raman induced polarization spectroscopy
SFG	Sum frequency generation
SHG	Second harmonic generation
TDSE	Time dependent Schrödinger equation
TISE	Time independent Schrödinger equation

Constants (SI units)

$c = 299792458$ m/s speed of light
$e = 1.602176462\times10^{-19}$ C elementary charge
$\epsilon_0 = 8.854187\times10^{-12}$ F/m dielectric permittivity of vacuum
$h = 6.626069\times10^{-34}$ J s Planck constant
$\hbar = 1.054571\times10^{-34}$ J s reduced Planck constant
$k_B = 1.386650\times10^{-23}$ J/K Boltzmann constant
$m_u = 1.66057\times10^{-27}$ kg atomic mass unit
$N_A = 6.022142\times10^{23}$ 1/mol Avogadro number
$R = 8.314472$ J/(mol K) universal gas constant

Conversion of units

Frequency and energy

	cm^{-1}	eV	J	MHz
1 cm^{-1}	1	1.239842×10^{-4}	1.986447×10^{-23}	2.997925×10^{4}
1 eV	8065.54	1	1.602177×10^{-19}	2.417988×10^{-8}
1 J	5.03411×10^{22}	6.2415406×10^{18}	1	1.509189×10^{27}
1 MHz	3.33564×10^{-5}	4.135669×10^{-9}	6.626076×10^{-28}	1

Pressure

	atm	mbar	Pa
1 atm	1	1013.3	1.0133×10^{5}
1 mbar	9.8692×10^{-4}	1	100
1 Pa	9.8692×10^{-6}	0.01	1

Abstract

The non-adiabatic alignment of diatomic molecules is examined in experiment and numerical simulations using as an example the nitrogen molecule.

Numerical simulations are carried out to elucidate alignment of rotationally excited molecules, in particular for laser pulse duration and in the transition region between the non-adiabatic and adiabatic regimes. Depending on the M quantum number, the interaction with the laser field can involve emission of energy as well as absorption, and these two processes lead to opposite motion of the molecular axis with respect to the laser polarization direction. For a moderately strong laser pulse with a duration comparable to the molecular rotational period, we show that the crossover from non-adiabatic to adiabatic limits is well described by a convolution of excitation pulse envelope and sinusoidal molecular response and it takes place in a uniform way in the region between 0.1 and 1 for the ratio of pulse duration to rotational period. For higher intensities, the rotational wave packet contains a greater manifold of coupled rotational levels, for which the degree of adiabaticity varies. Differences in the rotational period in the excited transitions for appropriate laser pulse parameters lead to the formation of a region in which anti-alignment, or rotational cooling, dominates over alignment, or rotational heating. Based on the dependence of post-pulse alignment on the ratio of rotational time and pulse duration, a method for controlling the J composition of a rotational wave packet is proposed. The laser pulse duration is used as parameter to achieve selective non-adiabatic interaction in the rotationally cold part of the thermal distribution. By optimizing the duration of a single pulse, arbitrarily narrow distributions at low J levels can be formed. A double pulse excitation, where a longer second pulse acts as a selective dump pulse, allows to prepare non-thermal distributions centered at high J values.

Experimentally, the decay of alignment in nitrogen and mixtures of nitrogen with hydrogen and several noble gases was investigated using ultrafast optical Kerr effect spectroscopy. The very high sensitivity of a collinear modification of the standard setup is quantitatively determined, and it provides a large dynamic range for decay studies. It is demonstrated that the analysis of the shape of the homodyne alignment signal contains information on the ratio of population and coherence parts of alignment, and that thus the small population part can be quantified even at moderate laser power. The integrated area of the homodyne detected alignment revivals is shown to be a robust measure of the degree of coherence in the rotational wave packet even in the presence of centrifugal distortion. Experiments at different temperatures display long-lived coherences at high temperature. The cross section for decoherence in pure nitrogen is measured in a temperature range from at 80 K to room temperature, and it decreases from 102 Å^2 to 48 Å^2. At room temperature, the cross section for decoherence is equal to the gas-kinetic cross section and to the cross section for rotational depopulation. In this case, thus pure dephasing does not occur in the decay of rotational coherence. This is also confirmed for mixtures of nitrogen with hydrogen, helium and argon. For nitrogen and nitrogen-foreign gas mixtures, the cross sections for decoherence grow stronger with atomic mass than the geometric size of the particles.

Kurzfassung

In dieser Arbeit wird das nicht-adiabatische Alignment von zweiatomigen Molekülen am Beispiel von Stickstoff experimentell und mittels numerischer Simulationen untersucht.

Die numerischen Simulationen beleuchten das Alignment von Molekülen in angeregten Rotationszuständen, besonders für Laserpulse im Bereich des Übergangs vom nicht- adiabatischen zum adiabatischen Grenzfall. Die Wechselwirkung mit dem elektrischen Feld des Lasers kann, abhängig von der magnetischen Quantenzahl M, sowohl durch Absorption als auch durch induzierte Emission erfolgen. Diese Prozesse führen zu entgegengesetzten Bewegungen der Molekülachse relativ zur Polarisationsrichtung des Feldes. Wir zeigen, dass für einen Laserpuls von moderater Intensität, dessen Dauer vergleichbar zur molekularen Rotationsperiode ist, der Übergang vom nicht-adiabatischen zum adiabatischen Grenzfall durch eine Faltung von Pulsform und sinusförmiger molekularer Antwort beschrieben wird, und dass er in einheitlicher Weise im Bereich von 0.1 und 1 für das Verhältnis von Pulsdauer zu Rotationsperiode stattfindet. Ein Rotationswellenpaket, das mit höherer Laserintensität angeregt wird, enthält eine große Zahl von gekoppelten Rotationszuständen. Höher angeregte Rotationszustände werden dabei aufgrund ihrer schnellen Rotationsperiode bei wachsender Pulsdauer stärker unterdrückt. Für geeignete Laserpulsparameter entsteht eine Region, in der Anti-Alignment, und damit die Abkühlung der Rotationsfreiheitsgrade, über Alignment, gleichbedeutend mit dem Heizen der Rotation, dominiert.

Die Abhängigkeit der Amplitude des feldfreien Alignments vom Verhältnis von Rotationsperiode und Pulslänge wird dazu benutzt, eine Methode zur Kontrolle der J- Zusammensetzung eines Rotationswellenpakets zu entwickeln. Die Pulsdauer wird als Kontrollparameter eingesetzt, um gezielt kohärente nicht-adiabatische Wechselwirkung im kalten Teil der Rotationsverteilung zu erzielen. Mit optimierter Pulsdauer kann eine beliebig schmale J-Verteilung am kalten Ende des Spektrums erzeugt werden. Nicht-thermische Verteilungen in bezug auf die Rotation können durch eine Doppelpulsstrategie, in der der zweite Puls als selektiver Dump-Puls fungiert, erreicht werden.

Im experimentellen Teil der Arbeit wurde das Abklingen des Alignments in Stickstoff und Gemischen von Stickstoff und Wasserstoff sowie verschiedenen Edelgasen mittels optischer Kerr-Effekt Spektroskopie untersucht. Die extrem gute Empfindlichkeit, die durch kolineare Propagation von Pump- und Probestrahl in einer Abwandlung des Standardaufbaus erreicht wird, kann quantitativ bestimmt werden. Es kann damit ein großer Messbereich für die Bestimmung der Abklingzeiten der Kohärenz erreicht werden. Eine Analyse der Kurvenform des homodyn detektierten Alignmentsignals zeigt, dass die Größe des Populationsbeitrags zum Alignment relativ zum kohärenten Beitrag aus dem Kurvenverlauf bestimmt werden kann. Der kleine Populationsbeitrag kann damit auch für mäßig intensive Anregungspulse bestimmt werden. Wir zeigen weiterhin, dass die integrierte Fläche der homodyn detektierten Stickstoff-Revivals trotz der durch Zentrifugalkräfte verursachten Änderungen der Form ein stabiles Maß für den Kohärenzgrad des Rotationswellenpakets darstellt. Experimente über einen großen Temperaturbereich zwischen 80 K und 300 K zeigen langlebige Kohärenzen auch bei hohen Temperaturen. Der Dekohärenzquerschnitt von reinem Stickstoff nimmt in diesem Temperaturbereich von 102 Å^2 auf 48 Å^2 ab. Bei Raumtemperatur entspricht das dem gaskinetischen Querschnitt und dem Querschnitt für Depopulation. Reine Dephasierung spielt damit in diesem Fall keine Rolle für den Abfall der Kohärenz. Das wird auch für Gemische von Stickstoff mit Wasserstoff, Helium und Argon bestätigt. Sowohl für reinen Stickstoff als auch für die Gasgemische wachsen die Dekohärenzquerschnitte stärker mit der molekularen Masse als der geometrische Querschnitt der Teilchen.

Inhaltsverzeichnis

Introduction

The orientation induced in a gas of polar molecules upon the interaction with an electric field became a "hot topic"for the first time in the late 1920's. Based on the theories of Langevin and Debye [1], the effect was used to determine dipole moments of various molecules. More detailed studies demand to achieve a significant reorientation of molecules. In a static electric field, however, this approach requires prohibitively high field strength [2, 3], and has therefore a limited practical applicability. High electric field strengths nevertheless can be routinely realized in a focused laser beam. Around 1990, the possibility to create rotationally cool ensembles in molecular beams together with the availability of lasers with sufficiently high intensity provided the experimental means to efficiently align molecules [4]. Here, the mechanism of the interaction is different from brute force static orientation, as in the rapid oscillations of the electromagnetic field the interaction with a permanent dipole is averaged out. Molecules in this case are aligned[1], rather than oriented, through the interaction of the field with the anisotropic polarizability [4–6].

Alignment can be created in a molecular sample not only in a cw laser field but also by using an intense laser pulse much shorter than the molecular rotational period. This so-called non-adiabatic alignment of molecules by ultrashort laser pulses has developed into an important topic over the last two decades. A peculiarity of this phenomenon is that due to the inertia of the nuclei, the coherent motion of molecules persists after the turn-off of the laser pulse in a rotational wave packet motion [7]. This field-free or post-pulse alignment, which - after initial dispersion - reconstitutes itself periodically in rotational revivals, has become one of the main tools for the generation of ensembles of molecules with controllable direction of molecular axes with respect to the laboratory frame (see e.g. [8–15] and references therein).

Within our project A3 of the Sonderforschungsbereich 450 (Analysis and control of ultrafast photoinduced reactions) we proposed to use non-adiabatic alignment to trigger direction-dependent chemical reactions of dopant molecules trapped in a crystalline host matrix [16, 17]. This required to develop a sensitive experimental method in order to detect the subtle effects caused by the laser-induced rotational response in a sample. After testing several techniques I found that the optical Kerr effect (OKE) spectroscopy provides the required high sensitivity for the detection of the anisotropy. In addition, a well-established set of analytical tools for the evaluation of data is available [18]. The implementation of OKE for our experiments, the detection of revival dynamics and its decoherence, and the quantitative analysis thereof constitute the topic of my thesis. To support the interpretation, I additionally carried out numerical simulations of alignment dynamics in nitrogen. In particular, in these simulations the effects of temperature and pulse duration on the alignment of rotationally excited molecules are elucidated. The nitrogen molecule is used as a molecular system throughout, because it is the work-horse of many studies devoted to investigate fundamental issues of molecular alignment (for references see e.g. [19–29]), and therefore allows for a quantitative treatment.

The mechanism of molecular alignment in terms of the relevant Hamiltonian and Schrö-

---

[1] The term *alignment* describes the arrangement or position of objects in a straight line or along parallel lines. Parallel and anti-parallel orientation are equivalent.

dinger equation is well known [5, 6, 30]. Analytical approaches to the calculation of molecular alignment, however, are limited to either the impulsive or the classical case in the rotational ground state due to the overwhelming algebraic complexity of the problem [31, 32]. Otherwise, much of the theoretical work is based on numerical simulations, which does not necessarily advance the understanding of the underlying physical processes. In the theoretical part of this work we use the fact that the relevant Schrödinger equation describes the molecular alignment well to identify in rotational state-resolved simulations the relevant physical processes in the alignment. Based on this, we develop analytical models to determine the outcome of an alignment experiment without resorting to full scale numerical simulations. Simulations were carried out after adapting, in collaboration with Burkhard Schmidt, the program code used in Refs. 16 and 17. In particular, two issues are addressed, the consequences of which were previously not qualitatively discussed in the literature.

The first issue is to treat alignment of molecules in rotationally excited states. In this case, the molecule can interact with the electromagnetic field by absorption as well as by emission of a quantum of energy. State-resolved numerical simulations show that these processes have opposite effects on the alignment of the molecular axis. Incorporating the relative phases of the rotation induced by the field into a simple analytical model allows to predict the outcome of an alignment experiment for finite temperature. The influence of the excitation pulse length on the amplitude of the post-pulse alignment is understood qualitatively by the trailing edge of the laser pulse coherently removing a part of the induced polarization. It can be accounted for quantitatively within the same model by a convolution of pulse envelope and system response. The results obtained on the directionality- and pulse length-dependence of molecular alignment are presented in Sec. 2.2 and are published in Refs. 33 and 34.

Additionally, based on the relationship between pulse duration and post-pulse alignment, a method is developed to selectively create a rotational wave packet in the cold or the hot part of a thermal distribution of molecules. This in principle allows to investigate rotational state-dependent properties using molecular alignment. The proposed method is described in Sec. 2.3 and published in Ref. 33.

The technical part of this thesis is devoted to the setting up and characterization of an ultrafast OKE experiment. Implementation and characterization of a standard OKE setup is described in Sec. 3.2 in continuation of the diploma thesis of Philipp Giese (Ref. 35). It turned out, however, that a modification of the standard OKE setup with collinearly propagating pump and probe beams provides much better sensitivity under our experimental conditions. This collinear setup was combined with a sample cell in a helium-bath cryostat to perform temperature-resolved measurements of alignment decay in gases. This setup and its characterization is described in Sec. 3.2. The present work then focused on investigating alignment in dissipative media, and the effect of pulses with a duration exceeding the strictly non-adiabatic limit. The sample cell is a part of Falk Königsmann's setup for the growth and investigation of para-hydrogen crystals. He will use the OKE method to study rotational and phonon dynamics in these crystals [36].

All processes involving rotational wave packets require the persistence of rotational coherence in time, and this naturally creates an interest in the time scales and mechanisms that lead to the decay of rotational coherence in the aligned ensemble. In the experimental part of the thesis, we use non-adiabatic alignment in nitrogen to track and quantify the decay of coherence in the rotational wave packet. Apart from the coherent revivals, non-adiabatically aligned molecules also display an increased average alignment in the direction of the laser polarization. This contribution under normal experimental circumstances is at least one order of magnitude smaller than the revival amplitude, and thus hard to reliably detect. In experiments on nitrogen at low temperature we show that the average alignment is observable even at relatively low excitation energies in the particular shapes of the alignment transients. We find evidence for a slower decay of the average alignment with respect to the coherent revivals, meaning that the randomization of the M quantum number requires on average more than one inelastic collision. These results are presented in Sec. 3.3.4.

In the last section of the experimental chapter we report results on the magnitude of cross sections for alignment decay in nitrogen. Previous experiments [37, 38] observed the decay in nitrogen at room temperature, and applied a multi-parameter scaling law analysis using state-resolved decay rates, which did not allow to extract a meaningful cross section from the data. We show that the decoherence cross section for nitrogen can be obtained in a straightforward way from the decay of the peak area of revivals in the homodyne detected optical Kerr effect signal. The approach allows to derive the relevant cross section for pure nitrogen and a variety of collision partners without relying on modeling. The cross section for decoherence for pure nitrogen shows a strong dependence on temperature, increasing by more than a factor of two upon lowering the temperature from room temperature to 80 K. This leads to the decay rate of molecular alignment becoming almost independent of temperature at a constant number density of the gas. The resulting stability of revivals with respect to temperature may be relevant for the implementation of quantum information schemes [21, 39]. First results are contained in Jochen Maurer's diploma thesis (Ref. 40) and Anna Ott's bachelor's thesis (Ref. 41). The complete results are presented in Sec. 3.3. and published in Ref. 42.

In the general introduction in Chapter 1, the basic concepts of molecular rotations, wave packet dynamics and laser-induced alignment are briefly reviewed. The theoretical Chapter 2 and the experimental Chapter 3 are each self-contained and can be read in arbitrary order.

1 Basic concepts

1.1 Molecular rotation

1.1.1 Rotation of linear molecules

A molecule moving in space without any external perturbation can be described by a sum of its center-of-mass translational motion and motion governed by internal degrees of freedom. These include the radial (vibrational) and angular (rotational) motion of the nuclei and the electronic response to the nuclear displacement. Within the Born-Oppenheimer approximation the electronic response is considered instantaneous and is reduced to an effective potential in which the nuclei are moving.

The molecular Hamiltonian [1] is thus expressed as a sum

$$H_{\text{mol}} = H_{\text{cm}} + H_{\text{vib}} + H_{\text{rot}}. \tag{1.1}$$

Small molecules usually have large fundamental vibrational frequencies, in the case of nitrogen $\omega_0 = 2360\ \text{cm}^{-1}$. This value exceeds by far the thermal energy of $kT = 210\ \text{cm}^{-1}$ at room temperature and the bandwidth of $120\ \text{cm}^{-1}$ of the pulsed excitation sources employed in this work. Therefore the vibrational degrees of freedom will not be discussed further.

Describing rotations of complex molecules with respect to a space-fixed frame of reference demands extensive algebra involving the third rank tensor of inertia and rotations about the Euler angles. For linear molecules, however, the problem is considerably simplified and can be tackled analytically with moderate efforts.

1.1.1.1 The rigid rotor

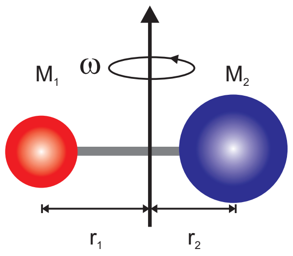

Abbildung 1.1: *The rigid rotor.*

The simplest way to describe a rotating linear molecule is to consider the molecule as two point masses M_1 and M_2 connected by a massless rod of fixed length $R = r_1 + r_2$ and rotating about its center of mass with angular velocity ω (Fig. 1.1). The moment of inertia for such a system is expressed as $\Theta = \sum_i M_i r_i^2 = \mu R^2$, with $\mu = (M_1 + M_2)/(M_1 M_2)$ being the reduced mass and R being the distance between the atoms. The operator for the rotational Hamiltonian H_{rot} can thus be written as [44]

$$H_{\text{rot}} = \frac{\mathbf{J}^2}{2\Theta} = \frac{\mathbf{J}^2}{2\mu R^2}. \tag{1.2}$$

Here $\mathbf{J}$ denotes the angular momentum operator of the molecule, and J the quantum number characteristic of its magnitude. $\mathbf{J}$ obeys the usual

---

[1] This is the so-called Coulomb Hamiltonian [43]. The full molecular Hamiltonian additionally includes terms originating from the spin of electrons and nuclei. The contribution of these terms becomes the more important the more massive the atoms constituting the molecule.

angular momentum algebra, in particular $[H_{\mathrm{mol}}, J_z] = 0$ and $[H_{\mathrm{mol}}, \mathbf{J}^2] = 0$, and its eigenvalues equal $\sqrt{\hbar^2 J(J+1)}$ with J being an integer [45, 46]. The corresponding eigenfunctions are the spherical harmonics $Y_J^M(\theta, \varphi)$. The spherical harmonics are defined as

$$Y_J^M(\theta, \varphi) = \sqrt{\frac{(2J+1)(J-M)!}{4\pi(J+M)!}} P_J^M(\cos\theta) e^{iM\varphi}, \tag{1.3}$$

and form a complete set of orthogonal basis functions:

$$\int Y_J^{M*}(\theta, \varphi) Y_{J'}^{M'}(\theta, \varphi) dV = C\delta(J, J')\delta(M, M'), \tag{1.4}$$

where the constant C depends on the particular normalization of the associated Legendre polynomials $P_J^M(\cos\theta)$ [47].

For every J value there exist $2J+1$ different functions with projection $M = -J, -J+1, \ldots, J-1, J$ of angular momentum on an external axis z, which add up to an isotropic distribution for every J number individually.

The rotational energy in the rigid rotor approximation is expressed as

$$E_{\mathrm{rot}} = B_v J(J+1), \tag{1.5}$$

where the moment of inertia has been absorbed into the rotational constant B_v, a quantity characteristic of the rotational level spacing of the particular molecule. The subscript v refers to the number of the vibrational level, as the internuclear distance R is in general a function of v. Due to the small transition energies of rotational excitations, the rotational constant is usually expressed in units of wave numbers, $B_v = h/(8\pi^2 c\Theta)$ [cm^{-1}], where 1 cm^{-1} = 5.034×10^{-22} J. The rotational constant of the $^{14}N_2$ molecule in the vibrational ground state is $B_0 = 1.989$ cm^{-1} [44]. It increases for lighter molecules, the lightest existing molecule H_2 having $B_0 = 60.8$ cm^{-1} [44]. For comparison, some rotational constants of diatomic molecules are collected in Table 1.1. Additionally, frequently an equilibrium rotational constant B_e appears in the literature, in which the internuclear distance has been averaged to yield an equilibrium value R_e. The vibrational excitation energy exceeds the thermal energy by a factor of 10 for the nitrogen molecule at room temperature. In this work we therefore use B_0 for the vibrational ground state in all calculations.

Pure rotational excitations appear in spectroscopy as a series of almost evenly spaced lines. The reason for the regular pattern is a quadratic increase of rotational level spacing with J that leads to the appearance of linearly spaced transition frequencies

$$\Delta E_{\mathrm{rot}} = B_v(J+1)(J+2) - B_v J(J+1) = 2J+2 \tag{1.6}$$

between neighboring rotational levels J and $J+1$.

1.1.1.2 The non-rigid rotor

Though the rigid rotor is a very good model for low J-numbers, in case of highly excited molecules or long observation times of wave packet propagation it becomes necessary to account for a bond softening as a consequence of the centrifugal force acting on a fast rotating molecule (Fig. 1.2(a)). The potential for fast rotating molecules thus changes following the change in internuclear separation, and therefore rotational and vibrational motions become coupled. Mathematically this corresponds to the Schrödinger equation being no longer separable for rotational and vibrational degrees of freedom. Far away from

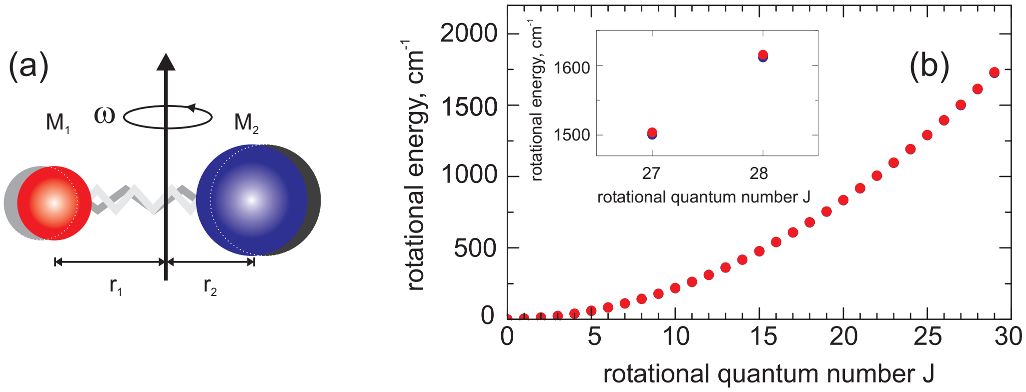

Abbildung 1.2: *(a) Non-rigid rotor. The molecular bond connecting the atoms is flexible and expands with centrifugal distortion in fast rotations. (b) Rotational energy vs. rotational quantum number J for* $^{14}N_2$*. The red symbols show the rigid rotor approximation, the hardly visible blue symbols correspond to the dependence corrected for centrifugal distortion. The inset shows a zoom into the high-J region, where deviations start being visible.*

a vibrational resonance, however, it proved to be sufficient to describe the rotational energy as a power series in J

$$E_{\mathrm{rot}} = B_v J(J+1) - D_v J^2(J+1)^2 - H_v J^3(J+1)^3 + \dots . \tag{1.7}$$

The series is in most practical cases terminated after the second order term, where the constant D_v accounts for the increasing moment of inertia due to centrifugal distortion. D_v normally is several orders of magnitude smaller than B_v (see Table 1.1). For nitrogen the centrifugal distortion is especially small owing to the rigidity of the triple bond, and D_0 for $^{14}N_2$ equals $5.76 \cdot 10^{-6}$ cm^{-1} [44]. Figure 1.2(b) shows the magnitude of the centrifugal correction to the rotational energy for nitrogen.

Despite its smallness, the centrifugal dephasing is observable in rotational wave packets that span many rotational levels. The bond softening upon rotational excitation has been brought to an extreme in the optical centrifuge, where a diatomic molecule is spun so fast that it eventually is torn apart into its two constituting atoms [48].

	B_0 in cm^{-1}	D_0 in cm^{-1}
H_2	60.853	0.0459
D_2	30.443	0.0114
$^{14}N_2$	1.989	5.76×10^{-6}
$^{15}N_2$	1.857	5.20×10^{-6}
$^{127}I_2$	0.037	4.25×10^{-9}

Tabelle 1.1: *Rotational constants* B_0 *and centrifugal constants* D_0 *in the vibrational ground state of various diatomic molecules [44, 49]. The rotational constant decreases with increasing mass, the magnitude of the centrifugal contribution is determined by the character of the internuclear bond.*

Rotational transitions can couple to the electromagnetic field. To resonantly excite a rotational level one has to use radiation in the far infrared to microwave region. Because of the exceedingly low rate of spontaneous emission in the long wavelength regime[2] rota-

---

[2] The density of states for the electromagnetic field in free space grows as ω^2, which in case of a dipole emitter in free space results in the expression for the Einstein coefficient for spontaneous emission $A = \omega^3 d_{12}^2/(3\pi\epsilon_0\hbar c^3)$.

tional transitions are not observed in spontaneous emission but rather in absorption or as stimulated emission. In homonuclear molecules, transitions between neighboring rotational levels are forbidden [45]. Homonuclear molecules do, however, show rotational Raman spectra since transitions mediated by an induced dipole via the anisotropy of polarizability are allowed [50, 51].

1.1.2 Homonuclear molecules

The rotational spectra of homonuclear molecules display lines of alternating intensities. As an example, in Fig. 1.3 the rotational Raman spectrum of $^{15}N_2$ is displayed. This structure is owing to the fact that in homonuclear molecules, and generally all molecules possessing a center of inversion, the nuclei behave as indistinguishable particles, and therefore the total molecular wave function must be symmetric for bosonic nuclei or antisymmetric for fermionic ones [45]. Rotational states with even J number are symmetric (even parity), states with odd J number antisymmetric (odd parity):

$$Y_J^M(\pi - \theta, \varphi + \pi) = (-1)^J Y_J^M(\theta, \varphi). \tag{1.8}$$

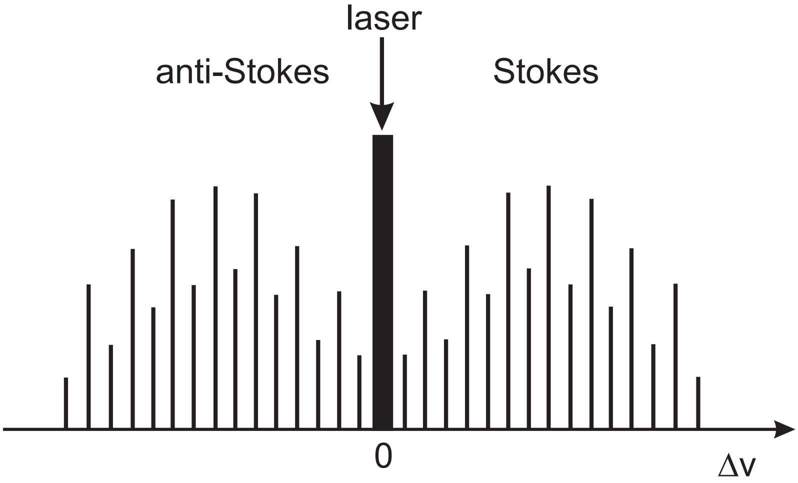

Abbildung 1.3: *Schematic pure rotational Raman spectrum of a homonuclear molecule displaying lines with alternating intensities.*

For two nuclei with nuclear spin I there are $(2I + 1)I$ possibilities to construct an antisymmetric spin wave function, and $(2I + 1)(I + 1)$ symmetric ones. Including the $(2J + 1)$fold degeneracy of a rotational level, one obtains the following weights g_s and g_a for symmetric and antisymmetric rotational states :

$$g_s^{\text{boson}} = g_a^{\text{fermion}} = (2J + 1)(2I + 1)(I + 1), \tag{1.9}$$

$$g_a^{\text{boson}} = g_s^{\text{fermion}} = (2J + 1)(2I + 1)I. \tag{1.10}$$

Generally, one has for the ratio of the weight factors:

$$\frac{g_a}{g_s} = \frac{I}{(I + 1)}, \tag{1.11}$$

and the weight of the relative population $w_T(J)$ of a particular J-level is obtained as a normalized product of degeneracy times the Boltzmann factor $e^{-E_J/kT}$:

$$w_T(J) = \frac{N_J}{N} = \frac{g_J e^{-E_J/kT}}{Q(T)}, \tag{1.12}$$

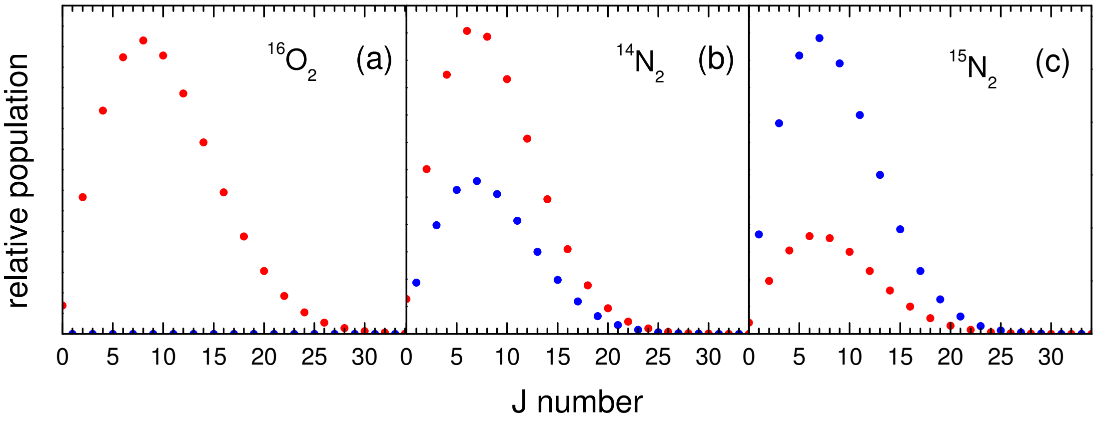

Abbildung 1.4: *Population of rotational levels for the homonuclear molecules* $^{16}O_2$ *(a),* $^{14}N_2$ *(b), and* $^{15}N_2$ *(c) at room temperature. The red symbols correspond to even J numbers, the blue symbols to odd J numbers.*

where $Q(T) = \sum_{J=0}^{\infty} g_J e^{-E_J/kT}$ is the partition function of the canonical ensemble. In $^{14}N_2$ with a nuclear spin $I = 1$, the ratio of population of even to odd rotational states is 2:1. The rotational distributions of $^{16}O_2$, and the two nitrogen species $^{14}N_2$ and $^{15}N_2$ are shown in Fig. 1.4. Usually, the more abundant species is termed ortho-, and less abundant one para-, thus the even parity species would be ortho-nitrogen, and the odd parity one para-nitrogen. The convention leads to sometimes confusing classifications, e.g. the even spin species of the hydrogen isotopes are para-hydrogen but ortho-deuterium.

1.2 Wave packet dynamics

1.2.1 Quantum mechanical wave packets

In order to describe a quantum system, it is necessary to specify its state. This is accomplished with minimal complexity using the eigenstates $\mid \Phi_n\rangle$ of the system, which are the solutions of the time-independent Schrödinger equation (TISE)

$$H \mid \Phi_n\rangle = E_n \mid \Phi_n\rangle, \qquad H = -\frac{\hbar^2}{2m}\Delta + V(r), \tag{1.13}$$

with E_n being the corresponding eigenvalue [45]. The eigenstates form a complete orthonormal basis for the description of the quantum system under the given boundary conditions. The unperturbed system is assumed to reside in one of its eigenstates, or a superposition of eigenstates with an e.g. thermal distribution of the statistical weight. In the first case, one refers to a pure state, in the second case the state is a so-called mixed state. A pure state is fully defined by a set of numbers corresponding to the eigenvalues of its constituting eigenstates. A quantum system in an eigenstate, the state being the solution of the TISE, does not display any time-dependence.

If the quantum system is now subjected to an additional potential, e.g. created by a laser electric field, the states defined by Eq. (1.13) are no longer eigenstates for the new combination of system and field. Still, it is convenient to retain the field-free eigenstates in the mathematical description if the perturbation is weak or time-dependent. To describe the action of the perturbation it is now necessary to modify the original state by an admixture of other eigenstates, much as in the decomposition of a spectrum into its Fourier components. The physical mechanism in the interaction is that the system is driven into a new equilibrium configuration imposed by the additional external potential. If the excitation is short compared to the time scale of the response, the system remains in a coherent superposition of field-free eigenstates. The coherence stems from the fixed phase relation given by the well defined instant in time of the excitation. An excitation of this kind may be well localized in time and space and evolve, at least initially, analogous to a bunch of classical trajectories. In this case, the prepared state is termed a wave packet. Wave packet states are now widely used to study nuclear and electron dynamics in a time-resolved way [52–54].

The extent to which the wave packet-like motion of a quantum system corresponds to a classical trajectory depends on the nature of the potential the wave packet is evolving in. Figure 1.5(a) shows the displacement versus time for the probability density of a wave packet created at the time t_0 at a displacement r_0 in a harmonic potential. The wave packet oscillates in the potential between the two turning points r_0 and r_{max} with a period τ_{cl} corresponding to the classical frequency of the harmonic oscillator. Throughout the propagation, the shape of the wave packet is retained. This is, however, a peculiarity of the harmonic potential, as it is the only potential in which frequency does not depend on energy. Generally potentials show dispersion, and thus a wave packet is maximally localized only at one particular time instant, the focusing time τ_{foc}. If the wave packet is created by resonant excitation, the focusing time can be shifted within a limited region by applying an excitation pulse with suitable chirp [55]. Under realistic conditions, however, it is impossible to have it propagate retaining its shape[3]. This is illustrated in Fig. 1.5(b) for a wave packet propagating in an anharmonic (Morse[4]) potential. The difference in the frequencies

---

[3] Sometimes this is referred to as dephasing. Mostly, however, the term dephasing is reserved for the loss of phase coherence and in this work it will be used in this context.

[4] The Morse potential is defined as $V(r) = D_e(1 - \exp[-\sqrt{k_e/2D_e}(r - r_e)])^2$ with D_e being the depth

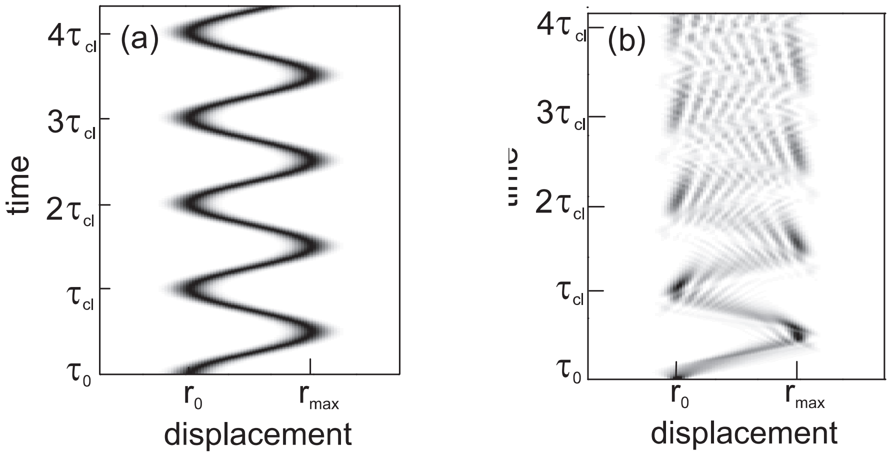

Abbildung 1.5: *(a) Probability density for a Gaussian wave packet displaced from the center of a harmonic potential to a starting point r_0 propagating in time between r_0 and r_{max}. The classical round trip time is denoted as τ_{cl}. (b) Gaussian wave packet propagating in an anharmonic (Morse) potential. [57].*

associated with the different energy levels leads to the probability density becoming less localized with increasing propagation time, until it covers the whole propagation region between r_0 and r_{max}. The small structures are caused by multiple interferences between the states composing the wave packet. This dispersion is a fully deterministic process and does not involve a loss of coherence, and the states of the wave packet thus can show interference even if the localization is lost.

1.2.2 Revivals of quantum wave packets

Dispersion leads to a broadening of a wave packet with increasing time. However, after the initial spread the oscillations of the states, or of a subset of the states, will rephase in many cases and form revivals. During these revivals, the wave function takes on a shape that is close, but not necessarily equal, to its original shape. Revivals are exemplified in Fig. 1.6 for rotational wave packets upon displacive and impulsive excitation. For the orientational state of a molecule, the relevant observable is usually the squared cosine of the angle θ between the molecular axis and the laser polarization direction. It will be discussed in greater detail in Sec. 1.3.2 and Fig. 1.9. In the displacive case, the excitation creates a strain on the medium from which it relaxes back into a new equilibrium. The wave packet thus at the instant of its creation finds itself displaced from the new equilibrium position and the dynamics in the substates starts at maximum amplitude with a common phase. The result are cosine-shaped oscillations, as exemplified in Fig. 1.6(a) for a rotational wave packet excited by rapidly switching off an external potential. In the impulsive case, the system receives a kick from the excitation, meaning that the substates start their propagation at zero displacement and propagate from there, resulting in sine-like oscillations as displayed in Fig. 1.6(b) for a rotational wave packet upon the excitation with a short symmetric laser pulse. The revivals in both cases are an almost ideal copy of the wave packet at the time of its creation. The small effect of centrifugal distortion, however, leads to a progressive modification of the shape of revivals with increasing time.

To characterize the time development of the wave function, frequently the autocorrela-

---

of the potential well, r_e the equilibrium bond distance and k_e the force constant. The expression is approximating the potential for vibrations in a diatomic molecule allowing for analytical solutions [56].

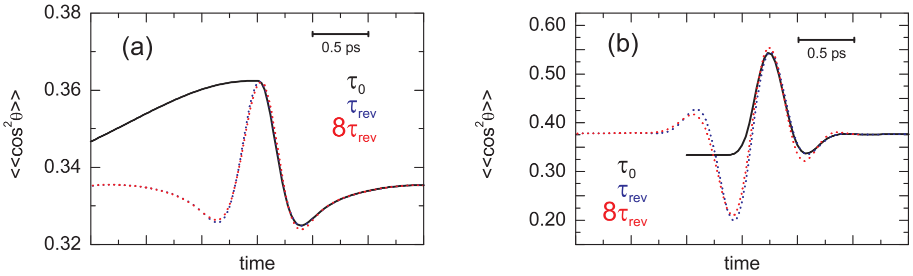

Abbildung 1.6: *Numerical simulation of revivals in the squared alignment cosine in the propagation of a rotational wave packet in nitrogen at 80 K. (a) Excitation with a laser pulse with 3 ps rise time and 30 fs fall time and a power density of 5 TW/cm^2, and (b) excitation with a Gaussian laser pulse of 150 fs FWHM duration and a power density of 50 TW/cm^2. Black: Shape of the wave packet at the time of its creation τ_0. Blue: The wave packet resumes at the first revival time τ_{rev}. Red: Wave packet at the eighth revival. The time scales are shifted by τ_{rev} and $8\tau_{\text{rev}}$, respectively, to show the similarity of shape. [62].*

tion $A(t) = \langle \Psi(t) | \Psi_0 \rangle$ is used, which yields the overlap of the propagated wave function $\Psi(t)$ at time t with the initial wave function Ψ_0. In case the initial wave function has a smooth, e.g. Gaussian shape, this amounts to a convolution with a smooth function, the effect of which is just to broaden the peaks. In these cases, a common and more intuitive presentation is the time-dependent probability density $\langle \Psi(t) \mid \Psi(t) \rangle$. For a rotational wave packet, the characteristic quantity is the time dependence of the projection of the wave packet $\langle\langle \cos^2\theta \rangle\rangle$ on an external axis[5].

A Taylor analysis of the dependence of energy E_n on the quantum level n, as it is performed in Ref. 59, gives insight into the mechanism that leads to the appearance of revivals. The propagation of the wave packet appears to be governed by distinct time scales:

$$\tau_{\text{cl}} = \frac{2\pi\hbar}{|E'(n_0)|}, \quad \tau_{\text{rev}} = \frac{2\pi\hbar}{|E''(n_0)|/2}, \quad \text{and} \quad \tau_{\text{superrev}} = \frac{2\pi\hbar}{|E'''(n_0)|/6}, \tag{1.15}$$

where $E'(n_0) = (\partial E/\partial n)|_{n=n_0} \ldots$ τ_{cl} is associated with the classical period of motion in the bound state (cf. Fig. 1.5), τ_{rev} is the quantum revival time, and τ_{superrev} is governing the behavior on even longer time scales. Inserting the relation $E(J) = BJ(J+1)$ for the rigid rotor approximation, one obtains a revival time of $1/2B$ (see also Sec. 1.3.2). The exact treatment using the formalism of Ref. 59 can be found in Ref. 60. In the case of nitrogen, the difference in the calculated revival times for the non-rigid rotor is negligible due to the smallness of the centrifugal correction. For systems with purely quadratic energy dependence, like e.g. the rigid rotor, no times beyond the revival time exist, and the motion repeats itself perfectly after a time interval corresponding to one revival time. In most realistic cases, however, the quadratic energy scale is an approximation, and corrections like centrifugal effects in rotation lead to the recurrences becoming more and more imperfect with time (Fig. 1.6). In this case, the rephasing would again lead to a better reproduction of the original shape on the superrevival time scale [61]. This time, however, under experimental conditions by far exceeds the achievable coherence times.

---

[5] Another wide spread function used to analyze the propagation of wave packets in position- and momentum space is the Wigner function. The Wigner transform maps quantum mechanical operators onto phase space:

$$W(\mathbf{r}, \mathbf{p}) = \frac{1}{(2\pi)^3} \int \Psi^*(\mathbf{r} + \hbar\mathbf{s}/2)\Psi(\mathbf{r} - \hbar\mathbf{s}/2)e^{i\mathbf{ps}} d^3 s. \tag{1.14}$$

Though it is a powerful tool in the study of quantum wave packets and interferences, the Wigner transform for the higher rotational eigenstates is not established in the literature [58].

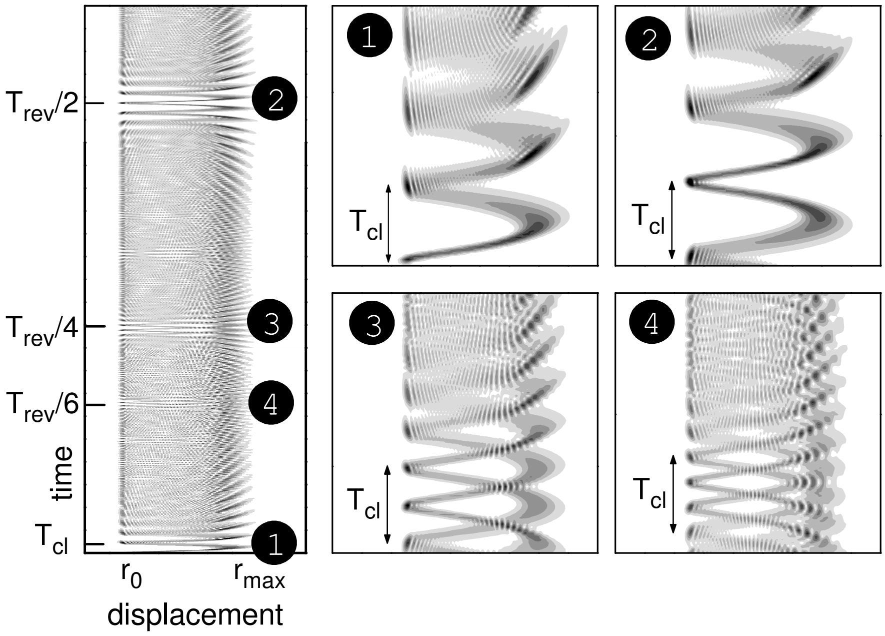

Abbildung 1.7: *Left panel: Wave packet propagating in a Morse potential at various time instants. Four distinct points in time are marked by numbers from 1 to 4 and shown with expanded time scale in the right panels. 1: The wave packet at the time of its creation. 2: Time corresponding to half of the revival time τ_{rev}. 3: The wave packet at a quarter of the revival time. 4: The wave packet at one sixth of the revival time [66].*

1.2.3 Fractional revivals

A closer look at the wave packet between revival times reveals a rich structure of bursts of coherence with different amplitudes exhibiting frequencies that are multiples of the classical rotational period [63, 64]. These fractional revivals for a wave packet propagating in a Morse potential are displayed in Fig. 1.7. Shortly after the time of its creation, the wave packet oscillates between the two turning points r_0 and r_{max} with the classical oscillation time τ_{cl} ((1) in Fig. 1.7), breaking up into increasingly small structures with time. At times between τ_0 and the full revival time τ_{rev}, several particular instants can be found, where the wave packet fully or partially regains its initial shape. At half of the full revival time, the wave packet has resumed its original shape and the oscillation proceeds with the classical period ((2) in Fig. 1.7). This is termed a half revival. At a quarter of the full revival time τ_{rev}, twice the classical period appears in the motion ((3) in Fig. 1.7), corresponding to the formation of two copies of the initial wave packet at opposite sides of the classical trajectory (the “cat state”, named after Schrödingers (in)famous cat [65]). At one sixth of τ_{rev}, an oscillation at three times the classical frequency is observable, corresponding to the breaking up of the original wave packet into three parts ((4) in Fig. 1.7).

This behavior can be understood by analyzing in detail the phase relationships arising in the time evolution of the individual states forming the wave packet and is treated in detail in Refs. 59 and 63. In particular, at $t = \tau_{\text{rev}}/2$, the wave packet appears to reform and oscillate at the classical frequency, however half a period out of phase. For a rotational wave packet, the projection with $\cos^2\theta$ averages out any fractional revivals higher than half revivals. As an exception, quarter revivals can be observed in homonuclear molecules, and they also show a mirror symmetry similar to the one observed in half and full revivals. The

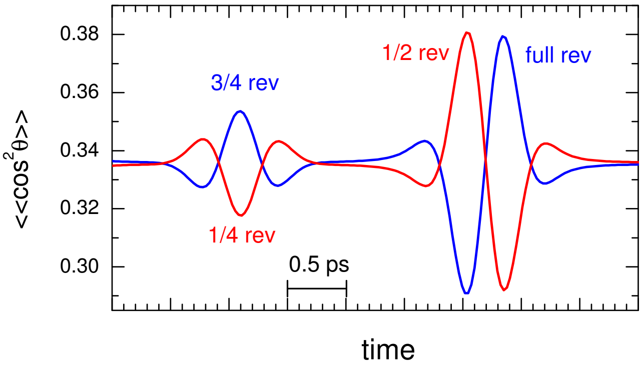

Abbildung 1.8: *Mirror symmetry in fractional revivals. Numerical simulation of the squared alignment cosine for the first revival period of a rotational wave packet in nitrogen gas at 80 K. Four distinct recurrences appear, the full revival at τ_{rev}, the half revival at $\tau_{\mathrm{rev}}/2$, the quarter revival at $\tau_{\mathrm{rev}}/4$, and the three quarter revival at $3\tau_{\mathrm{rev}}/4$. To emphasize the mirror symmetry, the red curve is an alignment trace shifted by $\tau_{\mathrm{rev}}/2$ to later times with respect to the blue curve [62].*

phase relationships for rotational revivals and quarter revivals are exemplified in Fig. 1.8.

1.2.4 Decoherence: dephasing and dissipation

Coherence is defined as a fixed phase relation between waves. In a wave packet, coherence is established as the excitation process imposes a common phase on the oscillations between eigenstates. In the subsequent propagation, the wave packet can interact with its environment, and thus its phase and possibly energy will be modified compared to free propagation. The processes and effects that lead to the wave packet losing its original shape are:

- **Dispersion:** Dispersion is the broadening of the wave packet due to the difference in phase velocities of the elementary waves. Though the amplitude of the wave packet is decreased progressively, dispersion does not correspond to a loss of coherence.

- **Dissipation, Depopulation or Energy relaxation:** Energy relaxation is the exchange of energy of a wave packet component with the environment. The mechanism in our case is a statistical collision and it necessarily is connected with a statistical change in phase.

- **Dephasing:** Dephasing is the loss of coherence by energy relaxation or by **pure dephasing**, i.e. loss of phase without transfer of energy. Pure dephasing takes place for example if the individual molecules making up the wave packet are surrounded by different potentials.

- **Decoherence:** Decoherence refers to the loss of coherence and is used synonymously with dephasing.

Dissipation or energy relaxation is associated with a characteristic time scale T_1. The loss of energy in general comes along with a loss of the common phase (dephasing), which is characterized by the dephasing time T_2. The characteristic time related to pure dephasing is termed T_2^*. It is important to notice that it is not the interaction with the environment that destroys coherence but rather the randomness of the processes affecting different particles[6]. Decoherence therefore is an effect that occurs as the individual members of an ensemble of coherently moving particles lose the fixed phase relation in the course of the propagation.

---

[6] Various experiments show that even in the presence of collisions the motion of a sub-ensemble of particles can stay coherent, if only the history of all particles in this sub-ensemble is the same [67–70].

1.3 Laser-induced molecular alignment

1.3.1 State of the art in the field

To manipulate the orientation of molecules with respect to the laboratory frame has been an active field of research over already many decades. The aim is to study direction-dependent properties of molecules without averaging over orientations or to use the oriented ensemble as a tool, e.g. to manipulate radiation or to control chemical reactions. One way to fix the orientation of particles like molecules and nano-objects is to embed them in a matrix like a glass [71], cryogenic noble gases [72], or polymers [73, 74] that can additionally be stretched to control the direction in which molecules are oriented [75, 76]. If the molecules are to be oriented in free space this can be achieved by employing static magnetic or electric fields [77, 78]. This approach, also known as *brute force orientation*, has the drawback of requiring extremely high dc field strength due to the smallness of molecular dipole moments. Very high field strengths, however, are easily reached in the focus of an intense, or a pulsed, laser beam.

The slow rotational dynamics can be addressed already with picosecond pulse sources, and thus the ivestigation of coherent rotational dynamics was an object of interest already relatively early in the history of wave packet studies. The existence of revivals of rotational wave packets, termed susceptibility echoes, in linear molecular gases was predicted theoretically in Ref. 79 by Lin, Heritage and Gustafson in 1971, and later realized experimentally by the same authors in CS_2 vapor [80]. A detailed theoretical treatment of coherent rotational states can be found in Refs. 81 and 82. To study molecular properties such as rotational and centrifugal constants supported by an analytical theoretical approach based on second-order perturbation theory, the Raman-Induced Polarization Spectroscopy (RIPS) or Rotational Coherence Spectroscopy (RCS) was developed in later years [83]. It differs from what is now commonly termed alignment in the laser intensities applied, which in the framework of RIPS/RCS are in the perturbative limit. In this limit one observes rotational wave packet dynamics with alternating peaks of alignment and anti-alignment, while the overall anisotropy is still negligible. RIPS has been successfully applied to describe and study rotational coherence in complex symmetric and asymmetric top molecules [84–88], and to extract either concentrations [89, 90] or polarizability ratios [91, 92] and temperature [93] from gas mixtures. The alignment of molecules involves the creation of an anisotropy in the sample, in addition to the coherent revivals which yield no net alignment. Under steady-state conditions, alignment is caused by the formation of pendular states in the laser field ([4–6]), for a short pulse by a non-thermal population of M-quantum levels ([7, 9, 30]). Experimental demonstrations of alignment in intense laser fields were first carried out in species with large anisotropic polarizability like iodine [94–96]. Later, lighter molecules, as well as symmetric [97] and asymmetric top molecules [86, 98–100] were treated. Beyond the application of single Gaussian-shaped pulses an optimization of alignment in the non-adiabatic regime was found to be possible using vibrational resonance [101, 102] as well as pulse shaping [25, 27, 103–106] and optimal control strategies [107–110]. A combination of a static electric field allows to orient rather than align molecules with a permanent dipole [111, 112], and a combination of adiabatic turn-on with rapid turn off of a laser pulse was put forward as possible optimization strategy [113, 114]. Large molecules are aligned in two [115] or three dimensions [116] using elliptically polarized laser pulses. Control of alignment of large molecules [14, 117] by shaping the electric field of the pulse was extended theoretically even to control of intra-molecular torsion [118].

Beyond the study of the phenomenon of alignment itself, aligned ensembles of molecules are used to provide targets with well-defined spatial orientation for subsequent investigation or manipulation. These include the study of direction-dependent properties, e.g. ionization [26, 119–123], imaging of molecular orbitals through x-ray diffraction [124–126] or the generation of high harmonics [12, 13, 20, 28, 127]. Aligned ensembles are also used as tools, e.g. for the generation of attosecond laser pulses [120, 128–131] or the shaping of femtosecond pulses [132–137].

In all these experiments, the so-called post-pulse or field-free alignment [7] and rotational revivals are exploited. With the revival period governed by the least common multiple of the frequencies associated with the transitions excited, the motion of a rotational wave packet is a relatively slow process compared to the also widely studied vibrational or electronic wave packets [138, 139]. A manifold of approaches has been developed for the manipulation of these recurrences by adequately timed control pulses [21–23, 29, 31–33, 107, 140–148] and even use in quantum information schemes has been demonstrated [21, 39, 140].

1.3.2 The Schrödinger equation for rotational alignment

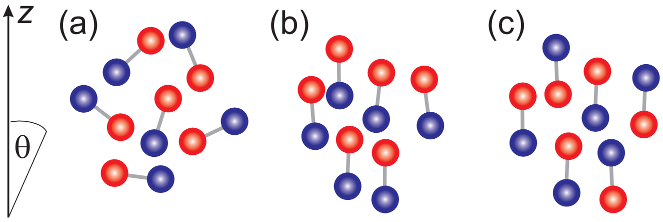

Abbildung 1.9: *(a) An ensemble of randomly oriented linear molecules. (b) Oriented molecules. (c) Aligned molecules.*

The term alignment refers to the molecular axes taking on a definite direction with respect to a space-fixed coordinate system. In contrast to orientation, alignment does not contain any discrimination between *up* and *down* directionality (Fig. 1.9). For the interaction with a linearly polarized laser pulse, the preferred z-axis of this coordinate system is usually given by the direction of the electric field vector of the laser beam. Here we will limit the discussion to only the case of linear diatomic molecules. In this case, the angle θ the molecular axis forms with the electric field direction z is sufficient to characterize the alignment of the molecule.

Consider an ensemble of randomly oriented molecules as in Fig. 1.9(a). To quantify the degree of directionality the molecules show with respect to an external axis z, usually the expectation value $\langle\cos\theta\rangle$ of the angle θ the molecular axis forms with the z axis is calculated, and subsequently averaged over the ensemble. The ensemble averaged expectation value will be denoted as $\langle\langle\cos\rangle\rangle$. For an isotropic ensemble all directions are equally probable, and thus $\langle\langle\cos\theta\rangle\rangle = 0$. For the oriented ensemble one has $\langle\langle\cos\theta\rangle\rangle > 0$, however, an aligned ensemble again has $\langle\langle\cos\theta\rangle\rangle = 0$. Therefore, to characterize the degree of alignment, the expectation value of the squared orientation cosine is used. $\langle\langle\cos^2\theta\rangle\rangle = 1/3$ for an isotropic ensemble, and it deviates from this value for oriented as well as for aligned ensembles.

The interaction of a molecule with the electric field of a laser pulse is mediated via the polarizability α by the induced dipole arising from the electrons following the fast oscillations of the electric field (Fig. 1.10). Even if the molecule possesses a permanent dipole moment, the effective potential averaged over the fast oscillations of the laser field is zero and only the induced dipole contributes to the interaction. The potential created by the electric field is determined by the difference in polarizabilities along the main axes of the molecule. For a diatomic molecule in an electronic Σ-state, $\alpha_{\|}$ parallel to the molecular axis is larger than $\alpha_{\perp}$ perpendicular to it. The anisotropy of the polarizability $\Delta\alpha$ for a linear molecule is the difference between the polarizability $\alpha_{\|}$ parallel to the molecular axis

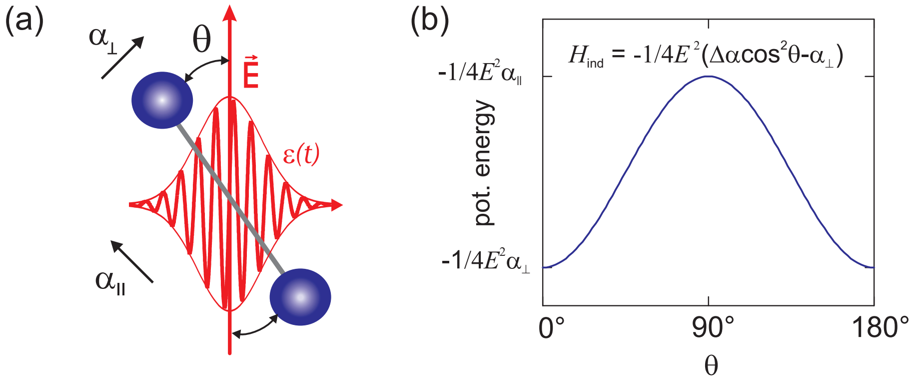

Abbildung 1.10: *(a) A molecule in an aligning laser field with field strength E and pulse envelope $\varepsilon(t)$. A force on the molecule results if the polarizabilities $\alpha_{||}$ and $\alpha_\perp$ are different. (b) Potential energy of a molecule with anisotropic polarizability $\Delta\alpha = \alpha_{||} - \alpha_\perp$ in an electric field E versus orientation angle θ. The potential has $\cos^2\theta$ shape with minima both for parallel and antiparallel orientation of molecular axis and field vector.*

and the polarizability $\alpha_\perp$ perpendicular to the axis:

$$\Delta\alpha = \alpha_{||} - \alpha_\perp. \tag{1.16}$$

Far away from any resonance the potential a linear molecule experiences in a rapidly alternating field[7] is described as [5, 6]

$$H_{\text{ind}}(\theta, t) = -\frac{1}{4}\Delta\alpha E^2(t)\cos^2\theta - \frac{1}{4}\alpha_\perp E^2(t). \tag{1.17}$$

The electric field $E(t)$ is the amplitude of the electric field of the laser. The inertia of the nuclei corresponds to a rotation on a picosecond time scale, and except for the lightest molecule H_2 [58], does not allow them to follow the fast femtosecond oscillations of the field. The interaction potential is thus determined by only the laser pulse envelope.

The rotational alignment of a linear diatomic molecule is described by the time dependent Schrödinger equation (TDSE), rewritten in dimensionless form for generality:

$$\frac{i\hbar}{B}\frac{\partial}{\partial t}\Psi = \frac{H(t)}{B}\Psi. \tag{1.18}$$

Here, Ψ is the molecular wave function, and B the rotational constant of the molecule [141]. Analytical solutions of Eq. (1.18) exist for the impulsive and the classical limit [31, 32], as well as in the approximation of second-order perturbation theory [37]. For strong non-adiabatic pulses of finite duration, however, one has to resort to numerical evaluation of the rotational dynamics. Our numerical simulations of alignment dynamics were carried out by adapting a MATLAB code modeling the interaction of a diatomic molecule with a laser field with Gaussian pulse envelope, as it was used in Refs. 16 and 17. It is based on the WavePacket 4.7 software package [152], and will be described in greater detail in the following chapter.

The Hamiltonian for the non-resonant molecule field interaction is the sum of the Hamiltonian of the free molecule H_0 and the potential induced by the electric field $H_{\text{ind}}(t)$:

$$H(t) = H_0 + H_{\text{ind}}(t), \tag{1.19}$$

---

[7] This is the leading term of the multipole expansion derived by applying the rotating wave approximation. The derivation is outlined in Refs. 6 and 149 following Refs. 82, 150, 151.

where

$$H_0 = B\mathbf{J}^2 \quad \text{with} \quad H_0|JM\rangle = \left(BJ(J+1) - DJ^2(J+1)^2\right)|JM\rangle, \tag{1.20}$$

and $\mathbf{J}$ denoting the angular momentum operator. B is the rotational constant and $|JM\rangle$ is a rotational eigenstate characterized by the angular momentum quantum number J and its projection onto the laser polarization direction M. The last J- and time-independent term in Eq. (1.17) for the induced Hamiltonian is usually dropped at this point, as it does not give rise to any dynamics.

Frequently, the parameters $\Delta\alpha$, E, and B are combined to yield a dimensionless quantity $\Delta\omega$ characteristic of the strength of the interaction of the particular molecule with the laser field:

$$\omega_{\parallel} = \frac{\alpha_{\parallel}E^2(t)}{4B}, \qquad \omega_{\perp} = \frac{\alpha_{\perp}E^2(t)}{4B}, \tag{1.21}$$

$$\Delta\omega = \omega_{\parallel} - \omega_{\perp} = \frac{\Delta\alpha E^2(t)}{4B}. \tag{1.22}$$

For the $^{14}\mathrm{N}_2$-molecule in the vibrational ground state one has $B/hc = 1.989\ \mathrm{cm}^{-1}$ [44] and $\Delta\alpha = 0.89\ \text{Å}^3$ [1] with a characteristic rotational molecular time unit of $\hbar/(2B) = 8.38$ ps. A weak pulse is characterized by a $\Delta\omega$ of order of 10, strong pulses translate into $\Delta\omega$ of several 100. The limit of the experimentally feasible power density is given by the onset of competing nonlinear processes such as ionization. For nitrogen, this limit is reached around $\Delta\omega = 500$, corresponding to a power density of $10^{14}\ \mathrm{W/cm}^2$ for a 165 fs pulse [153, 154]. At this power density, the interaction potential exceeds the rotational energy up to the $J = 15$ rotational level in nitrogen. In the experimental part of this work, pulses will be applied with $\Delta\omega \approx 50$, corresponding to the rotational energy of the $J = 4$ level.

The rotational quantum state of a molecule is usually expanded in terms of eigenstates of the free rotor $|J'M'\rangle$ as

$$|\Psi_{JM}(t)\rangle = \sum_{J'M'} c^{(JM)}_{J'M'}(t)|J'M'\rangle, \tag{1.23}$$

where the time-dependence of the coefficients is accounting for the mixing of free rotor states during the pulse and after and where the initial conditions are given by $c^{(JM)}_{J'M'}(t = 0) = \delta_{JJ'}\delta_{MM'}$. After the termination of the pulse, the dynamics is reduced to analytical propagation of the coefficients for the functions representing the eigenstates of the free rotor.

Spherical harmonics are a convenient choice for the set of basis functions, being the eigenstates of the free rotor. With M being still a good quantum number owing to $\Delta M = 0$ for the excitation process with linearly polarized light, they form a natural basis even for the combined molecule-field system.

1.3.3 Density matrix representation

The alignment of a diatomic molecules is quantified by the expectation value of the squared alignment cosine $\cos^2\theta$ of the angle between molecular axis and laser pulse polarization direction. In a standard experiment, a thermal ensemble of molecules is studied. It can be conveniently described by the density matrix formalism, which was introduced to the field of alignment in Refs. 155 and 156. The density matrix $\hat{\rho}$ for a system in a mixed state is defined as $\hat{\rho} = \sum_J w(J)|\Psi_{JM}(t)\rangle\langle\Psi_{JM}(t)|$, which can be cast in $|JM\rangle$-representation as

$$\hat{\rho}(t) = \sum_{J'M'}\sum_{J''M''} \rho_{J'M'J''M''}(t)|J'M'\rangle\langle J''M''| \tag{1.24}$$

with

$$\rho_{J'M'J''M''}(t) = \sum_{JM} w(J)(c^{(JM)}_{J''M''}(t))^* c^{(JM)}_{J'M'}(t). \tag{1.25}$$

The time-evolution of the density operator $\hat{\rho}$ is expressed in terms of the quantum Liouville-von-Neumann equation:

$$\frac{d\hat{\rho}(t)}{dt} = -\frac{i}{\hbar}[\hat{H}_0 + \hat{H}_{\mathrm{ind}}(t), \hat{\rho}], \tag{1.26}$$

where the initial density is chosen corresponding to a thermal ensemble. Though alignment of quantum state-selected molecules has recently been demonstrated experimentally [14, 15, 157], separating molecules into specific quantum states remains a very demanding task [158]. Thus, with few exceptions, e.g. para-hydrogen [36], in an experiment, one observes a "density packet" resulting from averaging of densities rather than wave functions in the thermal ensemble. The dynamics of the ensemble is characterized by the ensemble averaged squared alignment cosine $\langle\langle\cos^2\theta\rangle\rangle(t)$, which is expressed in terms of the density operator $\hat{\rho}(t)$ as

$$\langle\langle\cos^2\theta\rangle\rangle(t) = \mathrm{Tr}\{\cos^2\theta\hat{\rho}(t)\}, \tag{1.27}$$

where Tr denotes the trace of the matrix product.

With alignment in a thermal ensemble one has to carefully distinguish between the values associated with individual molecules in originally pure rotational states, and the thermal average. In our notation, the expectation value $\langle\cos^2\theta\rangle_{JM}$ describes the mean alignment of a wave packet, as the dynamics originates solely from the coherent superposition of rotational transitions excited in the molecule-field interaction of one originally pure state $|J, M\rangle$. The wave packet state is denoted as $|\Psi_{JM}\rangle$ with the probability density ρ_{JM}, with the subscript JM referring to the initial pure state characterized by a set of quantum numbers J and M. $\langle\langle\cos^2\theta\rangle\rangle_J$ represents the mean alignment averaged over all wave packets originating from the rotational level J. The corresponding density packet is described as incoherent averaging with equally weighted M-states:

$$\rho_J(t) = \frac{1}{2J+1}\sum_{M=-J}^{J}\rho_{JM}(t). \tag{1.28}$$

The mean alignment of a thermal density packet with additional averaging over all populated rotational levels is represented as $\langle\langle\cos^2\theta\rangle\rangle_T$. The time-dependent density in this case is expressed as

$$\rho_T(t) = \sum_J w_T(J)\rho_J(t), \tag{1.29}$$

with the distribution of the coefficients $w_T(J)$ given by the thermal Boltzmann distribution and nuclear spin effects according to Eq. (1.12).

1.3.4 Adiabatic alignment

According to the adiabatic theorem, the transition probability for a quantum system to a different state upon a perturbation becomes infinitely small if only the perturbation is evolving slow enough and there is a sufficient energy gap between the occupied state and other possible eigenstates [159–161]. For adiabatic alignment, the laser pulse must be much longer than the characteristic rotational timescales in the aligned system. Molecules are aligned only during the interaction with the field, the rotational states being transferred into their adiabatically correlated pendant, the so-called pendular states [4, 162, 163]. The

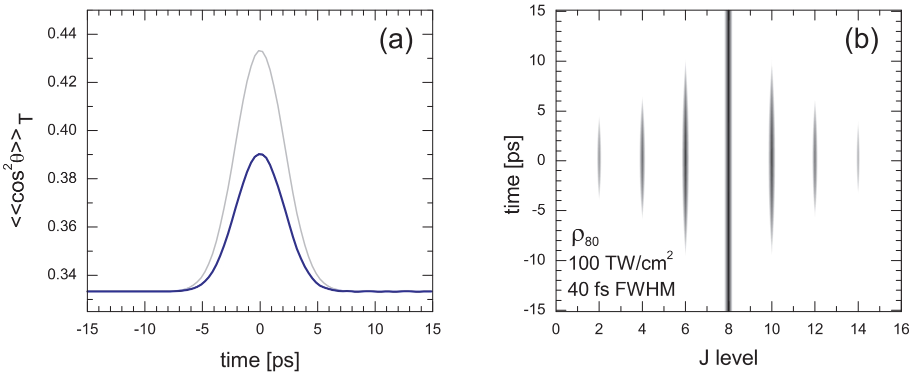

Abbildung 1.11: *Numerical simulation of adiabatic alignment induced in* $^{14}N_2$ *at 80 K by a Gaussian laser pulse with 5 ps FWHM and a power density of 10 TW/cm*^{2}*. (a)* $\langle\langle \cos^2\theta \rangle\rangle$ *versus time (blue line). The pulse envelope is shown as a gray line. Alignment is high only during the pulse and removed with the trailing edge. (b) Logarithmic plot of the population of J levels for the state* $\mid \Psi_{80}\rangle$*. The state during the rising edge of the pulse is described by an increasingly large number of populated J levels, while the M quantum number is conserved. With the trailing edge of the pulse, the distribution is returned to its initial value [62].*

pendular states are eigenstates for the combined molecule-field system, which in their shape reflect the cylinder symmetry of the problem. For every free rotor state there is an adiabatically correlated pendular state characterized by the quantum numbers M, which for linearly polarized light is conserved and still a good quantum number and $\bar{J}$, the nominal value of the angular momentum that adiabatically correlates with the free rotor state. For a long laser pulse, the free rotor states adiabatically evolve into pendular states during the leading edge of the pulse and back into free rotor states during the trailing edge. The ensemble averaged expectation value of the squared alignment cosine and the evolving distribution of free rotor states in the $\mid \Psi_{80}\rangle$ rotational wave packet describing adiabatic alignment is shown in Fig. 1.11 for $^{14}\mathrm{N}_2$ at 80 K. High degrees of alignment can be reached by Rabi-type oscillations via rotational ladder climbing during the pulse with the applicable field strength only limited by the onset of ionization in the sample [164, 165]. The adiabatic alignment of molecules is used in the experiment mostly to align large molecules, for which the time scale for possible revivals is exceedingly large because of very small rotational level spacing [14, 157, 166]

1.3.5 Non-adiabatic alignment

In the non-adiabatic limit the laser pulse is significantly shorter than the rotational period of the molecule. In this case, the molecular response time is too slow to follow the rapidly changing potential. The induced polarization cannot be coherently re-emitted, and thus the rotationally excited molecules persist in their motion after the turn-off of the pulse. Figure 1.12(a) displays the coherent rotational motion in a selection of $\mid \Psi_{JM}\rangle$ rotational levels.

The common phase imprinted in the rotationally excited ensemble by the laser pulse yields wave packet dynamics with revivals of alignment after the turn-off of the pulse, as is it shown in Fig. 1.12(b). For very short pulses, due to the inertia of nuclei, the maximum of alignment is reached after the maximum of the pulse. This situation is referred to as post-pulse or field-free alignment [7, 30]. The period with which the pattern repeats itself is given by the inverse of twice the rotational constant of the molecule. This periodicity can be understood by considering the rotational frequencies of the excited molecules.

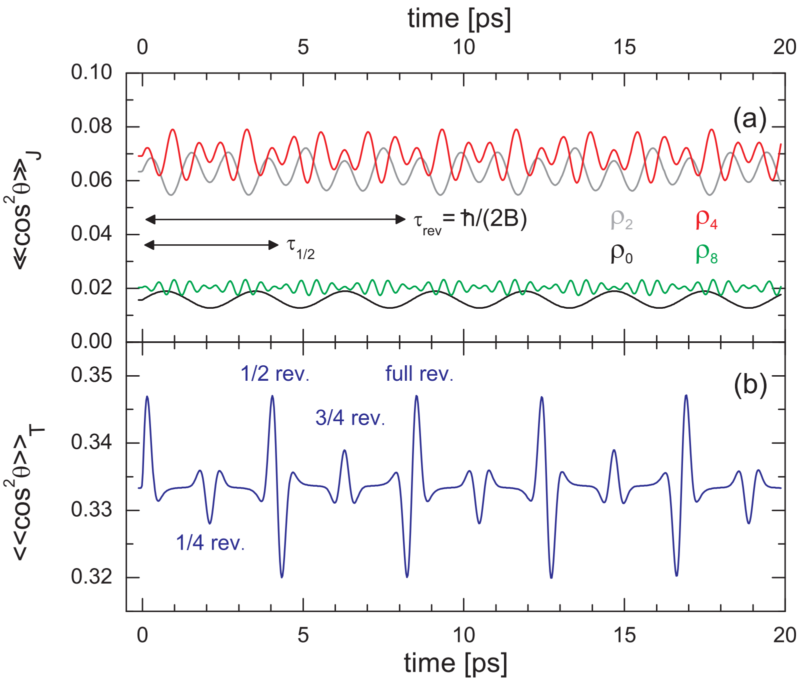

Abbildung 1.12: *Numerical simulation of rotational dynamics in an ensemble of* $^{14}N_2$ *at 80 K induced by a Gaussian laser pulse with 40 fs FWHM and a power density of 10 TW/cm*^{2}*. (a) Dynamics in the* ρ_0*,* ρ_2*,* ρ_4*, and* ρ_8 *rotational density packets and the ensemble average displaying prominent revival features at characteristic time intervals (b). Oscillations in the individual rotational levels add up constructively to form overall revivals at times defined by the GCD of the frequencies. The full revival time is indicated in (a) as* τ_{rev} *and the time characteristic for the half revival as* $\tau_{1/2}$ *[62].*

Every rotational eigenstate J is associated with an energy $E(J) = BJ(J+1)$. The transition frequencies ω_{rot} for Raman-type transitions with $\Delta J = \pm 2$, represent the oscillation frequencies of these superpositions, and are expressed as

$$\omega_{\mathrm{rot}} \propto E(J_f) - E(J_i) = B(J_i \pm 2)(J_i \pm 2 + 1) - BJ_i(J_i + 1) = 2B(\pm J_i + (2 \pm 1)), \quad (1.30)$$

where $J_f = J_i \pm 2 \geq 0$ must be fulfilled.

In case of only one initial state J excited by a weak pulse, the post-pulse dynamics would proceed with exactly this frequency (Fig. 1.12(a)). For a thermal ensemble, however, the observable oscillations arise from the beating of rotations of molecules with a thermal initial J distribution. The beating pattern displays dynamics governed by the greatest common divisor (GCD) of the beating frequencies. In the case of the frequencies of Eq. (1.30) one has $\omega_{0\to 2} = 6B, \omega_{1\to 3} = 10B, \omega_{2\to 4} = 14B, \omega_{3\to 5} = 18B, \ldots$. The GCD for this series is exactly $2B$ and determines the timescale for the appearance of full revivals, denoted as τ_{rev} in Fig. 1.12(a) (see slso Sec. 1.2.2). At half of this time (denoted as $\tau_{1/2}$) a half revival appears, which is a mirror image of the full revival as discussed Sec. 1.2.2. Both major revivals show a sine-like shape typical for an impulsive excitation process. Half and full revivals appear in the temporal alignment trace of all diatomic molecules. The features around one quarter and three-quarters of the revival time are, however, peculiar for homonuclear molecules.

Homonuclear molecules in general exist in two subspecies with symmetric and antisymmetric nuclear spin states (cf. Sec. 1.1.2). These species do not easily convert into each other, as the conversion requires a nuclear spin flip. In $^{14}N_2$ with the nuclear spin $I = 1$,

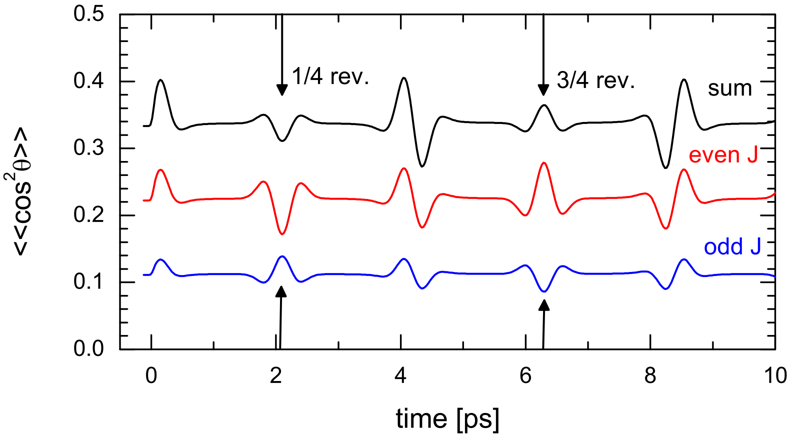

Abbildung 1.13: *Numerical simulation of rotational dynamics in an ensemble of* $^{14}N_2$ *at 80 K induced by a Gaussian laser pulse with 40 fs FWHM and a power density of 50 TW/cm*^{2}*. The total squared alignment cosine (black line) is additionally shown decomposed into the parts due to even (red line) and odd (blue line) rotational states. Times for quarter and three-quarter revivals are indicated by vertical arrows [62].*

molecules in even rotational levels are twice as abundant (ortho-nitrogen) as molecules in odd rotational states (para-nitrogen). Raman-type excitations do not mix the two subspecies due to the $\Delta J = \pm 2$ selection rule. Each species has a progression of rotational frequencies as in Eq. (1.30) with the spacing in energy increased by a factor of two, and thus the spacing in time decreased equally by a factor of two. The alignment transients for ortho- and para-nitrogen are plotted separately in Fig. (1.13) as red and blue lines, respectively. The transients add up constructively at the half and full revival times. At times that correspond to one quarter and three quarters of the revival time, however, alignment peaks appear to be in opposite phase for even and odd rotational states. For heteronuclear molecules these quarter- and three-quarter-revivals exactly cancel each other, for homonuclear molecules they partially survive due to even or odd states being more populated [140]. An extreme case is represented by ^{16}O, where due to the nuclear spin $I = 0$, only even rotational levels are populated, and the quarter revivals display the same amplitude as half and full revivals [167, 168].

1.3.6 Population and coherence parts of alignment

For a random ensemble of diatomic molecules, all angles of orientation of the molecular axis with respect to an external axis appear with equal probability, and the average of the squared orientation cosine amounts to $\langle\langle\cos^2\theta\rangle\rangle = 1/3$. The coherent post-pulse alignment results in deviations to the positive as well as to the negative side around an average value larger than 1/3. Oscillations and the offset from 1/3 are contained in the off-diagonal and in the diagonal elements of the density matrix, respectively, which can easily decomposed into these parts. In the diagonal elements projecting a state $|JM\rangle$ onto itself the population of the eigenstates $|JM\rangle$ is represented. The diagonal population part of the squared alignment cosine will be referred to as $\langle\langle\cos^2\theta\rangle\rangle_p$ following the convention of Ref. 155:

$$\langle\langle\cos^2\theta\rangle\rangle_p(t) = \sum_{J'M'} \langle J'M'|\cos^2\theta|J'M'\rangle \rho_{J'M'J'M'}(t), \tag{1.31}$$

which is time-dependent only as long as population is redistributed under the action of the external field. The $\Delta M = 0$ selection rule for excitation with linearly polarized light leads

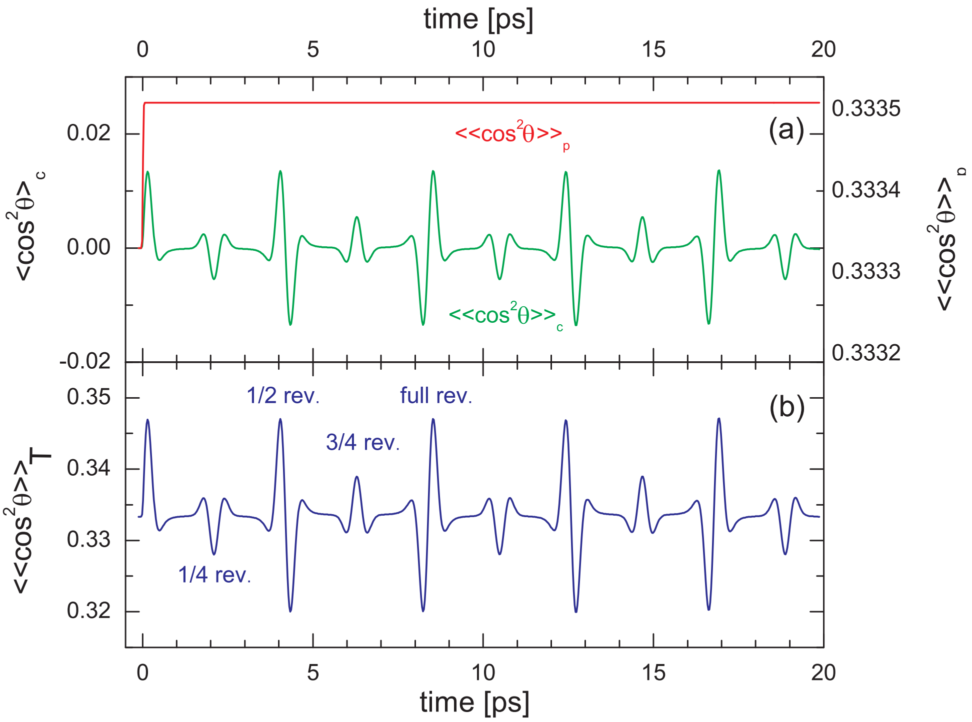

Abbildung 1.14: *Numerical simulation of rotational dynamics in an ensemble of* $^{14}N_2$ *at 80 K induced by a Gaussian laser pulse with 40 fs FWHM and a power density of 10 TW/cm*^{2}*. (a) Squared alignment cosine decomposed into its* $\langle\langle\cos^2\theta\rangle\rangle_c(t)$ *and* $\langle\langle\cos^2\theta\rangle\rangle_p(t)$ *parts. (b) Total* $\langle\langle\cos^2\theta\rangle\rangle$*, corresponding to the sum of the* $\langle\langle\cos^2\theta\rangle\rangle_c(t)$ *and* $\langle\langle\cos^2\theta\rangle\rangle_p(t)$ *parts [62].*

to the value of $\langle\langle\cos^2\theta\rangle\rangle_p$ increasing beyond the isotropic value of $1/3$ as for every additional J level reached in the rotational ladder climbing the highest M quantum numbers, which have the smallest projection on the polarization axis, are not populated.

The coherence part of the squared alignment cosine is accordingly [155] expressed as

$$\langle\langle\cos^2\theta\rangle\rangle_c(t) = \sum_{\substack{J'\neq J'' \\ M'\neq M''}} \langle J'M'|\cos^2\theta|J''M''\rangle\rho_{J'M'J''M''}(t). \tag{1.32}$$

The off-diagonal matrix elements represent the coherences between different eigenstates and for a particular non-zero $\rho_{J'M'J''M''}$ oscillate at the beating frequency of the two eigenenergies. The coherence contribution $\langle\langle\cos^2\theta\rangle\rangle_c$ can by definition take on positive or negative values, depending on whether the direction of molecular axes at a particular instant in time tends to increase or to diminish the alignment with respect to the laser field direction. The total alignment trace and its decomposition into $\langle\langle\cos^2\theta\rangle\rangle_c$ and $\langle\langle\cos^2\theta\rangle\rangle_p$ is shown in Fig. 1.14. By definition, for all times one has $\langle\langle\cos^2\theta\rangle\rangle(t) = \langle\langle\cos^2\theta\rangle\rangle_p(t) + \langle\langle\cos^2\theta\rangle\rangle_c(t)$. Note that the changes in $\langle\langle\cos^2\theta\rangle\rangle_p$ under our experimental conditions are only about $2{\times}10^{-3}$, and one order of magnitude smaller than for $\langle\langle\cos^2\theta\rangle\rangle_c(t)$.

2 Numerical simulations

2.1 Simulation methods

Within the framework of Raman Induced Polarization Spectroscopy (RIPS) and Rotational Coherence Spectroscopy (RCS) analytical expressions for the time dependence of $\langle\langle \cos^2\theta \rangle\rangle$ were derived by a second order perturbation theory analysis [37, 83]. This approach captures the dynamics resulting from coherent coupling of rotational levels by a single Raman transition, however, it fails if a significant repopulation of rotational levels is involved. This repopulation, on the other hand, contributes to the dynamics already at moderate field strengths ($\Delta\omega \approx 10$, comparable to our experimental conditions). Therefore, as soon as non-perturbative laser intensities are employed, the problem is referred to as alignment of molecules rather than rotational coherence, and one has to resort to numerical modeling of the dynamics.

Our numerical simulations of non-adiabatic alignment were carried out in collaboration with Dr. Burkhard Schmidt (project C5 of Sfb 450, Department for Mathematics, Free University Berlin). They were performed by adapting a MATLAB code used in Refs. 16 and 17 to model the interaction of a diatomic molecule with a laser field, using the WavePacket 4.7 software package [152]. The program numerically solves the dimensionless Schrödinger equation

$$i\frac{\hbar}{B}\frac{\partial \mid \Psi_{JM}\rangle(t)}{\partial t} = \frac{H(t)}{B} \mid \Psi_{JM}\rangle(t), \tag{2.1}$$

in state space with subsequent thermal averaging. This is equivalent to the solution of a set of coupled ordinary differential equations (ODE) for the time-dependent coefficients $d_{JM}(t)$ of a state vector $\Psi = \sum_{JM} d_{JM}(t) Y_J^M$. The statistical weight $w(J)$ for every $|\Psi_{JM}(t)\rangle$ state is determined from the multiplicity $w_I(J)$ of symmetric and anti-symmetric nuclear spin states and the rotational partition function (see also Sec. 1.1.2) according to

$$w(J) = w_I(J)(2J+1)\frac{e^{-BJ(J+1)/k_BT}}{\sum_J w_I(J)(2J+1)\exp\left[-BJ(J+1)/k_BT\right]}, \tag{2.2}$$

where T denotes the rotational temperature and k_B being the Boltzmann constant. In units of k_B/B the dimensionless temperature Θ for $^{14}N_2$ corresponds to 28 at 80 K, and 105 at 300 K. Due to the small spacing of rotational levels a large number of states is populated even at low temperature. The ^{14}N isotope is a boson with $I = 1$. Thus the homonuclear molecule $^{14}N_2$ displays two subspecies with symmetric and antisymmetric nuclear spin states with $w_I^{\text{even}} = (2I+1)(I+1) = 6$ and $w_I^{\text{odd}} = (2I+1)I = 3$.

The original code used in Refs. 16 and 17 was extended to account for nuclear spin statistics, and to decompose the squared alignment cosine into its coherence and population parts (see Sec. 1.3.3). If not otherwise stated, all graphs displaying rotational alignment dynamics were generated using this program.

The numerical solution of the Schrödinger equation Eq. (2.1) is performed for every populated rotational state $\mid JM\rangle$ using a MATLAB inbuilt ODE solver (ode113) optimized for the solution of non-stiff problems based on a variable order multistep Adams-Bashforth-Moulton algorithm with adaptive timesteps [169]. All computations are performed in dimensionless units using molecular time units $\hbar/B$ to achieve optimal accuracy. The cutoff in J for the initial state vector is set to typically 10^{-4} of the total population. The numerical basis was extended to more than the populated states to account for rotational ladder climbing during excitation. This overhead ranges from 10 states for moderate intensities to 30 states for high intensities or adiabatic alignment to assure that numerical convergence is achieved. On the time axis, the numerical integration is extended to typically $\pm 5\sigma$ with σ being the variance of the laser pulse. In this part of computations, the centrifugal distortion effects are neglected due to the relative shortness of the time scale. The numerical integration routine then returns a new wave function $\Psi_{JM} = \sum_{J'M'} c_{J'M'}^{(JM)} \mid J'M' \rangle$ which is already a superposition of pure rotational states. This new wave function is then propagated under field-free conditions by multiplication with the propagator $e^{-iH(t-t_0)}$ with the time t in reduced molecular time units $\hbar/B$, and a resolution corresponding to typically 33 fs to match the resolution of experimental data:

$$\mid \Psi_{JM}(t)\rangle = e^{-iH(t-t_0)} \mid \Psi_{JM}(t_0)\rangle, \qquad H = J(J+1) - DJ^2(J+1)^2/B. \tag{2.3}$$

For every $\Psi_{JM}(t)$ the time-dependent expectation value of the squared alignment cosine is split into its population and coherent part and evaluated in a spherical harmonics basis according to

$$\langle JM| \cos^2\theta \mid JM\rangle = \frac{1}{3} + \frac{2}{3}\frac{(J(J+1) - 3M^2)}{(2J+3)(2J-1)} \tag{2.4}$$

for the diagonal elements giving $\langle \cos^2\theta\rangle_p$ and

$$\langle JM| \cos^2\theta \mid (J+2)M\rangle = \frac{((2J+1)(2J+5)(J+1-M)(J+2-M)(J+1+M)(J+2+M))^{\frac{1}{2}}}{(2J+1)(2J+3)(2J+5)}, \tag{2.5}$$

$$\langle JM| \cos^2\theta \mid (J-2)M\rangle = \frac{((2J-3)(2J+1)(J-1-M)(J-M)(J-1+M)(J+M))^{\frac{1}{2}}}{(2J-3)(2J-1)(2J+1)}. \tag{2.6}$$

for the off-diagonal elements coupling different states and yielding $\langle \cos^2\theta\rangle_c$. These are the only non-vanishing matrix elements, which, keeping in mind that $\cos^2\theta = Y_2^0$, can be found by evaluating the corresponding Wigner 3j symbols [170]. $\langle \cos^2\theta\rangle_p$ and $\langle \cos^2\theta\rangle_c$ are calculated for every state J by summing up the contributions of all existing M levels. From this, the ensemble averaged expectation values $\langle\langle \cos^2\theta \rangle\rangle_p$ and $\langle\langle \cos^2\theta \rangle\rangle_c$ are then calculated by summing up the individual contributions of all states $\mid JM\rangle$ multiplied with their respective statistical weight $w(J)$.

Computations were run on personal computers with typically 1.5 GHz processors and 512 MB RAM. With these settings, the calculation of $\langle\langle \cos^2\theta \rangle\rangle$ at the experimentally relevant temperature of 80 K for an excitation pulse of 165 fs, corresponding to numerically computing the dynamics of all states up to $J = 17$, took about 5 minutes. The time consumption is relatively weakly dependent on the total length of the trace, as the propagation after the pulse turn-off requires only the fast matrix multiplication. Most of the computation time is required by the ODE solver. With every state $\mid JM\rangle$ being computed successively, the computational complexity scales approximately as $\sum_J (J+1) \approx J^2$. Additionally, the duration of the excitation pulse determines the time span covered by numerical integration, and thus the pulse length enters linearly in the computation time. Though the shape of the oscillations is mainly determined by highly populated J levels, and within these mainly by states with low M number, for a quantitative analysis it is nevertheless important to include also states with little influence on the dynamics, as they are important in obtaining correct values for the population contribution and the isotropic starting value of 1/3.

2.2 Laser-induced alignment of rotationally excited molecules

In this Section, we numerically investigate the post-pulse alignment of rotationally excited diatomic molecules. We show that:

- **Depending on the M quantum number, the interaction with the laser field can involve emission of energy as well as absorption, and that these two processes lead to opposite motion of the molecular axis with respect to the laser polarization direction.**
- **For a laser pulse duration comparable to the molecular rotational period, the crossover from non-adiabatic to adiabatic limits is well described by a convolution of excitation pulse envelope and sinusoidal molecular response and that it takes place in a uniform way in the region between 0.1 and 1 for the ratio of pulse duration to rotational period.**
- **For higher intensities, the rotational wave packet contains a greater manifold of coupled rotational levels, for which the degree of adiabaticity varies. Differences in the rotational period in the excited transitions for appropriate laser pulse parameters lead to the formation of a region in which anti-alignment, or rotational cooling, dominates over alignment, or rotational heating.**

2.2.1 Directionality effects

Rotationally excited molecules can exchange energy with the laser field by absorption and by stimulated emission in Stokes- and anti Stokes-processes. With the additional selection rule $\Delta M = 0$ in a linearly polarized field, this leads to a modification of the mean alignment of the molecules. Figure 2.1 shows the mean alignments

$$p^0_{JM} = \langle JM|\cos^2\theta|JM\rangle, \tag{2.7}$$

from $M = 0$ to $M = 8$, where $\langle JM|\cos^2\theta|JM\rangle$ is given by Eq. (2.4), of a state $|JM\rangle$ onto the laser polarization direction. For constant M, corresponding to the states coupled in the interaction with a linearly polarized laser, the curves are monotonically increasing functions of J, approaching a common limiting value of $1/2$. The only exception is the curve for $M = 0$, which overshoots at small J and returns to $1/2$. For all rotational states one has

$$\langle\langle\cos^2\theta\rangle\rangle_J = \frac{1}{2J+1}\sum_{M=-J}^{J} p^0_{JM} = \frac{1}{3}\,. \tag{2.8}$$

A $\Delta J = +2, \Delta M = 0$ rotational transition thus leads to an increase in the mean alignment because of the increase in the value with J for constant M and also because the highest M states cannot be populated. In the following, we refer to this ascent of the ladder of rotational states as an aligning transition. Classically, this corresponds to a narrowing of the cone the molecular axis forms with the field polarization direction and at the same time an acceleration of the motion in the direction of the field vector, caused by the increase in rotational energy, see left inset of Fig. 2.1.

The $\Delta J = -2, \Delta M = 0$ rotational transition, on the other hand, decreases the mean alignment. This descent on the J-ladder will be referred to as anti-aligning transition. Classically, the molecule loses rotational energy to the field, and the axis moves away from the polarization direction into anti-alignment, see right inset of Fig. 2.1. In strong fields,

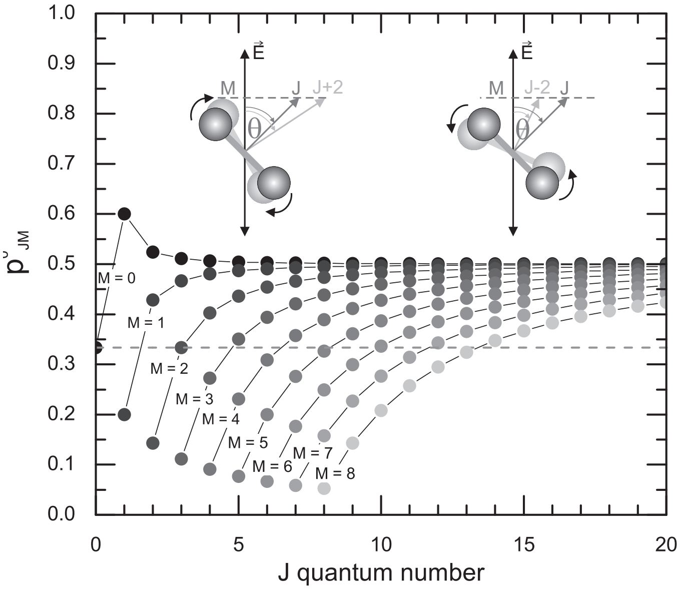

Abbildung 2.1: *Plot of the diagonal elements of the* $\cos^2\theta$*-matrix* $\rho^0_{JM} = \langle J, M|\cos^2\theta|J, M\rangle$ *from* $M = 0$ *to* $M = 8$. *The dashed horizontal line represents the average value of 1/3. Left inset: Increase in molecular alignment upon a* $\Delta J = +2$, $\Delta M = 0$ *transition. Right inset: Decrease of alignment in a* $\Delta J = -2$, $\Delta M = 0$ *transition.*

the motion away from the polarization direction is eventually stopped and a librational motion about the polarization axis is enforced [2, 5].

The matrix elements for the ascending and descending transitions to the $J + 2$ and the $J - 2$ rotational levels are given by the off-diagonal elements of the transition matrix according to Eqs. (2.5) and (2.6) and will be abbreviated as

$$p^+_{JM} = \langle J, M|\cos^2\theta|J + 2, M\rangle, \quad \text{and} \tag{2.9}$$

$$p^-_{JM} = \langle J, M|\cos^2\theta|J - 2, M\rangle. \tag{2.10}$$

These matrix elements show a dependence very similar to the diagonal ones plotted in Fig. 2.1, rising for a constant M from a certain minimal value asymptotically to 1/2. Figure 2.2 shows the ratio p^+_{JM}/p^-_{JM} from $J = 2$ to $J = 8$. The transition to the higher rotational state is thus favored because of the better overlap, with the difference for probabilities of absorption and emission being most pronounced for $J \approx M$, i.e. the largest possible M. An exception is again the case of $M = 0$, where the curve is essentially J-independent after an initial increase.

The ensemble-averaged squared alignment cosine is expressed in terms of the coefficients of the wave function according to Eq. (1.25) and the projection matrix elements according to Eqs. (2.5) and (2.6) as

$$\langle\langle\cos^2\theta\rangle\rangle_T(t) = \sum_{\substack{J'M'\\J''M'}} \langle J'M'|\cos^2\theta|J''M'\rangle \sum_{JM} w_T(J)\rho^{(JM)}_{J'M'J''M'}(t), \tag{2.11}$$

where $w_T(J)$ is given by Eq. (1.12), and

$$\rho^{(JM)}_{J'M'J''M'}(t) = |\Psi_{J''M'}(t)\rangle\langle\Psi_{J'M'}(t)| = \left(c^{(JM)}_{J''M'}(t)\right)^* c^{(JM)}_{J'M'}(t)|J'', M'\rangle\langle J', M'|. \tag{2.12}$$

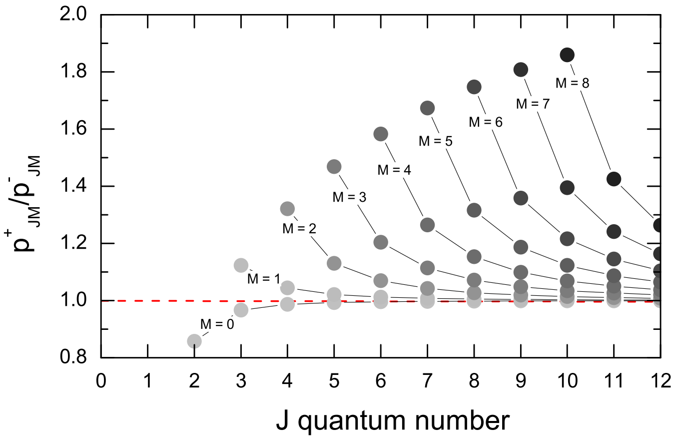

Abbildung 2.2: *Ratio of transition probabilities* p^+_{JM}/p^-_{JM} *to the* $J+2$ *and* $J-2$ *rotational levels for* $2 \leq J \leq 8$*. Equal probability is represented by the dashed horizontal line.*

For the coefficients of the freely evolving wave packet after the termination of the laser pulse at time t_f one has

$$c^{(JM)}_{J'M'}(t > t_f) = c^{(JM)}_{J'M'}(t_f) \exp\left[i\frac{B}{\hbar} J'(J'+1)(t-t_f) \right]. \tag{2.13}$$

Using Eqs. (2.4-2.6), Eq. (2.11) can be rewritten as

$$\begin{aligned} \langle\langle \cos^2\theta \rangle\rangle_T(t) = \quad & \textstyle\sum_{J'M'} p^0_{J'M'} \sum_{JM} w_T(J) \rho^{(JM)}_{J'M'}(t_f) \quad + \qquad (2.14) \\ & \textstyle\sum_{\substack{J'M' \\ J+2,M'}} p^+_{J'M'} \exp\left[-i\frac{B}{\hbar}(4J'+6)(t-t_f)\right] \sum_{JM} w_T(J) \rho^{(JM)}_{J'M'J+2M'}(t_f) \quad + \\ & \textstyle\sum_{\substack{J'M' \\ J-2,M'}} p^-_{J'M'} \exp\left[i\frac{B}{\hbar}(4J'+2)(t-t_f)\right] \sum_{JM} w_T(J) \rho^{(JM)}_{J'M'J-2M'}(t_f). \end{aligned}$$

Here, the time-independent first term gives the temporal average, about which the alignment is oscillating. The frequencies contributing to the time-dependent signal are

$$\begin{aligned} -B(4J'+6) \quad & \text{for} \quad \Delta J = +2, \quad \text{and} \qquad (2.15) \\ B(4J'+2) \quad & \text{for} \quad \Delta J = -2. \qquad (2.16) \end{aligned}$$

Note that Stokes- and anti-Stokes transitions contribute with opposite sign to the time-dependent alignment dynamics.

The post-pulse alignment observed in a ρ_{JM} rotational wave packet upon the non-adiabatic excitation with a short laser pulse of moderate power density is exemplified in Fig. 2.3(a) using the ρ_{80}, ρ_{86}, and ρ_{88} rotational wave packets. Plotted are the time-dependent squared alignment cosines $\langle \cos^2\theta \rangle_{JM}$ for the corresponding wave functions. According to Fig. 2.2, the observed dynamics should show some directionality-dependent peculiarities. For the ρ_{80} wave packet, the transition probabilities for $\Delta J = +2$ and $\Delta J = -2$ transitions are almost identical. For the case of ρ_{86}, the ratio of transition matrix elements is 1.7, favoring the $\Delta J = +2$ rotational transition. The resulting alignment pattern for the ρ_{80} and ρ_{86} wave packets thus is a beating of two oscillations, the frequencies of which are given by the transition energies of 75. 6 cm^{-1} to the $J = 10$ and 59.7 cm^{-1} for the $J = 6$ rotational levels. The rotational periods for these transitions are 0.441 ps and 0.559 ps, respectively. The value of $\langle \cos^2\theta \rangle_{JM}$ in the $J \rightarrow J+2$ transition is increased beyond p^0_{JM} (Fig. 2.1), while the value of $\langle \cos^2\theta \rangle_{JM}$ in the $J \rightarrow J-2$ transition is decreased. The

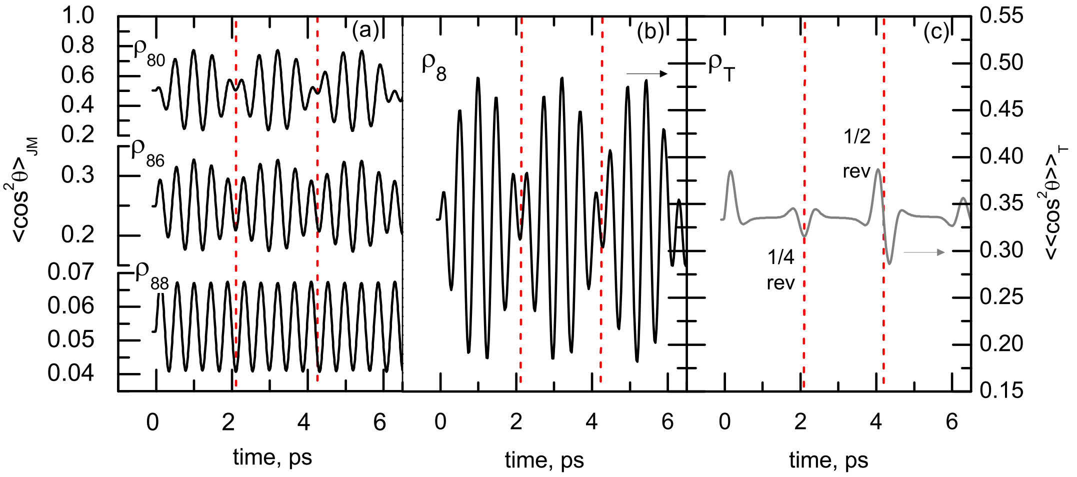

Abbildung 2.3: *(a) Numerical simulation of wave packet dynamics in the ρ_{80}, ρ_{86}, and ρ_{88} rotational states upon the excitation with a Gaussian laser pulse of 30 fs FWHM and a power density of 50 TW/cm^2. (b) Direction averaged densities ρ_8 under the same conditions. (c) Thermally averaged density packet ρ_T with weighting of states corresponding to 80 K. In all parts, the first quarter and half revival times are marked by vertical dashed lines.*

overall dynamics of the wave packet can thus be decomposed into two counterpropagating and thus beating parts.

For the ρ_{88} rotational wave packet, the coupling to the $J-2$ rotational level is forbidden, as $M > J-2$. The resulting dynamics, displayed in the lower trace in Fig. 2.3(a), are sinusoidal with the single frequency corresponding to the $J = 8 \rightarrow 10$ rotational transition. The directional average ρ_8 in Fig. 2.3(b) retains the characteristic beating amplitude, as for most of its M-substates the coupling to lower rotational levels is possible.

The ensemble average of the alignment at a temperature of 80 K is displayed in Fig. 2.3(c). It shows a pronounced revival peak at $\tau_{1/2} = \hbar/(4B) = 4.18$ ps and a smaller feature at $\tau_{1/4} = \hbar/(8B) = 2.1$ ps. This quarter revival is particular for homonuclear molecules and originates from the imperfect cancellation of contributions from even and odd rotational states due to the different statistical weights in the thermal distribution [63]. In the individual rotational levels, the quarter revivals appear with the same amplitude as full and half revivals [22].

The times for the first quarter and first half revivals are highlighted in the time traces of Fig. 2.3 by dashed vertical lines. Where both aligning and anti-aligning transitions are present, the curves for the individual wave packets in Fig. 2.3(a) display a remarkably low amplitude of alignment at the revival times. This is due to the mutual cancellation caused by the counterpropagating $\Delta J = +2$ and $\Delta J = -2$ parts. High values of alignment are reached at intermediate times. This alignment, however, is averaged out in the ensemble averaged $\langle\langle\cos^2\theta\rangle\rangle_T$., which explains the strong decrease of alignment amplitude in the revivals upon heating [164, 171]. At high temperature, a large fraction of molecules is thermally rotationally excited, and transitions occur to both the lower and the higher lying rotational states. The higher the original J rotational level, the more substates can make an anti-Stokes transition and the more complete is the mutual cancellation of alignment and anti-alignment around the revival times.

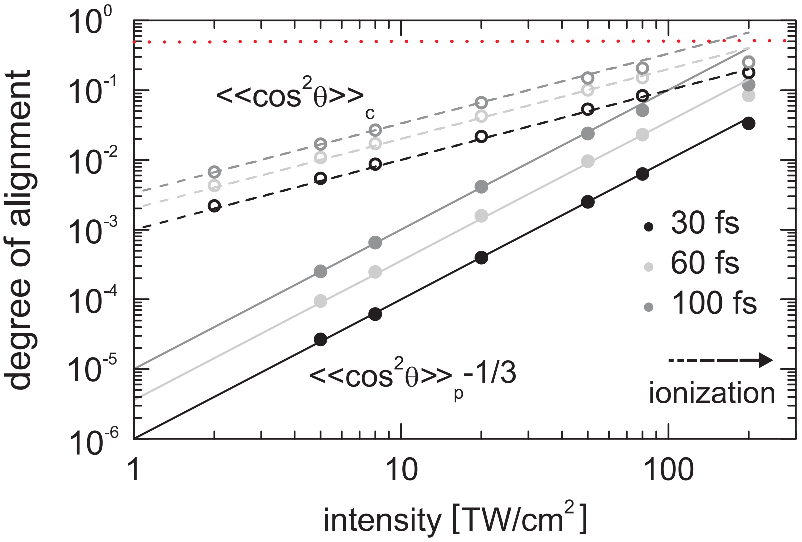

Abbildung 2.4: *Dependence of maximal deviation of post-pulse values of the ensemble averaged population contribution* $\langle\langle \cos^2\theta\rangle\rangle_p$ *(solid circles) and coherent contribution* $\langle\langle \cos^2\theta\rangle\rangle_c$ *(open circles) from their respective isotropic values on laser pulse power density. The results of numerical simulations for alignment in* $^{14}N_2$ *upon excitation by Gaussian laser pulses with pulse durations of 30 fs, 60 fs, and 100 fs FWHM at a temperature of 80 K are plotted on a double-logarithmic scale. Solid lines represent overlaid quadratic dependences, and dashed lines overlaid linear dependences. The limiting value of 1/2 is represented by the dotted horizontal line.*

2.2.2 Pulse power effects

To quantify the response of a system to a laser pulse with a given duration, additionally the influence of the pulse power density has to be taken into account. The efficiency of a Raman-type process like the non-resonant rotational excitation generating molecular alignment in general depends quadratically on the applied laser intensity. However, the quadratic dependence in population of levels does not necessarily translate into a quadratic dependence of the squared cosine $\langle\langle \cos^2\theta\rangle\rangle$. In Fig. 2.4 the maximal amplitudes reached in numerical simulations of alignment in $^{14}N_2$ at 80 K by the ensemble averaged expectation values $\langle\langle \cos^2\theta\rangle\rangle_p$ and $\langle\langle \cos^2\theta\rangle\rangle_c$ above their field-free values of 1/3 and zero, respectively, are plotted on a double-logarithmic scale. The population part, represented by solid circles and solid lines, very well follows a quadratic dependence over a wide range of power densities. The maximal amplitude reached by the coherence contribution $\langle\langle \cos^2\theta\rangle\rangle_c$ after the pulse equally well can be described by a linear dependence over a range of power densities up to 100 TW/cm^2, which corresponds to an interaction strength of $\Delta\omega \approx 500$ in dimensionless units. At higher power densities, both parts show a saturation behavior in the simulated alignment as they approach the limiting value of 1/2 [156], represented by the dotted red line. However, alignment in such high fields is competing with ionization, making this region inaccessible to alignment experiments. A closer inspection of the overlaid lines reveals that the intercepts at lines of constant intensity depend quadratically in the case of $\langle\langle \cos^2\theta\rangle\rangle_p$ and linearly in the case of $\langle\langle \cos^2\theta\rangle\rangle_c$ on the relative pulse power densities. Thus, for moderate intensities the parameter defining the amplitudes of alignment, i.e. $\langle\langle \cos^2\theta\rangle\rangle_c$, reached by non-adiabatic excitation is the total energy contained in the laser pulse, confirming the findings of Ref. 164. The same behavior was also noted for the classical limit [31].

2.2.3 Pulse duration effects

2.2.3.1 Adiabatic vs. non-adiabatic dynamics

A quantum wave packet with its characteristic recurrences in time is formed by coherently exciting a superposition of a finite number of quantum states with discrete frequencies, which persist in coherent motion after the excitation pulse is turned off [59, 63]. To initiate this post-pulse coherent dynamics, the perturbation of a set of quantum states by the laser field must be short compared to the characteristic transition frequencies. In this case, termed non-adiabatic, the coupling of states at the time of the excitation imprints a common phase on the subsequent evolution, and the laser field is turned off too fast to allow for complete elimination of the induced polarization (cf. Sec. 1.3.2). Non-adiabatically excited wave packets can be manipulated in a number of ways by applying shaped pulses or pulse trains to achieve constructive or destructive interferences, and thus to amplify or to erase the coherent post-pulse motion [172, 173] (cf. Sec. 1.3.1). In contrast, for an adiabatic interaction, the perturbation of the quantum system by the laser proceeds on a time scale slow enough for every state of the system to evolve into the adiabatically correlated state and to return fully reversibly back into its initial condition.

The parameter defining whether the interaction is classified as adiabatic or non-adiabatic is the ratio of the timescale characteristic of the molecular motion, in the present case the rotational period τ_{rot}, and the duration of the laser pulse τ_p the molecule interacts with. For very long pulses ($\tau_p \gg \tau_{\mathrm{rot}}$) the interaction is classified as adiabatic, and for very short pulses ($\tau_p \ll \tau_{\mathrm{rot}}$) it is classified as non-adiabatic. To determine the character of the interaction of a nitrogen molecule with a laser pulse of a given duration, one has to find the rotational state the molecule occupies and the characteristic rotational period associated with it. The rotational distribution for the $^{14}\mathrm{N}_2$-molecule is exemplified in Fig. 2.5(a) for 80 K, close to the liquefaction temperature of 77.4 K, and at room temperature. Due to the small spacing of rotational levels a large number of states is populated even at low temperature. With the frequencies derived from Eq. (1.30) as $(4J+6)B/\hbar$ for a transition from J to $J+2$ the characteristic rotational periods are 2.79 ps, 1.19 ps, 0.69 ps, 0.44 ps and 0.24 ps for the $J=0\rightarrow 2$, $J=2\rightarrow 4$, $J=4\rightarrow 6$, $J=8\rightarrow 10$, and $J=16\rightarrow 18$ transitions of the $^{14}\mathrm{N}_2$-molecule, respectively (Fig. 2.5(b)). The behavior of rotational quantum states interacting with a laser pulse in the completely adiabatic and the completely non-adiabatic regimes has been investigated in Refs. 164 and 111. These limiting cases, however, are not sufficient for a description of alignment under typical experimental conditions. For the nitrogen molecule and a typical Ti:sapphire laser pulse of 30 fs FWHM duration the partly adiabatic regime is reached already for the $J=12\rightarrow 14$ rotational Raman transition. At room temperature, molecules occupying rotational levels with $J\geq 12$ comprise about a quarter of the total population. The pulse duration of the wide-spread Ti:sapphire amplified fiber oscillators with 150 fs FWHM exceeds the strictly non-adiabatic limit in nitrogen for all except the $J=0\rightarrow 2$ rotational transitions. The segregation into adiabatic and non-adiabatic parts with the rotational distribution is therefore expected to play an important role under standard experimental conditions.

2.2.3.2 Interaction with a weak laser pulse

In Fig. 2.4 we showed that for moderate pulse power densities the parameter defining the amplitudes of alignment reached by non-adiabatic excitation is the total energy contained in the laser pulse. Deviations appear if the laser pulse starts approaching the rotational period of the molecules. Owing to the complexity of the problem, there is a lack of qualitative or semi-quantitative models explaining the physical processes behind this behavior and

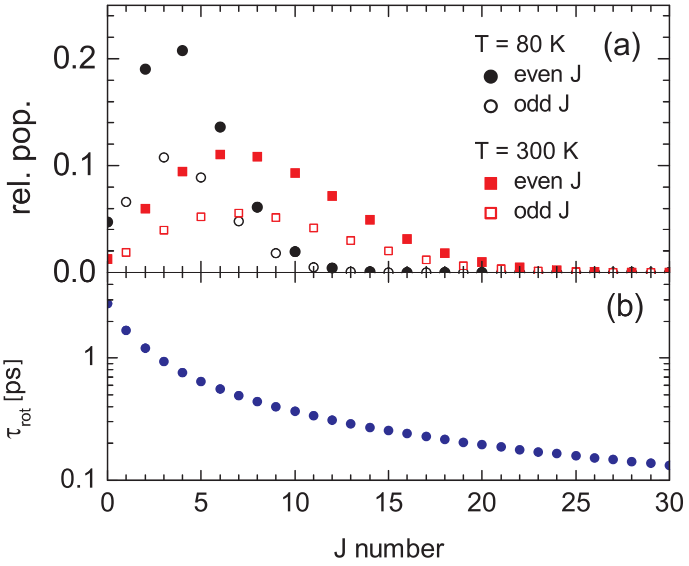

Abbildung 2.5: *(a) Population of rotational levels for* $^{14}N_2$ *at 80 K (black symbols) and 300 K (red symbols).* ^{14}N *being a boson with* $I = 1$*, nuclear spin statistics for homonuclear molecules requires the even J levels being twice more populated than the odd ones. (b) Semilogarithmic plot of rotational period* τ_{rot} *vs. J quantum number.*

allowing to develop an intuition as to the outcome of an alignment experiment under given conditions. The existing analytical descriptions, moreover are restricted to the $J = 0$ rotational state as calculations become prohibitively complex for rotationally excited levels. We show that for moderate laser power an analytical qualitative model, convolving the laser pulse envelope with a rotational response with appropriate frequency, describes surprisingly well the dynamic observed in individual rotational levels as well as the transition between the non-adiabatic and adiabatic regimes.

Within the approximation of an undepleted two-level system, the response of a quantum state to a perturbation is described by a sinusoidal oscillation at the beating frequency ω of the eigenenergy of the two levels [174]. For a Gaussian laser pulse with finite duration, the convolution of the sinusoidal system response with the laser pulse envelope can be evaluated analytically and leads to oscillatory post-pulse dynamics at the transition frequency ω with a maximal amplitude exponentially dampened by the squared ratio of rotational frequency to pulse duration:

$$\rho_{J'M'J'+2M'}(t) \propto \int_{-\infty}^{\infty} \exp\left(-at'^2\right) \sin\omega(t-t')dt'$$
$$= \int_{-\infty}^{\infty} \exp\left(-at'^2\right) \left[\sin\omega t \cos\omega t' + \sin\omega t' \cos\omega t\right] dt'. \tag{2.17}$$

The second term in the sum integrates to zero, and thus the expression is reduced to

$$\rho_{J'M'J'+2M'}(t) \propto \sin\omega t \int_{-\infty}^{\infty} \exp\left(-at'^2\right) \cos\omega t' dt' = \exp\left(-\frac{\omega^2}{4a}\right) \sin\omega t, \tag{2.18}$$

corresponding to oscillatory post-pulse dynamics at the transition frequency ω with a maximal amplitude exponentially dampened by the squared ratio of rotational frequency to pulse duration. In terms of rotational transitions, the convolution yields the magnitude of the off-diagonal elements of the density matrix $\rho_{J'M'J'\pm 2M'}(t)$ up to a J-dependent amplitude, and the frequency ω is the J-dependent frequency of the rotational transition. [37, 38].

Now we proceed to apply this model to the non-adiabatic to adiabatic transition and the decay of the alignment amplitude brought about by this. To characterize the rotational timescale we choose the transition to the $J+2$ rotational level because the oscillation is faster than for the $\Delta J = -2$ rotational transition and thus it poses a stricter limit on the pulse duration. The pulse duration is characterized by $a = 4\ln 2/\tau_p^2$, with τ_p being the FWHM of the pulse envelope. Transforming the units into the dimensionless ratio of pulse FWHM to rotational period (Fig. 2.5(b)) by setting $\omega_J^2/4a_p = \pi^2/(4\ln 2)(\tau_p/\tau_{rot}(J))^2$ one can transform Eq. (2.18) into a universal dependence

$$\rho_{J'M'J'+2M'}(t) \propto \exp\left[-\frac{\pi^2}{4\ln 2}\left(\frac{\tau_p}{\tau_{rot}(J')}\right)^2\right] \tag{2.19}$$

for the post-pulse amplitude of all J levels plotted as black solid curve in Fig. 2.6. To show that this dependence really holds for coherent rotational dynamics, we numerically solve Eq. (1.26) for a range of pulse durations from 20 to 1280 fs FWHM. The transition from the non-adiabatic to the adiabatic limit obtained from the numerical simulations for rotational levels between $J = 0$ and $J = 16$ is shown in Fig. 2.6 as colored symbols. The simulated maximal post-pulse amplitude of the coherent contribution $\langle\cos^2\theta\rangle_c$ normalized by the amplitude $\langle\cos^2\theta\rangle_{c,\max}$ reached for the shortest pulse is plotted for each J versus the ratio of pulse duration to rotational period τ_{rot} of the corresponding $J \to J+2$ transition. The variation of amplitudes with pulse duration confirms the analytic model of Eq. (2.17). A least squares fit of a Gaussian dependence (gray curve) to the data results in a FWHM of 1.01 in dimensionless units compared to $4\ln 2/\pi$ ($\approx$0.88) for the result of the convolution. Up to a ratio of 0.1, or the rotational period exceeding the pulse duration by at least a factor of 10, the relative values of $\langle\cos^2\theta\rangle_c$ remain close to unity for all J. Though the most efficient pulse appears to be a δ-pulse, the decay in amplitude is slow enough to justify the assumption that in this region the alignment amplitude depends only on integrated pulse power density. In the region around the flat top of the Gaussian, the interaction thus can be classified as non-adiabatic. In case of significant rotational ladder climbing, the limiting frequency for non-adiabatic interaction is the one of the highest excited transition. For ratios between 0.1 and 1, a pronounced decrease in amplitude appears, as the spread in phase accumulated during the pulse duration leads to a growing destructive interference between oscillations originating from the leading and the trailing edge of the pulse. Beyond a ratio of unity, and the pulse duration exceeding the rotational period, the amplitude of coherent post-pulse dynamics is reduced to zero. In this case, the fully adiabatic limit is approached.

It is remarkable that all J states follow the same decay on this dimensionless scale. For states separated by more than one order of magnitude in the timescale of their rotational period, there exists a completely adiabatic regime for the high energy state and almost non-adiabatic behavior for the low-energy state. Figure 2.6 together with Fig. 2.4 can be used to predict efficiencies of alignment for pulses with different lengths and for arbitrary temperatures by taking into account the proper statistical weight for every J state (Eq. (2.2)).

In Fig. 2.6, the alignment decay appears to be shifted to a somewhat longer timescale compared to the limit set by the $\Delta J = +2$ rotational transitions. This is accounted for by incorporating both J-increasing and J-decreasing rotational transitions into the model. For the rotational transitions allowed for a thermally excited molecule, the possible transition frequencies and periods are given according to Eqs. (2.15) and (2.16) by $\omega_+ = -B(4J+6)$

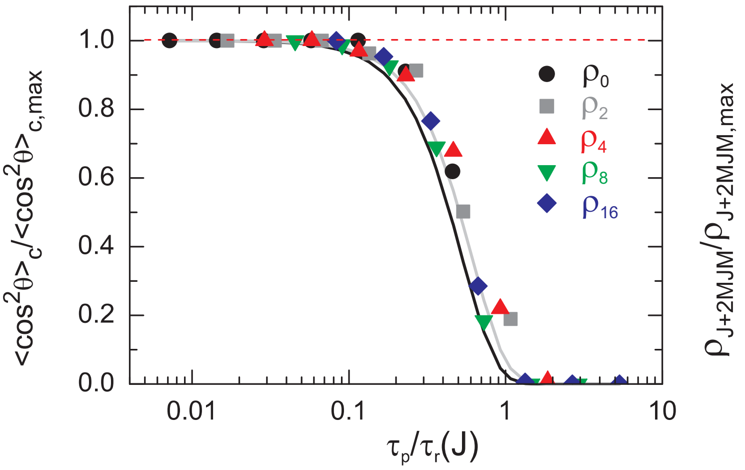

Abbildung 2.6: *Semilogarithmic plot of the relative post-pulse coherent contribution* $\langle\cos^2\theta\rangle_c$ *from selected* J *states (colored symbols) normalized by the respective coherent contribution after the shortest pulse* $\langle\cos^2\theta\rangle_{\mathrm{c,max}}$ *vs. ratio of Gaussian pulse FWHM to rotational period of the* $J \to J+2$ *transition. All pulses have identical integrated power density. The solid lines represent the square of a convolution of the Gaussian excitation pulse envelope with a sinusoidal response (black) and the least-squares fit of a Gaussian function to the data (gray). The dashed horizontal line represents the limiting value of unity.*

and $\tau_+ = 2\pi/\omega_+$ for $\Delta J = +2$, and by $\omega_- = B(4J-2)$ and $\tau_- = 2\pi/\omega_-$ for the $\Delta J = -2$ transition, which is allowed for all states with $M \le J-2$. In case both transitions are allowed, using Eq. (2.14) for the alignment cosine the mean alignment scales with the pulse duration as

$$\begin{aligned}\langle\cos^2\theta\rangle_{JM}(t) \propto p^0_{JM} \quad &+ \quad p^+_{JM}\exp\left(-\frac{\pi^2}{4\ln 2}\frac{\tau_p^2}{\tau_+^2}\right)\sin(\omega_+ t) \\ &+ \quad p^-_{JM}\exp\left(-\frac{\pi^2}{4\ln 2}\frac{\tau_p^2}{\tau_-^2}\right)\sin(\omega_- t)\,,\end{aligned} \tag{2.20}$$

where p^0_{JM} is the mean alignment of ρ_{JM}, and p^+_{JM} and p^-_{JM} are transition probabilities according to Eqs. (2.5) and (2.6).

Equations (2.17) and (2.20) show that the post-pulse amplitude of coherent oscillations depends on the ratio of pulse duration to rotational period. For long pulses, the amplitude is exponentially dampened with a damping constant $\pi^2\tau_p^2/(4\ln 2\tau^2_{J'\to J''})$. For rotational periods at least an order of magnitude slower than the laser pulse duration, the interaction can be classified as non-adiabatic, while the adiabatic limit is reached as soon as the laser pulse duration starts exceeding the rotational period.

With differing ratios of p^+_{JM} and p^-_{JM} (Fig. 2.2), the transition from the non-adiabatic to the adiabatic limit is expected to show a dependence on the M quantum number. As τ_- is always larger than τ_+, the anti-Stokes contribution is less dampened than the Stokes counterpart. Figure 2.7 shows a plot of the oscillatory component of the post-pulse amplitude of alignment normalized to its value in the non-adiabatic limit versus laser pulse duration for the ρ_{80}, ρ_{86}, and ρ_{88} rotational wave packets. The amplitude in the ρ_{88} rotational wave packet decreases faster than either of the two wave packets with both J-increasing and -decreasing oscillations, with the ρ_{86} packet showing a faster decrease than ρ_{80}. The post-pulse amplitude of the ρ_{88} wave packet follows almost ideally the curve given by Eq. (2.17) as $\exp[-\pi^2\tau_p^2/(4\ln 2\tau^2_{J=8\to 10})]$, represented in the figure by a solid line.

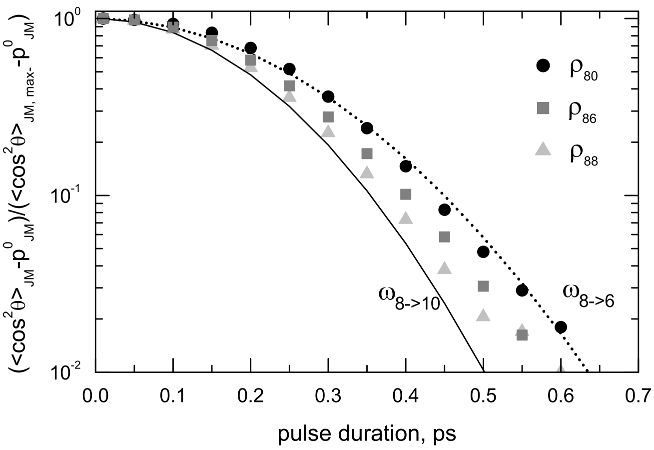

Abbildung 2.7: *M-dependence of the transition from non-adiabatic to adiabatic regime. The amplitude of the post-pulse alignment normalized to the non-adiabatic limit is plotted versus the FWHM duration of a Gaussian laser pulse with constant integrated power density corresponding to 50 TW/cm^2 for 30 fs FWHM for the ρ_{80}, ρ_{86}, and ρ_{88} rotational wave packets. The lines represent the transition according to Eq. (2.17) with the period of the rotational transitions $J = 8 \rightarrow 10$ (solid), and $J = 8 \rightarrow 6$ (dotted).*

The normalized amplitudes of the ρ_{80} wave packet is adequately described by substituting the frequency of the $J = 8 \rightarrow 6$ rotational transition into Eq. (2.17), represented by the dotted line in the figure.

The decrease of the amplitude of the post-pulse alignment is thus influenced by effects of rotational frequency as well as effects of directionality. The rotational periods of the two possible transitions set the limits for the non-adiabatic to adiabatic transitions, while the localization of a particular ρ_{JM} wave packet in this transition area is determined by its M quantum number.

2.2.3.3 Interaction with an intense laser pulse

After the interaction with an intense laser pulse, the final rotational density of a molecule is described by a superposition of many rotational levels, which are populated by sequential Raman transitions from the original $|J, M\rangle$ state. The phase shift between the corresponding oscillations and a significant transfer of population between rotational levels makes it difficult to apply the semi-empirical model (Eqs. (2.17) and (2.20)) described above. Figure 2.8(a) shows the J distribution resulting from the excitation of the $|J = 8, M = 0\rangle$ rotational level with a laser pulse of 30 fs FWHM duration and a power density of 50 TW/cm^2, with the time axis corresponding to $\pm 5\sigma$. Here, we select the $M = 0$ substate because in this case directionality effects are irrelevant as $p^+_{J0} \approx p^-_{J0}$ (Fig. 2.2). A broad distribution of rotational levels is populated after the termination of the pulse. In Fig. 2.8(b) the magnitude of the population of the rotational levels after the termination of the pulse is displayed for the pulse of Fig. 2.8(a) (green squares) and various laser pulses of different duration but identical integrated power density. On the side of low J levels, as in the case of a weak pulse, the distribution of population is similar for equal integrated power density. For short pulses, this is true also for the J-increasing transitions. Note that as expected from the transition probabilities displayed in Fig. 2.2 for $M = 0$, the $J + 2$ and $J - 2$ rotational states are populated with almost equal probability. This is not true for cases other than $M = 0$, where the J-increasing transition is favored by better overlap.

For longer pulses, however, one observes on the J-increasing side a less efficient transfer

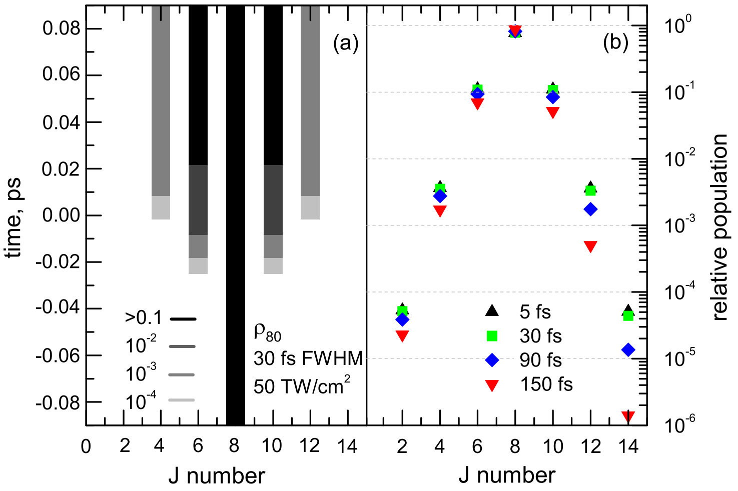

Abbildung 2.8: *(a) Logarithmic contour plot of the population of J rotational levels with the example of the ρ_{80} rotational wave packet upon the excitation with a Gaussian laser pulse of 30 fs FWHM duration and an power density of 50 TW/cm^2. (b) Semilogarithmic plot of the relative population of J levels at $t > t_f$ upon the excitation of the $|J = 8, M = 0\rangle$ state with laser pulse of various durations with integrated power density corresponding to the pulse in (a).*

of population. The higher the excited level, the stronger short pulses are favored, and the population of higher excited and faster oscillating rotational levels is notably reduced with increasing pulse duration. This behavior is caused by the non-adiabatic to adiabatic transition, which depends on the particular rotational frequency, see Fig. 2.7. This is an effect independent of the directionality, as it is governed only by the ratio of rotational period of the particular transition and laser pulse duration. If during the interaction with a strong laser pulse rotational ladder climbing leads to the population of multiple rotational levels, the different frequencies associated with the transitions cause a shifting of the onset of the non-adiabatic to adiabatic transition over the individual components of a wave packet originating from a single $|J, M\rangle$ state.

Figure 2.9 shows the population of rotational levels in the ρ_{80} rotational wave packet upon the excitation with a laser pulse of 0.5 ps FWHM, which is on the border of the adiabatic limit for the $J = 8$ rotational level. The time axis corresponds to $\pm 5\sigma$ of the laser pulse. The rotational periods associated with the $J = 8 \rightarrow 10$ and $J = 8 \rightarrow 6$ rotational transitions are 0.441 ps and 0.559 ps, respectively. In part (a) of Fig. 2.9, the case of a weak laser pulse of 5 TW/cm^2 is displayed. In this case, the dynamics is adiabatic for the Stokes-transition, with the population being completely transferred back with the trailing edge of the pulse from the $J = 10$ rotational level, and almost adiabatic with some remaining population in the $J = 6$ rotational level for the anti-Stokes transition.

Figure 2.9(b) shows the excitation with a strong laser pulse of 50 TW/cm^2. During the interaction, many rotational states are populated through rotational ladder climbing. The post-pulse population, however, is determined by the non-adiabatic to adiabatic transition, which depends on the particular period of the transitions. The population created at the high energetic side with high rotational frequency in the $J = 10$ to $J = 16$ rotational levels is largely transferred back with the trailing edge of the pulse. The slowly oscillating transitions to the lower rotational states already fall into the transition regime to the non-adiabatic case and do not respond in the same way to the trailing edge. A large part of the population transferred there is retained after the turn-off of the pulse. Note that this

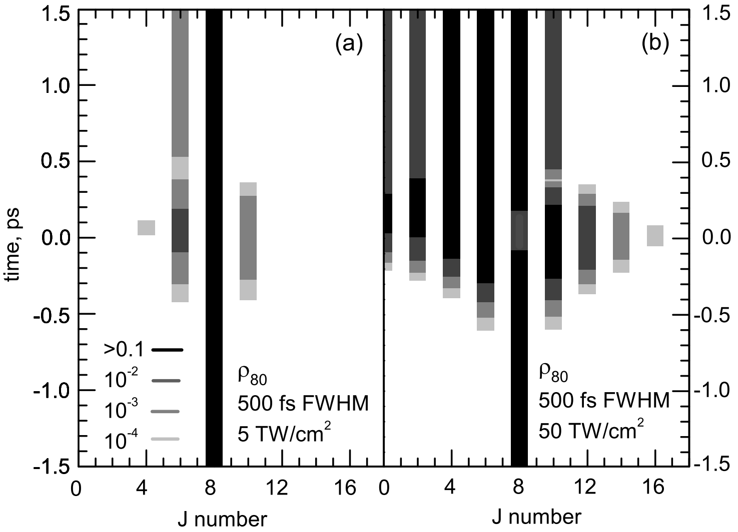

Abbildung 2.9: *Contour plot of the population of J rotational levels with the example of the* ρ_{80} *rotational wave packet upon the excitation with a Gaussian laser pulse of 0.5 ps FWHM duration and an power density of 5 TW/cm*^{2} *(a) and 50 TW/cm*^{2} *(b).*

corresponds to a decrease in mean rotational energy upon the interaction with a strong laser pulse. A similar behavior is observed in all M states, with the condition of $\Delta M = 0$ limiting the accessible lower lying rotational levels.

2.2.4 Rotational heating vs. rotational cooling

The results of the above two sections show, how J and M quantum numbers influence the molecular alignment in different ways. The state of rotational excitation, J, sets the overall time scale for non-adiabatic or adiabatic interaction through the rotational transition periods. The M quantum number determines whether along with absorption also stimulated emission of energy is allowed, and the relative contributions of each. Depending on the M state, thus two partial wave packets displaying aligning and anti-aligning motion can be created by the interaction with a linearly polarized laser pulse. Here, the transition matrix elements $p_{JM}^{+/-}$ favor a J-increasing transition for $M \approx J$, and tend to equal values for $J >> M$.

The transition from the non-adiabatic to the adiabatic regime depends on the ratio of rotational period and laser pulse duration, and thus is faster on the high J-side of the rotational distribution. For increasing laser pulse duration rotational energy is more efficiently transferred from the aligning than from the anti-aligning part of the rotational wave packet by the trailing edge of the laser pulse. Figure 2.9 exemplifies this for fixed pulse duration and two different powers. To determine, to which extent the rotational energy of the wave packet can be influenced by such effects we performed numerical simulations for the $|J = 8, M = 0\rangle$ state over a range of pulse durations between 0.01 ps and 0.6 ps and pulse powers between 1 TW/cm^2 and 100 TW/cm^2. Figure 2.10 shows surface plots of the rotational energy, represented by the expectation value of $\langle J(J+1)\rangle$, versus laser pulse power and duration for the ρ_{80}, ρ_{86}, and ρ_{88} rotational wave packets and the directional average ρ_8. The expectation value $\langle J(J+1)\rangle$ for the $J = 8$ rotational level is 72. Values close to this between 70 and 75 are displayed in the figure as gray area. Higher values are represented by contour lines of darker color, and lower values by lighter color. In Fig. 2.10(a) for the ρ_{80} rotational wave packet for short laser pulses up to a power density

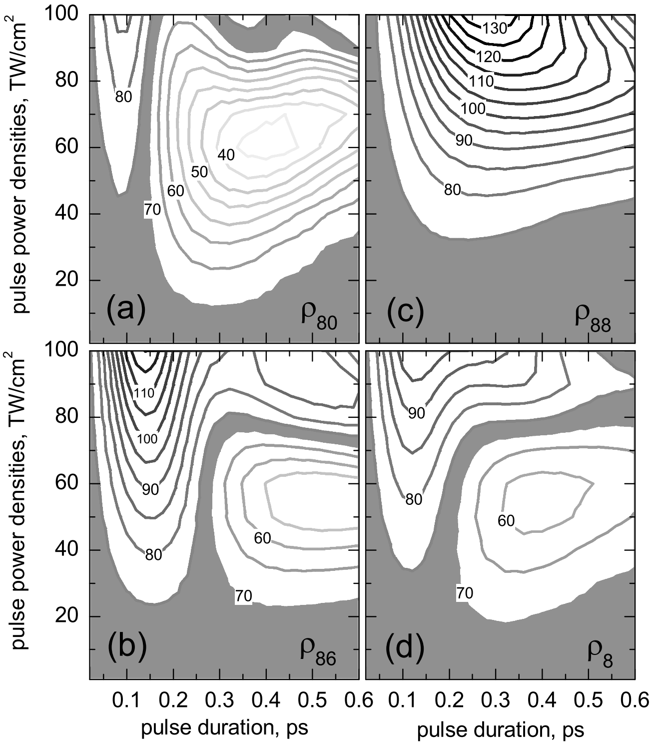

Abbildung 2.10: *Expectation value of* $J(J+1)$*, as a measure of rotational energy, as a function of laser pulse duration and power density for the (a)* ρ_{80}*, (b)* ρ_{86}*, and (c)* ρ_{88} *rotational wave packets, and the* M*-averaged* ρ_8 *density packet in (d). The gray area corresponds to* $70 < J(J+1) < 75$*, with the value for the initial* $J = 8$ *being 72.*

of 40 TW/cm^2 no significant change in the rotational energy is visible. Above this power density, an increase in rotational energy can be observed. An increase in the mean rotational energy corresponds to heating of the rotational degrees of freedom. Going to longer pulse duration, however, there appears at a pulse duration of about 0.15 ps, corresponding to about one third of the rotational period, an almost vertical line marking a region with no net transfer of energy. For shorter pulses, $\langle J(J+1)\rangle$ is increasing, but on the side of longer pulse duration the dominating effect is a decrease in the rotational energy, or rotational cooling. It reaches an extremum for a pulse with a power density of 60 TW/cm^2 and a duration of 400-450 fs. In this region the rotational energy is reduced by half compared to its original value.

A quite similar structure can be observed for the ρ_{86} rotational wave packet with a vertical border at 0.25 ps pulse duration separating the region with preferred rotational heating from the one with preferred rotational cooling independently of the pulse power (Fig. 2.10(b)) up to a power of about 70 TW/cm^2. Here, the region of rotational heating is larger than in the case of ρ_{80}, as expected from the transition probabilities of Fig. 2.2. For the ρ_{88} wave packet in Fig. 2.10(c), the emission of energy is forbidden due the requirement of M conservation, and thus the surface shows the expected increase in mean energy with pulse power and pulse duration up to the onset of the adiabatic regime. The M-averaged values for ρ_8 in Fig. 2.10(d) yield a region with preferred heating for short pulses and very high power, and a region with preferred cooling for long pulses of moderate to high power.

This change in rotational energy is expected to influence the post-pulse alignment observed in the particular wave packets. In Fig. 2.11 we plot the relative deviation of the

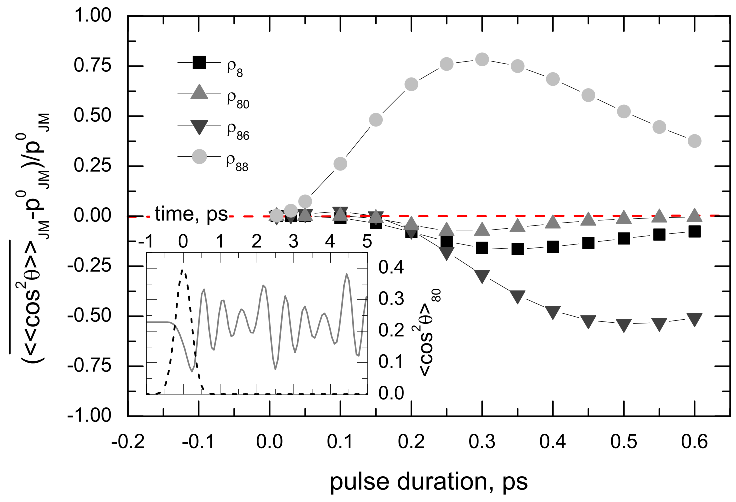

Abbildung 2.11: *Relative deviation from p^0_{JM} of the time-averaged post-pulse alignment $\langle\langle\cos^2\theta\rangle\rangle_{p,JM}$ for the ρ_{80}, ρ_{86}, and ρ_{88} rotational wave packets and the M-average ρ_8. The inset shows the time-dependent alignment of ρ_{80} upon the excitation with a Gaussian laser pulse of 0.5 ps FWHM duration and a power density of 50 TW/cm^2.*

time-averaged post-pulse alignment $\langle\langle\cos^2\theta\rangle\rangle_{p,JM}$ from the value of p^0_{JM} given by Eq. (2.4) for pulse durations between 0.01 ps and 0.6 ps and a constant power density of 50 TW/cm^2 for the densities of Fig. 2.10. The time-averaged post-pulse alignment is a measure for the overall anisotropy created in the sample by the laser pulse. It corresponds to the population part of alignment, as defined in Sec. 1.3.3. The curves show a behavior expected from the transfer of energy surface of Fig. 2.10, with the ρ_{80} and ρ_{86} wave packets displaying a decrease in alignment for all but the shortest pulses, and the ρ_{88} wave packet showing an increase. In all cases one observes a maximum or minimum, respectively, after which the transition to the adiabatic limit tends to reduce the post-pulse anisotropy to zero.

The inset of Fig. 2.11 shows the time-dependent alignment dynamics $\langle\cos^2\theta\rangle(t)$ in the ρ_{80} wave packet in response to a laser pulse of 0.5 ps FWHM duration and a power density of 50 TW/cm^2. The coherent superposition of rotational transition gives rise to an oscillatory post-pulse alignment pattern. While the laser pulse is on, the molecule is forced into anti-alignment, as expected from the net transfer of energy out of the molecules shown in Fig. 2.9.

From Fig. 2.10(a) and (b) it is obvious that the rotational energy is decreased more efficiently in the $M = 0$ case than in the case of $M = 6$. In Fig. 2.11, however, $\langle\langle\cos^2\theta\rangle\rangle_{p,86}$ shows a much more pronounced decrease than $\langle\langle\cos^2\theta\rangle\rangle_{p,80}$. The average anisotropy is thus not only related to the overall amount of rotational energy in the wave packet but also to the M quantum number of the states. Indeed, Fig. 2.1 shows, that the change in alignment upon a rotational transition depends on J and on M. A rotational transition, in which $J \gg M$ does not lead to any notable change in alignment. In the case of Fig. 2.11, this is best fulfilled by the ρ_{80} wave packet, which indeed does show a relatively small change in average alignment despite a large change in rotational energy. The alignment decrease is more pronounced in the case of ρ_{86}, which in comparison loses less energy to the pulse.

2.2.5 Discussion

In this section, we examined the influence of directionality and pulse duration on the rotational alignment of rotationally excited molecules. Molecules in rotationally excited states can interact with a laser pulse not only by absorbing energy but also by stimulated emission. The extent to which these processes are present in the interaction depends on one hand via the M quantum number on the directionality of the molecular angular momentum, and on the other hand via the particular transition frequencies to higher and lower lying rotational states also on the pulse duration. The transition to higher rotational levels corresponds to an aligning motion of the molecule, and the transition to lower rotational levels to an anti-aligning motion. A semi-empirical approach combining two two-state models can qualitatively account for the shape and amplitude of post-pulse alignment induced by a laser pulse of moderate power density. With increasing J number, a decreasing amplitude of alignment at the rotational revival times is observed due to the mutual cancellation of aligning and anti-aligning dynamics. At high laser power, rotational ladder climbing and a phase shift accumulating between oscillatory components causes deviations from this simple behavior. The difference in the frequencies associated with the respective rotational transitions leads to the possibility of the faster oscillating aligning part of the wave packet being more affected by the laser pulse duration than the anti-aligning part. For an appropriate combination of laser pulse duration and energy and molecular rotational frequency, a region is created in which rotational cooling, and thus post-pulse anti-alignment, prevails over rotational heating, or post-pulse alignment.

2.3 State selection in non-resonant excitation of wave packets

In this Section, we demonstrate that the J composition of a rotational wave packet in a thermal ensemble can be controlled by using the laser pulse duration as parameter. In particular, we show that:

- **By optimizing the duration of a single pulse, arbitrarily narrow distributions at low J levels can be formed.**
- **A double pulse excitation, where a longer second pulse acts as a selective dump pulse, allows to prepare non-thermal distributions centered at high J values.**

2.3.1 Formation of rotationally cold wave packets

In case of resonantly excited transitions, the laser frequency distribution serves as parameter to address a specific set of quantum states and to determine the frequency content of a wave packet. For non-resonantly excited wave packets like rotational wave packets excited by Raman transitions, however, to achieve selectivity appears more challenging. In this and the following subsection, we propose a method to shape the composition of rotational wave packets by using the pulse duration as an active tool for selectively tuning the interaction from non-adiabatic to adiabatic for a subset of quantum states. For a fixed pulse length low J states lie on the non-adiabatic and high J levels on the adiabatic side, with the border shifting to higher J for shorter pulses. We illustrate that, starting from a thermal ensemble, long pulses can be used to excite the slow, and thus low-energy part of the J distribution. In a consequent extension we demonstrate that a combination of a short pump and a long dump pulse enables to select the high energetic part. The dump pulses therefore can be shaped to quench non-adiabatically only the cold side of the distribution generated by the pump, leaving the dynamics of rotationally hot molecules unchanged.

As the coherent response to pulses of equal integrated power density can be considered equal within the non-adiabatic limit (Fig. 2.4), we carry out all following simulations for pulses with identical energy content but different pulse length. Pulse duration and power densities are correlated with 80 fs, 160 fs, 320 fs, 640 fs, and 1280 fs FWHM laser pulse duration corresponding to 16 TW/cm^2, 8 TW/cm^2, 4 TW/cm^2, 2 TW/cm^2, and 1 TW/cm^2, respectively, and to simplify the notation we will state only the pulse duration in the following.

In Fig. 3.26 the response to excitation with pulses of identical integrated power density and different duration is exemplified by numerical simulations of $\langle\langle\cos^2\theta\rangle\rangle_{c,J}$ for selected rotational states. The non-adiabatic limit of interaction is represented in Fig. 2.12(a) for dynamics for the ρ_0 rotational density packet upon excitation with laser pulses of 80 fs, 320 fs, and 640 fs FWHM. The pulse durations are short compared to the 2.79 ps rotational period of the $J = 0 \rightarrow 2$ transition. The dynamics following the 80 fs and 320 fs excitation appears identical, and only for the 640 fs excitation pulse a small reduction in amplitude is observed. The crossover to adiabatic behavior is visible in numerical simulations for dynamics starting from initially $J = 8$ in Fig. 2.12(b). With the same pulse parameters as above, large amplitude post-pulse oscillations appear only for the shortest excitation pulse of 80 fs FWHM, for 320 fs excitation the amplitude of coherent oscillations is much lower, and it is essentially reduced to zero for the longest pulse examined. The dominant timescale in this case is the 440 fs rotational period for the $J = 8 \rightarrow J = 10$ transition, bringing the 320 fs excitation pulse well into the crossover region from non-adiabatic to adiabatic, and causing completely adiabatic behavior for the 640 fs FWHM pulse.

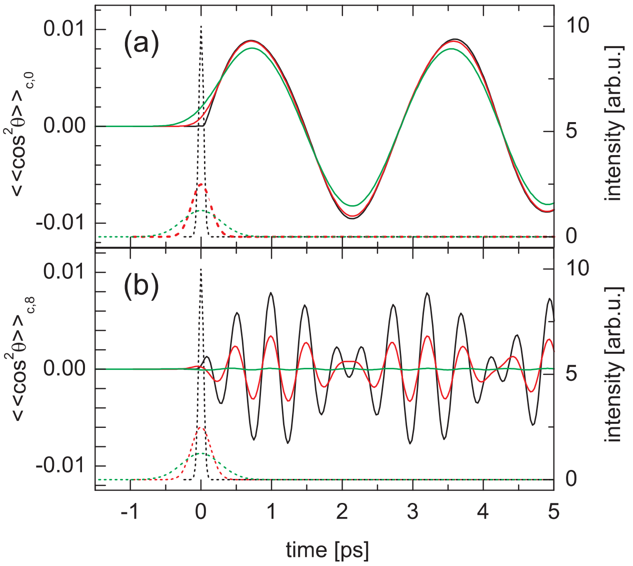

Abbildung 2.12: *(a) Numerical simulation of* $\langle\langle\cos^2\theta\rangle\rangle_c$ *in* $^{14}N_2$ *for the* ρ_0 *rotational density packet upon excitation with Gaussian laser pulses with the same integrated power density and a FWHM of 80 fs (solid black line), 320 fs (solid red line), and 640 fs (solid green line). The respective laser pulse envelopes are represented by dashed lines. (b) Numerical simulation of alignment dynamics for the* ρ_8 *rotational density packet with pulse lengths and intensities as in (a).*

For short pulses, the amplitudes created during the pulse duration add up constructively and coherent motions persists after the pulse turn-off. For longer pulse durations, the polarization induced during the leading edge of the pulse is coherently removed with the trailing edge. Within the adiabatic approximation, the free rotor states evolve into pendular states [5], the eigenstates of the combined molecule-electric field system, and back into free rotor states, while the population of adiabatically corresponding levels is maintained at all times. Thus, for a long pulse, no net excitation is transferred to the system and alignment is high only during the pulse.

In the experimental observable $\langle\langle\cos^2\theta\rangle\rangle$ all regimes of response can be contained depending on the number of populated rotational levels and laser pulse duration. The rotational transitions contributing to the post-pulse alignment can be recovered from the Fourier transform of the time-dependent alignment trace. Using Eq. (2.14) the Fourier transform of $\langle\langle\cos^2\theta\rangle\rangle(t)$ is expressed as

$$\langle\langle\cos^2\theta\rangle\rangle(\omega) = \int_{-\infty}^{\infty} e^{-i\hbar\omega t}\langle\langle\cos^2\theta\rangle\rangle(t)dt$$

$$= \sum_{\substack{J'M'\\J''M''}} \rho_{J'M'J''M''}(t_f)\langle J'M'|\cos^2\theta|J''M''\rangle \times \delta(BJ'(J'+1) - BJ''(J''+1) - \hbar\omega). \quad (2.21)$$

With the appropriate selection rules $\Delta J = \pm 2, \Delta M = 0$ for the matrix elements of $\cos^2\theta$, this expression for $\omega > 0$ is reduced to

$$\langle\langle\cos^2\theta\rangle\rangle(\omega) = \quad (2.22)$$

$$\sum_{J'} \delta(-B(4J'+6) - \hbar\omega) \sum_{M'} \rho_{J'+2,M',J'M'}(t_f)\langle J'M'|cos^2\theta|J'+2M'\rangle +$$
$$\sum_{J'} \delta(B(4J'+2) - \hbar\omega) \sum_{M'} \rho_{J'-2,M',J'M'}(t_f)\langle J'M'|cos^2\theta|J'-2M'\rangle.$$

The Fourier transforms thus contain the contribution of the off-diagonal elements of the density matrix. The population part, being time-independent after the pulse, does not

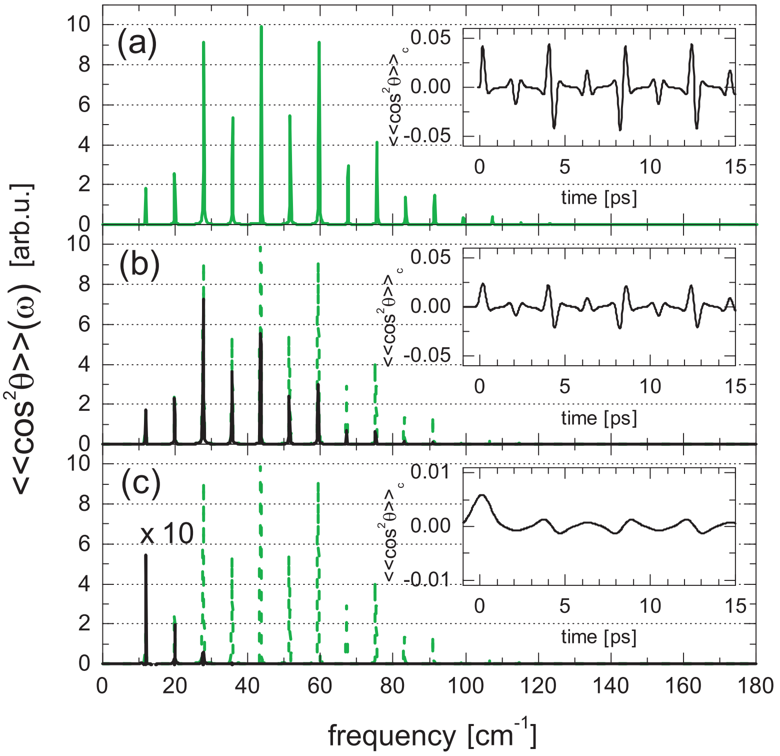

Abbildung 2.13: *Fourier transforms of alignment traces from numerical simulations of* $\langle\langle\cos^2\theta\rangle\rangle_{c,T}$ *in* $^{14}N_2$ *at 80 K upon excitation with Gaussian laser pulses of 40 fs (a), 320 fs (b), and 1280 fs (c) FWHM (solid lines). The curve in (c) has been multiplied by a factor of 10. The green line in (b) and (c) represents the Fourier transform upon 40 fs excitation. The respective* $\langle\langle\cos^2\theta\rangle\rangle_{c,T}$ *vs. time is plotted in the insets.*

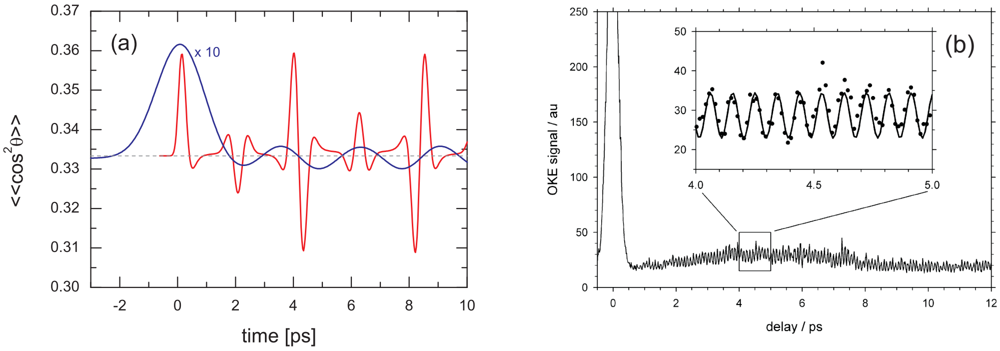

Abbildung 2.14: *(a) Numerical simulation of* $\langle\langle\cos^2\theta\rangle\rangle$ *in* $^{14}N_2$ *at 80 K upon excitation with a laser pulse of 40 fs FWHM with an power density of 10* TW/cm^2 *(red line) and a laser pulse of 2 ps FWHM and an power density of 0.2* TW/cm^2 *(blue line). For better visibility, the amplitude of the blue line has been multiplied by a factor of 10. (b) Rotational dynamics observed in an experiment on solid para-*H_2 *upon excitation with a laser pulse of 160 fs FWHM, the pulse duration greatly exceeding the fundamental rotational period* $\hbar/6B$ *of 90 fs [36].*

contribute to the non-zero frequency part of the Fourier spectrum. The amplitudes with which individual coherences appear are determined by $\rho_{J'\pm 2M'J'M'}$ and the respective projections $\langle J'M'|\cos^2\theta|J'\pm 2M'\rangle$ [175].

The crossover to adiabatic behavior with increasing pulse duration can be used to create a rotationally cold density packet within a thermal ensemble by selectively exciting only molecules in low rotational levels. Selective excitation in this context refers to the post-pulse dynamics, as the alignment induced in rotationally hot molecules during the pulse is adiabatically removed with the trailing edge. Fourier power spectra derived from numerically simulated post-pulse coherent dynamics by solving Eq. (1.26) and Eq. (1.32) upon excitation of a thermal ensemble of $^{14}N_2$ at 80 K with laser pulses of 40 fs, 320 fs, and 1280 fs FWHM are displayed in Fig. 2.13(a), (b), and (c), respectively. The time traces are given in the corresponding insets. The Fourier spectrum upon excitation with the 40 fs pulse (Fig. 2.13(a)) spans about 10 rotational transition frequencies, while the number of rotational levels significantly populated at a temperature of 80 K is about 11 (Fig. 2.5(a)). The crossover to adiabatic behavior for this pulse length starts at $J = 9$, at a fraction of 0.1 of the timescale of the $J = 9 \to 11$ transition of 400 fs. Up to this level, the amplitudes of the individual rotational transitions are not masked by partial destructive interferences during the pulse duration. At room temperature, however, a large part of the populated rotational states would already fall into the crossover region to adiabatic behavior for 40 fs pulse duration (Fig. 2.5), and for the fully non-adiabatic limit pulse durations of 19 fs and shorter have to be used.

For the thermal ensemble at 80 K, the crossover is realized by increasing pulse durations beyond 40 fs. In Fig. 2.13(b) the Fourier spectrum recovered upon excitation with a pulse of 320 fs FWHM (black line) is shown compared to the spectrum upon 40 fs excitation (dashed green line). The Fourier spectrum appears narrower and centered on the low-energetic side compared to the states populated in the thermal ensemble. The decrease in amplitude is significant starting from the peak representing the $J = 2 \to 4$ rotational transition, and the amplitude is essentially reduced to zero above $J = 8 \to 10$. The time trace in the inset of Fig. 2.13(b) shows broader revival structures compared to Fig. 2.13(a), also indicating a narrower frequency distribution. Extending the pulse duration further, the frequency content of the post-pulse dynamics can be narrowed even more, as is exemplified in Fig. 2.13(c) for a pulse of 1280 fs FWHM. Here the $J = 0 \to 2$ transition is dominating in the post-pulse dynamics, and all frequencies above $J = 2 \to 4$ are completely suppressed. Note that the Fourier spectrum in Fig. 2.13(c) has been multiplied by a factor of 10 for better visibility compared to the dashed green (thermal) spectrum. It is thus not the thermal ensemble of molecules being rotationally cooled by a long pulse, but rather the periodic dynamics is restricted to molecules in low rotational states. The small amplitude of coherent post-pulse oscillations (inset) is due to the low statistical weight of the contributing levels in the thermal ensemble. Characteristic of the adiabatic limit is the high amplitude of alignment during the pulse, which is not any more recovered in the post-pulse oscillations. The revival features in the time trace of Fig. 2.13(c) compared to Fig. 2.13(b) appear still broader, the time scale of the beating pattern, however, is similar in all cases, as it is governed by the largest common divisor of the rotational periods, i.e. $2B$ or 8.38 ps. In the extreme case, for excitation with pulses significantly exceeding the $J = 1 \to 3$ characteristic time in FWHM, only the $J = 0 \to 2$ transition will contribute and a crossover from a $2B$ to a $6B$ revival period will appear. This is exemplified by numerical simulations for nitrogen in Fig. 2.14(a), and in Fig. 2.14(b) by experimental observations on the fast rotating para-H_2, where a pulse of 160 fs FWHM already greatly exceeds the fundamental rotational period of 90 fs [36]. In these cases, the shape of the alignment trace changes from the typical beating pattern with sharp, well localized peaks to a sine-shaped oscillation at a single frequency. For experimental methods insensitive to an isotropic background, such as optical Kerr effect [36, 176] or transient grating [22, 177] detection, applying a long pulse thus serves to selectively monitor the coherent dynamics of rotationally cold molecules within thermal surroundings. A potential application is to study decoherence of rotational wave packets in a state-selective way.

2.3.2 Formation of rotationally hot wave packets

In the previous section, we discussed how a long pulse serves to prepare a J density packet distribution centered at low J. In this section, we introduce a scheme to shift the rotational distribution to high J quantum numbers. A first pulse excites a wide range of rotational transitions, and now an appropriately designed second pulse has to eliminate the low J part.

Constructive and destructive interference in rotational wave packets induced by a pair or train of laser pulses are well known from extensive studies in the literature. Our contribution complements these methods by allowing to selectively excite coherent rotational dynamics in molecules residing in a particular band of the rotational distribution of a thermal ensemble. In this way a non-thermal density-packet with adjustable J composition can be created from a thermal ensemble. As in the rotational wave packet nuclei are moving rather than electrons, the fast oscillations of the electric field within the laser pulse envelope are averaged out within the rotating wave approximation, and the only control parameter is the timing of the second pulse with respect to the first one [147]. To achieve destructive interference, the dump pulse has to be applied at half a revival time past the pump pulse, corresponding to 4.19 ps or the root of $\langle\langle\cos^2\theta\rangle\rangle_c$ at the half revival time for $^{14}N_2$. The density packet of the first pulse evolves up to the negative anti-alignment indicated by $\tau_{1/2}$ in Fig. 1.14(b) while the second pulse generates the alignment maximum visible in Fig. 1.14(b) just after $t = 0$. Both traces are mirror images of each other and in the superposition they cancel.

For the destructive interference to take place it is not necessary that the dump pulse be identical to the pump pulse. Pulses within the non-adiabatic limit create an almost identical response in a particular rotational state (Fig. 2.6), and therefore destructive interference can be achieved by applying a dump pulse differing in duration from the pump pulse if the integrated power density is the same. In Fig. 2.15 the effect of dump pulses of various duration following the excitation with a 40 fs pump pulse is quantified relative to the rotational period of a particular excited $J \to J + 2$ transition. The maximal amplitude of $\langle\cos^2\theta\rangle_c$ after the dump pulse normalized by the maximal post-pulse $\langle\cos^2\theta\rangle_c$ after the pump pulse is plotted as colored symbols versus the ratio of dump FWHM to rotational period for a range of J levels between 0 and 16. The curve gives the efficiency of de-excitation for a particular ratio of pulse length to rotational period, and thus can be used to predict efficiencies of dump pulses of various lengths for arbitrary temperatures. As for the dependence of the degree of alignment on pump duration shown in Fig. 2.6, the curve shows two distinct regimes with non-adiabatic and adiabatic behavior, and between those a crossover region covering one order of magnitude in pulse duration. Once more, a remarkable common behavior for all J is observable. As for the pump case, the non-adiabatic limit extends up to a pulse width of ten percent of the rotational period, in this region maximal destructive interference is achieved. The fully adiabatic region sets in at pulse durations equal to the rotational period, where the presence of the dump pulse does not affect the degree of alignment. The dependence can be qualitatively described by the model of a convolution of Gaussian pulse with sinusoidal response. Introducing a second

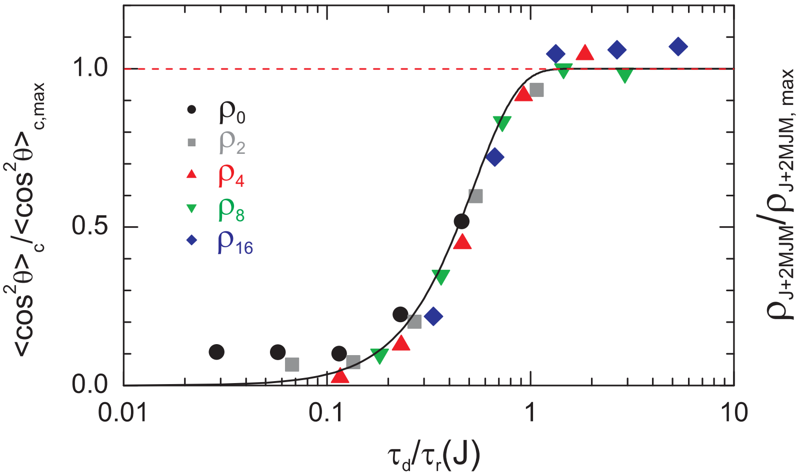

Abbildung 2.15: *Semilogarithmic plot of the relative coherent contribution* $\langle \cos^2\theta\rangle_c$ *after the dump pulse for non-adiabatic dynamics starting from selected* J *stated normalized by* $\langle \cos^2\theta\rangle_{c,\max}$ *after the pump vs. ratio of Gaussian pulse FWHM of dump pulse to rotational period of the* $J \to J+2$ *transition. All pulses have equal integrated intensities. The solid black curve represents the dependence of amplitude on dump pulse duration according to Eq. (2.24). The limiting value of unity is represented by the dashed horizontal line.*

pulse shifted in time by the half revival time $\tau_{1/2}$, the convolution can be written and analytically solved as

$$\begin{aligned}\rho_{J'+2M'J'M'}(t) \propto & \qquad\qquad\qquad\qquad\qquad\qquad\qquad\qquad\qquad\qquad (2.23)\\ & \int_{-\infty}^{\infty} \left[\sqrt{\tfrac{a_p}{\pi}}\exp\left(-a_p t'^2\right)\sin\omega(t-t') + \sqrt{\tfrac{a_d}{\pi}}\exp\left(-a_d t'^2\right)\sin\omega(t+\tau_{1/2}-t')\right] dt' \\ & \qquad = \left[\exp\left(-\tfrac{\omega^2}{4a_p}\right) - \exp\left(-\tfrac{\omega^2}{4a_d}\right)\right]\sin\omega t.\end{aligned}$$

Here the pump and dump pulses with durations τ_p and τ_d are characterized by $a_p = 4\ln 2/\tau_p^2$, and $a_d = 4\ln 2/\tau_d^2$, respectively, and the rotational transition frequency $\omega = (4J+6)B/\hbar$ as in Eq. (2.17). In case of a non-adiabatic pump, the first exponential tends to unity, and the maximal post-pulse amplitude of $\rho_{J'+2M'J'M'}(t)$ resulting from the interference of dynamics excited by the pair of pulses is accordingly expressed as

$$\rho_{J'+2M'J'M'} \propto 1 - \exp\left[-\frac{\pi^2}{4\ln 2}\left(\frac{\tau_d}{\tau_{\mathrm{rot}}}\right)^2\right]. \qquad (2.24)$$

This curve is plotted in Fig. 2.15 as solid black line and it very well describes the dependence of amplitudes on dump pulse duration. The relatively large scatter of data for different J states in the full simulation is due to a small phase shift appearing between the J levels of the ensemble. Varying the timing of the dump pulse can optimize the interaction with a particular state, there exists, however, no zero-effect pulse pair with which perfect destructive interference for all levels can be achieved. This behavior has been attributed in the literature to general properties of the three-dimensional rotor [148]. We prefer the explanation that the impossibility to coherently de-excite all states of the ensemble by an identical dump pulse is owing to an individual phase picked up by the population starting from different J rotational levels. Figure 2.16(a) shows the relative population of the rotational levels upon excitation of the $J = 8, M = 0$ level with a laser pulse of 40 fs FWHM and a power density of 100 TW/cm^2. At this high intensity, several J-levels

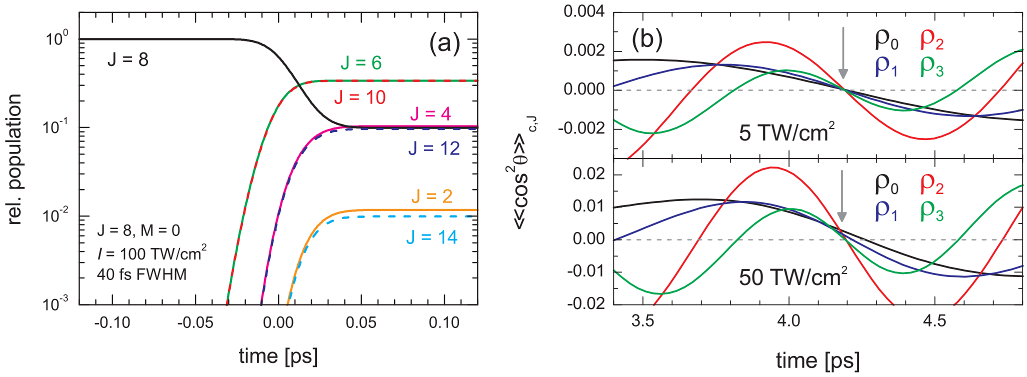

Abbildung 2.16: *(a) Numerical simulation of population of J rotational level during the interaction of the* $J = 8, M = 0$ *state of* $^{14}N_2$ *with a laser pulse of 40 fs FWHM with a power density of 100 TW/cm*^{2}*. Several rotational levels are populated by rotational ladder climbing, every step inducing a time delay in the population. (b)* $\langle\langle\cos^2\theta\rangle\rangle_{c,J}$ *for selected J levels in* $^{14}N_2$ *upon excitation with a pump pulse of 40 fs FWHM with a power density of 5 TW/cm*^{2} *(upper panel) and 50 TW/cm*^{2} *(lower panel). Half of the rotational revival time (4.19 ps) is indicated by the vertical arrow. The inversion point of the* $\langle\langle\cos^2\theta\rangle\rangle_c$*-curves coincides with this time for all states for low-intensity excitation, and is significantly different for different states for high-intensity excitation.*

are accessed by rotational ladder climbing, which therefore leads to a shift in time with the closest levels populated earlier than the remote ones. If one associates a sine-shaped oscillation with every of these transitions, their sum will display a phase shift with respect to the laser pulse maximum which additionally depends on the original rotational level via the rotational energy difference between neighboring levels. A small difference entails a fast population transfer, and thus the lowest rotational levels should pick up the largest phase shift in the excitation process. In Fig. 2.16(b) this effect is displayed together with the dependence of the phase shift on power. The top panel displays the oscillations in several rotational levels upon excitation with a relatively low-intensity laser pulse. This pulse leads to a coupling to only the $J \pm 2$ levels, with the oscillations being in phase and starting at the laser pulse maximum. The $\langle\cos^2\theta\rangle_c$ curves therefore all cross in one point, this point additionally being the center of inversion where a π-pulse would start the mirror image of the original wave packet. At higher intensity with more rotational levels accessed (Fig. 2.16(b)) the phase shift is significant, being more pronounced in the low rotational levels. We verified that indeed the optimal timing of a dump pulse, as expected from this figure, does shift to later times from originally half of the rotational revival time for the low rotational states. For an excitation power of 30 TW/cm^2 in a 40 fs FWHM laser pulse, the optimal timing for the dump pulse is shifted to 4.29 ps in the $J = 0$ rotational level compared to 4.2 ps for the $J = 8$ rotational level (Fig. 2.16(b)).

The effect of optimized dump pulses on dynamics in the $J = 0$ and $J = 8$ rotational levels is shown in Fig. 2.17. The timing of the dump pulses has been chosen to optimize the destructive interference in the particular state. In Fig. 2.17(a) dump pulses of 40 fs, 320 fs, and 640 fs FWHM are applied after excitation with a 40 fs pump pulse. For this rotational transition, all these dump pulse durations are well below the adiabatic limit, and consequently act almost equally on the dynamics. The 40 fs and 320 fs dump pulses essentially reduce the post-pulse oscillation amplitude to zero, while small amplitude oscillations are observed for the 640 fs dump pulse, indicating the onset of crossover to the adiabatic limit. With a 440 fs characteristic time for the $J = 8 \rightarrow 10$ rotational transition, the 320 fs and 640 fs FWHM dump pulses are well within the crossover region to adiabatic behavior.

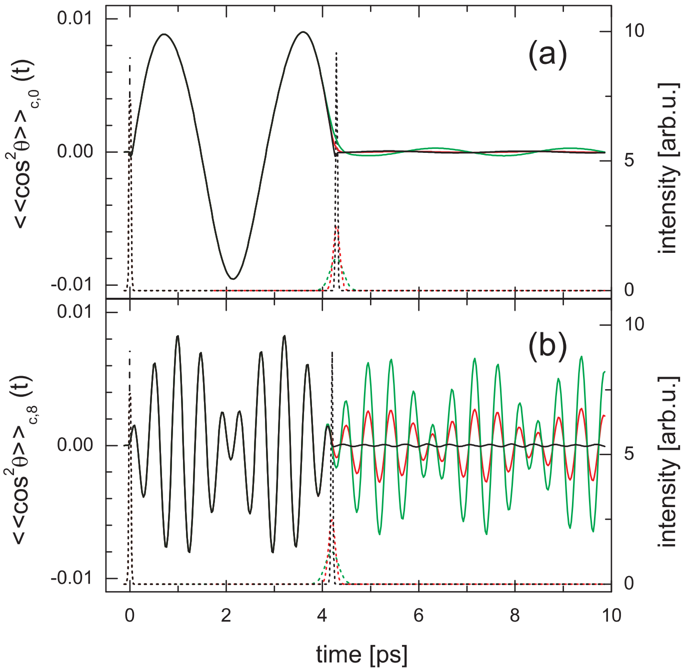

Abbildung 2.17: *$\langle\langle\cos^2\theta\rangle\rangle_{c,J}$ in $^{14}N_2$ form the ρ_0 rotational density packet upon excitation with a pump pulse of 40 fs and a dump pulse at a delay of 4.29 ps of 40 fs (solid black line), 320 fs (solid red line), and 640 fs (solid green line) FWHM. The respective laser pulse envelopes are represented by dashed lines. b) Numerical simulation of alignment dynamics for the ρ_8 rotational density packet with pulse lengths and intensities as in (a). The time delay of the dump pulse is 4.2 ps.*

This is demonstrated in Fig. 2.17(b), displaying post-pulse coherent oscillations starting from the $J = 8$ rotational level. The 40 fs dump pulse erases the oscillations, while large amplitude dynamics is observable after the 320 fs and 640 fs dump pulses. The presence of a slowly varying field thus does not affect the coherent dynamics. Naturally, the fixed phase relation, giving rise to coherent oscillatory motion, existing before the application of the adiabatic field persists also after its turn-off.

For a thermal ensemble with a distribution in J, the effect of a dump pulse of fixed duration thus changes over the J spectrum. In Fig. 2.18(a), the Fourier power spectrum for numerically simulated destructive interference in a thermal ensemble of $^{14}N_2$ at 80 K upon application of an identical pair of pump and dump laser pulses of 40 fs FWHM is plotted. The timing of the dump pulse was chosen to minimize the amplitude of post-pulse oscillations (inset). For comparison, the Fourier spectrum resulting from excitation with a 40 fs pump pulse (Fig. 2.13) is plotted as dashed green line. The symmetric dump pulse of Fig. 2.18(a) removes the bulk of the spectrum from the coherent dynamics, while in the wings small contributions are surviving. Note, however, that for better comparison of shape, the black spectrum was multiplied by a factor of 5, and thus in the plot appears overly large. The destructive interference in the different spectral regions can be further optimized by slight changes in the timing of the dump pulse [148]. From the discussion in the previous section, it follows that all pulses that contain the same energy but differ in duration have the same effect in coherently exciting a rotational wave packet, as long as they can be considered non-adiabatically short for the J set considered. Consequently, also a dump pulse must only be equal in the energy content to coherently de-excite the wave packet, however only within the non-adiabatic limit. Now we proceed to violate this condition for

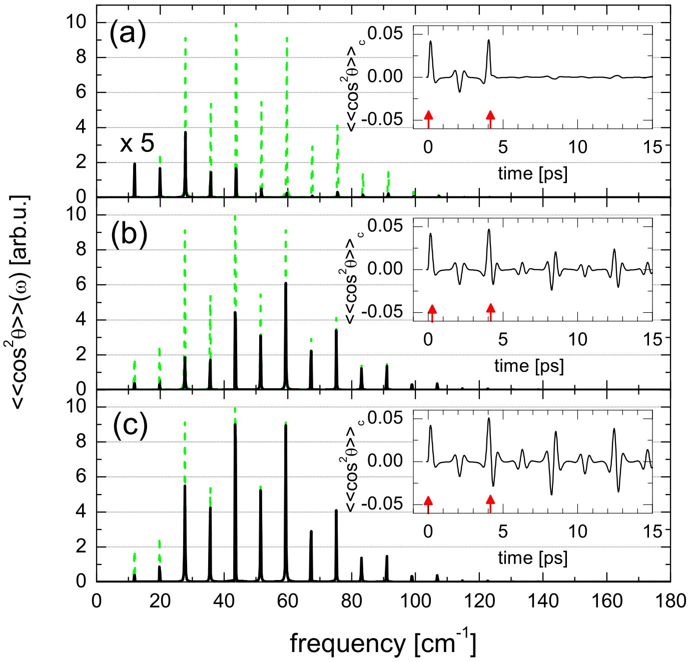

Abbildung 2.18: *Fourier transforms of alignment traces from numerical simulations of* $\langle\langle\cos^2\theta\rangle\rangle_{c,T}$ *in* $^{14}N_2$ *at 80 K upon application of a pair of Gaussian laser pulses of 40 fs duration for the pump and 40 fs (a), 320 fs (b), and 640 fs (c) FWHM (solid black lines) for the dump pulse delayed by 4.195 ps. The curve in (a) has been multiplied by a factor of 5. The green spectra represent the Fourier transform upon excitation with only a single 40 fs FWHM pump pulse. The respective* $\langle\langle\cos^2\theta\rangle\rangle_{c,T}$ *vs. time is plotted in the insets with the timing of the pulses indicated by vertical arrows.*

a subset of J levels. In Fig. 2.18(b) the effect on the Fourier spectrum of a dump pulse equal in timing and energy content to the case of Fig. 2.18(a) but with a pulse duration of 320 fs FWHM is plotted. In the time trace, the coherent oscillations persist after the dump pulse (inset), however with an amplitude that appears much reduced. The Fourier transform of the trace reveals that the spectrum after the dump pulse, represented by the black line, is lacking the low energy part compared to the single-pulse case (dashed green line). Figure 2.18(c) displays the Fourier transform of the oscillations after application of a 640 fs FWHM dump pulse. This pulse, as expected, appears to affect only the lowest J levels.

Long dump pulses thus interact selectively with the red part of the spectrum. Indeed, destructive interference is achieved irrespectively of the duration of the dump pulse as long as it is within the non-adiabatic limit, which is exactly true for the red wing of the rotational distribution. Rotational transitions for which the dump pulse is long enough to interact adiabatically, however, are not affected by its presence. As a result, the wave packet spectrum after application of an asymmetric pair of pump and dump pulses appears shifted to higher energies compared to the original case. The shift is not due to heating but rather due to selective de-excitation of the red wing of the wave packet spectrum back to the original isotropic distribution. Tuning the pulse width of the dump pulse allows to control the limits of de-excitation and to generate narrow non-thermal wave packet spectra.

The large crossover region form non-adiabatic to adiabatic, however, demands to sacrifice large amplitudes in case spectral purity is required.

2.3.3 Discussion

We thus demonstrated that adapting the pulse duration in non-resonant excitation of wave packet states can serve as a tool to achieve spectral selectivity otherwise not permitted by the non-resonant nature of the process. For a quantum system with transition frequencies strongly increasing with the quantum number, increasing the excitation pulse length leads to a selective excitation of the low energetic side of the spectrum, as higher lying levels are adiabatically transferred back into their original state. In double-pulse experiments, the length of the second (dump) pulse can be adjusted to selectively eliminate the red wing of the spectrum by tuning it into the adiabatic limit for the blue wing. The J composition of the resulting alignment signal may be far from the temperature of the environment. With both schemes together, low J and high J rotational density packets can be designed. The selectivity of the method depends on the non-equidistant spacing of quantum levels, and is expected to increase with increasing level spacing, e.g. for rotational wave packets in O_2 or H_2. Note, however, that in these approaches of shaping the spectra of coherent oscillations, no significant population transfer between states is involved but rather the coherent rotational motion is restricted to a certain subpopulation, with the bulk of molecules forming an isotropic thermal background. From the viewpoint of experiments, it is thus favorable to employ a technique only sensitive to deviations from isotropy such as, e.g. the detection of time-dependent changes in birefringence in an optical Kerr effect or transient grating experiment.

3 Experiments

3.1 Optical Kerr effect spectroscopy

Molecular alignment is measured experimentally by various techniques, including dissociative ionization (e.g. in Refs. 95, 96) and Coulomb explosion with subsequent fragment detection (e.g. in Refs. 14, 15, 178). Optical techniques measure the induced anisotropy via the optical Kerr effect [42, 176] or transient induced gratings [22, 177, 179]. The optical techniques offer a usually better signal to noise ratio, and additionally the measured signal amplitudes can be directly related to the microscopic alignment [176, 180–182]. In this work, we detect the alignment using ultrafast optical Kerr effect spectroscopy.

The Kerr effect corresponds to the induction of an anisotropy in a material by an electric field. It is named after John Kerr who discovered in 1875 that by application of a strong electric field an otherwise isotropic material can become birefringent [183]. The material dependent Kerr constant K relates the change in refractive index Δn to the square of the applied electric field:

$$\Delta n = \lambda_0 K E^2, \tag{3.1}$$

where λ_0 is the vacuum light wavelength. All media display a Kerr effect, while its linear counterpart, the so-called Pockels effect, can only appear in case of no inversion symmetry.

The electric field inducing the anisotropy can be created by an intense light source, such as a laser. The effect is then termed optical Kerr effect or AC Kerr effect. The nonlinear polarization in this case is expressed as

$$\mathbf{P} = \varepsilon_0 \left(\chi^{(1)} + \chi^{(3)} |E_\omega|^2 \right) \mathbf{E}_\omega . \tag{3.2}$$

Here $\chi^{(1)}$ and $\chi^{(3)}$ denote the linear and third order nonlinear susceptibility [184, 185], respectively, and $\mathbf{E}_\omega = \mathbf{E}_\omega \cos(\omega t)$ is the electric field of the light source. With the relation $n = \sqrt{1+\chi}$ for the refractive index, one obtains for $\chi^{(3)} << n_0^2$

$$n(\mathcal{I}) = n_0 + \frac{3\chi^{(3)}}{8n_0} |E_\omega|^2 = n_0 + n_2 \mathcal{I}, \tag{3.3}$$

where $\mathcal{I}(r,t)$ is the intensity, and n_2 with the dimension of 1/intensity is the so-called nonlinear refractive index.

Important effects following from n_2 for very high intensities are self-focusing [186], which is a consequence of its spatial part, and self-phase modulation [187] which is a consequence of the temporal part. At lower intensities, the optical Kerr effect is an important tool in spectroscopy. All materials display an instantaneous anisotropic response to an intense polarized laser pulse as the electronic orbitals are deformed in the field. In media consisting of non-spherical particles, reorientation can occur following the electronic polarization, and its build-up and decay is studied by optical Kerr effect spectroscopy. The instantaneous Kerr response from the electronic polarization and the slower reorientation dynamics of anisotropic particles are exemplified in Fig. 3.1(a) and (b), respectively.

In optical Kerr effect spectroscopy the anisotropy which builds up in a sample following excitation with linearly polarized light is studied [18, 188–190]. The use of short laser pulses

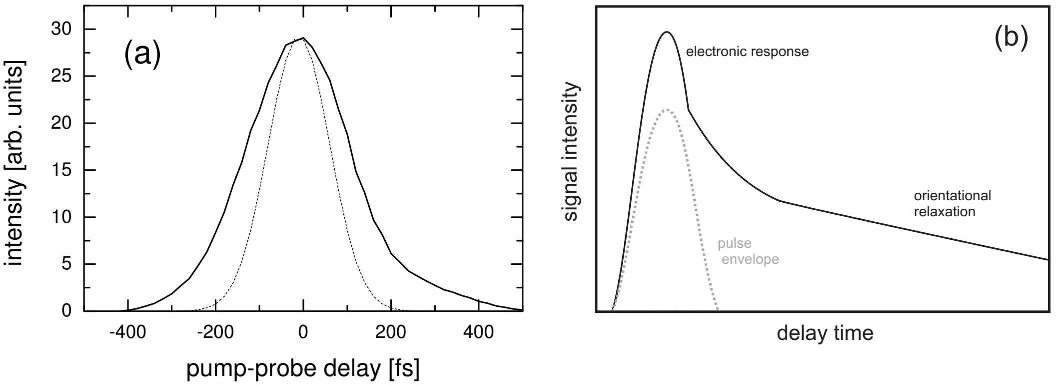

Abbildung 3.1: *(a) Optical Kerr effect response of 1600 mbar argon (solid line) at 300 K upon the excitation with a 780 nm laser pulse with 165 fs FWHM duration (dashed line) in our setup. The electronic response is instantaneous, the broadening relative to the pump pulse arises from a convolution with the probe pulse duration. (b) Schematic optical Kerr effect response of an anisotropic liquid. The dashed line represents the pulse envelope, the solid line the material response. Reorientation of the liquid molecules creates an anisotropy that persists even after turn-off of the pulse. The decay of the signal is related to orientational relaxation.*

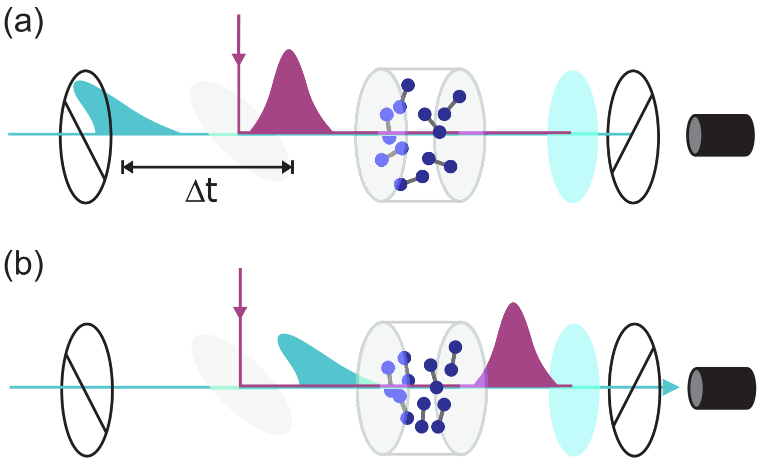

Abbildung 3.2: *Principle of an optical Kerr effect experiment.(a) A strong linearly polarized pump pulse (purple) passes an initially isotropic sample. The electric field of the pump induces an anisotropy in the sample. (b) A weak probe pulse (blue) polarized at 45 degrees with respect to the pump passes the sample with a time delay* Δt*. At the presence of an anisotropy in the sample, the polarization of the probe changes to elliptic, and a fraction of the intensity is transmitted through the analyzer set perpendicular to the initial probe polarization onto the detector.*

in time-resolved optical Kerr effect spectroscopy allows to follow the time-dependence of the anisotropy and thus to study reorientation and relaxation processes [191, 192]. An intense linearly polarized pump pulse far off resonance from any electronic, vibrational or rotational transition in the sample induces reorientation of the sample particles by interaction with either permanent or pump-induced dipole moments (Fig. 3.2(a)). The pump is followed by a weak linearly polarized probe pulse delayed by a variable time Δt, probing the birefringence that appears in the sample upon the reorientation of its particles. Under non-resonant conditions, as in this work, birefringence is the dominating effect induced by the pump laser. Approaching a resonance leads to a growing additional dichroism, which is neglected in our case [193]. The polarization of the probe becomes elliptic as it is split up into an ordinary and an extraordinary beam depending on the momentary position of the main axes of birefringence in the sample. An analyzer with its polarization set perpendicular to the original probe polarization in the presence of birefringence transmits the induced out-of-plane component of the probe electric field (Fig. 3.2(b)). By this method, the build-up, time-development and decay of non-resonant molecular alignment can be studied.

To describe the experiment quantitatively, one considers the effect of the system response to the pump pulse on the electric field of the probe pulse. Derivations of the system response in a Kerr effect experiment can be found in Refs. 190 and 18. Here we briefly outline the derivation following Ref. 18.

The electric field E_p of the probe laser pulse propagating in z direction at a time t can be written as

$$E_p(z,t) = \varepsilon_p e^{i(kz-\omega t)}, \tag{3.4}$$

where ε_p is the magnitude of the probe electric field before the sample, k is the wave vector, and ω the light frequency. In the presence of a pump intensity-dependent refractive index $n_2\mathcal{I}$, the wave vector becomes intensity-dependent according to $k(\mathcal{I}) = 2\pi/\lambda(\mathcal{I}) = \omega n(\mathcal{I})/c$, with $n(\mathcal{I}) = n_0 + n_2\mathcal{I}$. The probe electric field can thus be expressed as

$$E_p(z,t) = \varepsilon_p \exp\left[i\omega\left(\frac{(n_0+n_2\mathcal{I})z}{c} - t\right)\right] = \varepsilon_p \exp\left[i\omega\left(\frac{n_0 z}{c} - t\right)\right]\left(1 + \frac{i\omega n_2\mathcal{I}z}{c}\right) + \ldots, \tag{3.5}$$

where the right hand side is the first order of a Taylor series of the exponential for a small nonlinear refractive index. $n_2\mathcal{I}$ can be calculated by convolution from the system response tensor R_{1234} and the temporal profile of the pump intensity $\mathcal{I}_0(t)$:

$$n_2\mathcal{I} = \int_{-\infty}^{t} dt' R_{1234}(t-t')\mathcal{I}_0(t'). \tag{3.6}$$

The four indices of the system response tensor R_{1234} correspond to the four Cartesian components of the frequencies involved in pump and probe steps of the experiment (Fig. 3.3). ω_1 and ω_2 are frequencies contained in the bandwidth of the pump, exciting a rotational transition from $|1\rangle$ to $|2\rangle$ via a stimulated Raman process and a virtual level $|i\rangle$. ω_3 and ω_4 are responsible for the Raman-type probe process. Under our experimental conditions (Fig. 3.2), the polarizations of ω_1 and ω_2, and also of ω_3 and ω_4 are equal. The pump pulse in the experiment is linearly polarized and propagates in z

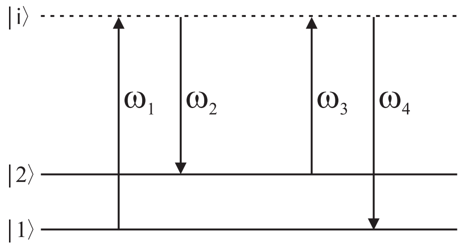

Abbildung 3.3: *The four frequencies interacting in the optical Kerr effect experiment. Transitions occur between the levels labeled $|1\rangle$ and $|2\rangle$ via the virtual level $|i\rangle$.*

direction, its polarization direction will be denoted as x. The probe pulse is polarized at an angle ϕ with respect to the pump pulse, and the analyzer is set perpendicular to the probe polarization at an angle ψ to the pump. The polarization geometry is shown in Fig. 3.4. Maximum sensitivity is achieved for $\phi = -\psi = 45$ degrees.

The electric field of the probe at time delay Δt in the direction of the analyzer ψ can thus be expressed as a superposition of the modified probe fields in x and y directions:

$$\begin{aligned} E_{p,\psi}(t,\Delta t) = &\left[\varepsilon_{p,i}(t-\Delta t)e^{i\omega\left(\frac{n_0 z}{c}-t+\Delta t\right)}\left(1+\frac{i\omega z}{c}\int_{-\infty}^{t} dt' R_{\mathrm{iiii}}(t-t')\mathcal{I}_0(t')\right)\right]\cos\psi \\ &+\left[\varepsilon_{p,j}(t-\Delta t)e^{i\omega\left(\frac{n_0 z}{c}-t+\Delta t\right)}\left(1+\frac{i\omega z}{c}\int_{-\infty}^{t} dt' R_{\mathrm{iijj}}(t-t')\mathcal{I}_0(t')\right)\right]\sin\psi. \end{aligned} \tag{3.7}$$

Here, i and j in the indices denote the unit vectors in x and in y directions. The relatively simple form of Eq. (3.7) is caused by the simple form of the system response tensor in an initially isotropic transparent medium. In this case, only the components R_{iiii} and R_{iijj} exist.

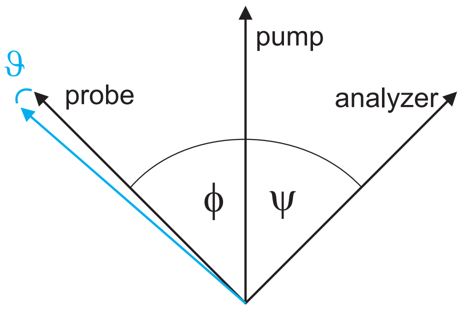

Abbildung 3.4: *Polarization settings in an optical Kerr effect experiment.*

In many experiments, the probe polarizer is detuned by a small angle ϑ from the perpendicular direction with the analyzer (Fig. 3.4). In this case, a small fraction of the probe intensity is transmitted onto the detector even in absence of birefringence in the sample. This time-independent signal is referred to as an out-of-phase local oscillator. Including the detuning by the angle ϑ, the probe electric field in x and y directions is expressed as

$$\varepsilon_{p,i} = \varepsilon_p(\cos\vartheta\cos\phi - i\sin\theta\sin\phi) \tag{3.8}$$

and

$$\varepsilon_{p,j} = \varepsilon_p(\cos\vartheta\sin\phi - i\sin\theta\cos\phi) \tag{3.9}$$

in terms of the initial probe envelope ε_p. The time-dependent intensity $\mathcal{I}(\Delta t)$ recorded by the detector is the time average of the square of the electric field $E_p(t)$. The recorded signal is expressed as a sum of three components:

$$\mathcal{I}(\Delta t) = \left\langle \mathcal{I}_p \sin^2\vartheta \right\rangle_t + \mathcal{I}_{\mathrm{hom}}(\Delta t) + \mathcal{I}_{\mathrm{het}}(\Delta t). \tag{3.10}$$

The first component is the constant contribution due to the local oscillator. The second component is the homodyne signal, also referred to as the quadratic signal, and the third component is the so-called heterodyne signal, or linear signal. The homodyne signal results from the square of the out-of plane electric field appearing as a consequence of the change in the probe polarization:

$$\mathcal{I}_{\mathrm{hom}} = \left\langle \left| \varepsilon_p(t-\tau)\frac{\omega z}{c}\int_{-\infty}^{t'} dt' R_a(t-t')\mathcal{I}_0(t') \right|^2 \right\rangle_t . \tag{3.11}$$

Here R_a is the effective system response tensor with $R_a = R_{\mathrm{iiii}}\cos\phi\cos\psi + R_{\mathrm{iijj}}\sin\phi\sin\psi$.

$\mathcal{I}_{\mathrm{hom}}$ is called the quadratic signal as it depends quadratically on the pump intensity $\mathcal{I}_0$. The homodyne signal is always positive, as it measures only a deviation from isotropy but not its direction.

The heterodyne signal results from the interference of the local oscillator with the modified electric field of the probe:

$$\mathcal{I}_{\text{het}} = 2 \left\langle \mathcal{I}_p(t-\tau) \sin\vartheta \frac{\omega z}{c} \int_{-\infty}^{t'} dt' R_a(t-t') \mathcal{I}_0(t') \right\rangle_t . \tag{3.12}$$

This is referred to as the linear signal as the dependence on pump intensity is linear. Depending on the detuning angle ϑ, the heterodyne signal can change its sign, the interference can be destructive or constructive. In addition to the amplitude of birefringence, the heterodyne signal contains information on the momentary position of the fast and the slow axis of birefringence in the sample due to the interference with the local oscillator.

The system response tensor is the macroscopic manifestation of microscopic reorientation processes that occur in the sample following the excitation by the linearly polarized pump. Now we return to the angle θ characterizing the alignment of the axis of a diatomic molecule with respect to the laser polarization direction (see Sec. 1.3.1). To extract meaningful information on the microscopic processes from the measured quantities $\mathcal{I}_{\text{hom}}$ and $\mathcal{I}_{\text{het}}$ a quantitative relation of R_a and the microscopic observable $\cos^2\theta$ has to be established. This was accomplished within the framework of RIPS and RCS by a perturbation theory approach [37]. In Refs. 176 and 194 it was confirmed that the proportional relation between the measured signal and the expectation value of $\cos^2\theta$ is universally valid also for non-perturbative pump intensities, and one has

$$\mathcal{I}_{\text{hom}} \propto \left[\langle\langle \cos^2\theta \rangle\rangle - \frac{1}{3} \right]^2 \tag{3.13}$$

for the homodyne detected signal and

$$\mathcal{I}_{\text{het}} \propto \left[\langle\langle \cos^2\theta \rangle\rangle - \frac{1}{3} + C \right]^2 \tag{3.14}$$

for the heterodyne detected signal. The related all-optical transient grating and four-wave mixing methods also are sensitive to $\langle\langle \cos^2\theta \rangle\rangle$ [180–182]. The full angular distribution is recovered in the Coulomb-explosion based detection of the distribution of molecular fragments [19, 178].

These expressions will be used in the following chapter to derive phase lags and intensity ratios for our experiment, thus providing a quantitative measure of the laser-induced alignment.

3.2 The experimental conditions

In the present work, the degree of molecular alignment induced by a strong pump pulse in gas phase nitrogen had to be detected in a range of temperatures between room temperature and the liquefaction temperature of the sample (80 K). To this end, two different setups have been constructed. In a standard setup for the ultrafast detection of the optically induced Kerr effect we derive pump and probe beam from the same laser beam and cross them in the sample at a small angle (Fig. 3.5). For the temperature dependent measurements a setup with collinear pump and probe of different colors for maximum overlap under the spatially restricted conditions of a helium-bath cryostat was used (Fig. 3.6) [1].

---

[1] An experimental setup with collinear pump and probe geometry was built for comparative evaluation within the diploma thesis of Jochen Maurer [40]. For the temperature-resolved experiments we used a similar setup constructed around a helium-bath cryostat by Falk Königsmann.

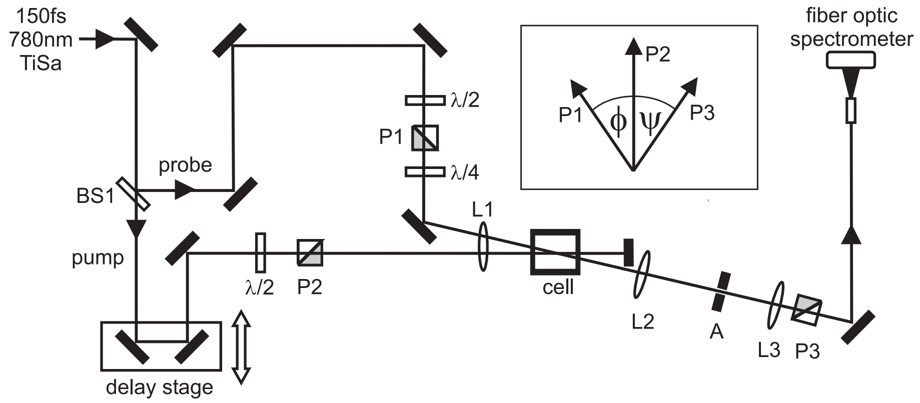

Abbildung 3.5: *Standard experimental setup for measurement of the ultrafast optically induced Kerr effect. Pump and probe are derived from the same laser beam and cross in the sample at a small angle (see text).*

3.2.1 Standard setup with crossed pump and probe

An optical Kerr effect experiment involves the creation of an anisotropy in a sample by a Raman-type process, and its time-resolved detection through the modification of the polarization status of a probe pulse. The requirements regarding the laser source are that pulses be short compared to the timescale of sample dynamics and relatively intense, given the non-resonant nature of the process. The particular color of the pump and probe laser beams is of minor importance as long as off-resonant processes prevail. In the standard optical Kerr effect setup therefore the fundamental of a Ti:sapphire laser is used to provide both pump and probe, which overlap in the sample at a small angle, and after the sample the probe beam is discriminated spatially (Fig. 3.5) by blocking the pump beam.

The laser source in our setup is a commercial Ti:sapphire amplified erbium-doped fiber oscillator (Clark CPA 2001 MXR) emitting pulses of 165 fs pulse duration (FWHM) with a repetition rate of 1 kHz at a central wavelength of 780 nm with a total power of 900 mW. A fraction of 10 percent of the total output is split at a beam splitter (BS1) into two parts, the stronger of wich (up to 90 mW) being used as a pump, and the weaker (up to 1 mW) as a probe.

The pump is passed by means of dielectric mirrors over a commercial (Physik Instrumente M.505PD) computer controlled delay stage with a resolution of down to 1μm (6.67 fs) and a total range of 15 cm (corresponding to 1 ns) to provide a tunable delay between pump and probe. After this it passes through a Glan-Thomson polarizer (P2), the polarization of which is set to an angle of 45 degrees with respect to the vertical. The tilted polarization of the pump was favored over tilted polarization of the probe, as in the beam path of the pump no dielectric mirrors are used after the polarizer. Before the pump polarizer, a half-wave plate ($\lambda/2$, Thorlabs) is inserted to act as a continuously tunable filter for the adjustment of intensity of the pump. Given the initially imperfect polarization of the input laser beam, this combination made it possible to cover almost two orders of magnitude in pump power (2 mW - 90 mW). The pump is then focused by a lens of 15 cm focal length (L1, quartz or BK7) into a home-built gas cell with a free optical path of 30 cm between two CaF_2 windows (diameter 1 in, thickness 2 mm), and after the sample is stopped by a beam block. The gas cell is constructed to host sample pressures from 10 mbar up 5 bar, monitored by pressure gauge (MKS Baratron).

The polarization of the probe is set to an angle of 45 degrees with respect to the pump by a Glan-Thomson polarizing prism (P1, Gebr. Halle Nachfl.) for homodyne detection, or deviating from this by few degrees for heterodyne detection. As in the beam pump path, a half wave plate ($\lambda/2$) in front of the polarizer acts as a continuously tunable filter. After the polarizer, a quarter wave plate ($\lambda/4$) is inserted in the probe beam path to compensate for strain-induced birefringence. Zero-order, low-order and broadband (450-800 nm) waveplates (all fabricated by Thorlabs) were tested and found to be equal in performance as the dominating effect introducing spurious ellipticity was the wavelength-dependence of the birefringence of the optical components rather than the quality of the wave plate. Probe and pump are then focused into the sample by the same 15 cm lens (L1) to overlap in the focus of the lens at a small angle. To separate the signal from out-of focus contributions as they can arise in e.g. windows, after the sample the probe beam is cleaned by confocal imaging of the overlap region via a 15 cm lens (quartz or BK7) in a 2f-geometry onto an aperture (A, 30 μm diameter pinhole). The transmitted beam is then collimated by another 15 cm focal length lens (L3, quartz or BK7) and filtered by an analyzing Glan Thomson polarizing prism (P3, Gebr. Halle Nachfl.), the axis of which is set to -45 degrees with respect to the pump. Probe polarizer and analyzer form a matched pair of polarizers with a nominal extinction ratio of up to $6{\cdot}10^{-5}$, though the achievable dynamic range is limited by the quality and strain-induced birefringence in the optical components.

The intensity transmitted through the analyzer is then detected by a fiber-coupled CCD-based optical spectrometer (Ocean Optics) with 2048 pixels and a resolution of 0.4 nm per pixel (total wavelength range 340-1150 nm) and recorded on a computer. The linearity of the detector was found to be excellent with respect to intensity as well as to integration time over more than three orders of magnitude [35]. The relatively low sensitivity of the Ocean Optics spectrometer compared to e.g. cooled CCD cameras is of minor importance as the signal level can be easily adjusted by changing the probe intensity. The dynamic range of the fiber-optic spectrometer of three orders of magnitude for a fixed integration time could not be matched by liquid-N_2 cooled CCD cameras available in the laboratory. The whole setup is steered from a personal computer by means of a home-written LabView routine controlling the step width of the delay stage, integration time and number of averages for the detector as well as the recorded wavelength range. The program was optimized using the LabView inbuilt profiler for fast performance, as a typical experiment covers a range of some 100 ps, corresponding to some 1000 steps with 40 μm (266 fs) resolution. The minimum time spent on measuring one point is set to 1 s to average over 1000 pulses for good data quality as the detector cannot be reliably triggered. For every second of measurement in the final version the program additionally takes an overhead of 200 ms. The total measuring time spent is typically about 1 hr per trace, during which sample and laser have to be kept stable.

3.2.2 Setup with collinear pump and probe

While the standard version of the setup was used successfully for measurements at room temperature, measurements at low temperature were performed with a setup connected to a He-bath cryostat hosting the sample compartment. The cryostat is otherwise used in the group for experiments on cryogenic hydrogen, and the sample is kept in a copper-enclosed cell of 3 cm thickness (Fig. 3.6) in thermal contact with liquid helium or nitrogen depending on the desired temperature regime. In this case, the restricted accessibility makes it necessary to deviate from the crossed pump and probe scheme, as during the adjustment the foci of the beams are likely to be placed on a window, with the intensity in both beams being substantially higher than the damage threshold of CaF_2. Therefore, an experimental approach described in Ref. 103 was adapted to our system, in which the pump and probe

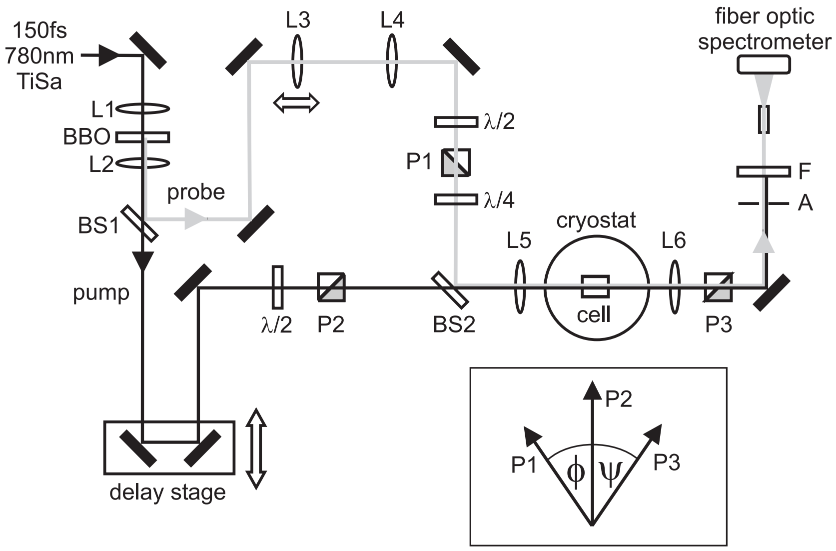

Abbildung 3.6: *Experimental setup for measurement of the ultrafast optically induced Kerr effect with collinear alignment of pump and probe beams (see text).*

beams propagate collinearly and are discriminated spectrally rather than spatially. Aside from easier adjustment, the approach has the additional advantage of providing a large interaction volume even for lenses with relatively short focal length. It can thus combine high intensity with high sensitivity.

The laser source was the same commercial Ti:sapphire amplifier (Clark CPA 2001 MXR) seeded by an inbuilt erbium-doped fiber oscillator, and at a later stage by an external fiber oscillator (IMRA femtolite 780). In both cases, the spectrum of the fundamental was centered around 780 nm with a pulse duration of 165 fs at a repetition rate of 1 kHz. Seeding by the inbuilt fiber oscillator resulted in an output power of up to 900 mW and pulse-to-pulse fluctuation exceeding 2 percent. The external oscillator showed improved values of 1 W total output power with a pulse-to-pulse stability of about 1 percent.

A fraction of the laser fundamental is frequency doubled in a nonlinear crystal (BBO, beta-barium borate) such that most of the intensity passes the crystal unmodified. The fundamental is then separated from the weak second harmonic by means of a dichroic mirror (BS1), and passed through a pump beam path similar to the one described in the previous section. The second harmonic, to be used as a probe, passes a variable telescope (L3, L4) to adjust the divergence of the beam as to compensate for the wavelength-dependence of refractivity of lenses. Otherwise the probe beam path before the sample is similar to the one described in the previous section. All lenses in the probe beam path are quartz, the ones in the pump beam path of quartz or BK7. Due to the wavelength-resolved nature of the detection, no efforts were made to compress the probe pulse after frequency doubling.

Before the entrance widow of the cryostat, the two beams are overlapped spatially on a dichroic mirror (BS2), and focused into the sample by a 15 cm lens (L5, quartz). The sample compartment is an enclosed copper gas-cell of 3 cm length with two CaF_2 windows (diameter 1 in, thickness 2 mm). It is attached to the cold finger of a bath cryostat (CryoVac), operated as a nitrogen-bath cryostat to provide tunable temperatures between close to liquid nitrogen temperature (80 K) and room temperature. The temperature is adjusted by regulating the flow of liquid nitrogen to the cold finger by a needle valve and monitored through the voltage across a semiconductor diode. The sample cell can host pressures between 1 mbar and 1000 mbar, monitored by a vacuum gauge. The cold finger

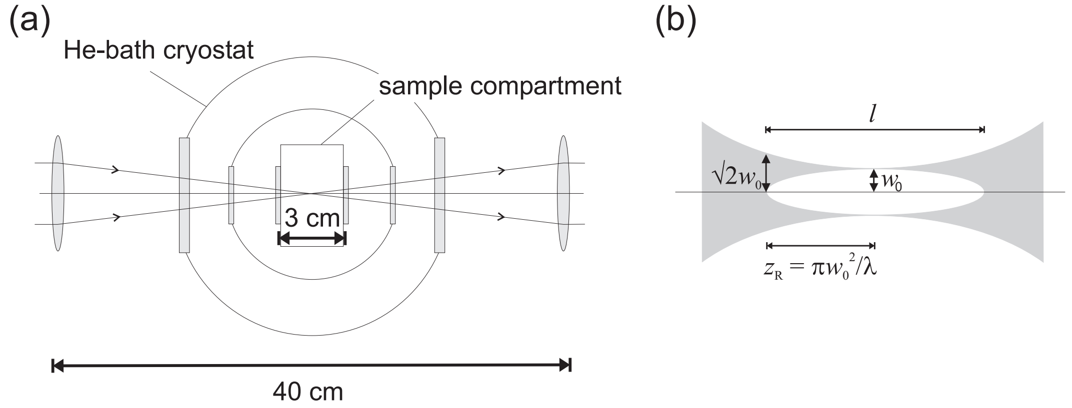

Abbildung 3.7: *(a) Schematic of the experimental geometry in the overlap region of pump and probe. The sample compartment is a copper-enclosed gas cell of 3 cm length mounted inside a He-bath cryostat, and surrounded by an additional radiation protection shield. (b) Schematic of a close-up of the interaction volume around the beam waist of the focused beams. The focal radius is given by* w_0*, the interaction region is denoted by* $l = 2z_R$*, with* z_R *being the Rayleigh length.*

is surrounded by a radiation shield, also with CaF_2 windows of 2 mm thickness, and the outer wall of the cryostat with CaF_2 windows of 4 mm thickness (Fig. 3.7(a)). A schematic close-up of the interaction volume of the pump and probe beams is shown in Fig. 3.7(b).

After passing through the sample, the two beams are collimated by a second lens identical to the focusing lens (L6) and passed though the analyzer (P3) set to - 45 degrees with respect to the pump polarization. An aperture (A, 30 μm pinhole) serves to select a small area of the collimated probe beam, as the number of windows passed within the cryostat deteriorates the polarization properties of the probe to an extent that severely limits the experimental resolution. Though the setup is in principle similar to the one used in the z-scan technique [195–197], capable of delivering information on nonlinear refraction and nonlinear absorption at the same time, the large inhomogeneities in altogether six windows did not allow this refinement. The nonlinear absorption, however, under our far off-resonant conditions is expected to be small compared to birefringence. After the sample, the intense pump radiation is then suppressed by spectral filtering by a colored glass filter (F, Newport, BG 38), and the transmitted probe is detected and recorded as described above.

3.2.3 Laser pulse properties

In all experiments, the fundamental of a Ti:sapphire laser was used as a pump laser. The pulse spectrum was characterized with CCD-based fiber-coupled optical multichannel analyzer (Ocean Optics), which was calibrated by means of mercury and neon spectral standards (Lambda Physik). A spectrum of the pump laser is shown in Fig. 3.8(a). The pulse is characterized by a close to Gaussian spectrum with a FWHM of 8 nm, centered a wavelength of about 780 nm. Slightly varying central wavelengths for the pulses in the following figures originate from the change of the seed source from inbuilt SErF oscillator to the external IMRA femtolite 780 in the course of the work. The FWHM of 8 nm corresponds to a bandwidth of 130 cm^{-1} in energy, within which rotational transitions with $\Delta J = 2$ up to $J = 20$ in nitrogen are contained. A FWHM bandwidth of $\Delta E_{1/2} = 130$ cm^{-1} or $\Delta\nu_{1/2} = 4$ THz for the pump translates into a Fourier-limited pulse width of $\Delta t_{1/2} \approx 110$ fs

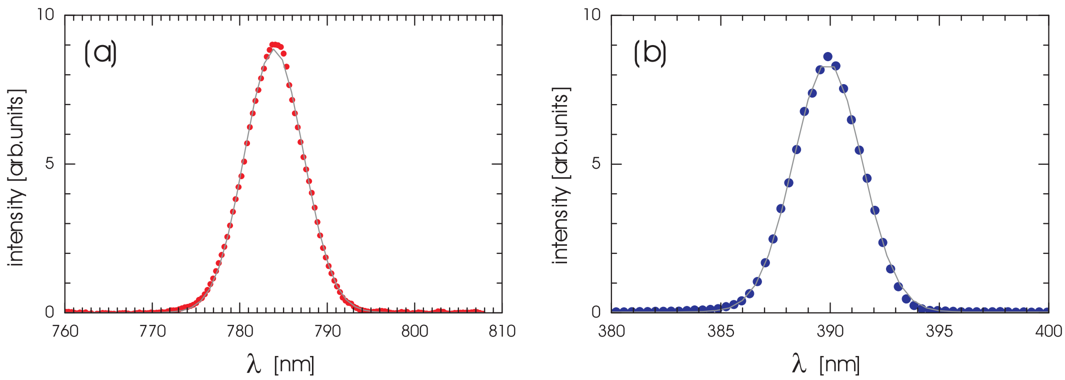

Abbildung 3.8: *Spectra of (a) the pump laser (Ti:sapphire fundamental) centered at 782 nm (red symbols) with a Gaussian fit with FWHM of 8 nm shown as gray line, and (b) its second harmonic at 390 nm (blue symbols) as it is used for probing in the collinear setup (Gaussian fit with 3.7 nm FWHM shown as gray line).*

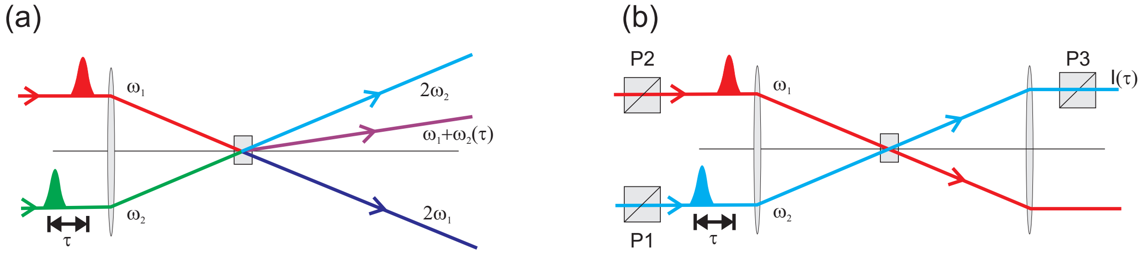

Abbildung 3.9: *Schematic setup for SFG FROG (a) and PG FROG (b). In a SFG FROG experiment, two pulses centered at the frequencies ω_1 and ω_2 overlap in space on a non-centrosymmetric nonlinear crystal, e.g. BBO. If the pulses overlap in time and in space, the sum frequency $(\omega_1 + \omega_2)(\tau)$ appears. A PG FROG setup is largely equivalent to an ultrafast optical Kerr effect setup. The observable is the elliptic component $\mathcal{I}(\tau)$ in the linearly polarized probe pulse (blue) induced if the pump pulse (red), polarized at 45 degrees with respect to the probe, overlaps in time and space with the probe in the nonlinear medium.*

FWHM according to [198]

$$\Delta t_{1/2} = \frac{2\ln 2}{\pi}\frac{1}{\Delta\nu_{1/2}}. \tag{3.15}$$

The actual pulse duration was determined by means of a frequency resolved optical gating (FROG) method [199]. In FROG, a gate pulse with well known properties serves to characterize a probe pulse by a nonlinear optical interaction in a nonlinear medium. The signal resulting from this interaction has to be separated from the individual effects of both pulses, and appears only at times, when both pulses overlap in the medium spatially and temporally with a possible additional dependence on the instantaneous phase, amplitude and wavelength of the gate pulse. FROG is a powerful tool that in principle allows to recover amplitude and phase of the probe pulse from inverting a energy vs. time delay surface by appropriate algorithms [199]. In our case, however, the detailed phase of the pulses is irrelevant to the experiment. Furthermore, spectra and temporal envelopes of the pulses display a close to Gaussian shape. Therefore, the analysis of the FROG traces was limited to extracting pulse width and chirp (change in color over the pulse duration) by assuming Gaussian envelopes.

The pump pulse (Ti:sapphire fundamental) was characterized by means of a sum frequency generation (SFG) FROG. In this method, the nonlinear interaction is SFG in a non-centrosymmetric nonlinear medium, in this case a 0.1 mm thick BBO crystal cut for

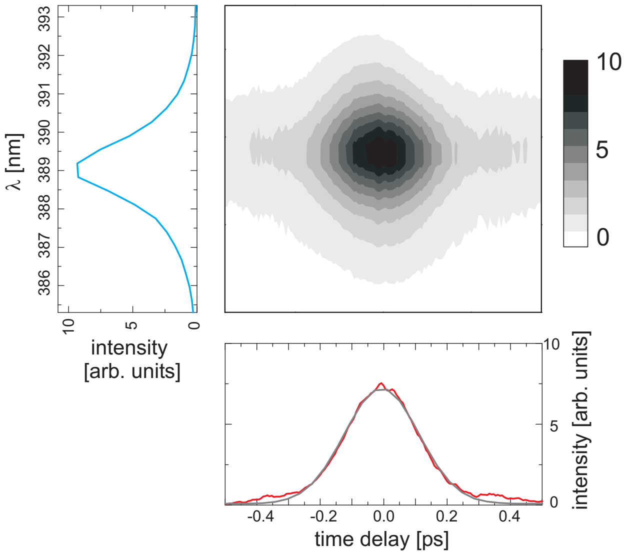

Abbildung 3.10: *SHG FROG surface of the Ti:sapphire fundamental, resulting from a convolution of pump and probe pulses, both of which are derived from the fundamental beam. On the left panel the projected spectrum of the second harmonic is displayed. On the bottom panel the integrated trace (red line) over time is plotted together with a least-squares fit to a Gaussian envelope (gray line) yielding a FWHM of (235 ± 5) fs for the convolution.*

type II phase matching [185]. The laser fundamental serves as both pump and probe, thus effectively a second harmonic generation (SHG) takes place. Both laser pulses create their second harmonic in the BBO independently of each other, however, frequency conversion has to satisfy not only energy conservation but also momentum conservation. The doubled frequency originating from interaction of both pulses therefore is emitted from the crystal along the center of the two beams (Fig. 3.9(a)). A wavelength vs. time delay surface from this experiment is shown in Fig. 3.10. Being a second-order method and equivalent to an autocorrelation, the SHG FROG trace is symmetric in time and does not reveal the presence of any chirp [199]. On the left panel of Fig. 3.10 the projected spectrum of the second harmonic is shown, and on the bottom panel the integrated intensity over delay time. The generation of the second harmonic takes place with an amplitude equal to the product of the two electric fields. In our case it amounts to a convolution of two identical Gaussian pulses, yielding a Gaussian envelope with the FWHM increased by a factor of $\sqrt{2}$:

$$\int_{-\infty}^{\infty} A_1 \exp\left(\frac{t^2}{2\Delta t^2}\right) A_2 \exp\left(\frac{(t-\tau)^2}{2\Delta t^2}\right) dt = \tilde{A} \exp\left(\frac{\tau^2}{2(2\Delta t)^2}\right). \tag{3.16}$$

The FWHM of the convolved trace was determined by least-squares fitting to a Gaussian envelope to be (235 ± 5) fs. Recalculated into the FWHM of the original pulse this corresponds to 165 fs, a value also supported by later measurements with a commercial autocorrelator.

For measurements at room temperature, the same parameters also apply to the probe pulse. This was verified by performing an in situ polarization gating (PG) FROG experiment in argon gas at 900 mbar pressure and room temperature in the sample compartment (Fig. 3.9(b)). The PG FROG method relies on the instantaneous electronic polarization in a nonlinear medium, which results in birefringence modifying the polarization of a probe pulse. The principle is the same as of the optically induced Kerr effect, the choice of nonlinear media, however, is limited to materials with purely electronic response, as slow reorientation of particles would distort the image of the trailing edge of the pulse. In a

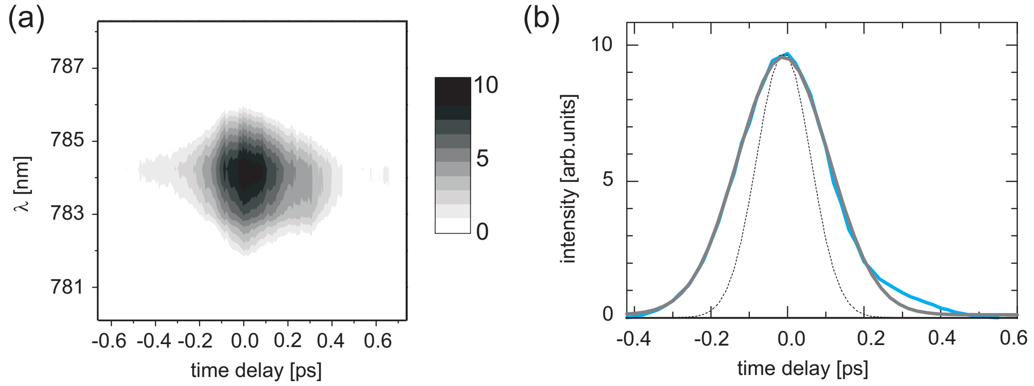

Abbildung 3.11: *(a) PG FROG surface of the probe pulse derived from the Ti:sapphire fundamental in argon gas at room temperature an 900 mbar pressure. The pattern is symmetric in time, indicating the absence of chirp. (b) PG FROG trace from (a) integrated over the spectrum (solid blue line) and Gaussian envelope fitted by a least-squares procedure (gray line). The Gaussian fit has a FWHM of (175 ± 4) fs, corresponding to a pulse FWHM of 157 fs (pulse envelope shown as dashed black line).*

PG FROG trace a chirp shows as a tilt of the resulting pattern in time. The trace resulting from using the fundamental as both pump and probe is shown in Fig. 3.11(a). It is symmetric in time and thus shows that the fundamental, when being used as a probe does not display any chirp. From this experiment the pulse width was determined by fitting the integrated spectrum with a Gaussian envelope (Fig. 3.11(a)) and extracting the width τ of the original pulse according to [199]

$$\tau_{\text{FROG}} = \sqrt{\frac{\tau_{\text{pump}}^2}{2} + \tau_{\text{probe}}^2}, \tag{3.17}$$

where τ_{FROG} is the FWHM of the convolution of two Gaussian functions with FWHM of τ_{pump} and τ_{probe} for pump and probe, respectively. The pulse width of the pump has to be halved as the Kerr effect depends quadratically on the electric field of the pump pulse. The Gaussian fit yields a FWHM of (175 ± 4) fs, resulting in a probe pulse width of 157 fs, largely consistent with the 165 fs for the pump obtained by SHG FROG.

For the ultraviolet probe pulse in the colinear geometry, *in situ* characterization via the PG FROG method delivered a probe FWHM too large to be consistent with the broadening observed in the rotational revivals. This is most likely due to an overwhelmingly large nonlinear response from the windows of the gas cell compared to argon gas as a nonlinear medium. The UV probe pulse duration was determined by fitting the numerically simulated alignment signal to the rotational revivals observed and was found to be about 130 fs FWHM for the unchirped pulse.

Color aberrations in the optical components of the setup lead to the ultraviolet probe usually displaying a chirp (Fig. 3.12(a)). Given the wavelength-resolved nature of the detection, no efforts were made to compensate for chirp in the experiment. To account for the effect of the chirp on our data, we implemented a computer code numerically removing the chirp by shifting data lines for individual points in the spectrum with respect to each other. The goal is achieved if the signal appears at the same time in all spectral channels. Figure 3.12(b) shows the effect of computationally compensating for the chirp by shifting the traces at the longer wavelength pixels successively more backward in time. The typical tilted surface arising from a chirped pulse in turned into an upright one, thus reducing the total width in time of the revival from 0.7 to 0.6 ps. In Fig. 3.12(c) the effect of this

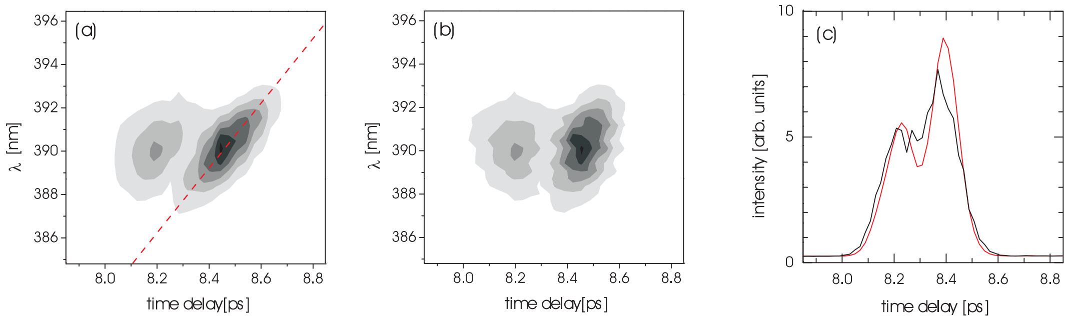

Abbildung 3.12: *(a) Wavelength vs. delay time surface plot of the second harmonic of the Ti:sapphire fundamental at the time of the first revival in* N_2*. The pulse displays a negative chirp highlighted by the dashed red line following the center of intensity of the alignment peak. (b) Chirp computationally compensated by shifting the red pixels backward in time to achieve a non-tilted surface. (c) Integrated intensity of the uncorrected signal (black) in comparison with the corrected one (red).*

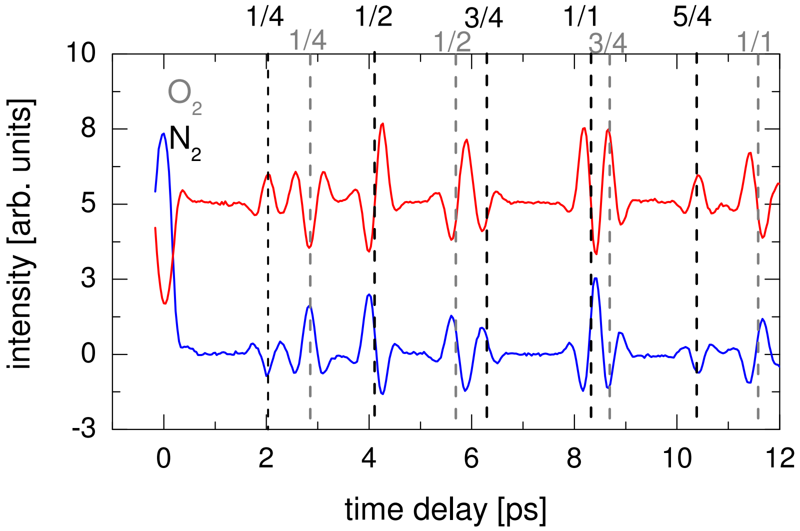

Abbildung 3.13: *Experimentally detected heterodyne signals in air under ambient conditions with opposite detuning* ϑ *(see Fig. 3.4) of the local oscillator in top and bottom traces. The sample is excited by a Gaussian laser pulse of 160 fs FWHM and a power density of 20 TW/cm*^{2}*. The revivals for nitrogen and oxygen are marked by black and gray vertical lines, respectively.*

compensation on the integrated spectrum is shown. The corrected signal (red) is better modulated and narrower in time than one derived from the raw data (black).

3.2.4 Homodyne vs. heterodyne detection

Molecular alignment is detected in a Kerr effect experiment through modification of the polarization properties of a probe pulse. The total detected intensity (cf. Sec. 3.1) is in general a sum of the contributions of a local oscillator E_{Lo}^2, the heterodyne signal $2E_{\mathrm{Lo}}E_s$ and the homodyne signal E_s^2 [18], see also Eqs. (3.13) and (3.14):

$$I_{\mathrm{det}} \propto E_{\mathrm{Lo}}^2 \pm 2E_{\mathrm{Lo}}E_s + E_s^2. \tag{3.18}$$

For heterodyne detection, the amplitude of the local oscillator is chosen to be larger than the expected signal. The heterodyne contribution then dominates with respect to the ho-

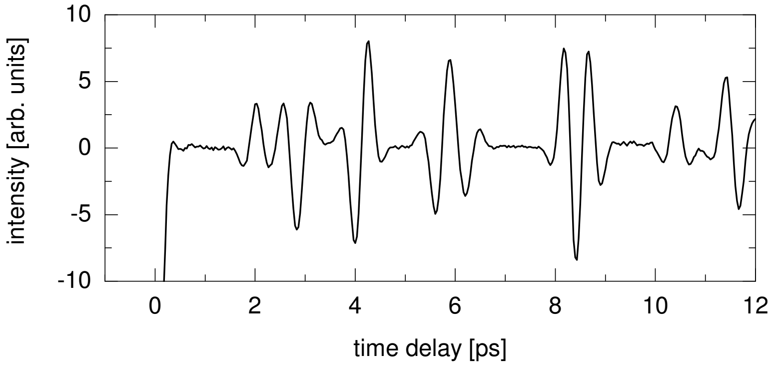

Abbildung 3.14: *Difference of the two experimental traces of Fig. 3.13 yielding the pure heterodyne signal. In addition to the amplitude of the birefringence signal it also measures the relative direction of fast and slow axes in the sample.*

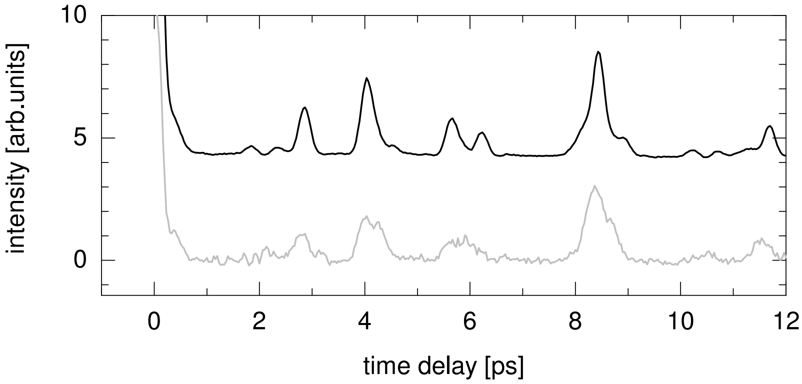

Abbildung 3.15: *Sum of the two experimental traces of Fig. 3.13 yielding the pure homodyne signal (gray line). The black line is the signal from an experiment with detection adjusted to* $\vartheta = 0$ *for homodyning (scaled down and upshifted for better visibility). In the homodyne signal, all deviations from the isotropic sample lead to positive deviations from a baseline ideally equal to zero.*

modyne one. It depends linearly on the interference of the signal electric field and the local oscillator and thus shows deviations from the isotropic value to the negative as well as to the positive side, depending on the relative phase of signal and local oscillator.

The local oscillator is created by turning the probe polarizer by a small angle ϑ (Fig. 3.4 of Sec. 3.1). This creates a small elliptic polarization in the probe, with the direction of rotation of the electric field vector determined by the direction in which the probe polarizer was detuned with respect to the quarter-wave plate. The resulting perpendicular electric field interferes with the elliptic component induced by the birefringence in the sample, and the interference can be constructive and destructive depending on the relative phase. In this sense, heterodyne detection measures in addition to the amplitude of the birefringence signal also the direction of fast and slow axes in the sample.

In a single experimental run, however, according to Eq. (3.18), the heterodyne signal is always overlaid by a homodyne contribution. The relative amplitude of this homodyne signal can be suppressed by increasing the amplitude of the local oscillator. This comes at the expense of reducing the dynamic range in the detector, as the quadratic influence of the local oscillator electric field quickly leads to saturation. To obtain a pure heterodyne signal one therefore in general has to perform two successive experiments with opposite setting of the local oscillator. The scheme is illustrated by a set of measurements for air at room temperature in Fig. 3.13. The traces show a superposition of nitrogen and oxygen dynamics leading to a complex pattern of recurrences. Every peak of the revival trace can be assigned to a particular species. Note that in the contributions from oxygen the quarter revivals are as pronounced as the full and half revival due to the peculiar nuclear spin statistics. The relative weight of the oxygen contribution is greater than the partial pressure due to the larger anisotropy of the polarizability. The detected intensities are described as

$$I^+_{\mathrm{det}} \propto E^2_{\mathrm{Lo}} + 2E_{\mathrm{Lo}}E_s + E^2_s \tag{3.19}$$

$$I^-_{\mathrm{det}} \propto E^2_{\mathrm{Lo}} - 2E_{\mathrm{Lo}}E_s + E^2_s. \tag{3.20}$$

The difference of the two intensity traces yields the pure heterodyne signal:

$$I^+_{\mathrm{det}} - I^-_{\mathrm{det}} \propto E_{\mathrm{Lo}}E_s. \tag{3.21}$$

The pure heterodyne signal derived from the two experimental runs shown in Fig. 3.13 is displayed in Fig. 3.14.

The sum of the intensities of the two experimental runs yields the homodyne signal:

$$I^+_{\mathrm{det}} + I^-_{\mathrm{det}} \propto E^2_{\mathrm{Lo}} + E^2_s. \tag{3.22}$$

The homodyne signal derived from the two traces of Fig. 3.13 is shown in Fig. 3.15 as gray line. For a homodyne experiment, the amplitude of the local oscillator is set to zero. The signal is always positive as it depends only on the square of the amplitude of the signal electric field. The homodyne signal of air is shown in Fig. 3.15 as a black line. Homodyning has the advantage over heterodyning of requiring only a single experimental run. In addition, the signal is essentially background-free, which is optimal regarding the sensitivity of the detection. Additionally, homodyning is less demanding regarding stability of the laser system and sample as it requires no exact reproduction of experimental conditions.

3.3 Analysis of revival signal

This section is devoted to the analysis of the alignment signal. We show that:

- **The collinear pump-probe geometry of our setup offers an interaction length of up to 1 mm and a high sensitivity.**
- **A spectrally broad probe pulse introduces an intrinsic local oscillator with wavelength-dependent phase.**
- **In a homodyne detected experiment, the small population contribution can be observed simultaneously with the large coherence contribution by analyzing the signal shape.**
- **Changes in alignment signal shape upon collision-induced decay give evidence of a slower decay of the population part with respect to the coherence part.**

3.3.1 Dependence on pressure, intensities and temperature

A Kerr effect experiment including the pump and the probe process is described as a $\chi^{(3)}$ nonlinear optical process (cf. Sec. 3.1). Its magnitude should depend on the applied intensities to the third power, composed of a quadratic dependence on pump intensity and a linear dependence on the intensity of the probe [180]. We verified both dependencies for our setup. Figure 3.16(a) shows the dependence of the signal intensity on pump power, which is indeed to very good approximation quadratic. In Fig. 3.16(b) the linear dependence on probe power is displayed. Both measurements show that the expected dependences are reproduced experimentally in a quantitative way.

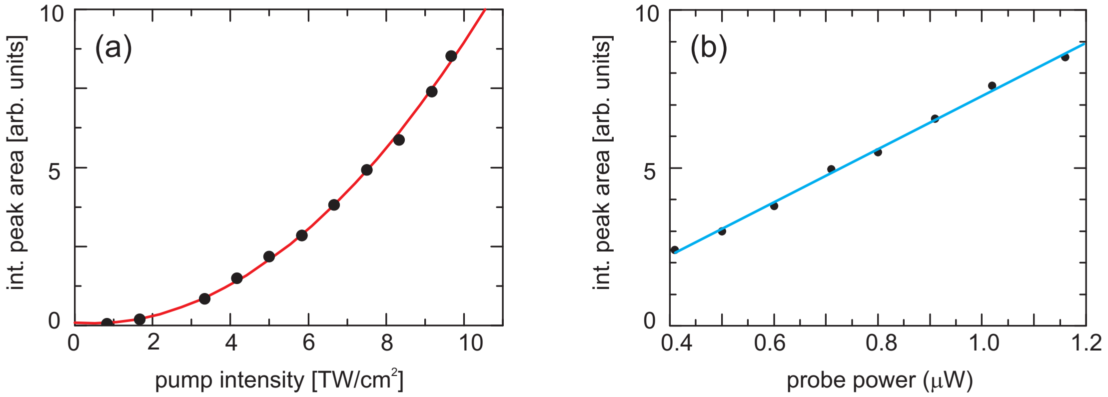

Abbildung 3.16: *(a) Dependence of the intensity of the homodyne detected signal on pump intensity in nitrogen under ambient conditions. The black dots represent measured data, and the red line a least-squares fit of a parabola to the data. The quadratic dependence expected for a second-order nonlinear optical process (stimulated pump-induced Raman process) is verified. (b) Dependence of the intensity of the homodyne detected signal on probe power in nitrogen at room temperature. The intensity of the detected signal (black dots) is linearly related to the intensity of the probe (linear regression shown as blue line).*

The non-adiabatic alignment of an ensemble of molecules is equivalent to the creation of a rotational wave packet [7]. A rotational wave packet is a coherent superposition of rotational dynamics of individual particles, and thus the amplitude of the wave packet grows quadratically with the number of particles in the ensemble. Every particle amplitude

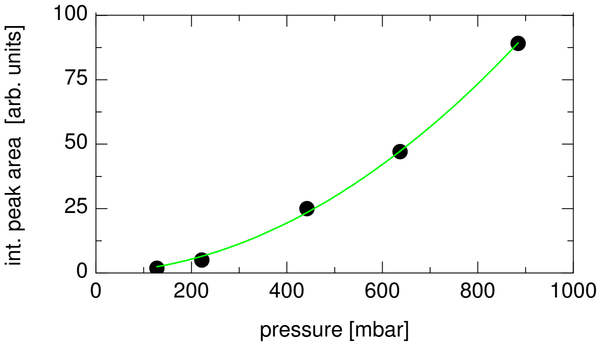

Abbildung 3.17: *Dependence of the intensity of the homodyne detected signal in nitrogen on pressure. The black dots represent measured signal intensities at a series of pressures, the green line is a least-squares fit of a parabola to the data. The quadratic dependence is clearly verified, and also substantiated by further measurements up to 5 bar (data not shown).*

adds in phase, i.e. interferes constructively with the others in the wave packet. The intensity recorded by a detector is proportional to the time-average of the square of the electric field. For a number of oscillators with electric field amplitude E_i and frequency ω_i, the instantaneous intensity for an incoherent and a coherent superposition is given as:

$$\mathcal{I}_{\text{incoh}} = \sum_{i=1}^{N} (E_i \sin \omega_i t)^2 \propto N \tag{3.23}$$

$$\mathcal{I}_{\text{coh}} = \left(\sum_{i=1}^{N} E_i \sin \omega_i t \right)^2 \propto N^2. \tag{3.24}$$

The signal intensity is found by subsequent time averaging. In the incoherent superposition, the intensities of the individual oscillators add up independently, leading to a linear increase with the number N (Eq. (3.23)). In a coherent superposition, the electric fields of the oscillators add up in phase, and the intensity is calculated as the square of the sum of electric fields. In this case, represented by Eq. (3.24), the intensity grows proportional to the number of oscillators squared.

In the experiment, this coherent behavior of the aligned ensemble of gas molecules shows as a quadratic increase of signal intensity with pressure, displayed in Fig. 3.17. It should be noted that the wave packet-like behavior of the gas molecules is the result of the fact that the molecules do not interact. They rather evolve independently of each other in the same potentials and thus modify in the same way the probe electric field which reads out the degree of alignment.

In Fig. 3.18, numerically calculated curves for the homodyne detected signal at two different power densities are overlaid with experimentally measured data points. The agreement between theory and experiment is excellent, which will allow in the following sections to draw quantitative conclusions from the comparison of the experimental data with numerical simulations.

Additionally, the temperature dependence of the detected signal is a valuable tool to investigate the agreement between theory and experiment. A rise in the temperature increases the number of populated J-levels (see Fig. 2.5). According to the reasoning of Sec. 2.2, this decreases the amplitude of oscillations around the revival times. Figure 3.19 demonstrates the excellent agreement of simulation with the experiment by comparing the simulated homodyne signal from $^{14}N_2$ following an excitation pulse with experimentally

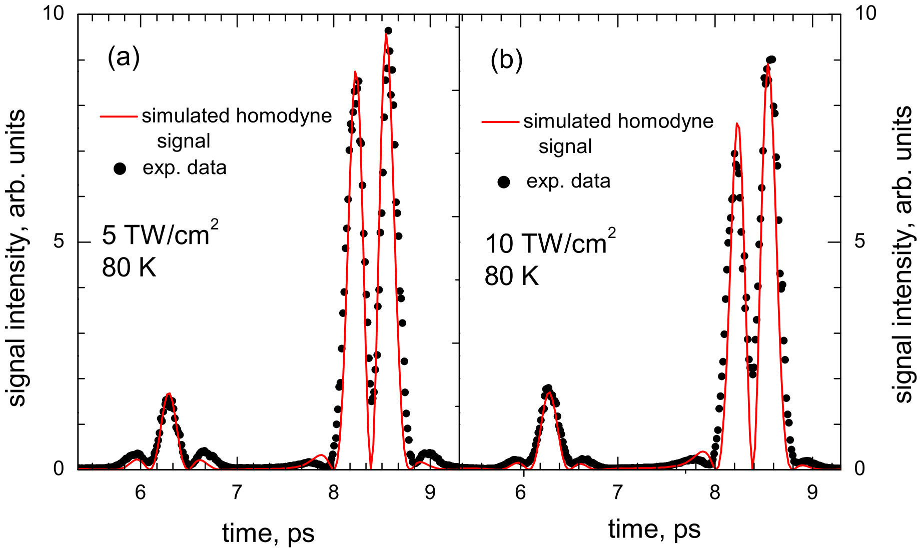

Abbildung 3.18: *Comparison of numerically simulated (red solid line) and experimentally measured (black circles) homodyne detected alignment signal from three-quarter revival to first revival in nitrogen gas at 80 K and a laser pulse intensity of (a) 5 TW/cm^2 and (b) 10 TW/cm^2.*

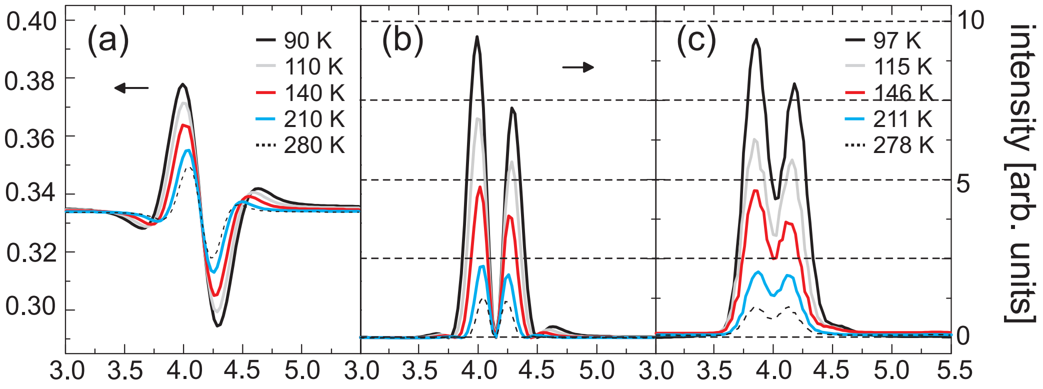

Abbildung 3.19: *(a) Numerical simulation of $\langle\langle \cos^2\theta \rangle\rangle_T$ (see Eq. (2.11)) in $^{14}N_2$ upon excitation with a Gaussian pump pulse of 160 fs FWHM with an intensity of 8 TW/cm^2 at the time of the first half revival. (b) Homodyne intensity calculated from the simulated trace according to $(\langle\langle \cos^2\theta\rangle\rangle - 1/3)^2$ (see Eq. (3.13)). (c) Experimentally detected homodyne signal at similar temperatures and a pressure of 900 mbar corrected for the influence of density. The signal appears broadened with respect to the simulation due to the convolution with the probe pulse, the quantitative agreement with the simulation after correcting for particle density is very good.*

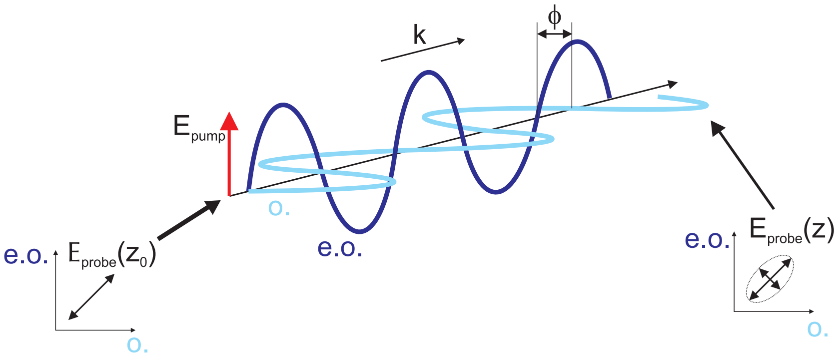

Abbildung 3.20: *Effect of the presence of birefringence in a sample on the polarization of the probe pulse. The probe pulse is initially linearly polarized at 45 degrees (see Fig. 3.4) with respect to the pump polarization (left inset). The polarization at the exit is turned into an elliptic one (right inset).*

determined parameters (pulse FWHM 160 fs, intensity 8×10^{12} W/cm^2, Gaussian envelope) with the experimentally measured signal at a constant pressure of 0.9 atm. The experimental signal has been corrected for the influence of increasing number density with decreasing temperature by multiplication with a factor proportional to the temperature. The increase in the value of the squared alignment cosine with decreasing temperature expected from the simulated traces and Fig. 2.5 is very well reproduced in the experimentally detected signal intensities. With this agreement of simulation and experiment, we use the comparison of simulated and experimental data to quantify the degree of rotational alignment in the sample. As an alternative, one may deduce the degree of alignment from a direct measurement of the nonlinear refractive index [200, 201], however, this method would suffer from large uncertainties in the reference values.

3.3.2 The interaction volume

In a homodyne, or quadratic, detection scheme, probe polarizer and analyzer are crossed, yielding ideally no transmitted intensity in the presence of an isotropic sample (see Eq. (3.13)). All deviations from isotropy give rise to an elliptic component in the probe and thus a signal on the detector (Fig. 3.20). The amount of ellipticity to be expected under our experimental conditions can be calculated from the phase lag accumulated by the component of the probe electric field in the direction of the aligned molecular axes (extra-ordinary beam, e.o.) compared to the component perpendicular to it (ordinary beam, o.). With the wavelength in the sample being $\lambda_{\mathrm{o./e.o.}} = \lambda/n_{\mathrm{o./e.o.}}$, where λ is the vacuum wavelength, and $n_{\mathrm{o./e.o.}}$ the ordinary or extraordinary refractive index, the probe beam accumulates a phase shift ϕ between ordinary and extraordinary component. The polarization at the exit then is elliptic rather than linear.

Elliptically polarized light is usually described in the form of an electric field vector with two components E_x and E$_y$, corresponding to ordinary and extraordinary direction:

$$\mathbf{E_p}(\mathbf{r},t) = E\begin{pmatrix}\cos(k_{\mathrm{o.}}z-\omega t)\\ \cos(k_{\mathrm{e.o.}}z-\omega t)\end{pmatrix} = E\begin{pmatrix}\cos(\frac{2\pi n_{\mathrm{o.}}}{\lambda}z-\omega t)\\ \cos(\frac{2\pi n_{\mathrm{e.o.}}}{\lambda}z-\omega t)\end{pmatrix}. \tag{3.25}$$

Here, ω is the light frequency, and z the propagation direction. The difference in refractive index between the directions is given as $\Delta n = n_{\mathrm{e.o.}} - n_{\mathrm{o.}}$. Inserting this equation into the expression for the electric field vector Eq. (3.25) results in

$$\mathbf{E_p}(\mathbf{r},t) = E \begin{pmatrix} \cos(\frac{2\pi n_{o.}}{\lambda} z - \omega t) \\ \cos(\frac{2\pi n_{o.}}{\lambda} z - \omega t + \phi(z)) \end{pmatrix}, \tag{3.26}$$

where the phase lag ϕ between x (o.) and y (e.o.) components is introduced according to

$$\phi = \frac{2\pi\Delta n}{\lambda} z. \tag{3.27}$$

The refractive index of a gas at moderate densities can be approximated using the Lorentz-Lorenz equation [202] as $n \approx 1{+}2\pi N\alpha$, where N is the number density of molecules per unit volume, and α the polarizability. The maximal anisotropy of polarizability in the aligned ensemble is given by $\Delta\alpha(\langle\langle\cos^2\theta\rangle\rangle - \frac{1}{3})$, where the anisotropy of polarizability is weighted by the degree of alignment achieved. The difference in refractive index for the probe beam is thus given by

$$\Delta n = 2\pi N \Delta\alpha \left(\langle\langle\cos^2\theta\rangle\rangle - \frac{1}{3} \right). \tag{3.28}$$

For nitrogen the number densities at 1 atm pressure at 295 K and 80 K are $N = 2.4 \times 10^{19}$ cm^{-3} and $N = 9.1 \times 10^{19}$ cm^{-3}, respectively. With the anisotropic polarizability $\Delta\alpha$ of about $0.89{\times}10^{-24}$ cm^3 (Ref. 1), the maximal possible Δn for perfect alignment equals $\Delta n_{max} = 3.4 \times 10^{-4}$ for 80 K, and $\Delta n_{max} = 8.7 \times 10^{-5}$ for 295 K.

To determine the power density of the pump laser, the foci of several lenses employed in the experiment were measured by a scanning knife-edge method [203]. In the diffraction limited case, the beam waist w_0 (Fig. 3.7(b)) equals [202]

$$w_0 = \frac{1.78\lambda f}{D}, \tag{3.29}$$

where f is the focal length of the lens, λ the laser wavelength, and D the diameter of the beam on the lens. The theoretical limit corresponds to about 10 μm for a $f = 15$ cm lens and a beam diameter of 2 cm. Experimentally, for lenses between 5 cm and 20 cm focal length a value of about 35 μm was determined [35, 40], depending only weakly on the focal length f. Thus, as the focal diameter is relatively far from its diffraction-limited value and apparently dominated by optical aberrations rather than the focal length of the particular lens, we assume a focal diameter of $2w_0 = 35$ μm for all our experiments. With the focal diameter as determined above, the power density in the temperature-dependent measurements was set to 10 TW/cm^2 or below in the focus.

Along the optical axis z, the beam then expands according to

$$w(z) = w_0 \sqrt{1 + \left(\frac{z}{z_R}\right)^2}, \tag{3.30}$$

where $z_R = \pi w_0^2/\lambda \approx 1$ mm is the so-called Rayleigh length, resulting in an effective interaction volume of the shape schematically depicted in Fig. 3.7(b). This has to considered as an upper limit in our case, since our w_0 is substantially exceeding the diffraction limited value. Due to the geometry of the setup a relatively long focal length of 15 cm had to be used with the consequence of an only slowly expanding beam, and higher power densities are already likely to damage the windows in the cell. The maximal value for $(\langle\langle\cos^2\theta\rangle\rangle - \frac{1}{3})$ that can be obtained under our experimental conditions is calculated from numerical simulations to be about 0.087 at 80 K and 0.047 at room temperature, using a power density of 10

TW/cm^2. The theoretical calculation for Δn under experimental conditions therefore yields 4.7×10^{-5} at 80 K and 0.61×10^{-5} at room temperature.

The accumulated phase lag per unit length according to Eq. 3.27) thus amounts to $\phi/$(z [mm]) = 44 degrees/mm at 80 K, and 6 degrees/mm at room temperature. Under optimal conditions, the resolution of a matched pair of polarizers is 10^{-5} degrees. With a collinear pump-probe geometry, the spatial overlap can be close to 1 mm. Depending on the amount of spurious birefringence, thus a dynamic range of 5 orders of magnitude can be achieved in the experiment.

To confirm this high sensitivity, we determined the ellipticity induced in a linearly polarized probe pulse by 0.9 atm of nitrogen at a temperature of 80 K upon the excitation with a pump pulse of 160 fs duration and an intensity of 8 TW/cm^2. Extrapolating the above values to these conditions [33] we arrive at a theoretical phase lag of 25 degrees/mm.

The phase lag from the experimental side can be determined from the ratio of total probe intensity and the intensity of the elliptic component after the passage of the sample. With the coordinate system defined as in Fig. 3.20, the projection of the probe electric field onto its original polarization direction is given by the vector product with the vector $1/\sqrt{2}(1,1)$, and the projection on the direction orthogonal to the original polarization is given by the vector $1/\sqrt{2}(1,-1)$. The electric field in these directions is expressed as

$$\mathbf{E} \cdot \frac{1}{\sqrt{2}} \begin{pmatrix} 1 \\ \pm 1 \end{pmatrix} = \frac{E}{\sqrt{2}} \left[\cos\left(\frac{2\pi n_{\mathrm{o.}}}{\lambda} z - \omega t \right) \pm \cos\left(\frac{2\pi n_{\mathrm{o.}}}{\lambda} z - \omega t + \phi(z) \right) \right], \tag{3.31}$$

with the $-$ signifying orthogonal detection and the $+$ signifying parallel detection. The detected intensity is proportional to the time-average of the square of the electric field in the respective direction:

$$\begin{aligned} \mathcal{I}_{\|} \propto \Big\langle E^2 \Big[1 + \cos\phi(z) + \frac{1}{2} \cos\left(\frac{4\pi n_{\mathrm{o.}}}{\lambda} z - 2\omega t \right) \\ + \cos\left(\frac{4\pi n_{\mathrm{o.}}}{\lambda} z - 2\omega t + \phi(z) \right) + \frac{1}{2} \cos\left(\frac{4\pi n_{\mathrm{o.}}}{\lambda} z - 2\omega t + 2\phi(z) \right) \Big] \Big\rangle_t \end{aligned} \tag{3.32}$$

$$\begin{aligned} \mathcal{I}_{\perp} \propto \Big\langle E^2 \Big[1 - \cos\phi(z) + \frac{1}{2} \cos\left(\frac{4\pi n_{\mathrm{o.}}}{\lambda} z - 2\omega t \right) \\ - \cos\left(\frac{4\pi n_{\mathrm{o.}}}{\lambda} z - 2\omega t + \phi(z) \right) + \frac{1}{2} \cos\left(\frac{4\pi n_{\mathrm{o.}}}{\lambda} z - 2\omega t + 2\phi(z) \right) \Big] \Big\rangle_t, \end{aligned} \tag{3.33}$$

where angular brackets with subscript t denote the time averaging, as an effect of which all temporally oscillating cosines cancel. Including only the surviving terms, the equations can accordingly be rewritten as

$$\mathcal{I}_{\|} \propto 1 + \cos\phi \tag{3.34}$$

$$\mathcal{I}_{\perp} \propto 1 - \cos\phi. \tag{3.35}$$

The experimentally observable quantity is the ratio of maximal $(\mathcal{I}_{\|} + \mathcal{I}_{\perp})$ to minimal intensity $\mathcal{I}_{\perp}$. By combining Eqs. (3.34) and (3.35) one obtains for the phase lag ϕ:

$$\frac{\mathcal{I}_{\perp}}{(\mathcal{I}_{\|} + \mathcal{I}_{\perp})} \approx \sin\frac{\phi}{2}. \tag{3.36}$$

From the ratio of intensities measured for parallel and perpendicular setting of probe polarizer and analyzer we derive an experimental phase lag of 13 degrees. The length of the overlap region z_0 thus can be estimated to be about 0.5 mm long using Eq. (3.27). This is also in good agreement with the experimentally determined upper limit of 1 mm for the Rayleigh length.

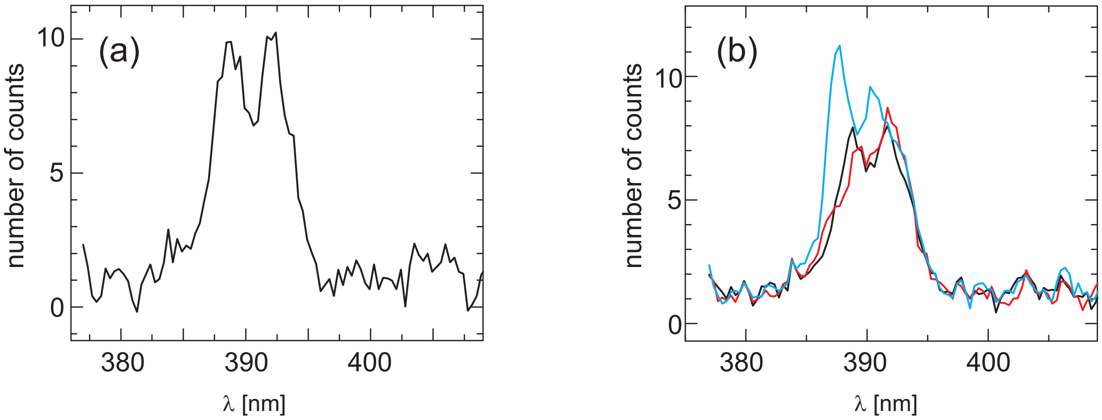

Abbildung 3.21: *(a) Spectrum of the probe pulse in the collinear experiment observed through crossed probe polarizer and analyzer. The spectrum displays a typical M-shape with the extinction being best in the center of the spectrum, and higher intensity in the wings due to the wavelength-dependence of birefringence of the optical components. Perfect extinction cannot be achieved across the whole spectrum with only diffractive optics. (b) Illustration of the relative phase of the electric field in the blue and red wing of the spectrum around a zero crossing of a rotational revival. The black line represents the intensity transmitted in the absence of birefringence in the sample. The blue and red lines show the shape of the transmitted intensity for small detuning. In one case (blue) the interference is constructive in the blue wing and destructive in the red wing, in the other case (red) the opposite is the case.*

3.3.3 Effects of a spectrally broad probe pulse

The optical Kerr effect technique with homodyne detection can offer a dynamic range of about 5 orders of magnitude (see Sec. 3.1) and is thus ideally suited to measure decays over many lifetimes. Care must be taken, however, to avoid the effects of spurious birefringence in the optical components of the setup and a possible unwanted heterodyne contribution introduced by this. In the standard implementation, an ultrafast detected optical Kerr effect experiment features a narrow-band filter in front of the (usually integrating) detector [18]. This is caused by the fact that strain-induced birefringence and other spurious effects arising from interaction of the probe laser field with components of the experimental setup tend to be wavelength-dependent. This dependence is small, however at extinction ratios of 10^{-4} or 10^{-5} between crossed polarizers, achievable in this type of experiment, even small variations across the pulse spectrum lead to a significant influence on the detected signal. Using the full spectral information content in the probe pulse can reveal additional information on the particular processes taking place in the interaction of sample and laser [204–207]. Multidimensional Raman techniques have been reviewed in Ref. 208.

The probe laser pulses employed in this work exhibited a bandwidth of 8 nm for the Ti:sapphire fundamental centered at 780 nm, and 3.5 nm for its second harmonic centered at 390 nm (Fig. 3.8(a) and (b), respectively). After careful adjustment of the polarizing optics for minimal transmission, the wavelength-dispersed intensity distribution on the spatially resolving CCD detector reproducibly showed an M-like shape with a minimum at the center wavelength and higher intensity in the wings (Fig. 3.21). This phenomenon can be explained by assuming that the polarization of the electric field of the probe pulse acquired a wavelength-dependent elliptical component.

The electric field of elliptically polarized light is described as in Eq. (3.25) as a two-

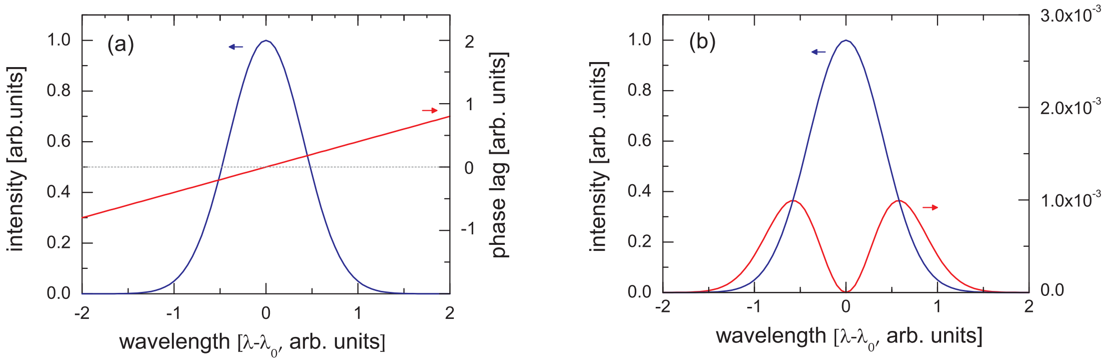

Abbildung 3.22: *(a) Envelope of a Gaussian spectrum (blue line) centered around* λ_0 *and amplitude of the electric field in the direction perpendicular to the original probe polarization (red line) for a phase lag linear in* $(\lambda-\lambda_0)$ *(see Eq. (3.39)). The dashed gray line represents zero elliptical polarization, and the elliptic component is growing linearly with increasing detuning from the center wavelength. (b) Envelope of the electric field of the Gaussian spectrum (blue line) and the projection of a field with elliptic polarization according to (a) onto the axis perpendicular to the polarizer (red line). Perfect extinction is achieved in the center, and the M-shaped pattern observed in the experiment shows up in the wings with opposite direction of the ellipticity in blue and red wing.*

component vector

$$\mathbf{E}(\mathbf{r},t)=\begin{pmatrix} E_x\cos(kz-\omega t) \\ E_y\cos(kz-\omega t+\alpha_y)\end{pmatrix}, \tag{3.37}$$

where E_x and E_y are the magnitudes of the electric field vector $\mathbf{E}$ in x and y direction perpendicular to the propagation direction z, k is the common wave vector, ω the angular frequency, and α_y the phase shift between x and y components of the field. For a spectrally broad pulse, E_y and α_y can depend on the wavelength λ. The fraction of the field that is transmitted through an analyzer set in y direction is only the y component, and the intensity measured by the detector is proportional to the time-average of the square of the electric field. This time-average can be written as

$$\langle \mathbf{E^2}\rangle_t = E_y^2(\lambda)\left\langle \cos^2(\omega t+\alpha_y)\right\rangle_t . \tag{3.38}$$

Clearly, the wavelength-dependent phase in the cos-term becomes insignificant by time averaging. The dependence of the y component of the electric field on wavelength is to first order described as a linear gradient weighted by a Gaussian spectral envelope (Fig. 3.22(a))

$$E_y(\lambda)=(\lambda-\lambda_0)dE_y\, e^{-\frac{(\lambda-\lambda_0)^2}{2\Delta\lambda^2}} . \tag{3.39}$$

In the adjustment procedure, the center wavelength λ_0 is used to minimize $E_y(\lambda)$. The phase lag therefore crosses zero at $\lambda=\lambda_0$ (Fig. 3.22(a)) and determines the minimum in Fig. 3.22(b) (red line). Assuming that the interaction with the sample, being far off resonant, does not have any wavelength-dependence itself, the detected intensity I_{det} corresponds to the square of a wavelength-dependent sum of signal electric field $E_S(\lambda)$ and local oscillator :

$$I_{\text{det}}(\lambda)\propto (E_{\text{Lo}}(\lambda)+E_S(\lambda))^2 = E_{\text{Lo}}^2(\lambda)\pm 2E_S(\lambda)E_{\text{Lo}}(\lambda)+E_S^2(\lambda). \tag{3.40}$$

In absence of a signal electric field ($E_S=0$), this gives rise to an M-shaped intensity distribution on a wavelength resolving detector (Fig. 3.22(b)). This pattern acts as wavelength-dependent local oscillator $E_{\mathrm{Lo}}(\lambda)$ for the elliptic fraction of the probe that arises from dynamic birefringence in the sample. If integrating this signal over all wavelengths, a mixed homodyne- heterodyne behavior appears, with the heterodyne contribution in one wing being retarded, and in the other wing being advanced:

$$I_{\mathrm{int}} \propto \sum_{\lambda} E^2_{\mathrm{Lo}}(\lambda) + \sum_{\lambda} E^2_S(\lambda) + \sum_{\lambda<\lambda_0} 2E_S(\lambda)E_{\mathrm{Lo}}(\lambda) - \sum_{\lambda>\lambda_0} 2E_S(\lambda)E_{\mathrm{Lo}}(\lambda). \tag{3.41}$$

For a completely symmetric local oscillator profile, the two last sums on the right hand side cancel, however this is not necessarily the case. An asymmetry leads to a small heterodyne admixture surviving in the detected trace. In most cases, this effect can be safely neglected, as for homodyne detection one generally has $E^2_S \gg E^2_{\mathrm{Lo}}$, nevertheless it becomes important for a quantitative analysis of small signals, or tracing a decay over some orders of magnitude. The homodyne part of the detected trace around the center of the probe spectrum can be isolated by spectral filtering, thus minimizing the distortion. This comes, however, at the expense of a loss of signal intensity which is the higher, the narrower the selected wavelength range. In the analysis of our measurements, we use integrate over a narrow stripe of 1-5 pixels around the spectral maximum to obtain a clean homodyne signal. To test our detection system for temporal drifts, we additionally recorded the spectrally resolved background signal at several points throughout a measurement of alignment in nitrogen. As was discussed above, the shape of the spectrum transmitted through crossed polarizers is exceedingly sensitive to a change in phase and therefore reliably reveals any spurious changes in the local oscillator. Figure 3.23 shows the background signal recorded at a time delay of 12 ps (3/2 revival), 50 ps (9/2 revival), and 88 ps (15/2 revival). Apart from a small fluctuation of the amplitude, which does not affect the shape of the revival peaks, no changes in the spectrum are observable. This confirms that throughout this particular measurement the spectral position of the local oscillator did not change.

We point out here, that this heterodyning effect in the wings of the probe pulse spectrum need not be considered only as giving rise to artifacts. It can be used upon proper adjustment to perform a homodyne experiment at λ_0, and a full heterodyne measurement in the wings of the spectrum in a single run. Opposite detunings of the local oscillator are then realized in the red and blue wings of the spectrum, and the purely heterodyne signal could be extracted by subtraction of the two halves of the spectrum. In principle, using this method purely heterodyne measurements can be performed even if there are issues with sample and/or laser stability.

3.3.4 Simultaneous experimental detection of coherence and population contributions

According to the derivation in Sec. 1.3.6, the molecular alignment in a laser electric field can be decomposed into two distinct contributions. The first is the change in the average alignment of molecular axes with respect to the laser field. Following the convention of Ref. 155, this is termed the population part of alignment $\langle\langle\cos^2\theta\rangle\rangle_p$ (see Fig. 1.14(a)). For non-adiabatic alignment in the absence of collisions, the population part is constant after the turn-off of the pulse. Additionally, the coherent rotational motion of molecules about this new average alignment leads to an oscillatory contribution with revivals of alignment and anti-alignment (see Fig. 1.14(a)). This part is termed the coherence part of alignment $\langle\langle\cos^2\theta\rangle\rangle_c$, following Ref. 155. The total $\langle\langle\cos^2\theta\rangle\rangle$ is the sum of both contributions (see Fig. 1.14(b)):

$$\langle\langle\cos^2\theta\rangle\rangle(t) = \langle\langle\cos^2\theta\rangle\rangle_p(t) + \langle\langle\cos^2\theta\rangle\rangle_c(t). \tag{3.42}$$

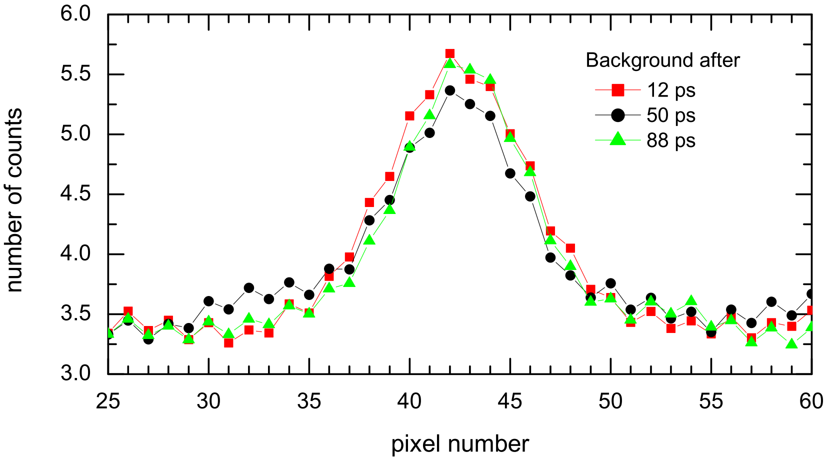

Abbildung 3.23: *Reference signal without pump recorded through crossed polarizers at various times during the measurement of alignment decay.*

In Fig. 2.4 of Sec. 2.2.2, we plotted the dependence of amplitudes of $\langle\langle\cos^2\theta\rangle\rangle_c$ and $(\langle\langle\cos^2\theta\rangle\rangle_p - 1/3)$ on the pulse power density. The strong-field limit of both contributions to the alignment is $1/2$. It is reached at pulse power densities above 200 TW/cm^2, adding up to perfect alignment in the limiting case. Otherwise, the population contribution to the molecular alignment appears to be much smaller than the coherent oscillations. The achievable field strength for alignment under realistic experimental conditions is limited by the onset of ionization to below 100 TW/cm^2 for small molecules like nitrogen, and still less for larger ones with weaker bound electrons [119, 153]. Most experiments are therefore performed in the region between 10 TW/cm^2 and 100 TW/cm^2, where the coherence contribution for nitrogen grows linearly from about 10^{-3} to 10^{-1}, and the deviation of the $\langle\langle\cos^2\theta\rangle\rangle_p$ part from $1/3$ grows quadratically from about 10^{-5} to 10^{-2} at 80 K. In particular, under our experimental conditions with a maximal power density of 10 TW/cm^2, $\langle\langle\cos^2\theta\rangle\rangle_p$ is 1.5 orders of magnitude smaller than $\langle\langle\cos^2\theta\rangle\rangle_c$. To quantitatively extract both contributions from the experimentally measured alignment signal is thus challenging.

For optical Kerr effect detection, the relation of the observed signal amplitude to the microscopic $\langle\langle\cos^2\theta\rangle\rangle$ is given by (see Ref. 176 and Eq. (3.14) of Sec. 3.1)

$$\mathcal{I}_{\text{het}} = A\left[C \pm \langle\langle\cos^2\theta\rangle\rangle - \frac{1}{3}\right]^2, \tag{3.43}$$

where A is a scaling parameter. The subscript *het* refers to heterodyne detection, where the signal generated in the sample is overlaid with a reference beam, the so-called local oscillator denoted by C (see Ref. 18 and Sec. 3.1). Usually C is chosen to be large, such that $C\langle\langle\cos^2\theta\rangle\rangle$ becomes the dominating term in the expression:

$$\mathcal{I}_{\text{het}} \approx A\left[C^2 \pm C\left(\langle\langle\cos^2\theta\rangle\rangle - \frac{1}{3}\right)\right]. \tag{3.44}$$

For a homodyne detected experiment, one has $C = 0$, and thus the detected intensity depends quadratically on the degree of alignment:

$$\mathcal{I}_{\text{hom}} = A\left[\langle\langle\cos^2\theta\rangle\rangle - \frac{1}{3}\right]^2. \tag{3.45}$$

The method of choice to quantify the $\langle\langle\cos^2\theta\rangle\rangle_p$ part of alignment has been the heterodyne detection [209]. Heterodyning offers the advantage of linearity, thus the population part does not appear overly small compared to the coherence part and can be isolated at times between revivals, where the coherence part is zero. In Ref 209, experiments on alignment decay were performed on the CO_2 molecule. With a rotational constant of 0.39 cm^{-1} [44], and a corresponding revival time of 42.7 ps, the rotational revivals of CO_2 are well separated in time. Additionally, due to the large number of rotational states populated, the mutual cancellation of wave packets between revival peaks is almost complete, and thus the coherent contribution between revivals is negligible to good approximation. By applying laser pulses with high intensity, thus a detectable population offset can be created. The approach, however, has several drawbacks. One was encountered by the authors of Ref. 209, who found that they had to make severe adjustments in the intensity parameter to be able to match their numerical simulations with the experimental data. Deviations of the detected alignment signal from the simulated one at high laser power are a well-known problem, see e.g. Refs. 210, 211 and references therein. The reason are most likely spurious nonlinear effects arising at high laser powers. In contrast, at moderate laser intensities, the agreement of experiment and simulations is excellent, as is exemplified by a comparison of our measurements and numerical simulations for two different excitation powers in Fig. 3.18. In this case, however, the population part is too small to yield a detectable offset in the signal.

For the nitrogen molecule studied in this work, there is yet another feature complicating data interpretation. The close spacing of revivals in time and the relatively low number of populated rotational states make it difficult to identify a region in which the population contribution appears isolated, see Fig. 1.14(a) in Sec. 1.3.6. We therefore employ an at first glance counterintuitive approach, and use the information contained in the shape of the revivals in homodyne detection. We show in the following that the modification of the population part of alignment is amplified by the coherence part and shows up as an asymmetry in the revival features. For brevity, we will represent a deviation of $\langle\langle\cos^2\theta\rangle\rangle_p$ from its equilibrium value by

$$\Delta_p = \langle\langle\cos^2\theta\rangle\rangle_p - \frac{1}{3}. \tag{3.46}$$

Equation 3.45 can thus be rewritten as

$$\mathcal{I}_{\text{hom}} = A\left(\langle\langle\cos^2\theta\rangle\rangle_c + \Delta_p\right)^2. \tag{3.47}$$

Expanding the square shows that additionally to the squared contributions of Δ_p and $\langle\langle\cos^2\theta\rangle\rangle_c$, a cross term appears in the expression for the signal intensity:

$$\mathcal{I}_{\text{hom}} \propto \langle\langle\cos^2\theta\rangle\rangle_c^2 \pm 2\Delta_p\langle\langle\cos^2\theta\rangle\rangle_c + \Delta_p^2, \tag{3.48}$$

where the variable sign accounts for the sign change of $\langle\langle\cos^2\theta\rangle\rangle_c$, which by definition can take on negative as well as positive values (see Fig. 1.14(a) in Sec. 1.3.6). The Δ_p^2 term is, in absence of collisions, constant and comparatively very small, while the cross term $2\Delta_p\langle\langle\cos^2\theta\rangle\rangle_c$ modifies the amplitude of the coherence part as Δ_p is amplified by the much larger coherent oscillations. Since Δ_p is positive under our experimental conditions (this is not necessarily the case, see Sec. 2.2), the negative part of $\langle\langle\cos^2\theta\rangle\rangle_c$ is reduced, while the positive part is enhanced. This leads to an asymmetry in the pair of peaks forming a revival.

Figure 3.24 shows the effect of the cross term in Eq. (3.48) on the shape of the homodyne alignment signal for weak (a) and moderate (b) laser pulse power densities. In part (a) of the figure, the homodyne alignment signal is displayed upon the excitation of $^{14}N_2$ with a Gaussian laser pulse of 150 fs duration and a power density of 1 TW/cm^2 for 80 K (red curve) and 300 K (blue curve). At this power density, the Δ_p part of alignment is 2.5 orders

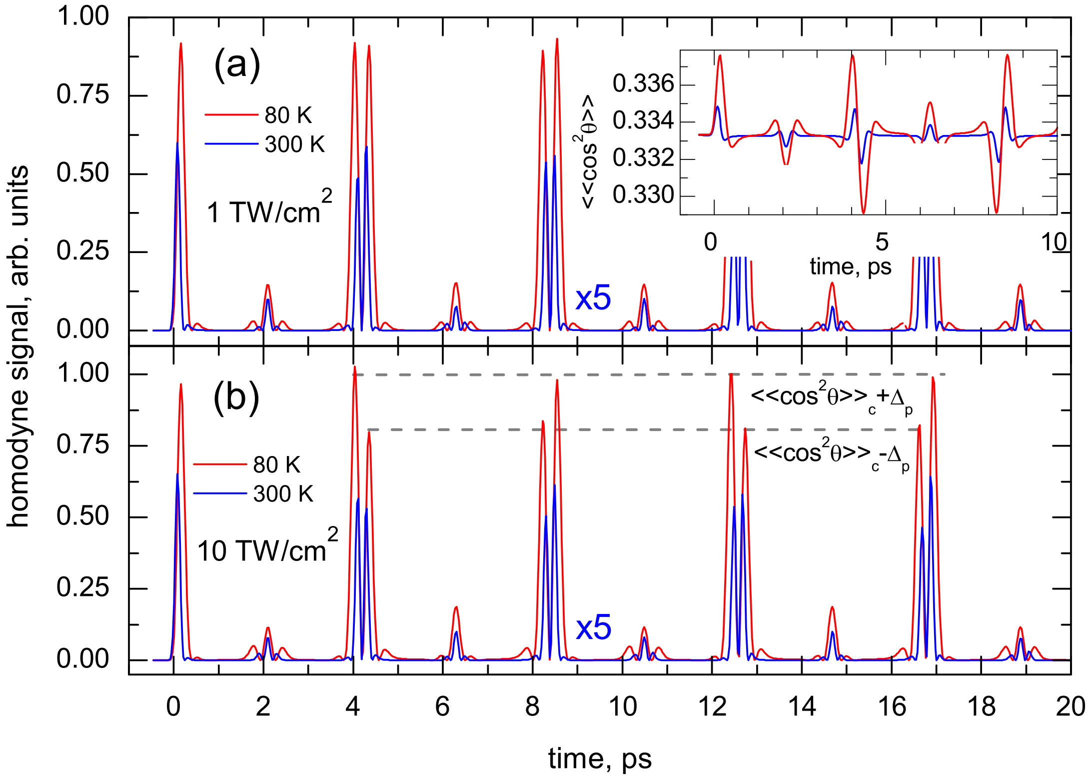

Abbildung 3.24: *Numerical simulation of the homodyne detected alignment signal from* $^{14}N_2$ *for a Gaussian laser pulse of 150 FWHM duration and pulse power densities of 1 TW/cm*^{2} *(a) and 10 TW/cm*^{2} *(b). The red curves represent results for 80 K, and the blue curves for 300 K multiplied by a factor of 5 for better visibility. Dashed horizontal lines in (b) highlight the effect of the relative sign of* $\langle\langle\cos^2\theta\rangle\rangle_c$ *and* Δ_p*. The inset in (a) shows the time-dependent* $\langle\langle\cos^2\theta\rangle\rangle$ *for 1 TW/cm*^{2} *excitation pulse power density at 80 K (red curve) and 300 K (blue curve).*

of magnitude smaller than the coherent oscillations (see Fig. 2.4). The oscillations of the $\langle\langle\cos^2\theta\rangle\rangle$ (shown in the inset) are thus almost symmetric about the value of 1/3, and the resulting double peaks in the homodyne signal are very similar in height. At a ten times higher excitation power density of 10 TW/cm^2, shown in part (b) of Fig. 3.24, there appears a pronounced asymmetry in the double peaks of the homodyne signal. Qualitatively, the shape of the alignment transient does not change at the higher intensity (see also Fig. 1.14), therefore we do not show a similar inset in part (b) of the figure. At 10 TW/cm^2, however, the amplitude of Δ_p has increased stronger than the coherence part. It is now only 1.5 orders of magnitude smaller than $\langle\langle\cos^2\theta\rangle\rangle_c$. This leads to the first peak of the half revival and the second peak of the full revival, where the cross term in Eq. (3.48) is positive being amplified, while their counterparts with negative cross term appear depressed. Note also the amplified or depressed wings of the quarter revivals in Fig. 3.24(b). The effect is much more pronounced at low temperature. The reason for the temperature effect can be found in the results of Sec. 2.2. At high temperature, the largest fraction of molecules is thermally rotationally excited and thus anti-alignment upon the interaction with the laser pulse is almost as likely as alignment. In the following, we will therefore limit the discussion to the low temperature case.

From the ratio of peak heights, indicated by the dashed gray lines in Fig. 3.24(b), the ratio of $\langle\langle\cos^2\theta\rangle\rangle_c$ and Δ_p can be directly obtained. In the higher peaks, the cross term of

Eq. (3.48) is positive to yield a signal strength $\mathcal{I}^+$, expressed as

$$\mathcal{I}^+ \propto \left(\langle\langle\cos^2\theta\rangle\rangle_c + \Delta_p\right)^2 \approx \langle\langle\cos^2\theta\rangle\rangle_c^2 + 2\langle\langle\cos^2\theta\rangle\rangle_c\Delta_p. \tag{3.49}$$

For the lower peak, one has the negative sign in Eq. (3.48), and thus

$$\mathcal{I}^- \propto \left(\langle\langle\cos^2\theta\rangle\rangle_c - \Delta_p\right)^2 \approx \langle\langle\cos^2\theta\rangle\rangle_c^2 - 2\langle\langle\cos^2\theta\rangle\rangle_c\Delta_p. \tag{3.50}$$

If $\Delta_p/\langle\langle\cos^2\theta\rangle\rangle_c \ll 1$, one obtains for the ratio $(\mathcal{I}^+ - \mathcal{I}^-)/(\mathcal{I}^+ + \mathcal{I}^-)$

$$\frac{\mathcal{I}^+ - \mathcal{I}^-}{\mathcal{I}^+ + \mathcal{I}^-} = \frac{2\Delta_p}{\langle\langle\cos^2\theta\rangle\rangle_c}. \tag{3.51}$$

In the particular case of Fig. 3.24(b), one obtains for $(\mathcal{I}^+ - \mathcal{I}^-)/(\mathcal{I}^+ + \mathcal{I}^-)$, and thus $\Delta_p/\langle\langle\cos^2\theta\rangle\rangle_c$ a value of 0.048. The values for Δ_p and $\langle\langle\cos^2\theta\rangle\rangle_c$ from the numerical simulation are 0.0022 and 0.045, respectively, yielding a ratio of 0.49. This is in good agreement also with the ratio of 0.054 for $\Delta_p/\langle\langle\cos^2\theta\rangle\rangle_c$ obtained from the additional experimental data measured with similar parameters and displayed in Fig. 3.18. From the experimental data measured at twice lower power density in Fig. 3.18(a), one obtains $\Delta_p/\langle\langle\cos^2\theta\rangle\rangle_c = 0.026$. Numerical simulations with a power density of 5 TW/cm^2 yield $\Delta_p = 0.00057$, and $\langle\langle\cos^2\theta\rangle\rangle_c = 0.02$. The resulting ratio is 0.028, once more in good agreement with the result for the ratio of experimental peak heights. The population part of alignment can thus be quantitatively determined from the signal shape of the homodyne detected revivals of alignment even at low to moderate laser power.

One of the issues that could be tackled using the proposed strategy of measuring the population offset is the question of how fast it decays relative to the coherent revivals. The effect of a dissipative environment on non-adiabatic alignment has been addressed recently in several theoretical publications [142, 155, 156, 212] and the determination of decay rates for coherence is the main subject of the next section. Here, we consider what can be learned from variations in the revival shape about the relation between the damping of the coherent and the population part.

Clearly, coherence is lost in every collision, and the coherence part of alignment is consequently dampened at a rate corresponding to the rate of collisions. Ramakrishna and Seideman [155, 156] conjectured that in the absence of pure dephasing, the population part should decay at the same rate as the coherence part. This has been tentatively supported by a recent experimental paper [209], though the application of very high laser fields complicated the interpretation of results. There is substantial experimental evidence from other techniques, however, showing that in a gas, the average alignment (or population part) can persist through several collisions, and even survive the thermalization of energy of the excited states [213–221].

Figure 3.25 shows a comparison of experimentally measured (a)-(b) and numerically simulated (c) homodyne alignment signal in nitrogen at 80 K upon the excitation with a laser pulse of 150 fs FWHM duration and a power density of 8 TW/cm^2. On the left panels, the signal shape immediately after the excitation pulse is shown. The right panels display the signal around the time of the 7th full revival, multiplied by a factor of 30 with respect to the left hand side for better visibility. The overall decay of signal amplitude is discussed in detail in the next section, here we will consider only the changes in the shape of the revivals. Due to effects of centrifugal distortion, in the numerically simulated signal of Fig. 3.25(c), the centers of the revival features are shifted to later times. This is apparent from the second peaks of the homodyne double peaks gaining weight relatively to the first ones, and from the appearance of trailing oscillations after the double peak of the revival. In the

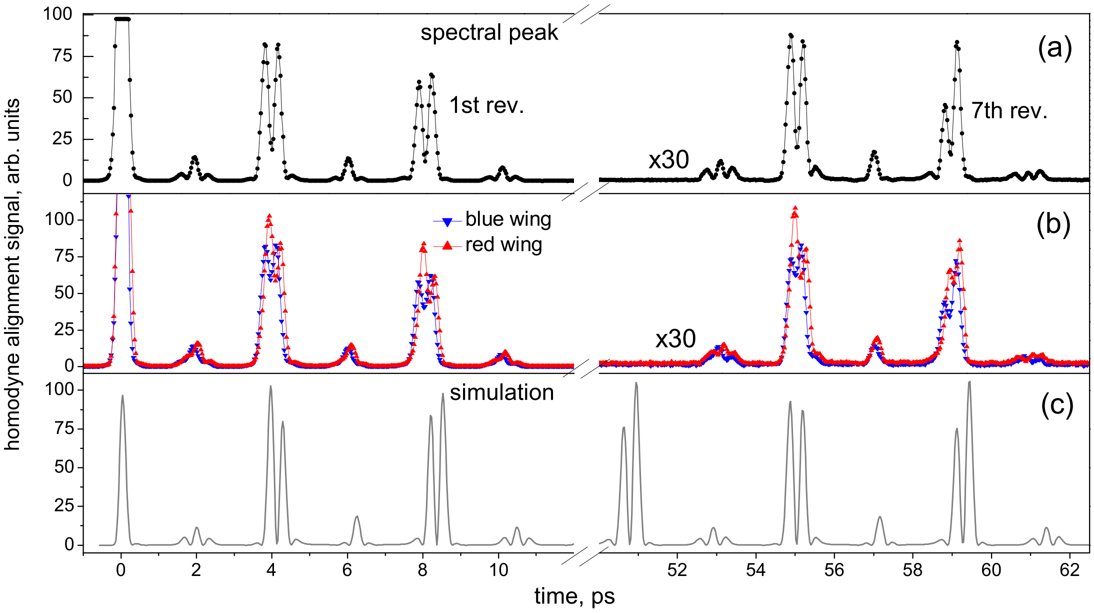

Abbildung 3.25: *Homodyne detected alignment signal in nitrogen at 80 K upon the excitation with a laser pulse of 150 fs FWHM and a power density of 8 TW/cm^2 at the peak (λ_0 of Fig. 3.22) of the probe pulse spectrum (a) and in the spectral wings of the probe pulse (b). (c) A numerical simulation of alignment in $^{14}N_2$ excited with a Gaussian laser pulse with parameters as in (a).*

experimental signal of Fig. 3.25(a), however, the observed change is qualitatively different. Here, we observe an increase in relative height in the first peak of the half revival and the second peak of the full revival. Furthermore, in the quarter revivals at 53 ps and 61 ps, the central peak is significantly depressed. Note that the effects are similar in the red and the blue wing of the probe pulse spectrum, displayed in Fig. 3.25(b). Possible artifacts due to a spurious local oscillator would display opposite phase in both wings of the spectrum, which is clearly not the case. The observed change is consistent with the population offset Δ_p increasing in relative weight compared to $\langle\langle\cos^2\theta\rangle\rangle_c$. The signal shape changes in the same way as upon an increase in excitation power, see also Fig. 3.24. In other words, our experimental data suggest a slower decay of the population part of alignment compared to the coherence part. In the following section we will show, that pure dephasing does not play any role in the alignment decay in nitrogen. This means, that more than one inelastic collision is necessary to thermalize the angular momentum direction, in agreement with the propensity for M-conservation in collisions found by various experimental techniques (see Ref. 222 and references therein).

3.4 Cross sections for rotational decoherence

In this section we report results of experiments on the decay of alignment in nitrogen and mixtures of nitrogen with hydrogen and several noble gases. We show that:

- **The integrated area of the homodyne detected alignment signal is a robust measure of the degree of coherence in the rotational wave packet even in the presence of centrifugal distortion.**
- **The cross section for decoherence in pure nitrogen decreases from 102 Å^2 at 80 K to 48 Å^2 at room temperature, leading to long lived coherences at high temperature.**
- **The room temperature cross section for decoherence in nitrogen is equal to the cross section for rotational depopulation. Pure dephasing does not play any role in the decay of rotational coherence. This is also confirmed for mixtures of nitrogen with hydrogen, helium and argon.**
- **For nitrogen and nitrogen-foreign gas mixtures, the cross sections for decoherence grow stronger with atomic mass than the geometric size of the particles.**

3.4.1 Collision-induced decay of rotational alignment

In this section, we discuss the decay of rotational coherence in nitrogen gas between the liquefaction temperature of 77 K and room temperature. In this range of temperatures, the time between bimolecular collisions is expected to be of order of picoseconds. Observing the decay of rotational revivals should therefore provide an ideal clock to study collisional dynamics.

Events causing the loss of coherence are separated into those due to pure dephasing while maintaining the population of the specific quantum state and those related to energy relaxation, i.e. the exchange of population between quantum states while the system is relaxing toward its thermal equilibrium [53]. Referring to energy relaxation one distinguishes further between the initial depopulation event of an excited level and the overall relaxation of the system under investigation to its thermal equilibrium. The initial collisional depopulation of specific rotational levels is addressed in experiments measuring the broadening of the rovibrational transition lines in the stimulated Raman Q-branch [223, 224]. Another class of experiments determines the cross section for rotational relaxation by measuring the development of rotational temperature in a molecular beam [225, 226] or ultrasound absorption in a gas flow [227, 228]. The term relaxation rather than depopulation here refers to the return to thermal equilibrium, which may involve several inelastic collision events. The cross section σ^r characterizing the rotational relaxation is thus smaller than the cross section σ^p for rotational depopulation [229]. Coherence is destroyed in all collisions, elastic as well as inelastic ones. One might thus expect that the cross sections σ^c for rotational decoherence is still larger than the cross sections for rotational depopulation. Rotational depopulation with σ^p is connected with a change ΔJ in the rotational quantum number J. Pure dephasing, i.e. elastic collisions, included in σ^c would require a change ΔM in the projection of J in alignment direction, without depopulation ($\Delta J = 0$). In the binary collision regime, which holds for diatomic gases under ambient conditions, it is commonly assumed, that pure dephasing does not play any role [213]. The depopulation cross sections σ^p derived from Raman Q-branch line broadening experiments should therefore well

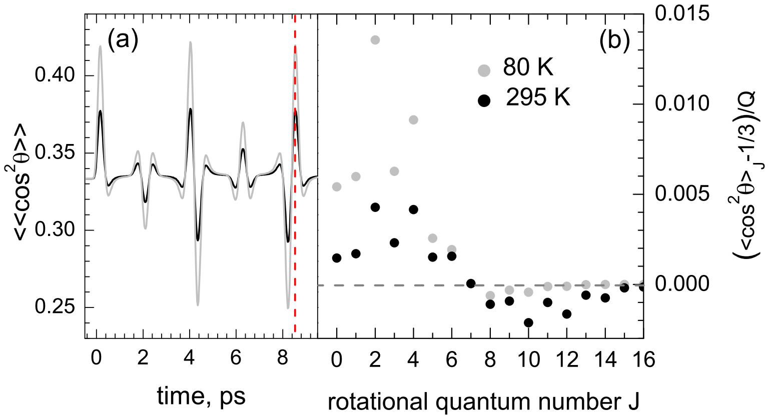

Abbildung 3.26: *(a) Numerical simulation of alignment in nitrogen upon the excitation with a Gaussian laser pulse of 150 fs FWHM duration and an intensity of 10 TW/cm^2 at 80 K (gray line) and 295 K (black line). (b) Deviation from the isotropic values in individual ρ_J states at the time $\tau_{rev}/2$ of the maximum of the half revival (dashed red line in (a)). The value taken on in an isotropic ensemble is represented by the dashed horizontal line.*

correspond to the decay rates and decoherence cross sections σ^c observed in rotational coherence experiments. Here, we present a systematic investigation of this relation over a wide temperature range and for various collision partners.

We induce alignment by a linearly polarized short laser pulse and detect the time-dependent modification of birefringence caused by recurrences of alignment in a homodyne detected optical Kerr effect experiment. The method is similar to the Raman induced polarization spectroscopy (RIPS [37]) that has been used in few pioneering studies of alignment decay in N_2, O_2, and CO_2 at room temperature [38, 167]. The alignment dynamics in these experiment appeared to be well explained by a multi-parameter scaling law analysis using state-resolved decay rates from Raman Q-branch experiments. The set of parameters is not unique, but the analysis suggests that for these examples at room temperature the predicted equality between σ^p and σ^c holds. We show in this section that σ^c for nitrogen can be obtained in a straightforward way from the decay of the peak area of revivals in the homodyne detected optical Kerr effect signal, without resorting to any modeling. We discuss several advantages our approach presents over frequency-domain measurements for the use in diagnostics. In addition to experiments with pure nitrogen, we then employ a variety of light (He), medium (Ar), and heavy (Kr) atomic perturbers. For molecular perturbers we use nitrogen itself with its resonant rotational structure, and hydrogen with a much larger rotational constant. Temperatures in our experiments are varied between the liquefaction temperature of nitrogen around 80 K and room temperature, and pressures between 0.1 and 1 atm are comparable to atmospheric conditions. This presents a set of data that allows to systematically check the relation between the depopulation cross section σ^p and the decoherence cross section σ^c.

In the experiments performed to measure the cross sections for rotational decoherence we employed the ultrafast optical Kerr effect method, which is discussed in detail in Section 3.1.

Numerical simulations of alignment in nitrogen for the first revival period are displayed in Fig. 3.26(a) for temperatures of 80 K and 295 K. The wave packet motion results in a periodic oscillatory pattern in the degree of alignment $\langle\langle\cos^2\theta\rangle\rangle$ on top of the value of 1/3 taken on for an isotropic distribution of molecular axes. Figure 3.26(b) shows the contributions of the individual $|\Psi_J\rangle$ states, i.e. the wave packets originating from the rotational level J. The symbols represent the deviation from the isotropic value for $\langle\cos^2\theta\rangle_J$

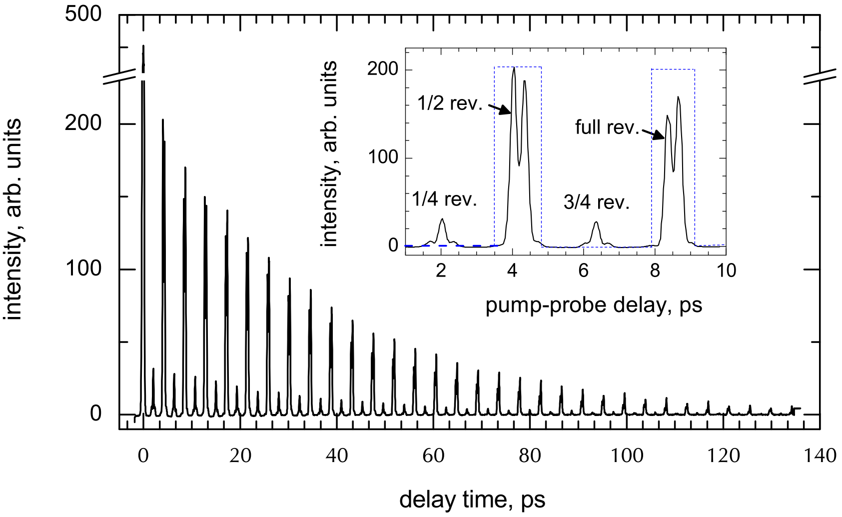

Abbildung 3.27: *Homodyne detected experimental signal of alignment in nitrogen gas at a pressure of 0.6 atm and 140 K. The inset shows a magnified view of the first half and full revivals, with the rectangles outlined in red representing the time integrated over in the analysis of the data.*

at the instant of the revival maximum, shown by the dashed vertical line in part (a) of the figure. This value is given by $\langle\langle\cos^2\theta\rangle\rangle_J$, the degree of alignment in one originally pure J state, divided by the sum over states $Q = \sum_J w_I(J)(2J+1)\exp[-BJ(J+1)/kT]$ (cf. Sec. 1.1.2). w_I here is a weight factor due to the degeneracy of the nuclear spin state, k the Boltzmann constant, and T is the rotational temperature. For both temperatures, the distributions are rather similar and peak at $J = 2$ and $J = 4$, though at room temperature the maxima are less pronounced.

3.4.2 Pure nitrogen

3.4.2.1 Temperature dependence

Figure 3.27 shows a typical homodyne detected signal of rotational alignment in nitrogen. Revivals of rotational coherence show up as periodic maxima with a full revival period of $\tau_r = 8.38$ ps for nitrogen. In between full revivals, half revivals are observed with equal amplitude and opposite phase, and additionally quarter revivals displaying a smaller amplitude. The revival amplitude decays due to collisions between N_2 molecules. To quantify the decay of alignment in our experiments we used the integrated peak areas of half and full rotational revivals as indicated in the inset of Fig. 3.27. The data analysis is based on the dependence of the homodyne detected signal on the number density of coherent molecules forming the rotational wave packet. To quantify this number density we use the integrated area of the homodyne detected alignment signal. Large centrifugal distortion leads to a change in the shape of revivals, which can significantly alter the amplitudes and shapes of revival features at long delay times. In nitrogen, due to the stiffness of the triple bond, the centrifugal correction to the rotational energy is relatively small, and thus the shape and amplitude of the revivals vary little with time. The ratio of the centrifugal energy correction to the rotational energy can be conveniently expressed as $(D_0/B_0^2)B_0J(J+1)$, with $D_0/B_0^2 = 1.45\times10^{-6}$ for nitrogen. For other molecules, this term can be higher, the extreme case being the hydrogen molecule [44] with $D_0/B_0^2 = 1.3\times10^{-5}$. The effect of the centrifugal bond softening on the alignment signal at 300 K is exemplified in Fig. 3.28

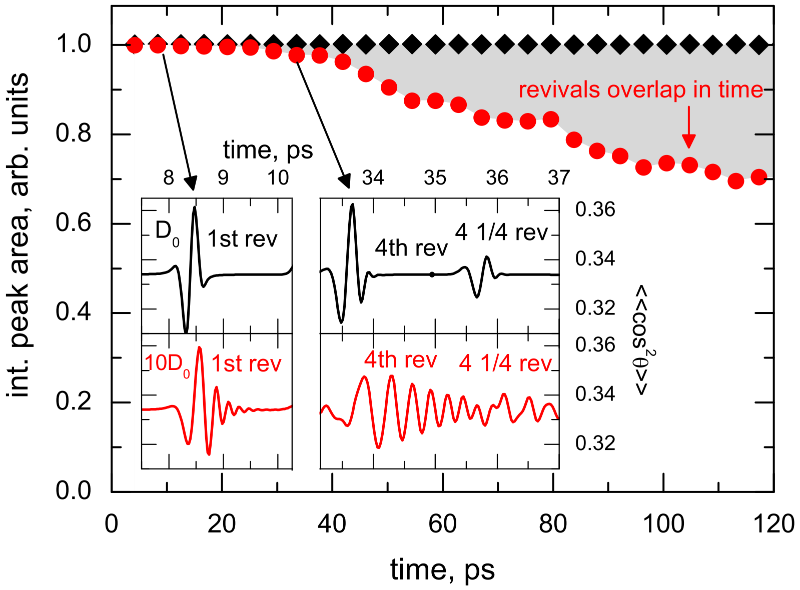

Abbildung 3.28: *Integrated peak areas of the simulated homodyne signal in* $^{14}N_2$ *at 300 K upon the excitation with a Gaussian laser pulse of 160 fs FWHM and 10 TW/cm*^{2} *with the centrifugal constant* $D_0 = 5.67 \times 10^{-6}$ *cm*$^{-1}$ *(black diamonds) and* $D = 10D_0$ *(red circles). The inset shows the shape and amplitude of the simulated alignment signal at the times of the first and fourth full revival.*

using the centrifugal constant of $D_0 = 5.67 \times 10^{-6}$ cm^{-1} for nitrogen [44] and also a ten times larger value. The integrated peak area of the homodyne signal is largely insensitive to the changes in the shape of the revival features caused by centrifugal distortion. The decay of the integrated area in the red trace for the case of $10D_0$ is caused by a starting overlap in time of the revival features rather than a decrease in the area of a single revival (see inset of Fig. 3.28). A broadening of the features up to overlapping, however, is observed in the experiment only at temperatures and intensities for which already vibrational excitation cannot be neglected [230], while we are concerned with purely rotational coherence effects. The integrated peak area can thus be reliably used to quantify the number density of coherent molecules forming the rotational wave packet.

A plot of the integrated peak areas of half and full revivals for alignment in nitrogen at 0.9 atm pressure for four different temperatures between 95 K and 280 K is displayed in Fig. 3.29. The solid lines are least-squares fits of single-exponential decays to the data. For all temperatures, no systematic deviation from a single-exponential behavior is observed. This exponential decay is due to molecules being removed from the coherently rotating ensemble by random bimolecular collisions.

Measurements of alignment decay times τ_{exp} were performed in pure nitrogen in a temperature range between 80 K and room temperature for pressures between 0.1 and 3 atm. The normalized decay time $\tau_{hom} = \tau_{exp} \times p$ derived from the observed decays did not show any dependence on the pressure p. The normalized lifetimes per unit pressure τ_{hom} in ps×atm for temperatures between 80 K and 295 K are collected in Table 3.1. τ_{hom} corresponds to half of the lifetime τ_c associated with the decay of alignment, the difference being caused by the quadratic nature of detection according to Eq. (3.24). Figure 3.30 shows a plot of τ_{hom} as a function of temperature between 80 K and room temperature as solid symbols. The error bars in the plot are estimated from the scatter of a set of typically about 5-10 individual measurements. Black symbols represent the experimentally determined τ_{hom} as

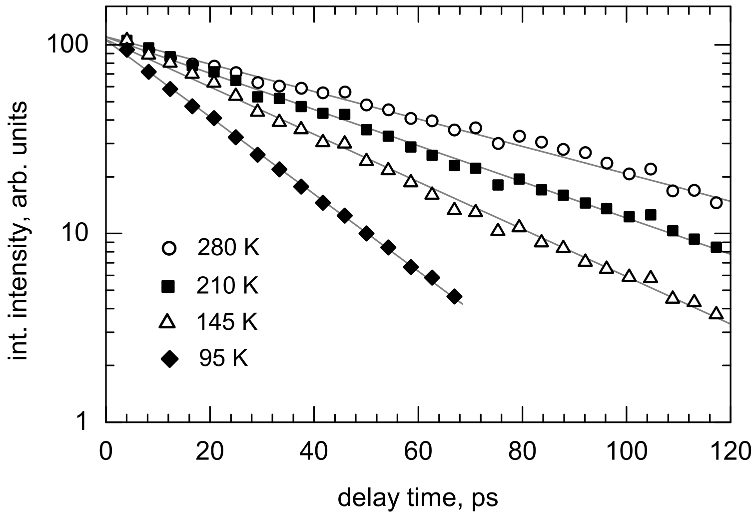

Abbildung 3.29: *Integrated revival peak intensities for homodyne detected alignment signals in pure nitrogen at 0.9 atm for various temperatures. The solid lines represent least-squares fits of a single-exponential decay to the data.*

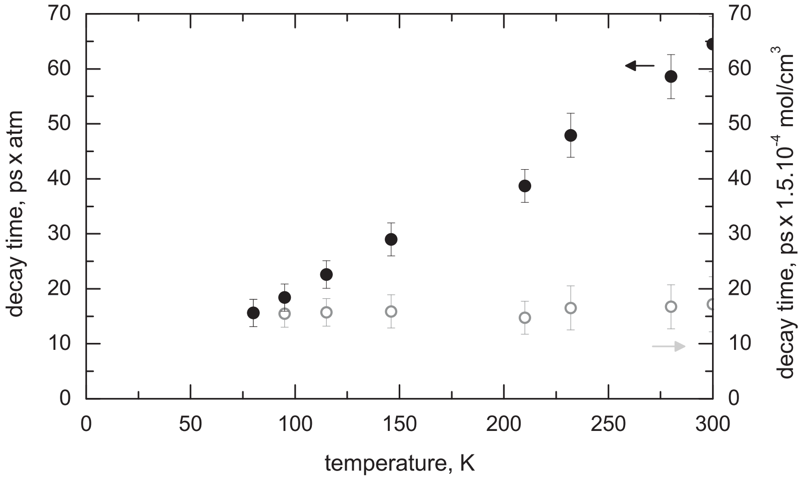

Abbildung 3.30: *Dependence of lifetime τ_{hom} of the homodyne detected alignment signal on temperature for pure nitrogen. Black symbols: Decoherence times per constant pressure. Gray symbols: Decoherence times for constant number density (corresponding to 1 atm at 80 K).*

a function of temperature normalized for a constant pressure of 1 atm. The gray symbols represent lifetimes as a function of temperature normalized for a constant number density in the gas volume. Though intuition tends to connect high temperatures with a rapid decay of coherence, and this is indeed true e.g. for effects depending on electronic coherence, we observe an increasing lifetime of rotational coherence with increasing temperature. τ_{hom} grows from 14 ps×atm at 80 K to 64.5 ps×atm at 295 K (black symbols in Fig. 3.30). To exclude the influence of the reduced number density in the gas upon heating we normalized the data to the number density corresponding to 1 atm at 80 K (1.5×10^{-4} mol/cm^3). Still, the lifetimes for rotational coherence, far from decreasing with increasing temperature, display almost constant values between 14 ps at 80 K and 17 ps at 295 K (gray symbols in Fig. 3.30). The longer lifetime is observed despite the higher frequency of collisions one would expect from a higher translational velocity. This clearly shows that the cross section

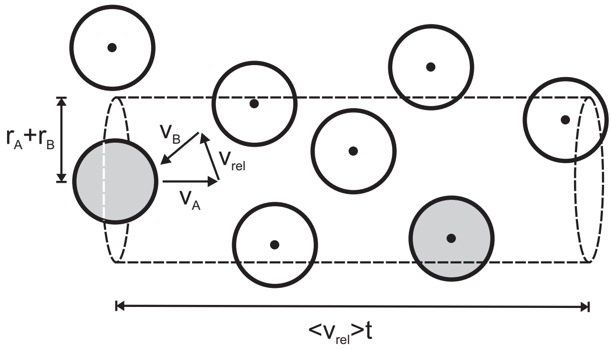

Abbildung 3.31: *Mean free path for a particle A (solid gray) in a gas. All particles with their center of mass (represented as black dot) inside the cylinder formed by the collision area and the distance particle A travels are counted as collision events.*

for a collision is temperature-dependent and decreases with increasing temperature.

3.4.2.2 Collision cross sections

To further quantify these results we use the measured decay rates to calculate cross sections for rotational decoherence via a mean-free path model. In the following we analyze pure nitrogen as well as nitrogen-foreign gas mixtures. We therefore give the derivation of the cross section in its general form, for a mixture of different particle species with different properties. The mean free path for a particle in a gas is the distance the particle on average travels between two collision events (Fig. 3.31). The frequency of the collision events is estimated by counting the number of collision partners inside a cylinder about the direction of propagation of the particle. The radius of this cylinder is given by the sum of radii of the original particle and the collision partner, while its length is determined by the distance the particle travels in a unit time t. A collision is counted if the center of mass of a collision partner (black dots in Fig. 3.31) is found inside this cylinder.

In general, the gas under consideration can consist of a mixture of different particle species with different properties. The number of collisions of a particle of species A with collision partners of species B within a unit time t is given by [231]

$$n_t = \frac{\pi (r_A + r_B)^2 \langle v_{\mathrm{rel}} \rangle t}{\rho_B}, \tag{3.52}$$

where $\rho_B = N_B/V$ is the number density of particles of species B in a volume V, r_A and r_B are the radii associated with the two species, and $\langle v_{\mathrm{rel}} \rangle$ is their relative velocity. The relative velocity is calculated as

$$\langle v_{\mathrm{rel}} \rangle = \sqrt{\langle v_A^2 \rangle + \langle v_B^2 \rangle}. \tag{3.53}$$

In recent publications, for the average velocity $\langle v \rangle$ the mean velocity $\bar{v} = \sqrt{8 k_B T / \pi m}$ with T being the temperature, m the molecular mass and k_B the Boltzmann constant, is chosen [232]. In the older literature, sometimes also the most probable velocity $v_p = \sqrt{2 k_B T / m}$ can be found [233, 234], as a result of which the calculated collision rates can differ by a factor of $2/\sqrt{\pi}$. We adhere to the modern practice and use $\bar{v}$ in all derivations. For nitrogen at 80 K and 300 K, the mean velocities are 348 m/s and 674 m/s, respectively.

The collision frequency $\nu_{A-B} = n_t/t$ is thus expressed as

$$\nu_{A-B} = \frac{\pi (r_A + r_B)^2 \langle v_{\mathrm{rel}} \rangle}{N_B/V}. \tag{3.54}$$

Using the ideal gas law $pV = Nk_BT$, the denominator can be expressed as $N_B/V = p_B/k_BT$, where p_B is the partial pressure of species B. Equation (3.54) can thus be rewritten as

$$\sigma_{A-B} = \pi(r_A + r_B)^2 = \frac{\nu_{A-B}k_BT}{\langle v_{\mathrm{rel}}\rangle p_B}, \tag{3.55}$$

yielding an expression for the collision cross section σ_{A-B}. Introducing the expression for the relative velocity, yields two formulas for the collision cross section for identical (σ_{A-A}) and foreign gas (σ_{A-B}) collisions:

$$\sigma_{A-A} = \frac{\nu_{A-A}\sqrt{\pi m k_BT}}{4p_A} \tag{3.56}$$

$$\sigma_{A-B} = \frac{\nu_{A-B}\sqrt{\pi\mu k_BT}}{\sqrt{8}p_B}, \tag{3.57}$$

where $\mu = m_Am_B/(m_A + m_B)$ is the reduced mass of particles A and B.

For a pure gas, collision cross sections can be extracted from the decay rates of the measured alignment signal just by substituting the decay rate into Eq. (3.56). In a gas mixture, collisions with identical as well as with foreign gas particles contribute to the decay of the signal. Here, the rates of collision add up to yield the measured decay rate:

$$\nu_{\mathrm{tot}} = \nu_{A-A} + \nu_{A-B} = \frac{4\sigma_{A-A}}{\sqrt{\pi m k_BT}}p_A + \frac{\sqrt{8}\sigma_{A-B}}{\sqrt{\pi\mu k_BT}}p_B. \tag{3.58}$$

The cross section σ_{A-B} can be extracted by performing a series of measurements in which the partial pressure of species A, and thus the first term in Eq. (3.58), is kept constant. σ_{A-B} is then contained in the slope of a plot of ν_{tot} as a function of p_B, the intercept corresponding to ν_{A-A}.

For reasons stated above, our usual method of detection was homodyning, i.e. quadratic detection. In this case, the signal intensity depends quadratically on the number density of particles in the coherent ensemble. To account for this, an additional factor of two has to be introduced to convert the decay rate of the homodyne detected signal to the rate at which particles are removed by setting

$$\nu_{\mathrm{hom}} = 2\nu_{\mathrm{tot}}. \tag{3.59}$$

The decays of the homodyne detected signal in our alignment experiments cover up to 2.5 orders of magnitude, and within this range showed no systematic deviation from a single-exponential decay. This indicates that the collision cross sections only weakly depend on the observed J quantum states. Strong variations with J would lead to a multi-exponential decay. Numerical simulations using the decay rates from Ref. 223 showed a single-exponential decay of the simulated homodyne signal over more than three orders of magnitude, in agreement with our experimental observation. We made an estimate of the limits on the J-dependence of cross sections for our experimental conditions by numerical simulations of the decay of the homodyne detected signal over a delay time range of 120 ps. A deviation from a single-exponential decay resulted upon a 25 percent variation of the time constant for one of the significantly populated rotational levels or for imposing an overall gradient of more than 15 percent with J.

The dynamic range in our experiment can in principle be increased to resolve the slowly decaying tail due to a J-dependence of the decoherence rates. The distribution of lifetimes would not yet be linked to the specific distribution of rotational levels. To obtain

Tabelle 3.1: *Decay times of the homodyne detected alignment signal* τ_{hom} *in ps×atm and the cross section for rotational decoherence* $\sigma^c_{N_2-N_2}$ *derived from* τ_{hom} *in pure nitrogen between 80 K and 295 K.*

T, K	τ_{hom}, ps×atm	$\sigma^c_{N_2-N_2}$, Å^2
80	15.6 ± 2.5	102 ± 5
95	18.4 ± 2.5	94 ± 5
115	22.6 ± 2.5	84 ± 4
146	29 ± 3	74 ± 6
210	38.7 ± 3	66.5 ± 6
232	47.9 ± 4	56.5 ± 6
280	58.6 ± 4	51 ± 7
295	64.5 ± 5	48 ± 8

state-resolved results from time-dependent experiments, one could resort to Fourier transformation of a heterodyne detected alignment signal and extract state-dependent life times from the linewidth of the Fourier components. The Fourier transform method, however, requires to cover long delays in order to resolve the line shape of the components. In Sec. 3.1 we proposed a method to manipulate the state composition of a rotational wave packet by applying appropriately shaped single or double laser pulses. It is thus possible to create wave packets that are hot or cool compared to the environment, which is left at its original temperature. The method could be used to achieve state resolution in the analysis of rotational decoherence, isolating individual J states and determining their respective τ_{hom}.

The observed monoexponential decay means that within the limits of our accuracy discussed above τ_{hom} is independent of the rotational level. This statement holds for the range of rotational levels from $J = 0$ to 6, which are relevant to our observations according to the weight distribution of Fig. 3.26(b). In the discussion of the cross sections derived from our experiments in the following sections we indicate the relative contributions of the respective rotational level to our detected alignment signal by the size of the symbols in figures.

High velocities at high temperatures lead to more frequent encounters between molecules, and thus one would expect that an increased rate of collisions leads to a faster decay of the observed signal. In Fig. 3.30 we already showed that this is not the case for pure nitrogen, and that for a constant number density the lifetime of coherence becomes almost independent of temperature. The only term that can balance the increase in velocity in Eq. (3.54) to cause a nearly constant rate of decoherence, is the decoherence cross section σ^c of the molecules. Figure 3.32 shows the decrease in σ^c with increasing temperature derived from our experiments. The value determined at room temperature within the error margins coincides with the gas kinetic cross section (red square in Fig. 3.32) and thus the geometric size of the molecule. The cross section σ^p for rotational depopulation derived from the measurements of line broadening of the Raman Q-branch in Ref. 223 for the $J = 2$ rotational level is plotted as a gray circle. From the quantitative agreement we conclude in agreement with previous results [167, 213] that pure dephasing, i.e. elastic collisions, does not play a significant role in diatomic gases under ambient conditions.

The cross sections for decoherence σ^c derived from our experiments increase from 48 Å^2 at 295 K to 102 Å^2 at 80 K. Values for τ_{hom} and $\sigma^c_{N_2-N_2}$ in the range between 80 and 295 K are collected in Table 3.1. An increase with decreasing temperature is observed experimentally also in rotational depopulation cross sections at high temperature [237] as

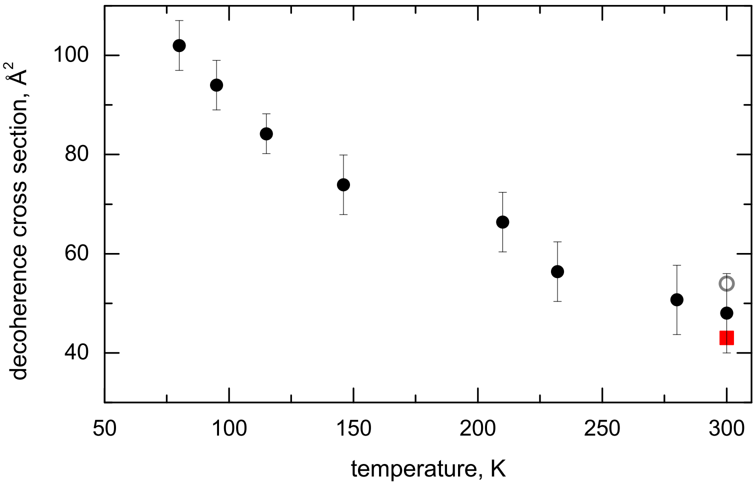

Abbildung 3.32: *Cross sections σ^c for rotational decoherence derived from the decay times of Fig.3.30 vs. temperature. The red square denotes the gas kinetic cross section of 50 Å^2 [235], and the gray circle denotes the thermally averaged cross section σ^p of 54 Å^2 from Raman Q-branch measurements [223, 224].*

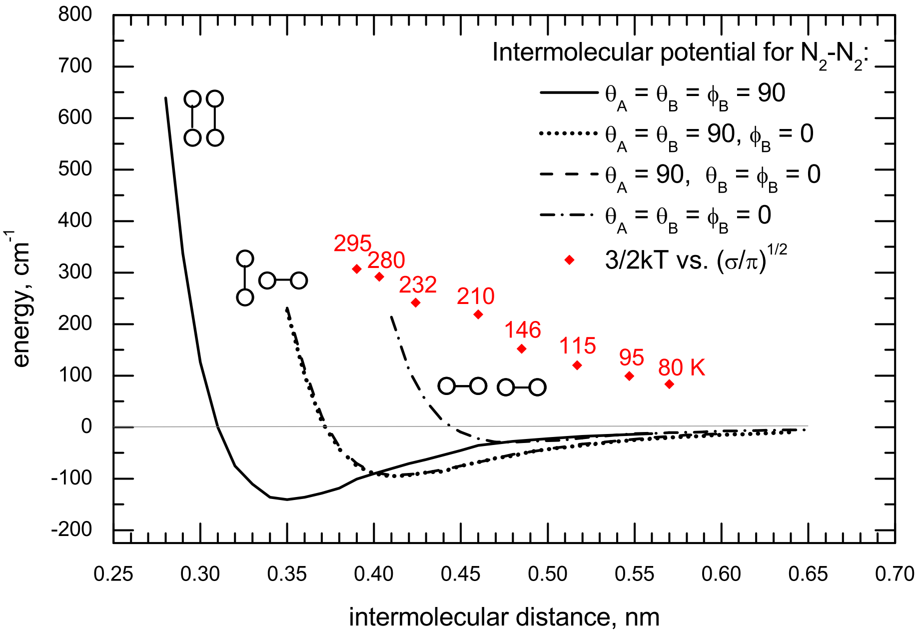

Abbildung 3.33: *Intermolecular potentials [236] for the N_2-N_2 system for various relative orientations of the two molecules compared to the average kinetic energy vs. decoherence distance (red diamonds) derived from our σ^c for temperatures between 80 K and 295 K.*

well as in rotational relaxation cross sections [225, 226] for pure nitrogen.

Figure 3.33 shows the intermolecular potentials for the N_2-N_2 system for various mutual orientations of the two molecules [236]. The deepest potential well of about 150 cm^{-1} at an intermolecular separation of 3.4 Å corresponds to the value of kT at about 170 K. At temperatures below this, there exists the possibility of the formation of a bound state of two nitrogen molecules. For comparison, the average kinetic energy $3/2\ kT$ for the temperatures at which our experimental cross sections σ^c have been determined are plotted along with the potential curves. The decoherence distances are calculated from the cross sections as $r = \sqrt{\sigma/\pi}$. Only at the highest temperatures the molecules approach close to location of the potential minimum. In this case, however, the average kinetic energy appears to be about a factor of 3 larger than the depth of the potential well. Interaction at high temperature therefore is mostly through the repulsive branch of the potential curve, in agreement with the finding that the cross section for decoherence is equal in size to the gas kinetic cross section of the molecule. At lower temperatures, the cross section for decoherence is so large, that the corresponding intermolecular distance points to an effect on the rotational energy already with the onset of the attractive part of the intermolecular potential. For an intermolecular separation of 5.7 Å, corresponding to a cross section of 102 Å^2, at 80 K, the average kinetic energy exceeds the depth of the intermolecular potential well by about an order of magnitude.

Reference 238 gives a theoretical analysis of line broadening coefficients by the energy corrected sudden (ECS) exponential power analysis, in which several temperature-dependent parameters are used to describe the behavior of the rotational depopulation. The main contributions are found to be the maximum angular momentum that can be transferred between rotational and translational degrees of freedom in a collision, which is proportional to the translational temperature, an amplitude factor accounting for density, which scales as $(T/T_0)^{-\beta}$ and the interaction time, approximately proportional to the inverse of the square root of the temperature. For mixtures of nitrogen and rare gases, the limit of angular momentum exchange per collision is calculated in Ref. 239 and found to be strongly dependent on the rare gas species. For different scaling laws, however, different sets of parameters, which are additionally interdependent, can be found in the literature to describe the observed cross sections. In our experiments at different temperatures, the main changes are in the rotational J-composition of the thermal ensemble, and in the distribution of translational energy. We conclude, based upon the fact that the rotational levels observed in the alignment signal do not significantly vary (Fig. 3.26(b)), that the low translational velocities are mainly responsible for high cross sections at low temperature. This suggests that orbiting collisions [240–242] are important at low temperature, and it would be desirable that scaling law analyses work out this effect in a more obvious way.

3.4.2.3 Comparison with J resolved line broadening of Raman Q-branch at room temperature

The standard way to determine depopulation of rotational levels is the measurement of the pressure-dependent line broadening of the stimulated Raman Q-branch. In experiments of this kind a line broadening coefficient γ in cm^{-1}/atm, which additionally depends on temperature, is determined. In the line broadening coefficient, the frequency of inelastic collision events is expressed [233, 243]. The method provides a J-resolution that stems from the very small change in the moment of inertia with the rotational quantum number due to centrifugal distortion of the molecular bond. Results of measurements in nitrogen at room temperature from Refs. 223 and 224 are plotted in Fig. 3.34 as gray and black symbols, respectively. The Q-branch method allows for rotational state resolved determination of

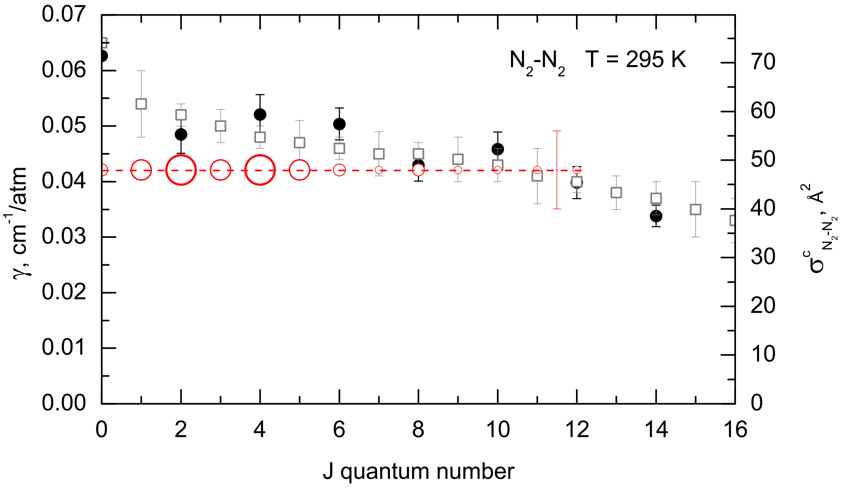

Abbildung 3.34: *Line broadening coefficients γ (HWHM) for the Raman Q-branch from Ref. 223 (gray symbols) and Ref. 224 (black symbols) for nitrogen at 295 K compared to our result (dashed line) together with the related σ^c and σ^p cross sections. The size of the open circles corresponds to the weight of the particular state in the total alignment signal.*

depopulation rates. The line broadening coefficients vary from 0.054 cm^{-1}/atm for $J = 1$ to 0.03 cm^{-1}/atm for $J = 18$, where the numerical value refers to the half width at half maximum (HWHM) of the transition line. For a quantitative comparison of these state-resolved coefficients with our averaged cross section we plot in Fig. 3.34 the result obtained by us for a temperature of 295 K as a dashed horizontal line. Red circles of different sizes represent the magnitude of the contribution of the particular rotational state to the alignment signal. At room temperature, the alignment signal is nevertheless dominated by low J levels, especially the $J = 2$ and $J = 4$ rotational levels (Fig. 3.26(b)). The thermal distribution of molecules has its maximum around $J = 10$, however, the interaction mechanism of the molecular alignment favors low J levels. Odd rotational states are twice less populated and therefore generally less visible. The error bar for the averaged value is derived from the scatter of several independent measurements. For better comparison, we recalculated our measured decay times also into the units of γ via $\gamma = 1/2\pi\tau_c$ (Ref. 243) assuming a Lorentzian line shape. The σ^c-axis in Fig. 3.34 gives the values for cross sections derived from the decay time τ_c, where a single-exponential decay was assumed. The requirement for comparison with the Raman Q-branch and the calculation of σ^p is that the line shape be a Lorentzian. We determine a decoherence cross section $\sigma^c_{N_2-N_2}$ of 48 ^{2} from a decay constant of 129 ps×atm for the alignment (64.5 ps×atm for the homodyne detected signal), which corresponds to a line broadening coefficient $\gamma = 0.042$ cm^{-1}/atm.

In the region between $J = 2$ and $J = 5$, dominating in the alignment signal, our averaged cross section $\sigma^c_{N_2-N_2}$ within the error bars agrees well with the depopulation rates determined in Refs. 223 and 224. Compared to the literature values we find an even smaller cross section, whereas a significant contribution of pure dephasing would have increased the value of σ^c beyond the one for σ^p. The literature data furthermore show that the variation of the rates with J number is weak in this range. No major deviations for single rotational states are observed. This agrees well with the single-exponential behavior of the alignment decay observed by us.

For pure nitrogen, our results confirm that decoherence at room temperature proceeds via inelastic population transfer and the rate of pure dephasing by elastic collisions is

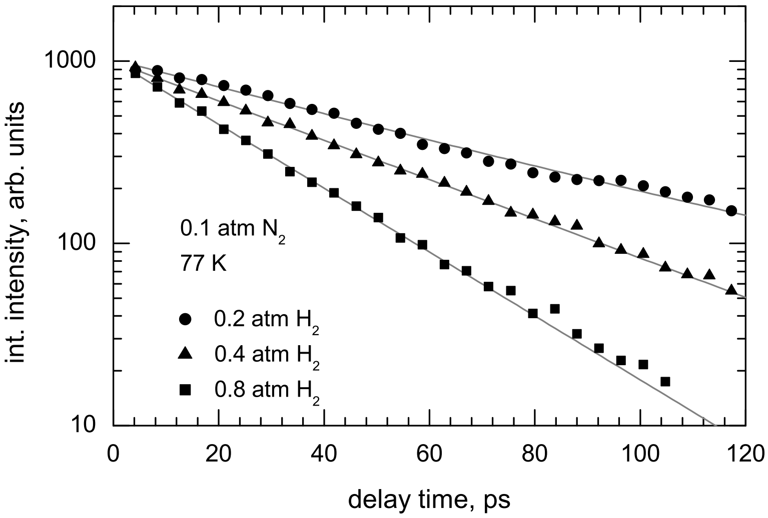

Abbildung 3.35: *Decay of integrated peak area of the homodyne detected signal vs. time in a mixture of nitrogen and hydrogen at 77 K with varying hydrogen pressure (solid symbols). The solid lines are least-squares fits of single-exponential decay to the data.*

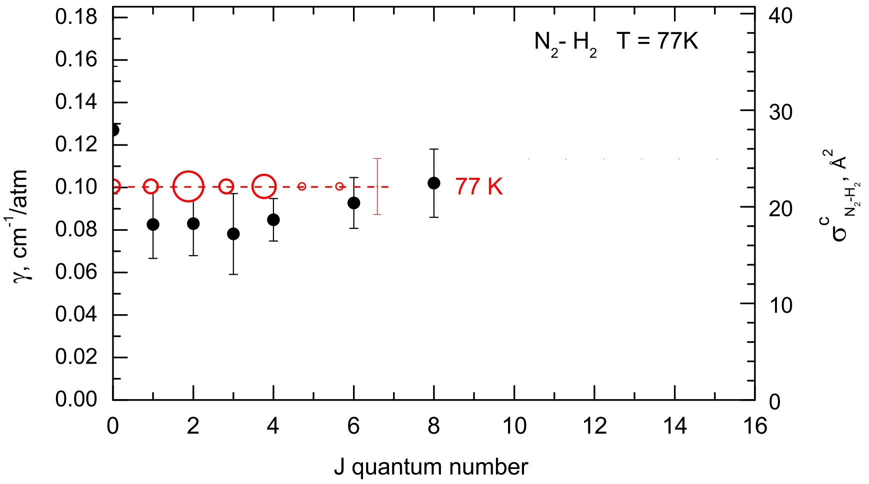

Abbildung 3.36: *Line broadening coefficients γ (HWHM) for the Raman Q-branch from Ref. 244 (black symbols) for a mixture of nitrogen and hydrogen at a temperature of 77 K compared to the values derived from the alignment decays measured at 77 K (red horizontal line). The size of the red symbols corresponds to the weight of the particular state in the total alignment signal.*

negligible. Unfortunately, for low temperatures, no Raman data are available.

3.4.3 Nitrogen-foreign gas mixtures and comparison with Raman Q-branch

3.4.3.1 Nitrogen-hydrogen

For the mixture of nitrogen and hydrogen a series of experiments were performed at a temperature of 77 K varying the pressure of hydrogen between 0.2 atm and 0.8 atm with a constant nitrogen pressure of 0.1 atm. Though hydrogen as a diatomic molecule with an anisotropy of polarizability can show alignment itself [245], in our case the pulse duration is long compared to the hydrogen rotational period of 90 fs, and thus the nonadiabatic alignment dynamics in hydrogen is suppressed. The signal detected originates exclusively from the nitrogen fraction in the mixture. The integrated peaks areas of the homodyne signal for a series of measurements with 0.2 atm, 0.4 atm, and 0.8 atm hydrogen partial pressure are shown in Fig. 3.35 together with least-squares fits of single-exponential decays.

The decay rate depending on H_2-pressure was found to be $\nu^c_{N_2-H_2} = 0.022$ ps^{-1}atm^{-1} at 77 K, corresponding to a decay time of alignment of $\tau_c = 51.3$ ps (102.6 ps^{-1}atm^{-1} for the homodyne detected signal) and a cross section $\sigma^c_{N_2-H_2}$ for dephasing of 22.1 ^{2}. To obtain these values, the decay rates ν_{tot} measured in the nitrogen-hydrogen mixture were corrected by the pure nitrogen contribution of 0.0038 ps^{-1} for 0.1 atm of nitrogen at 77 K extrapolated from the values of Fig. 3.30 and Table 3.1 and subsequent averaging over the series of hydrogen measurements. We observed no systematic dependence of the normalized, i.e. pressure-corrected, decay rate on the hydrogen partial pressure.

In addition to experiments with normal hydrogen, we employed an ortho-para hydrogen converter[2] and carried out measurements with 99.8 percent pure para-hydrogen. Within our experimental accuracy the decay rates in mixtures of nitrogen with normal and para-hydrogen did not show a significant difference. In Ref. 244 the authors calculate the depopulation cross sections for the nitrogen-hydrogen system and differentiate in the calculation between para-hydrogen, which at low temperature is predominantly in the spherical $J = 0$ rotational state and ortho-hydrogen, which mostly populates the $J = 1$ rotational level and displays quadrupole-quadrupole interaction. Unfortunately the authors do not comment on the difference this fact may have on the cross sections.

For the nitrogen-hydrogen gas mixture, results of Raman Q-branch line broadening experiments at 77 K have been published in Ref. 244. The values obtained are plotted as black symbols in Fig. 3.36 together with the averaged cross section we derive from our data at the same temperature (red dashed line). As in Fig. 3.34, the size of the red symbols signifies the relative contribution of the respective rotational level to the detected alignment signal. Under our experimental conditions, the alignment signal at both room temperature and 77 K is mainly determined by small J numbers, especially the $J = 2$ and $J = 4$ rotational levels and should therefore be compared with the corresponding literature values. The error bar for our value is estimated from the scatter of a number of individual experiments.

The cross section $\sigma^c_{N_2-H_2}$ determined by us for the nitrogen-hydrogen mixture at 77 K is a bit larger than the Raman Q-branch line broadening coefficients determined in Ref. 244 but still lies within the error bars of the literature measurements. The average of the experimental broadening coefficient γ from Ref. 244 is about 0.08 cm^{-1}/atm, compared to our value of 0.1 cm^{-1}/atm, which amounts to a difference of 20 percent. The experimental depopulation rates of Ref. 244 have been found to be in excellent agreement with close-coupling theory based on *ab initio* quantum chemical potentials [246] and an ECS theory [247]. The reason for the discrepancy could be a small fraction of elastic collisions, or reorientation without depopulation, in the nitrogen-hydrogen system. Elastic depolarization has been reported in the literature for various polar molecules as OH [215, 216] and NO [214], the rates for elastic encounters, however, have been found to be low for light collision partners and significant only for mixtures with argon and xenon.

3.4.3.2 Nitrogen-helium

Alignment experiments on the nitrogen-helium gas mixture were performed at room temperature at a constant partial pressure of nitrogen of 0.3 atm and at 80 K at 0.1 atm

---

[2] The home-built (by Falk Königsmann and Mizuho Fushitani) converter consists of copper tubing packed with a paramagnetic $Fe(OH)_3$ catalyst. The spin flip from ortho- to para-hydrogen is induced by flowing supercooled with respect to rotation natural hydrogen gas through the catalyst ($2B_0 = 121.6$ cm^{-1} or 170.5 K for hydrogen). At 20 K 99.8 percent of ortho-hydrogen is converted into the para-species.

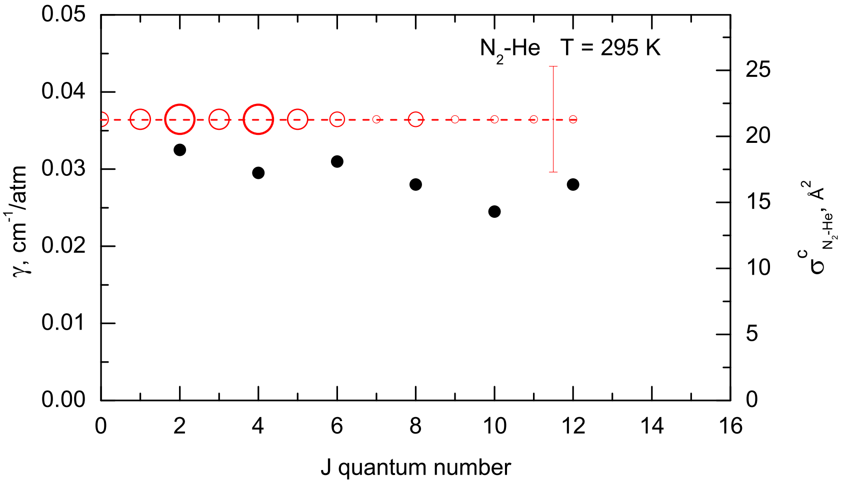

Abbildung 3.37: *Line broadening coefficients γ (HWHM) for the Raman S-branch from Ref. 248 (black symbols) for a mixture of nitrogen and helium at a temperature of 295 K compared to the cross section σ^c from the alignment decay (horizontal line). The size of the red symbols corresponds to the weight of the particular state in the total alignment signal.*

nitrogen pressure. The pressure of helium was varied between 0.4 atm and 3 atm.

At room temperature we determine a decoherence rate $\nu^c_{N_2-He}$ of 0.007 ps^{-1}atm^{-1}, corresponding to an alignment decay time τ_c of 143 ps×atm or a τ_{hom} of 71.5 ps×atm for the homodyne detected signal. The values were derived from averaging over a series of measurements with different partial pressures of helium after correcting for the decoherence rate of 0.0024 ps^{-1} estimated from Fig. 3.30 for 0.3 atm of nitrogen. The rate of decay translates into a cross section $\sigma^c_{N_2-He}$ of 21.3 Å^2.

At 80 K we measure a decay time for the homodyne signal τ_{hom} of 43.7 ps×atm, corresponding to $\nu^c_{N_2-He}$ of 0.0114 ps^{-1}atm^{-1} or a cross section $\sigma^c_{N_2-He}$ of 18.1 Å^2. As opposed to pure nitrogen, here we observe a small increase in the cross section with temperature. An increase of the collision cross section with the temperature is also known in the literature for the N_2-H_2 system, with hydrogen and helium being very close in size and weight. From the line broadening data of the Raman Q-branch published for N_2-H_2 in Ref. 244, one can calculate a cross section $\sigma^p_{N_2-H_2}$ of 17.7 Å^2 for the $J = 2$ rotational level at 77 K, growing to 19.4 Å^2 at 298 K and even 28.4 Å^2 at 580 K. The increase in $\sigma^{p/c}$ with decreasing temperature observed for pure nitrogen therefore does not seem to be a universal appearance but does depend on the system under investigation.

Experimental data on Raman line broadening in the nitrogen-helium system are limited to values for the Raman S-branch in Ref. 248 and are plotted in Fig. 3.37 as black symbols together with our averaged cross section. Again, the line broadening coefficients can be well accounted for by a scaling theory [249]. As in the case of hydrogen, our estimated value for γ of 0.037 cm^{-1}/atm is slightly larger than the 0.033 cm^{-1}/atm for the dominating $J = 2$ contribution in the Raman S-branch line broadening.

3.4.3.3 Nitrogen-argon

For the nitrogen-argon gas mixture we performed measurements of alignment decay at 90 K and at room temperature. At low temperature a constant partial pressure of nitrogen of 0.1 atm was diluted by a variable partial pressure of argon between 0.2 and 0.8 atm. At 90 K we determine a signal decay time τ_{hom} of 22.7 ps×atm, corresponding to a collision rate of ν_{N_2-Ar} of 0.022 $\mathrm{ps}^{-1}\mathrm{atm}^{-1}$ and a cross section for decoherence $\sigma^c_{N_2-Ar}$ of 80.5 Å^2.

At room temperature, the nitrogen partial pressure was kept at 0.3 atm, and the argon pressure was varied between 0.4 and 3.2 atm. We obtain a collision rate ν_{N_2-Ar} of 0.0077 $\mathrm{ps}^{-1}\mathrm{atm}^{-1}$, which corresponds to a decay time τ_{hom} of 65 ps×atm in the experiment or a decoherence cross section σ_{N_2-Ar} of 51.1 Å^2. The collision rates and decay times seem surprisingly close to the ones measured for pure nitrogen-helium and the nitrogen-helium mixture, given the difference in size between helium/argon and nitrogen molecules. This can be understood in a qualitative way, as the decay rate is determined by the size of the molecule through its cross section as well as by the frequency of encounters between molecules. Though argon has a much larger cross section than helium, the higher average velocity of the light helium molecules leads to more frequent encounters with nitrogen and thus a comparable decay rate at equal pressure of the rare gas. The pronounced temperature dependence of the decoherence cross section that was observed in pure nitrogen also becomes manifest in the mixture of nitrogen with argon.

Results of line broadening measurements of the Raman Q-branch for the nitrogen-argon system have been published in Ref. 250 and Ref. 251 for 140 K and 295 K. In Fig. 3.38, results for γ of Ref. 250 (black symbols) and Ref. 251 (gray symbols) at room temperature are displayed in comparison with the averaged cross section $\sigma^c_{N_2-Ar}$ of 51.1 Å^2 derived from the alignment decay. The average line broadening coefficient γ from the literature values at $J = 2$ is about 0.04 cm^{-1}/atm, and our cross section corresponds to a γ of 0.041 cm^{-1}/atm, in perfect agreement with the literature values. At room temperature therefore, the decay of coherence in the nitrogen-argon system can be explained by rotational depopulation. It should be noted that in Ref. 250 a theoretical description of depopulation rates based on potentials from Refs. 252 and 253 was attempted, which captured well the shape of the dependence of γ on J, but underestimated the rate severely. The same problem also appeared for the theoretical description of the depopulation rates at 140 K.

The literature data for the Raman line broadening are limited to a temperature of 140 K, whereas our measurements were performed at 90 K. For pure nitrogen the cross sections in Fig. 3.32 show a decay with increasing temperature that can be approximated by a straight line. If one assumes a similar monotonic decay for the N_2-Ar system, the cross section at 140 K can be estimated from a linear interpolation between 90 K and 300 K. The resulting comparison of literature values from Ref. 250 (black symbols) with our value (gray dashed line) is displayed in Fig. 3.39. Our original data at 90 K yield a γ of 0.117 cm^{-1}/atm and are shown as red dashed line. Note that the axis for the cross sections is temperature-dependent and valid only for 140 K. In Ref. 250 at 140 K a line broadening coefficient for $J = 2$ of γ of 0.079 cm^{-1}/atm is determined. The extrapolated value to 140 K from the alignment decay for the cross section $\sigma^c_{N_2-Ar}$ is 73.5 Å^2. This corresponds to a γ of 0.085 cm^{-1}/atm. Within the error bars, this again agrees with the depopulation rates measured by the broadening of the lines in the Raman Q-branch, and we can confirm the absence of pure dephasing also for the nitrogen-argon mixture at low temperature.

3.4.3.4 Nitrogen-krypton

We performed experiments on the nitrogen-krypton gas mixture at room temperature at a constant nitrogen partial pressure of 0.3 atm, while the krypton pressure was varied between 0.4 and 2.5 atm and at 120 K for a nitrogen partial pressure of 0.1 atm. For this system, measurements proved to be difficult and had to be performed at lower pump pulse intensity than the other experiments reported in this paper, as the onset of nonlinear processes due to the large electronic polarizability of krypton [254] leads to increased fluctuations. At room temperature we find a signal decay time τ_{hom} of 59 ps×atm, corresponding to a

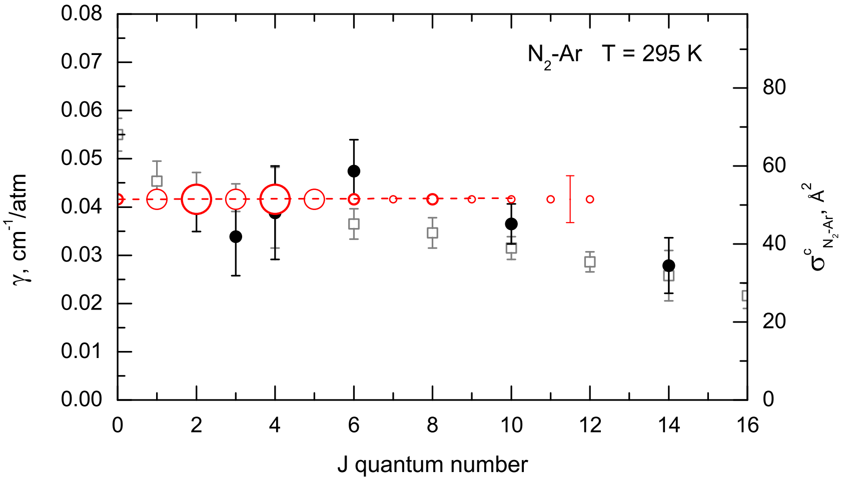

Abbildung 3.38: *Line broadening coefficients γ (HWHM) for the Raman Q-branch from Ref.250 (black symbols) and Ref.251 (gray symbols) for a mixture of nitrogen and argon at a temperature of 295 K compared to the cross section from the alignment decay (horizontal line). The size of the red symbols corresponds to the weight of the particular state in the total alignment signal.*

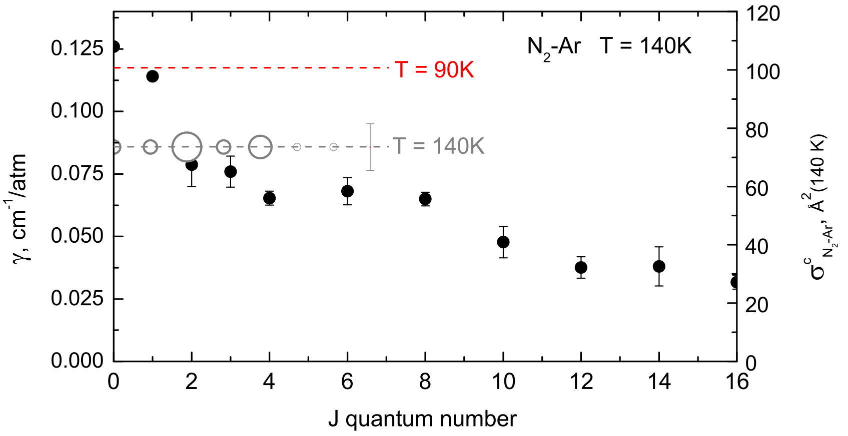

Abbildung 3.39: *Line broadening coefficients γ (HWHM) for the Raman Q-branch from Ref.250 (black symbols) for a mixture of nitrogen and argon at a temperature of 140 K compared to the Line broadening from the alignment decay measured at 90 K (red horizontal line) and extrapolated to 140 K (gray horizontal line). The size of the red symbols corresponds to the weight of the particular state in the total alignment signal.*

collision rate of ν_{N_2-Kr} of 0.0085 ps^{-1}atm^{-1}. The cross section $\sigma^c_{N_2-Kr}$ derived from the data is 63.9 Å^2. The decay time results in a hypothetical line broadening coefficient γ of 0.045 cm^{-1}/atm.

For a temperature of 120 K the decay time τ_{hom} for alignment is 32.6 ps×atm, corresponding to $\nu_{N_2-Kr} = 0.015$ ps^{-1}atm^{-1} and $\sigma^c_{N_2-Kr}$ of 71.2 Å^2. From these data a line broadening coefficient γ of 0.081 cm^{-1}/atm is obtained. To the best of the author's knowledge, no published data on the broadening of transition lines in the nitrogen-krypton system are available.

Tabelle 3.2: *Lifetimes of the homodyne detected signal* τ_{hom} *in pure nitrogen and the gas mixtures, the collision rates of nitrogen with the respective partners* ν_{N_2-X}*, and the cross sections for rotational dephasing* $\sigma^c_{N_2-X}$ *derived from the signal decay of alignment. For comparison we show the cross section for depopulation* $\sigma^p_{N_2-X}$ *derived from the literature values for* γ *for the* $J = 2$ *rotational level, and the gas kinetic cross section* σ^{kin} *at room temperature.*

	τ_{hom}, ps×atm			ν_{N_2-X}, ns^{-1}atm^{-1}		$\sigma^c_{N_2-X}$, Å^2	
	low T		295 K	low T	295 K	low T	295 K
N_2-H_2	22.9 ± 3	(77K)	–	22 ± 4	–	22.1 ± 4	–
N_2-He	43.7 ± 4	(80 K)	71.5 ± 8	11 ± 2	7 ± 1	18.1 ± 3	21.3 ± 3
N_2-N_2	15.6 ± 2.5	(80 K)	64.9 ± 5	36 ± 6	8 ± 1	102 ± 5	48 ± 8
N_2-Ar	22 ± 3	(90 K)	65 ± 6	22 ± 3	8 ± 1.5	80.5 ± 8	51.1 ± 8
N_2-Kr	32.6 ± 4	(120 K)	59 ± 6	15 ± 2	8.5 ± 1.5	71.2 ± 8	63.8 ± 8

	$\sigma^p_{N_2-X}(J = 2)$, Å^2		$\sigma^{kin}_{N_2-X}$, Å^2
	295 K		295 K
N_2-H_2	19.4[1]	(17.8[1] at 77 K)	32[2]
N_2-He	19.1[3]		26.5[2]
N_2-N_2	57[4]		43[2]
N_2-Ar	56[5]	(66[5] at 140 K)	40.8[2]
N_2-Kr	–		47.5[2]

[a] from Ref. 244
[b] from Ref. 248
[c] from Ref. 235
[d] from Ref. 224 and Ref. 223
[e] from Ref. 250

3.4.4 Discussion

We obtained the cross section for rotational decoherence from the evaluation of the signal decay of non-adiabatic alignment in nitrogen and mixtures of nitrogen with different perturbers. The results are collected together with the available literature data in Table 3.2. In the non-adiabatic alignment a laser pulse, which is short compared to the rotational period of the molecule, imprints a common phase on all rotational transitions excited. At the half and full revival times, all rotations excited by the pump pulse line up in phase, due to the common divider of $2B$ in the rotational periods, and thus pronounced peaks of alignment or anti-alignment are observed. Upon a collision, rotational energy is redistributed among the collision partners, and the rotational motion acquires a random phase, even though the common factor of $2B$ in rotational energy is retained. With the collision times statistically distributed, the molecule is lost for the phase-sensitive revival amplitudes we use to quantify the decay of rotational coherence. The increased average alignment, however, may still not disappear completely and a small overall anisotropy in the sample may remain. In Ref. 213, the authors find in a stimulated Raman experiment on pure nitrogen that the M quantum number is not randomized in an inelastic collision, and thus the initially prepared alignment decays at a slower rate than the non-equilibrium population. Due

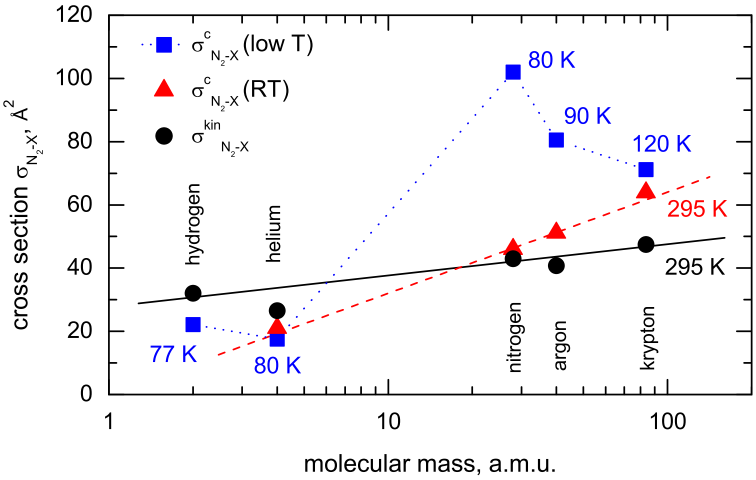

Abbildung 3.40: *Cross sections for decoherence $\sigma^c_{N_2-X}$ at low temperature (blue squares) and at room temperature (red triangles) as a function of the molecular mass of the collision partner. For comparison the gas kinetic cross sections $\sigma^{kin}_{N_2-X}$ at room temperature are shown as black circles. The lines are guides to the eye.*

to the smallness of the time-independent alignment under our experimental conditions (cf. Secs. 2.2 and 3.3.4), however, this contribution does not affect the integrated revival area.

First, we consider the rotational state dependence of the cross section for decoherence σ^c. The observed single-exponential decay of the homodyne detected alignment signal in all combinations indicates that σ^c does not depend significantly on J within the range relevant of $J = 1$ to $J = 5$ under our experimental conditions. The slow variation of σ^p with J found in theoretical approaches and Raman Q-branch experiments is illustrated in Fig. 3.34 and Figs. 3.36–3.39 and it supports this observation. The problem in this case reduces to a single cross section characterizing the response of all contributing J levels.

Next, we inspect the relation of σ^c to σ^p based on the comparison in Table 3.2. In general, we find a good agreement for similar temperature between our set of σ^c values and the available σ^p values measured by different groups for all gas mixtures. For pure nitrogen and the nitrogen-argon mixture our values are essentially within the error bars of the literature data or lower, only for the light collision partners hydrogen and helium we find somewhat larger decoherence rates compared to the published depopulation data. The equality of σ^c and σ^p means that rotational coherence in these examples is destroyed in a $\Delta J \neq 0$ type of collision and pure dephasing with $\Delta J = 0$ is insignificant. We can draw this conclusion for the range of pressures between 0.1 atm and 1 atm, corresponding to the binary collision regime of the dilute gas. At high densities, and especially in liquids, pure dephasing is expected to be of major importance. The equality of σ^c and σ^p holds in our experiments for the temperature range from close to liquefaction temperature of nitrogen (80 K) up to room temperature.

Finally, in Fig. 3.40 we compare our σ^c values to the gas kinetic cross section σ^{kin}. We use the standard cross sections at room temperature for pure perturbers from Ref. 235 and determine the combined cross section $\sigma^{kin}_{N_2-X}$ analogous to Eq. 3.57. The number of electrons Z and thus size and polarizability scale with the molecular mass m, and therefore the increase of $\sigma^{kin}_{N_2-X}$ in Fig. 3.40 is expected. To separate H_2 from He we plot the cross sections not as functions of Z, but rather as functions of molecular mass m, and use a semilogarithmic scale to better visualize the spread in m. In this scale, σ^{kin}_{N-2-X} is increasing almost linearly (solid black line in Fig. 3.40), with the only the He atom deviating toward a smaller value caused by the tighter binding of electrons in He. The $\sigma^{kin}_{N_2-X}$ values are compared to the $\sigma^{c}_{N_2-X}$ values at room temperature, plotted as red triangles in Fig. 3.40 and connected by a straight dashed line as a guide to the eye. For the N_2-N_2 system obviously σ^{kin} and σ^{c} are almost identical. This leads to the very intuitive notion that the loss of rotational coherence requires a hard sphere collision. Figure 3.40 shows, however, that the dependence of the decoherence cross section on molecular mass is steeper than in the case of the gas kinetic cross section, and the lines describing the dependences cross coincidentally for the N_2-N_2 system. At both limits, consequently deviations toward larger as well as smaller values appear. Decoherence cross sections for the nitrogen-krypton system are larger than the gas kinetic cross section, while for the light perturbers hydrogen and helium σ^{kin} significantly exceeds σ^{c}. The loss of rotational coherence and population for the nitrogen-hydrogen and nitrogen-helium systems therefore requires more than one hard sphere collision. In the mechanistic picture of a collision event it is expected that a collision partner approaching in the rotational plane has a stronger impact than in the vertical direction [222]. This should be more strictly valid for the atomic perturbers which do not possess a plane of rotation themselves. Furthermore, the large rotational constant of 60 cm^{-1} of the hydrogen molecule, 30 times larger than for nitrogen, may inhibit the coupling of rotational degrees of freedom. This is supported by the fact that in our experiments para-hydrogen, predominantly in $J = 0$, and normal hydrogen, predominantly in $J = 1$ with a quadrupole moment, do not lead to a significant difference in the decay of rotational coherence. For the heavy Kr atom, the relative Kr-N_2 velocity decreases compared to the light perturbers, and the large σ^{c} in this case might be governed by the same mechanism as the temperature dependence we will discuss now.

The values for σ^{c} at low temperature are shown in Fig. 3.40 as blue squares, together with the temperature they were obtained at. The temperature varies between 77 K for hydrogen and 120 K for krypton to avoid liquefaction of one of the components. The effect of cooling on σ^{c} for pure nitrogen is dramatic, with $\sigma^{c}_{N_2-N_2}$ at 80 K exceeding the gas kinetic cross section σ^{kin} (295 K) by more than a factor of two. Unfortunately, no data on $\sigma^{p}_{N_2-N_2}$ at low temperature are published. A similar strong increase is observed, however, for the cross section for rotational relaxation σ^{r} [225–228]. This growth results from the small translational velocities a low temperature. For low temperature, the long range attractive part of the intermolecular potential and so-called orbiting collisions [240–242] come into play and increase the cross section beyond the radius in the hard sphere model.

To measure the molecular alignment we used the optical Kerr effect method for pressures up to some atmospheres, however, the pressure range the method can be applied in has no fundamental limit. Even our analysis based on the integrated area of revival peaks allows to increase the pressure by an order of magnitude, and heterodyning instead of homodyning will slow down the decay of the signal. For higher pressure and liquids there exist a well developed set of methods for data analysis based on Fourier analysis [18]. The suitability for high pressure is an advantage compared to the frequency-domain Raman Q-branch method, where overlapping lines already at 1 atm pose a serious problem for data evaluation. Also, temperature is not a limitation, e.g we have applied the Kerr effect method successfully to study dynamics in hydrogen at 10 K [36]. This flexibility, together with the excellent agreement of experiment and theory for alignment of diatomics at moderate laser intensities, makes it an ideal method to obtain values for the cross sections for rotational decoherence, which are important for the use of rotational revivals in spectroscopy as well as in quantum information schemes.

Summary

This thesis presents results of the investigation of the alignment of rotationally excited diatomic molecules in experiment and numerical simulations. Laser-induced rotational alignment has become an important topic in molecular physics over the past two decades and is nowadays widely used tool for the creation of molecular ensembles with controllable directionality with respect to the laboratory frame.

In the **theoretical part** of the thesis, we presented results of rotational state-resolved numerical simulations of molecular alignment. Due to the algebraic complexity of the problem, analytical approaches to the molecular alignment are available for only the impulsive and classical limits in the rotational ground state. Otherwise, the analysis of alignment is largely based on numerical simulations, which does not necessarily advance the physical understanding. The state resolution in our approach allows to identify the basic physical processes contributing to the response of a molecule to the linearly polarized electric field of a laser, and to disentangle the particular effects of the J and the M quantum numbers. Based on these insights, we developed a simple analytical model that allows to estimate the amplitude of the post-pulse molecular alignment for given experimental parameters. In this model, we explicitly took into account that molecules in rotationally excited states can interact with a laser pulse not only by absorbing energy but also by stimulated emission. The extent to which these processes are present in the interaction depends on one hand via the M quantum number on the directionality of the molecular angular momentum, and on the other hand via the particular transition frequencies to higher and lower lying rotational states also on the pulse duration.

The transition to higher rotational levels corresponds to an aligning motion of the molecule, and the transition to lower rotational levels to an anti-aligning motion. In the ensemble average, these effects can at least partially cancel. The ratio of absorption to emission processes therefore determines the shape of the post-pulse alignment transient. The amplitude of the alignment on the other hand is mainly determined by the efficiency of energy exchange between the laser field and the molecule. The longer the laser pulse, the more likely it is that the polarization induced by the leading edge of the pulse will be removed by the trailing edge. In the limit of adiabatic alignment, the net energy exchange is zero, and the system is brought back to its initial equilibrium condition. We showed that for a laser pulse duration comparable to the molecular rotational period, the crossover from non-adiabatic to adiabatic limits is well described by a convolution of excitation pulse envelope and sinusoidal molecular response and that it takes place in the region between 0.1 and 1 for the ratio of pulse duration to rotational period. This timescale is roughly determined by the rotational period, and thus the J quantum number. The rotational period corresponding to the aligning transition gives the lower limit of the permissible pulse duration, and the rotational period corresponding to the anti-aligning transition gives the upper limit. Individual rotational levels display decays between these to limits, which are also accounted for within our analytical model.

For higher intensities of the laser electric field, the rotational wave packet contains a greater manifold of coupled rotational levels, over which the degree of adiabaticity varies. The difference in the frequencies associated with the respective rotational transitions leads to the possibility of the faster oscillating aligning part of the wave packet being more affected by the laser pulse duration than the anti-aligning part. For an appropriate combination of laser pulse duration and energy and molecular rotational frequency, a region is created in which rotational cooling, and thus post-pulse anti-alignment, prevails over rotational heating, or post-pulse alignment.

The results on the non-adiabatic to adiabatic transition of the molecular alignment with increasing laser pulse duration were used further to propose a control scheme, in which the pulse duration is tuned to address specific rotational transitions. For a quantum system with transition frequencies strongly increasing with the quantum number, increasing the excitation pulse length leads to a selective excitation of the low energetic side of the spectrum, as higher lying levels are adiabatically transferred back into their original state. In double-pulse experiments, the length of the second (dump) pulse can be adjusted to selectively eliminate the red wing of the spectrum by tuning it into the adiabatic limit for the blue wing. This effect was demonstrated by numerically calculating spectrally controlled destructive interference in non-resonantly excited rotation of diatomic molecules. The J composition of the resulting alignment signal may be far from the temperature of the environment. We thus demonstrated that adapting the pulse duration in non-resonant excitation of wave packet states can serve as a tool to achieve spectral selectivity otherwise not permitted by the non-resonant nature of the process.

With both schemes together, low J and high J rotational density packets can be designed. In this way effects of non-equilibration of rotational and translational degrees of freedom, as they occur for example in a typical molecular beam expansion experiments, can be studied in a controlled way. Additionally, shaping of rotational wave packets could be used to study state-dependent alignment decay rates or to remove a dominant low-energy contribution to an alignment signal. Additionally, we point out that the approach is not limited to the case of rotational excitation, but can be extended to those cases of wave packet dynamics for which a transition from adiabatic to non-adiabatic pulse length is permitted by the experiment and energy spacings between levels vary significantly, as it is the case e.g. in Rydberg progressions.

The **experimental part** of this work deals with rotational decoherence, and its rates and temperature dependence. To this end, a setup for the detection of the ultrafast optically induced Kerr effect was implemented and characterized. The characterization included quantification of the detected alignment signal in dependence of gas number density, and the quantitative determination of the geometry of the interaction volume of laser radiation and gas. We found excellent agreement between our experiment and the numerical simulations. In particular, the shape of the experimentally measured revival peaks Based on this, we proposed to directly determine the relative magnitude of the small population part of alignment by analyzing the shape of the homodyne detected alignment signal. This will allow to directly quantify the population part of alignment in a model-free way, which had been accessible up to now only at too high laser pulse power densities near the ionization threshold.

Furthermore, we quantitatively determined cross sections for rotational decoherence in pure nitrogen, and in mixtures of nitrogen with hydrogen and several noble gases. Knowledge of these rates constitutes an important contribution to the field of research, as hitherto no systematic study of the rates for decoherence had been available.

At the half and full revival times of non-adiabatic molecular alignment, all rotations excited by the pump pulse line up in phase, due to the common divider of $2B$ in the rotational periods. Thus pronounced peaks of alignment or anti-alignment are observed. The integrated area of the homodyne detected alignment signal is robust to the effects of centrifugal distortion, and thus serves as a measure of the degree of coherence in the rotational wave packet. Upon a collision, rotational energy is redistributed among the collision partners, and the rotational motion acquires a random phase. With the collision times statistically distributed, the molecule is lost for the phase-sensitive revivals. To reliably measure the decay of revival area, the very high sensitivity of the setup was quantitatively determined and provided a dynamic range of several orders of magnitude. Using a mean-free path model, we extracted cross sections for rotational decoherence from the integrated areas of the detected alignment signal. This approach is a new and model-free method to quantify cross sections for decoherence, and it can be applied to a wide variety of gases, the only necessary condition being that they show rotational revivals non-overlapping in time. It is in principle possible to obtain additional rotational frequency resolution by shaping the composition of the rotational wave packets with suitably designed excitation pulses using the method developed in the theoretical part of the thesis.

In pure nitrogen, we found that the cross section for decoherence decreases from 102 Å^2 at 80 K to 48 Å^2 at room temperature. This leads to the lifetime of rotational coherence becoming almost independent of temperature for a constant number density of gas. Quite counter-intuitively, at constant pressure, the lifetime for rotational coherence even increases with increasing temperature. This stability of rotational revivals with respect to temperature may be relevant for the implementation of quantum information schemes.

In the literature, a number of cross sections for rotational depopulation measured via the line broadening in the stimulated Raman Q-branch are available. In general, we find a good agreement for similar temperature between our set of decoherence cross sections and the available depopulation cross sections measured by different groups for all gas mixtures. For pure nitrogen and the nitrogen-argon mixture our values are essentially within the error bars of the literature data or lower, only for the light collision partners hydrogen and helium we find somewhat larger decoherence rates compared to the published depopulation data. The equality of the cross sections for decoherence and depopulation means that rotational coherence in these examples is destroyed in a $\Delta J \neq 0$ type of collision and pure dephasing with $\Delta J = 0$ is insignificant. We can draw this conclusion for the range of pressures between 0.1 atm and 1 atm, corresponding to the binary collision regime of the dilute gas. At high densities, and especially in liquids, pure dephasing is expected to be of major importance.

The geometric size of a particle is described by its gas-kinetic cross section. We found that for pure nitrogen at room temperature, decoherence cross section, depopulation cross section, and gas kinetic cross section are similar. This means that destroying rotational coherence requires a hard sphere collision. For lower temperature and gas mixtures, however, the situation appears more complex. Decoherence cross sections for the nitrogen-krypton system are larger than the gas kinetic cross section, while for the light perturbers hydrogen and helium the gas kinetic cross section significantly exceeds the decoherence cross section. The loss of rotational coherence and population for the nitrogen-hydrogen and nitrogen-helium systems therefore requires more than one hard sphere collision. For low temperature, the long range attractive part of the intermolecular potential and orbiting collisions come into play and increase the cross section beyond the radius in the hard sphere model. This qualitatively strong effect is implicitly well accounted for by theory, keeping in mind that the existing calculations mostly reproduce the observed depopulation cross sections well. It would be helpful for experimenters, however, if the underlying physical mechanism could be worked out in a more explicit way in the presentation of theoretical results.

References and notes

[1] J. O. Hirschfelder, C. F. Curtiss, and R. B. Bird. *Molecular Theory of Gases and Liquids.* Wiley, New York, 1954.

[2] P. R. Brooks. Reactions of oriented molecules. *Science*, 193:11, 1976.

[3] D. H. Parker and R. B. Bernstein. Oriented molecule beams via electrostatic hexapole-preparation, characterization, and reactive scattering. *Annu. Rev. Phys. Chem.*, 40:561, 1989.

[4] B. Friedrich and D. Herschbach. Spatial orientation of molecules in strong electric-fields and evidence for pendular states. *Nature*, 353:412, 1991.

[5] B. Friedrich and D. Herschbach. Alignment and trapping of molecules in intense laser fields. *Phys. Rev. Lett.*, 74:4623, 1995.

[6] B. Friedrich and D. R. Herschbach. Polarization of molecules induced by intense nonresonant laser fields. *J. Phys. Chem.*, 99:15686, 1995.

[7] T. Seideman. Revival structure of aligned rotational wave packets. *Phys. Rev. Lett.*, 83:4971, 1999.

[8] H. Stapelfeldt. Alignment of molecules by strong laser pulses. *Eur. Phys. J. D*, 26:15, 2003.

[9] T. Seideman and E. Hamilton. Nonadiabatic alignment by intense laser pulses. Concepts, theory and directions. *Adv. At. Mol. Opt. Phys.*, 52:289, 2006.

[10] Y. Ohshima and H. Hasegawa. Coherent rotational excitation by intense nonresonant laser fields. *Int. Rev. Phys. Chem.*, 2010.

[11] R. de Nalda, E. Heesel, M. Lein, N. Hay, R. Velotta, E. Springate, M. Castillejo, and J. P. Marangos. Role of orbital symmetry in high-order harmonic generation from aligned molecules. *Phys. Rev. A*, 69:031804, 2004.

[12] T. Kanai, S. Minemoto, and H. Sakai. Quantum interference during high-order harmonic generation from aligned molecules. *Nature*, 435:470, 2005.

[13] R. Torres, N. Kajumba, J. G. Underwood, J. S. Robinson, S. Baker, J. W. G. Tisch, R. de Nalda, W. A. Bryan, R. Velotta, C. Altucci, I. C. E. Turcu, and J. P. Marangos. Probing orbital structure of polyatomic molecules by high-order harmonic generation. *Phys. Rev. Lett.*, 98:203007, 2007.

[14] L. Holmegaard, J. H. Nielsen, I. Nevo, H. Stapelfeldt, F. Filsinger, J. Küpper, and G. Meijer. Laser-induced alignment and orientation of quantum-state-selected large molecules. *Phys. Rev. Lett.*, 102:023001, 2009.

[15] O. Ghafur, A. Rouzee, A. Gijsbertsen, W. K. Siu, S. Stolte, and M. J. J. Vrakking. Impulsive orientation and alignment in quantum-state selected NO molecules. *Nat. Phys.*, 5:289, 2009.

[16] T. Kiljunen, B. Schmidt, and N. Schwentner. Intense-field alignment of molecules confined in octahedral fields. *Phys. Rev. Lett.*, 94:123003, 2005.

[17] T. Kiljunen, B. Schmidt, and N. Schwentner. Aligning and orienting molecules trapped in octahedral crystal fields. *Phys. Rev. A*, 72:053415, 2005.

[18] N. A. Smith and S. R. Meech. Optically heterodyne detected optical Kerr effect: Applications in condensed phase physics. *Int. Rev. Phys. Chem.*, 21:75, 2002.

[19] P. W. Dooley, I. V. Litvinyuk, K. F. Lee, D. M. Rayner, M. Spanner, D. M. Villeneuve, and P. B. Corkum. Direct imaging of rotational wave packet dynamics of diatomic molecules. *Phys. Rev. A*, 68:023406, 2003.

[20] J. Itatani, J. Levesque, D. Zeidler, H. Niikura, H. Pepin, J. C. Kieffer, P. B. Corkum, and D. M. Villeneuve. Tomographic imaging of molecular orbitals. *Nature*, 432:867, 2004.

[21] K. F. Lee, D. M. Villeneuve, P. B. Corkum, and E. A. Shapiro. Phase control of rotational wave packets and quantum information. *Phys. Rev. Lett.*, 93:233601, 2004.

[22] S. Fleischer, I. S. Averbukh, and Y. Prior. Selective alignment of molecular spin isomers. *Phys. Rev. Lett.*, 99:093002, 2007.

[23] S. Fleischer, Y. Khodorkovsky, Y. Prior, and I. S. Averbukh. Controlling the sense of molecular rotation. *New J. Phys.*, 11:105039, 2009.

[24] Y.-H. Chen, S. Varma, A. York, and H. M. Milchberg. Single-shot, space- and time-resolved measurement of rotational wavepacket revivals in H_2, D_2, N_2, O_2, and N_2O. *Opt. Express*, 15:11341, 2007.

[25] R. de Nalda, C. Horn, M. Wollenhaupt, M. Krug, L. Banares, and T. Baumert. Pulse shaping control of alignment dynamics in N_2. *J. Raman Spectrosc.*, 38:543, 2007.

[26] D. Pavicic, K. F. Lee, D. M. Rayner, P. B. Corkum, and D. M. Villeneuve. Direct measurement of the angular dependence of ionization for N_2, O_2 and NO in intense laser fields. *Phys. Rev. Lett.*, 98:243001, 2007.

[27] T. Suzuki, Y. Sugawara, S. Minemoto, and H. Sakai. Optimal control of nonadiabatic alignment of rotationally cold N_2 molecules with the feedback of degree of alignment. *Phys. Rev. Lett.*, 100:033603, 2008.

[28] B. K. McFarland, J. P. Farrell, P. H. Bucksbaum, and M. Gühr. High harmonic generation from multiple orbitals in N_2. *Science*, 322:1232, 2008.

[29] J. P. Cryan, P. H. Bucksbaum, and R. N. Coffee. Field-free alignment in repetitively kicked nitrogen gas. *Phys. Rev. A*, 80:063412, 2009.

[30] T. Seideman. On the dynamics of rotationally broad, spatially aligned wave packets. *Phys. Rev. Lett.*, 83:4971, 1995.

[31] M. Leibscher, I. S. Averbukh, and H. Rabitz. Molecular alignment by trains of short laser pulses. *Phys. Rev. Lett.*, 90:213001, 2003.

[32] M. Leibscher, I. S. Averbukh, and H. Rabitz. Enhanced molecular alignment by short laser pulses. *Phys. Rev. A*, 69:013402, 2004.

[33] N. Owschimikow, B. Schmidt, and N. Schwentner. State selection in nonresonantly excited wave packets by tuning from nonadiabatic to adiabatic interaction. *Phys. Rev. A*, 80:053409, 2009.

[34] N. Owschimikow, B. Schmidt, and N. Schwentner. Laser-induced alignment and anti-alignment of rotationally excited molecules. *Phys. Chem. Chem. Phys.*, 2011. DOI: 10.1039/c0cp02260h.

[35] P. Giese. Rotationswellenpaketdynamik von Stickstoff in Edelgasen. Master's thesis, Department of Physics, Free University Berlin, 2007.

[36] F. Königsmann, M. Fushitani, N. Owschimikow, D. T. Anderson, and N. Schwentner. Femtosecond pump-probe 2D optical Kerr effect spectroscopy of molecular hydrogen crystals. *Chem. Phys. Lett.*, 458:303, 2008.

[37] M. Morgen, W. Price, P. Ludowise, and Y. Chen. Tensor analysis of femtosecond Raman-induced polarization spectroscopy: Application to the study of rotational coherence. *J. Chem. Phys.*, 99:8780, 1995.

[38] B. Lavorel, O. Faucher, M. Morgen, and R. Chaux. Analysis of femtosecond Raman-induced polarization spectroscopy (RIPS) in N_2 and CO_2 by fitting and scaling laws. *J. Raman Spectrosc.*, 31:77, 2000.

[39] E. A. Shapiro, M. Spanner, and M. Y. Ivanov. Quantum logic in coarse grained control of wavepackets. *J. Mod. Opt.*, 52:897, 2005.

[40] J. Maurer. Temperature and pressure dependence of rotational wavepackets: Polarization dynamics of N_2. Master's thesis, Department of Physics, Free University Berlin, 2008.

[41] A. Ott. Dephasierung der Rotation von Stickstoffmolekülen durch Stösse, 2009. Bachelor's Thesis, Department of Physics, Free University Berlin.

[42] N. Owschimikow, F. Königsmann, J. Maurer, P. Giese, A. Ott, B. Schmidt, and N. Schwentner. Cross sections for rotational decoherence in perturbed nitrogen measured via decay of laser-induced alignment. *J. Chem. Phys.*, 133:044311, 2010.

[43] H. Meyer. The molecular Hamiltonian. *Annu. Rev. Phys. Chem.*, 53:141, 2002.

[44] G. Herzberg. *Molecular Spectra and Molecular Structure. I. Spectra of Diatomic Molecules.* Krieger Publishing Company, Malabar, FL, reprint edition, 1989.

[45] A. Messiah. *Quantum Mechanics: Vol. 1.* North-Holland, Amsterdam, 1970.

[46] R. Zare. *Angular Momentum: Understanding Spatial Aspects in Chemistry and Physics.* Wiley, New York, 1988.

[47] M. Abramowitz and I. A. Stegun. *Handbook of Mathematical Functions.* Dover, New York, 1971.

[48] D. M. Villeneuve, S. A. Aseyev, P. Dietrich, M. Spanner, M. Yu. Ivanov, and P. B. Corkum. Forced molecular rotation in an optical centrifuge. *Phys. Rev. Lett.*, 85:542, 2000.

[49] R. J. Butcher and W. J. Jones. Study of the rotational Raman spectra of $^{14}N^{15}N$ and $^{15}N_2$, using a Fabry-Perot etalon. *J. Chem. Soc., Faraday Transact.*, 2:560, 1974.

[50] C. V. Raman and K. S. Krishnan. A new type of secondary radiation. *Nature*, 121:501, 1928.

[51] J.-C. Diels and W. Rudolph. *Ultrashort Laser Pulse Phenomena.* Academic Press, San Diego, 1995.

[52] J. A. Yeazell and T. Uzer, editors. *The Physics and Chemistry of Wave Packets.* Wiley, New York, 2000.

[53] D. J. Tannor. *Introduction to Quantum Mechanics: A Time-Dependent Perspective.* University Science Books, Sausalito, 2007.

[54] M. Gruebele and A. H. Zewail. Femtosecond wave packet spectoscopy: Coherences, the potential, and structural determination. *J. Chem. Phys.*, 98:883, 1993.

[55] B. Kohler, V. V. Yakovlev, J. Che, J. L. Krause, M. Messina, K. R. Wilson, N. Schwentner, R. M. Whitnell, and Y.-J. Yan. Quantum control of wave packet evolution with tailored femtosecond pulses. *Phys. Rev. Lett.*, 74:3360, 1995.

[56] P. M. Morse. Diatomic molecules according to the wave mechanics. II. Vibrational levels. *Phys. Rev.*, 34:57, 1929.

[57] The figure was generated by adapting the har_analytic.m MATLAB code by Efrat Rosenman (1998) available via David Tannor's homepage at http://www.weizmann.ac.il/chemphys/tannor/Matlab_TDQM_SourceCodes/Chapter6/.

[58] Burkhard Schmidt, personal communication.

[59] R. W. Robinett. Quantum wave packet revivals. *Phys. Rep.*, 392:1, 2004.

[60] M. F. Gelin, C. Riehn, V. V. Matylitsky, and B. Brutschy. Rotational recurrences in thermal ensembles of nonrigid molecules. *Chem. Phys.*, 290:307, 2003.

[61] R. Bluhm and V. A. Kostelecky. Long-term evolution and revival structure of Rydberg wave packets. *Phys. Lett. A*, 200:308, 1995.

[62] The figure was generated using the MATLAB code described in Sec. 2.2.

[63] I. S. Averbukh and N. F. Perelman. Fractional revivals. *Phys. Lett. A*, 139:449, 1989.

[64] M. J. J. Vrakking, D. M. Villeneuve, and A. Stolow. Observation of fractional revivals of a molecular wave packet. *Phys. Rev. A*, 54:R37, 1996.

[65] E. Schrödinger. Die gegenwärtige Situation in der Quantenmechanik. *Naturwissenschaften*, 23:807, 823, 844, 1935.

[66] The figure was generated by adapting the i2_pump_probe.m MATLAB code by Jim Faeder (2000) available via David Tannor's homepage at http://www.weizmann.ac.il/chemphys/tannor/Matlab_TDQM_SourceCodes/Chapter13/.

[67] M. Gühr, M. Bargheer, and N. Schwentner. Generation of coherent zone boundary phonons by impulsive excitation of molecules. *Phys. Rev. Lett.*, 91:085504, 2003.

[68] H. Ibrahim, M. Hejjas, and N. Schwentner. Tracing, amplifying and steering chromophore-bath coherences by pulse trains. *Phys. Rev. Lett.*, 102:088301, 2009.

[69] C. Wan, M. Gupta, J. S. Baskin, Z. H. Kim, and A. H. Zewail. Caging phenomena in reactions: Femtosecond observation of coherent, collisional confinement. *J. Chem. Phys.*, 106:4353, 1997.

[70] K. B. Møller and A. H. Zewail. The concept of coherent resonances in the nuclear motion of bimolecular collisions: Femtosecond probing and the classical picture. *Chem. Phys. Lett.*, 309:1, 1999.

[71] G. Banfi, V. Degiorgio, and D. Ricard. Nonlinear optical properties of semiconductor nanocrystals. *Adv. Phys.*, 47:447, 1998.

[72] V. A. Apkarian and N. Schwentner. Molecular photodynamics in rare gas solids. *Chem. Rev.*, 99:1481, 1999.

[73] E. Leontidis, U. W. Suter, M. Schutz, H. P. Luthi, A. Renn, and U. P. Wild. The mechanism of spectral shift and inhomogeneous broadening of an aromatic chromophore in a polymer glass. *J. Am. Chem. Soc.*, 117:7493, 1999.

[74] J.-P. Salvetat, S. Bhattacharyya, and R. B. Pipes. Progress on mechanics of carbon nanotubes and derived materials. *J. Nanosci. Nanotech.*, 6:1857, 2006.

[75] H. L. Anderson. Supramolecular orientation of conjugated porphyrin oligomers in stretched polymers. *Adv. Mat.*, 6:834, 1994.

[76] L. Jin, C. Bouwer, and O. Zhou. Alignment of carbon nanotubes in a polymer matrix by mechanical stretching. *Appl. Phys. Lett.*, 73:1197, 1998.

[77] H. J. Loesch. Orientation and alignment in reactive beam collisions - recent progress. *Annu. Rev. Phys. Chem.*, 46:555, 1995.

[78] W. Kong. Studies of electronic properties of medium and large molecules oriented in a strong uniform electric field. *Int. J. Mod. Phys.*, 15:3471, 2001.

[79] C. H. Lin, J. P. Heritage, and T. K. Gustafson. Susceptibility echos in linear molecular gases. *Appl. Phys. Lett.*, 19(10):397, 1971.

[80] J. P. Heritage, T. K. Gustafson, and C. H. Lin. Observation of coherent transient birefringence in CS_2 vapor. *Phys. Rev. Lett.*, 34:1299, 1975.

[81] L. Fonda, N. Mankoč-Borštnik, and M. Rosina. Coherent rotational states. Their formation and detection. *Phys. Rep.*, 158:160, 1988.

[82] N. Mankoč-Borštnik, L. Fonda, and B. Borštnik. Coherent rotational states and their creation and time evolution in molecular and nuclear systems. *Phys. Rev. A*, 35:4132, 1987.

[83] C. H. Lin, J. P. Heritage, T. K. Gustafson, R. Y. Chiao, and J. P. McTague. Birefringence arising from the reorientation of the polarizability anisotropy of molecules in collisionless gases. *Phys. Rev. A*, 13:813, 1976.

[84] P. M. Felker and A. H. Zewail. Purely rotational coherence effect and time-resolved sub-Doppler spectroscopy of large molecules. I. Theoretical. *J. Chem. Phys.*, 86:2460, 1987.

[85] J. S. Baskin, P. M. Felker, and A. H. Zewail. Purely rotational coherence effect and time-resolved sub-Doppler spectroscopy of large molecules. II. Experimental. *J. Chem. Phys.*, 86:2483, 1987.

[86] A. Rouzee, S. Guerin, V. Boudon, B. Lavorel, and O. Faucher. Field-free one-dimensional alignment of ethylene molecule. *Phys. Rev. A*, 73:033418, 2006.

[87] P. M. Felker. Rotational coherence spectroscopy: Studies of the geometries of large gas-phase species by picosecond time-domain methods. *J. Phys. Chem.*, 96:7844, 1992.

[88] H. M. Frey, P. Beaud, T. Gerbe, B. Mischler, P. P. Radi, and A. P. Tzannis. Determination of rotational constants in a molecule by femtosecond four-wave mixing. *J. Raman Spectrosc.*, 31:71, 2000.

[89] E. Hertz, R. Chaux, O. Faucher, and B. Lavorel. Concentration measurements in molecular gas mixtures with a two-pump pulse femtosecond polarization spectroscopy technique. *J. Chem. Phys.*, 115:3598, 2001.

[90] H. Tran, B. Lavorel, O. Faucher, R. Saint-Loup, and P. Joubert. Determination of concentrations in ternary and quaternary molecular gas mixtures using femtosecond Raman spectroscopy. *J. Raman Spectrosc.*, 33:872, 2002.

[91] E. Hertz, B. Lavorel, O. Faucher, and R. Chaux. Femtosecond polarization spectroscopy in molecular gas mixtures: Macroscopic interference and concentration measurements. *J. Chem. Phys.*, 113:6629, 2000.

[92] S. Minemoto, H. Tanji, and H. Sakai. Polarizability anisotropies of rare gas van der Waals dimers studied by laser-induced molecular alignment. *J. Chem. Phys.*, 119:7737, 2003.

[93] H. Tran, B. Lavorel, O. Faucher, R. Saint-Loup, and P. Joubert. Temperature measurement in gas mixtures by femtosecond Raman-induced polarization spectroscopy. *J. Raman Spectrosc.*, 34:994, 2003.

[94] H. Sakai, C. P. Safvan, J. J. Larsen, K. M. Hillingsoe, K. Hald, and H. Stapelfeldt. Controlling the alignment of neutral molecules by a strong laser field. *J. Chem. Phys.*, 110:10235, 1999.

[95] F. Rosca-Pruna and M. J. J. Vrakking. Experimental observation of revival structures in picosecond laser-induced alignment of I_2. *Phys. Rev. Lett.*, 87:153902, 2001.

[96] F. Rosca-Pruna and M. J. J. Vrakking. Revival structures in picosecond laser-induced alignment of I_2 molecules. I. Numerical modelling. *J. Chem. Phys.*, 116:6579, 2002.

[97] E. Hamilton, T. Seideman, T. Ejdrup, M. D. Poulsen, C. Z. Bisgaard, S. S. Viftrup, and H. Stapelfeldt. Alignment of symmetric top molecules by short laser pulses. *Phys. Rev. A*, 72:043402, 2005.

[98] M. D. Poulsen, E. Peronne, H. Stapelfeldt, C. Z. Bisgaard, S. S. Viftrup, E. Hamilton, and T. Seideman. Nonadiabatic alignment of asymmetric top molecules: Rotational revivals. *J. Chem. Phys.*, 121:783, 2004.

[99] E. Peronne, M. D. Poulsen, H. Stapelfeldt, C. Z. Bisgaard, E. Hamilton, and T. Seideman. Nonadiabatic laser-induced alignment of iodobenzene molecules. *Phys. Rev. A*, 70:063410, 2004.

[100] E. Peronne, M. D. Poulsen, C. Z. Bisgaard, H. Stapelfeldt, and T. Seideman. Nonadiabatic alignment of asymmetric top molecules: Field-free alignment of iodobenzene. *Phys. Rev. Lett.*, 91:043003, 2003.

[101] L. P. Yatsenko, S. Guerin, M. Amniat-Talab, and H. R. Jauslin. Enhanced alignment and orientation of polar molecules by vibrational resonant adiabatic passage. *J. Chem. Phys.*, 126:034305, 2007.

[102] S. Zou, G. G. Balint-Kurti, and F. R. Manby. Vibrationally selective optimal control of alignment and orientation using infrared laser pulses: Application to carbon monoxide. *J. Chem. Phys.*, 127:044107, 2007.

[103] C. Horn, M. Wollenhaupt, M. Krug, T. Baumert, R. de Nalda, and L. Banares. Adaptive control of molecular alignment. *Phys. Rev. A*, 73:031401, 2006.

[104] J. Ortigoso. Design of tailored microwave pulses to create rotational coherent states for an asymmetric top molecule. *Phys. Rev. A*, 57:4592, 1998.

[105] C. Siedschlag, O. M. Shir, T. Bäck, and M. J. J. Vrakking. Evolutionary algorithms in the optimization of dynamic molecular alignment. *Opt. Commun.*, 264:511, 2006.

[106] E. Hertz, A. Rouzee, S. Guerin, B. Lavorel, and O. Faucher. Optimization of field-free molecular alignment by phase-shaped laser pulses. *Phys. Rev. A*, 75:031403, 2007.

[107] O. Atabek, C. M. Dion, and A. B. Yedder. Evolutionary algorithms for the optimal laser control of molecular orientation. *J. Phys. B*, 36:4667, 2003.

[108] C. M. Dion, A. Ben Haj-Yedder, E. Cances, C. Le Bris, A. Keller, and O. Atabek. Optimal laser control of orientation: The kicked molecule. *Phys. Rev. A*, 65:063408, 2002.

[109] O. Masihzadeh, M. Baertschy, and R. A. Bartels. Optimal single-pulse excitation of rotational impulsive molecular phase modulation. *Opt. Express*, 14:2520, 2006.

[110] A. Pelzer, S. Ramakrishna, and T. Seideman. Optimal control of molecular alignment in dissipative media. *J. Chem. Phys.*, 126:034503, 2007.

[111] B. Friedrich and D. Herschbach. Enhanced orientation of polar molecules by combined electrostatic and nonresonant induced dipole forces. *J. Chem. Phys.*, 111:6157, 1999.

[112] L. Cai, J. Marangos, and B. Friedrich. Time-dependent alignment and orientation of molecules in combined electrostatic and pulsed nonresonant laser fields. *Phys. Rev. Lett.*, 86:775, 2001.

[113] J. G. Underwood, M. Spanner, M. Y. Ivanov, J. Mottershead, B. J. Sussman, and A. Stolow. Switched wave packets: A route to nonperturbative quantum control. *Phys. Rev. Lett.*, 90:223001, 2003.

[114] B. J. Sussman, J. G. Underwood, R. Lausten, M. Y. Ivanov, and A. Stolow. Quantum control via dynamic Stark effect: Application to switched rotational wave packets and molecular axis alignment. *Phys. Rev. A*, 73:053403, 2006.

[115] J. J. Larsen, K. Hald, N. Bjerre, H. Stapelfeldt, and T. Seideman. Three-dimensional alignment of molecules using elliptically polarized laser fields. *Phys. Rev. Lett.*, 85:2470, 2000.

[116] J. G. Underwood, B. J. Sussman, and A. Stolow. Field-free three dimensional molecular axis alignment. *Phys. Rev. Lett.*, 94:143002, 2005.

[117] S. S. Viftrup, V. Kumarappan, S. Trippel, H. Stapelfeldt, E. Hamilton, and T. Seideman. Holding and spinning molecules in space. *Phys. Rev. Lett.*, 99:143602, 2007.

[118] S. Ramakrishna and T. Seideman. Torsional control by intense pulses. *Phys. Rev. Lett.*, 99:103001, 2007.

[119] V. Loriot, E. Hertz, B. Lavorel, and O. Faucher. Field-free molecular alignment for measuring ionization probability. *J. Phys. B*, 41:015604, 2008.

[120] R. Velotta, N. Mason, M. Castillejo, and J. P. Marangos. High-order harmonic generation in aligned molecules. *Phys. Rev. Lett.*, 87:183901, 2001.

[121] I. V. Litvinyuk, K. F. Lee, P. W. Dooley, D. M. Rayner, D. M. Villeneuve, and P. B. Corkum. Alignment-dependent strong field ionization of molecules. *Phys. Rev. Lett.*, 90:233003, 2003.

[122] M. Tsubouchi and T. Suzuki. Photoionization of homonuclear diatomic molecules aligned by an intense femtosecond laser pulse. *Phys. Rev. A*, 72:022512, 2005.

[123] M. Comstock, V. Senekerimyan, and M. Dantus. Ultrafast laser induced molecular alignment and deformation: Experimental evidence from neutral molecules and from fragment ions. *J. Phys. Chem. A*, 107:8271, 2003.

[124] P. J. Ho, D. Starodub, D. K. Saldin, V. L. Shneerson, A. Ourmazd, and R. Santra. Molecular structure determination from x-ray scattering patterns of laser-aligned molecules. *J. Chem. Phys.*, 131:131101, 2009.

[125] E. R. Peterson, C. Buth, D. A. Arms, R. W. Dunford, E. P. Kanter, B. Krassig, E. C. Landahl, S. T. Pratt, R. Santra, S. H. Southworth, and L. Young. An x-ray probe of laser-aligned molecules. *Appl. Phys. Lett.*, 92:094106, 2008.

[126] C. Buth and R. Santra. Theory of x-ray absorption by laser-aligned symmetric-top molecules. *Phys. Rev. A*, 77:013413, 2008.

[127] S. Ramakrishna and T. Seideman. Information content of high harmonics generated from aligned molecules. *Phys. Rev. Lett.*, 99:113901, 2007.

[128] W. Boutu, S. Haessler, H. Merdji, P. Breger, G. Waters, M. Stankiewicz, L. J. Frasinski, R. Taieb, J. Caillat, A. Marquet, P. Monchicourt, B. Carre, and P. Salieres. Coherent control of attosecond emission from aligned molecules. *Nat. Phys.*, 4:545, 2008.

[129] J. Itatani, D. Zeidler J. Levesque, M. Spanner, D. M. Villeneuve, and P. B. Corkum. Controlling high harmonic generation with molecular wave packets. *Phys. Rev. Lett.*, 94:123902, 2005.

[130] J. Levesque, Y. Mairesse, N. Dudovich, H. Pepin, J.-C. Kieffer, P. B. Corkum, and D. M. Villeneuve. Polarization state of high-order harmonic emission from aligned molecules. *Phys. Rev. Lett.*, 99:243001, 2007.

[131] Y. Mairesse, J. Levesque, N. Dudovich, P. B. Corkum, and D. M. Villeneuve. High harmonic generation from aligned molecules-amplitude and polarization. *J. Mod. Opt.*, 55:2591, 2008.

[132] K. Hartinger, S. Nirmalgandhi, J. Wilson, and R. A. Bartels. Efficient nonlinear frequency conversion with a dynamcially structures nonlinearity. *Opt. Express*, 13:6919, 2005.

[133] R. A. Bartels, T. C. Weinacht, N. Wagner, M. Baertschy, C.H. Greene, M. M. Murnane, and H. C. Kapteyn. Phase modulation of ultrashort light pulses using molecular rotational wave packets. *Phys. Rev. Lett.*, 88:013903, 2002.

[134] H. Cai, J. Wu, A. Couairon, and H. Zeng. Spectral modulation of femtosecond laser pulses induced by molecular alignment revivals. *Opt. Lett.*, 55:827, 2009.

[135] K. Hartinger, S. Nirmalgandhi, J. Wilson, and R. A. Bartels. Efficient nonlinear frequency conversion with a dynamically structured nonlinearity. *Opt. Express*, 13:6919, 2005.

[136] M. Comstock, V. V. Lozovoy, and M. Dantus. Rotational wavepacket revivals for phase modulation of ultrafast pulses. *Chem. Phys. Lett.*, 372:739, 2003.

[137] I. V. Fedotov, A. D. Savvin, A. B. Fedotov, and A. M. Zheltikov. Controlled rotational Raman echo recurrences and modulation of high-intensity ultrashort laser pulses by molecular rotations in the gas phase. *Opt. Lett.*, 32:1275, 2007.

[138] K. Ohmori. Wave packet and coherent control dynamics. *Annu. Rev. Phys. Chem.*, 60:487, 2009.

[139] M. Gühr, M. Bargheer, M. Fushitani, T. Kiljunen, and N. Schwentner. Ultrafast dynamics of halogens in rare gas solids. *Phys. Chem. Chem. Phys.*, 9:779, 2007.

[140] M. Spanner, E. A. Shapiro, and M. Ivanov. Coherent control of rotational wave-packet dynamics via fractional revivals. *Phys. Rev. Lett.*, 92:093001, 2004.

[141] J. Ortigoso, M. Rodriguez, M. Gupta, and B. Friedrich. Time evolution of pendular states created by the interaction of molecular polarizability with a pulsed nonresonant laser field. *J. Chem. Phys.*, 110:3870, 1999.

[142] D. Sugny, C. Kontz, and H. R. Jauslin. Target states and control of molecular alignment in a dissipative medium. *Phys. Rev. A*, 74:053411, 2006.

[143] D. Sugny, A. Keller, O. Atabek, S. Daems, C. M. Dion, S. Guerin, and H. R. Jauslin. Control of mixed-state quantum systems by a train of short pulses. *Phys. Rev. A*, 72:032704, 2005.

[144] C. Z. Bisgaard, M. D. Poulsen, E. Peronne, S. S. Viftrup, and H. Stapelfeldt. Observation of enhanced field-free molecular alignment by two laser pulses. *Phys. Rev. Lett.*, 92:173004, 2004.

[145] E. Hertz, O. Faucher, B. Lavorel, F. Dalla Via, and R. Chaux. Quantum control of ground-state rotational coherence in a linear molecule. *Phys. Rev. A*, 61:033816, 2000.

[146] K. F. Lee, I. V. Litvinyuk, P.W.Dooley, M. Spanner, D. M. Villeneuve, and P. B. Corkum. Two-pulse alignment of molecules. *J. Phys. B*, 37:L43, 2004.

[147] Y. X. Li, P. Liu, S. T. Zhao, Z. A. Zeng, R. X. Li, and Z. Z. Xu. Active control of the molecular rotational wave packet using two laser pulses. *Chem. Phys. Lett.*, 475:183, 2009.

[148] K. F. Lee, E. A. Shapiro, D. M. Villeneuve, and P. B. Corkum. Coherent creation and annihilation of rotational wave packets in incoherent ensembles. *Phys. Rev. A*, 73:033403, 2006.

[149] T. Seideman. Manipulating external degrees of freedom with intense light: Laser focusing and trapping of molecules. *J. Chem. Phys.*, 106:2881, 1997.

[150] P. S. Pershan, J. P. van der Ziel, and L. D. Malmstrom. Theoretical discussion of the inverse Faraday effect, Raman scattering and related phenomena. *Phys. Rev.*, 143:574, 1966.

[151] B. W. Shore. *The Theory of Coherent Atomic Excitation*, volume 2. Wiley, New York, 1990.

[152] B. Schmidt and U. Lorenz, 2009. WavePacket 4.7: A program package for quantum-mechanical wavepacket propagation and time-dependent spectroscopy. Available via http://wavepacket.sourceforge.net.

[153] V. Loriot, E. Hertz, A. Rouzee, B. Sinardet, B. Lavorel, and O. Faucher. Strong-field molecular ionization: determination of ionization probabilities calibrated with field-free alignment. *Opt. Lett.*, 31:2897, 2006.

[154] V. Loriot, E. Hertz, B. Lavorel, and O. Faucher. Field-free molecular alignment for measuring ionization probability. *J. Phys. B*, 41:015604, 2008.

[155] S. Ramakrishna and T. Seideman. Intense laser alignment in dissipative media as a route to solvent dynamics. *Phys. Rev. Lett.*, 95:113001, 2005.

[156] S. Ramakrishna and T. Seideman. Coherence spectroscopy in dissipative media: A Liouville space pathway approach. *J. Chem. Phys.*, 122:0884502, 2005.

[157] F. Filsinger, J. Küpper, G. Meijer, L. Holmegaard, J. H. Nielsen, I. Nevo, J. L. Hansen, and H. Stapelfeldt. Quantum-state selection, alignment, and orientation of large molecules using static electric and laser fields. *J. Chem. Phys.*, 131:064309, 2009.

[158] S. Y. T. van de Meerakker, H. L. Bethlem, and G. Meijer. Taming molecular beams. *Nat. Phys.*, 4:595, 2008.

[159] M. Born. Das Adiabatenprinzip in der Quantenmechanik. *Z. Phys.*, 40:167, 1926.

[160] M. Born and V. Fock. Beweis des Adiabatensatzes. *Z. Phys.*, 51:12, 1928.

[161] T. Kato. On the adiabatic theorem of quantum mechanics. *J. Phys. Soc. Jap.*, 5:435, 1950.

[162] J. M. Rost, J. C. Griffin, B. Friedrich, and D. Herschbach. Pendular states and spectra of oriented linear molecules. *Phys. Rev. Lett.*, 68:1299, 1992.

[163] M. Leibscher and B. Schmidt. Quantum dynamics of a plane pendulum. *Phys. Rev. A*, 80:012510, 2009.

[164] R. Torres, R. de Nalda, and J. P. Marangos. Dynamics of laser-induced molecular alignment in the impulsive and adiabatic regimes: A direct comparison. *Phys. Rev. A*, 72:023420, 2005.

[165] V. Kumarappan, C. Z. Bisgaard, S. S. Viftrup, L. Holmegaard, and H. Stapelfeldt. Role of rotational temperature in adiabatic molecular alignment. *J. Chem. Phys.*, 125:194309, 2006.

[166] J. J. Larsen, H. Sakai, C. P. Safvan, I. Wendt-Larsen, and H. Stapelfeldt. Aligning molecules with intense nonresonant laser fields. *J. Chem. Phys.*, 111:7774, 1999.

[167] M. Morgen, W. Price, L. Hunziker, P. Ludowise, M. Blackwell, and Y. Chen. Femtosecond Raman induced polarization spectroscopy studies of rotational coherence in O_2, N_2 and CO_2. *Chem. Phys. Lett.*, 209:1, 1993.

[168] V. G. Stavros, E. Harel, and S. R. Leone. The influence of intense control laser pulses on homodyne-detected rotational wave packet dynamics in O_2 by degenerate four-wave mixing. *J. Chem. Phys.*, 122:064301, 2005.

[169] J. C. Butcher. *Numerical Methods for Ordinary Differential Equations.* Wiley, New York, 2nd edition, 2008.

[170] V. D. Kleiman, H. Park, R. J. Gordon, and R. N. Zare. *Companion to Angular Momentum.* Wiley, New York, 1998.

[171] Z. Q. Yang and X. X. Zhou. Effect of temperature on alignment of N_2 and O_2 in laser field. *Acta Phys.-Chim. Sin.*, 22:932, 2006.

[172] M. Dantus and V. V. Lozovoy. Experimental coherent laser control of physicochemical processes. *Chem. Rev.*, 104:1813, 2004.

[173] M. Shapiro and P. Brumer. Coherent control of molecular dynamics. *Rep. Prog. Phys.*, 66:859, 2003.

[174] J. I. Steinfeld. *Molecules and Radiation: An Introduction to Modern Molecular Spectroscopy.* Dover, Mineola, NY, 2nd edition, 2005.

[175] A. R. Edmonds. *Angular Momentum in Quantum Mechanics.* Princeton University Press, Princeton, 1960.

[176] V. Renard, M. Renard, S. Guerin, Y. T. Pashayan, B. Lavorel, O. Faucher, and H. R. Jauslin. Postpulse alignment measured by a weak field polarization technique. *Phys. Rev. Lett.*, 90:153601, 2003.

[177] Y. Mairesse, D. Zeidler, N. Dudovich, M. Spanner, J. Levesque, D. M. Villeneuve, and P. B. Corkum. High-order harmonic transient grating spectroscopy in a molecular jet. *Phys. Rev. Lett.*, 100:143903, 2008.

[178] H. Stapelfeldt, E. Constante, and P. B. Corkum. Wave-packet structure and dynamics measured by Coulomb explosion. *Phys. Rev. Lett.*, 74:3780, 1995.

[179] A. Rouzee, V. Renard, S. Guerin, O. Faucher, and B. Lavorel. Optical gratings induced by field-free alignment of molecules. *Phys. Rev. A*, 75:013419, 2007.

[180] S. Mukamel. *Nonlinear Optical Spectroscopy.* Oxford University Press, Oxford, 1995.

[181] B. I. Grimberg, V. V. Lozovoy, M. Dantus, and S. Mukamel. Ultrafast nonlinear spectroscopic techniques in the gas phase and their density matrix representation. *J. Phys. Chem. A*, 106:697, 2002.

[182] E. J. Brown, Q. Zhang, and M. Dantus. Femtosecond transient-grating techniques: Population and coherence dynamics involving ground and excited states. *J. Chem. Phys.*, 110:5772, 1999.

[183] J. Kerr. On a new relation between electricity and light: Dielectrified media birefringent. *Phil. Mag.*, 50:337, 1875.

[184] Y. R. Shen. *The Principles of Nonlinear Optics.* Wiley, Hoboken, NJ, 1984.

[185] R. W. Boyd. *Nonlinear Optics.* Elsevier, Oxford, 2nd edition, 2000.

[186] P. L. Kelley. Self-focusing of optical beams. *Phys. Rev. Lett.*, 15:1005, 1965.

[187] T. Brabec and F. Krausz. Intense few-cycle laser fields: Frontiers of nonlinear optics. *Rev. Mod. Phys.*, 72:545, 2000.

[188] G. L. Eesley, M. D. Levenson, and W. M. Tolles. Optically heterodyned coherent Raman spectroscopy. *IEEE J. Quant. Electron.*, 14:45, 1978.

[189] M. H. Cho. Coherent two-dimensional optical spectroscopy. *Chem. Rev.*, 108:1331, 2008.

[190] S. Kinoshita, Y. Kai, T. Ariyoshi, and Y. Shimada. Low frequency modes probed by time-domain optical Kerr effect spectroscopy. *Int. J. Mod. Phys. B*, 10:1229, 1996.

[191] B. I. Greene and R. C. Farrow. The subpicosecond Kerr effect in CS_2. *Chem. Phys. Lett.*, 98:273, 1983.

[192] C. Kalpouzos, W. T. Lotshaw, D. McMorrow, and G. A. Kenney-Wallace. Femtosecond laser-induced Kerr responses in liquid CS_2. *J. Phys. Chem.*, 91:2028, 1987.

[193] L. D. Ziegler, R. Fan, A. E. Desrosiers, and N. F. Scherer. Femtoseond polarization spectroscopy: A density matrix approach. *J. Chem. Phys.*, 100:1823, 1993.

[194] V. Renard, M. Renard, A. Rouzee, S. Guerin, H. R. Jauslin, B. Lavorel, and O. Faucher. Nonintrusive monitoring and quantitative analysis of strong laser-field-induced impulsive alignment. *Phys. Rev. A*, 70:033420, 2004.

[195] M. Sheik-Bahae, A. A. Said, T.-H. Wei, D. J. Hagan, and E. W. van Stryland. Sensitive measurement of optical nonlinearities using a single beam. *IEEE J. Quant. Electron.*, 26:760, 1990.

[196] A. Hochbaum. Simultaneous determination of two or more nonlinear refractive constants by z-scan measurements. *Opt. Lett.*, 15:2261, 1995.

[197] J. Wang, M. Sheik-Bahae, A. A. Said, D. J. Hagan, and E. W. Van Stryland. Time-resolved z-scan measurements of optical nonlinearities. *J. Opt. Soc. Am. B*, 11:1009, 1994.

[198] C. Rullière, editor. *Femtosecond Laser Pulses, Principles and Experiments*. Springer, New York, 2nd edition, 2005.

[199] R. Trebino, K. W. DeLong, D. N. Fittinghoff, J. N. Sweetser, M. A. Krumbügel, B. A. Richman, and D. J. Kane. Measuring ultrashort laser pulses in the time-frequency domain using frequency-resolved optical gating. *Rev. Sci. Instrum.*, 68:3277, 1997.

[200] E. T. J. Nibbering, M. A. Franco, B. S. Prade, G. Grillon, C. Leblanc, and Y. Mysyrowicz. Measurement of the nonlinear refractive index of transparent materials by spectral analysis after nonlinear propagation. *Opt. Commun.*, 119:479, 1995.

[201] E. T. J. Nibbering, G. Grillon, M. A. Franco, B. S. Prade, and Y. Mysyrowicz. Determination of the inertial contribution to the nonlinear refractive index of air, N_2, and O_2 by use of unfocused high-intensity femtosecond laser beam. *J. Opt. Soc. Am. B*, 14:650, 1997.

[202] M. Born and E. Wolf. *Principles of Optics: Electromagnetic Theory of Propagation, Interference and Diffraction of Light*. Cambridge University Books, Cambridge, 7th edition, 1999.

[203] D. R. Skinner and R. E. Whitcher. Measurement of the radius of a high-power laser beam near the focus of a lens. *J. Phys. E*, 5:237, 1971.

[204] S. Constantine, Y. Zhou, J. Morais, and L. D. Ziegler. Dispersed optical heterodyne birefringence and dichroism of transparent liquids. *J. Phys. Chem. A*, 101:5456, 1997.

[205] Y. Zhou, S. Constantine, S. Harrel, and L. D. Ziegler. The probe frequency dependence of nonresonant femtosecond pump-probe nuclear responses: Undercutting vibrational inhomogeneities. *J. Chem. Phys.*, 110:5893, 1999.

[206] M. N. Slipchenko, B. D. Prince, S. C. Ducatman, and H. U. Stauffer. Development of a simultaneously frequency- and time-resolved Raman-induced Kerr effect probe. *J. Phys. Chem. A*, 113:135, 2009.

[207] F. Königsmann, unpublished results.

[208] J. T. Fourkas. *Multidimensional Raman spectroscopy*, volume 117 of *Advances in Chemical Physics*. Wiley, New York, 2001.

[209] T. Vieillard, F. Chaussard, D. Sugny, B. Lavorel, and O. Faucher. Field-free molecular alignment of CO_2 mixtures in presence of collisional relaxation. *J. Raman Spectrosc.*, 694:39, 2008.

[210] M. F. Gelin, C. Riehn, M. Kunitski, and B. Brutschy. Strong field effects in rotational femtosecond degenerate four-wave mixing. *J. Chem. Phys.*, 132:134301, 2010.

[211] A. J. Pearson and T. M. Mortensen. Effect of electric-field fluctuations on rotational revival amplitudes. *Phys. Rev. A*, 80:053411, 2009.

[212] S. Ramakrishna and T. Seideman. Dissipative dynamics of laser induced nonadiabatic molecular alignment. *J. Chem. Phys.*, 124:034101, 2006.

[213] G. O. Sitz and R. L. Farrow. Preparation and decay of alignment in N_2 $(v = 1)$. *J. Chem. Phys.*, 101:4682, 1994.

[214] M. Brouard, H. Chadwick, Y. P. Chang, R. Cireasa, C. J. Eyles, A. O. La Via, N. Screen, F. J. Aoiz, and J. Klos. Collisional depolarization of NO(A) by He and Ar studied by quantum beat spectroscopy. *J. Chem. Phys.*, 131:104307, 2009.

[215] M. L. Costen, R. Livingstone, K. G. McKendrick, G. Paterson, M. Brouard, H. Chadwick, Y. P. Chang, C. J. Eyles, F. J. Aoiz, and J. Klos. Elastic depolarization of OH(A) by He and Ar: A comparative study. *J. Phys. Chem. A*, 113:15156, 2009.

[216] G. Paterson, S. Marinakis, M. L. Costen, K. G. McKendrick, J. Klos, and R. Tobola. Orientation and alignment depolarization in $OH(X^2\Pi)$ +Ar/He collisions. *J. Chem. Phys.*, 129:074304, 2008. Erratum. *J. Chem. Phys.*, 131:159901, 2009.

[217] M. C. van Beek, G. Berden, H. L. Bethlem, and J. J. ter Meulen. Molecular reorientation in collisions of OH plus Ar. *Phys. Rev. Lett.*, 86:4001, 2001.

[218] A. D. Rudert, J. Martin, W. B. Gao, H. Zacharias, and J. B. Halpern. Collisional effects on angular momentum orientation in acetylene $(\tilde{X})\ {}^1\Sigma_g^+\ (\nu_2^{''} = 1, j^{''})$. I. Preparation, detection and conservation in single collisions. *J. Chem. Phys.*, 111:9549, 1999.

[219] A. D. Rudert, J. Martin, W. B. Gao, H. Zacharias, and J. B. Halpern. Collisional effects on angular momentum orientation in acetylene $(\tilde{X})\ {}^1\Sigma_g^+\ (\nu_2^{''} = 1, j^{''})$. II. Disorientation by rotationally elastic and multiple inelastic collisions. *J. Chem. Phys.*, 112:9749, 2000.

[220] R. Dopheide and H. Zacharias. Rotational alignment by stimulated Raman pumping - $C_2H_2(\nu_2^{''} = 1, j^{''})$. *J. Chem. Phys.*, 99:4864, 1993.

[221] J. B. Halpern, R. Dopheide, and H. Zacharias. How a collision causes misalignment - alignment decay in acetylene-2(1). *J. Phys. Chem.*, 99:13611, 1995.

[222] M. L. Costen, S. Marinakis, and K. G. McKendrick. Do vectors point the way to understanding energy transfer in molecular collisions? *Chem. Soc. Rev.*, 37:732, 2008.

[223] G. J. Rosasco, W. Lempert, W. S. Hurst, and A. Fein. Line interference effects in the vibrational Q-branch spectra of N_2 and CO. *Chem. Phys. Lett.*, 97:435, 1983.

[224] G. O. Sitz and R. L. Farrow. Pump-probe measurements of state-to-state rotational energy transfer rates in N_2 $(v = 1)$. *J. Chem. Phys.*, 93:7883, 1990.

[225] L. Abad, D. Bermejo, V. J. Herrero, J. Santos, and I. Tanarro. Molecular relaxation in supersonic free jets of N_2 and CH_4 from stimulated Raman spectroscopy and time-of-flight measurements. *J. Phys. Chem. A*, 101:9276, 1997.

[226] F. J. Aoiz, T. Diez-Rojo, V. J. Herrero, B. Martinez-Haya, M. Menendez, P. Quintana, L. Ramonat, I. Tanarro, and E. Verdasco. Low-temperature rotational relaxation of N_2 studied with resonance-enhanced multiphoton ionization. *J. Phys. Chem. A*, 103:823, 1999.

[227] G. J. Prangsma, A. H. Alberga, and J. J. M. Beenakker. Ultrasonic determination of volume viscosity of N_2, CO, CH_4 and CD_4 between 77 and 300 K. *Physica*, 64:278, 1973.

[228] E. H. Carnevale, C. Carey, and G. Larson. Ultrasonic determination of rotational collision numbers and vibrational relaxation times of polyatomic gases at high temperatures. *J. Chem. Phys.*, 47:2829, 1967.

[229] J. G. Parker. Rotational and vibrational relaxation in diatomic gases. *Phys. Fluids*, 2:449, 1959.

[230] D. W. Broege, R. N. Coffee, and P. H. Bucksbaum. Strong-field impulsive alignment in the presence of high temperatures and large centrifugal distortion. *Phys. Rev. A*, 78:035401, 2008.

[231] L. B. Loeb. *The Kinetic Theory of Gases.* Dover Publications, Mineola, NY, reprint edition, 1961.

[232] S. Green. Raman linewidths and rotationally inelastic-collision rates in nitrogen. *J. Chem. Phys.*, 98:257, 1993. Erratum. *J. Chem. Phys.*, 99:4875, 1993.

[233] J. S. Murphy and J. E. Boggs. Collision broadening of rotational absorption lines. I. Theoretical formulation. *J. Chem. Phys.*, 47:691, 1967.

[234] P. J. Agg and D. C. Clary. Rotationally inelastic rates and Raman Q-branch linewidths for N_2+N_2. *Molec. Phys.*, 73:317, 1991.

[235] D. R. Lide, editor. *Handbook of Chemistry and Physics.* CRC Press, Boca Raton, 84th edition, 2003.

[236] P. Strak and S. Krukowski. Molecular nitrogen-N_2 properties: The intermolecular potential and the equation of state. *J. Chem. Phys.*, 126:194501, 2007.

[237] L. A. Rahn and R. E. Palmer. Studies of nitrogen self-broadening at high-temperature with inverse Raman-spectroscopy. *J. Opt. Soc. Am. B*, 3:1164, 1986.

[238] G. Millot. Rotationally inelastic rates over a wide temperature-range based on an energy corrected sudden exponential-power theoretical-analysis of Raman line broadening coefficients and Q-branch collapse. *J. Chem. Phys.*, 93:8001, 1990.

[239] P. Beaud, T. Gerber, P. P. Radi, M. Tulej, and G. Knopp. Rotationally inelastic collisions between N_2 and rare gases: An extension of the angular momentum scaling law. *Chem. Phys. Lett.*, 373:251, 2003.

[240] J. N. L. Connor. On semi-classical description of molecular orbiting collisions. *Mol. Phys.*, 15:621, 1968.

[241] J. P. Toennies, W. Welz, and G. Wolf. Molecular-beam scattering studies of orbiting resonances and the determination of van der Waals potentials for H-Ne, Ar, Kr, and Xe and for H_2-Ar, Kr, and Xe. *J. Chem. Phys.*, 71:614, 1979.

[242] D. W. Chandler. Cold and ultracold molecules: Spotlight on orbiting resonances. *J. Chem. Phys.*, 132:110901, 2010.

[243] A. Laubereau and W. Kaiser. Vibrational dynamics of liquids and solids investigated by picosecond light pulses. *Rev. Mod. Phys.*, 50:607, 1978.

[244] L. Gomez, D. Bermejo, P. Joubert, and J. Bonamy. Theoretical and experimental analysis of N_2-H_2 stimulated Raman spectra. *Mol. Phys.*, 104:1869, 2006.

[245] I. A. Bocharova, H. Mashiko, M. Magrakvelidze, D. Ray, P. Ranitovic, C. L. Cocke, and I. V. Litvinyuk. Direct Coulomb-explosion imaging of coherent nuclear dynamics induced by few-cycle laser pulses in light and heavy hydrogen. *Phys. Rev. A*, 77:053407, 2008.

[246] L. Gomez, R. Z. Martinez, D. Bermejo, F. Thibault, P. Joubert, B. Bussery-Honvault, and J. Bonamy. Q-branch linewidths of N_2 perturbed by H_2: Experiments and quantum calculations from an *ab initio* potential. *J. Chem. Phys.*, 126:204302, 2007.

[247] P. Joubert, J. Bonamy, L. Gomez, and D. Bermejo. N_2-H_2 isotropic Raman Q-branch linewidths: An energy-corrected sudden scaling law. *J. Raman Spectrosc.*, 39:707, 2008.

[248] K. S. Jammu, G. E. St. John, and N. L. Welsh. Pressure broadening of rotational Raman lines of some simple gases. *Can. J. Phys.*, 44:797, 1966.

[249] A. E. Belikov, R. G. Sharafutdinov, and A. V. Storozhev. Rotational relaxation of nitrogen in helium. *Chem. Phys.*, 213:319, 1996.

[250] D. N. Kozlov, R. L. Pykhov, V. V. Smirnov, K. A. Vereschagin, A. I. Burshtein, and A. V. Storozhev. Rotational relaxation of nitrogen in argon - collisional broadening of Q-branch components in coherent Raman-spectra of cooled gas. *J. Raman Spectrosc.*, 22:403, 1991.

[251] R. L. Farrow, R. P. Lucht, and L. A. Rahn. Measurements of the nonresonant 3rd-order susceptibilities of gases using coherent anti-Stokes Raman-spectroscopy. *J. Opt. Soc. Am. B*, 4:1241, 1987.

[252] M. D. Pattengill, R. A. La Budde, R. B. Bernstein, and C. F. Curtiss. Molecular collisions. 16. Comparison of GPS with classical trajectory calculations of rotational inelasticity for Ar-N_2 system. *J. Chem. Phys.*, 55:5517, 1971.

[253] P. G. Kistemaker and A. E. De Vries. Rotational relaxation-times in nitrogen-noble-gas mixtures. *Chem. Phys.*, 7:371, 1975.

[254] A. Couairon and A. Mysyrowicz. Femtosecond filamentation in transparent media. *Phys. Rep.*, 441:47, 2007.

Publications

Publications in peer-reviewed journals and book chapters,
from this work:

N. Owschimikow, B. Schmidt, and N. Schwentner
Laser-induced alignment and anti-alignment of rotationally excited molecules,
Themed issue *Analysis and control of ultrafast photon-induced processes* of *Phys. Chem. Chem. Phys.* **13**, 8671 (2011)

N. Owschimikow, F. Königsmann, J. Maurer, P. Giese, A. Ott, B. Schmidt, and N. Schwentner
Cross sections for rotational decoherence of perturbed nitrogen measured via decay of laser-induced alignment
J. Chem. Phys. **133**, 044311 (2010)

N. Owschimikow, B. Schmidt, and N. Schwentner
State selection in nonresonantly excited wave packets by tuning from nonadiabatic to adiabatic interaction
Phys. Rev. A **80**, 053409 (2009)

Other:

F. Königsmann, M. Fushitani, N. Owschimikow, D. T. Anderson, and N. Schwentner
Femtosecond pump-probe 2D optical Kerr effect spectroscopy of molecular hydrogen crystals
Chem. Phys. Lett. **458**, 303 (2008)

C. Gmachl, N. Owschimikow, A. Belyanin, A. M. Sergent, D. L. Sivco, M. L. Peabody, A. Y. Cho, and F. Capasso
Temperature dependence and single-mode tuning behavior of second-harmonic generation in quantum cascade lasers
Appl. Phys. Lett. **84**, 2751 (2004)

C. Gmachl, A. Belyanin, D. L. Sivco, M. L. Peabody, N. Owschimikow, A. M. Sergent, F. Capasso, and A. Y. Cho
Optimized second harmonic generation in quantum cascade lasers
IEEE J. Quant. Electron. **39**, 1345 (2003)

N. Owschimikow, C. Gmachl, A. Belyanin, V. Kocharovsky, D. L. Sivco, R. Colombelli, F. Capasso, and A. Y. Cho
Resonant second-order nonlinear optical processes in quantum cascade lasers
Phys. Rev. Lett. **90**, 043902 (2003)

L. Benmohammadi, A. Erodabasi, K. Koch, F. Laeri, N. Owschimikow, U. Vietze, G. Ihlein, F. Schüth, Ö. Weiß, I. Braun, M. Ganschow, G. Schulz-Eckloff, D. Wöhrle, J. Wiersig, and J. U. Nöckel
Microscopic lasers based on the molecular sieve $AlPO_4$-5
in *Host-Guest Systems Based on Nanoporous Crystals*, edited by F. Laeri, F. Schüth, U. Simon, and M. Wark, Wiley-VCH, Weinheim (2003)

Patent:

Nonlinear semiconductor light sources,
F. Capasso, A. Y. Cho, R. Colombelli, C. F. Gmachl, N. Owschimikow, and D. Sivco
U. S. Patent No. 6816530, granted Nov. 2004

Lebenslauf

Der Lebenslauf ist in der Online-Version aus Gründen des Datenschutzes nicht enthalten.

Danksagung

Viele Menschen haben auf unterschiedliche Arten und Weisen entscheidend zu dieser Arbeit beigetragen.

Zuallererst möchte ich Professor Nikolaus Schwentner danken, dafür dass er mir die Möglichkeit gegeben hat, diese Arbeit in seiner Gruppe anzufertigen und für die großartige Unterstützung in dieser Zeit. Durch seine physikalische Intuition und das Bestehen auf anschaulichen Erklärungen habe ich viel gelernt. Die Diskussionen um prinzipiellen Mechanismen und die kleinen Details des Alignments waren eine Herausforderung für das Verständnis und eine Inspiration für den theoretischen Teil der Arbeit. Danke auch für die vielen Feste in Kallinchen und anderswo und die geschichtlichen Ausflüge beim Mittagessen.

Mit Burkhard Schmidt durfte ich an den numerischen Simulationen des Alignments arbeiten. Er war dabei immer bereit, sein enormes Wissen zu teilen und mir mit unendlicher Geduld die Geheimisse der Computerphysik näherzubringen. Danke auch für die Nachhilfe im korrekten Formulieren "theoretischer"Gleichungen. Auch das Parkhaus hat an einigen Tagen wesentlich zu dieser Arbeit beigetragen.

Jochen Maurer, Philipp Giese, und Anna Ott haben in ihren Diplom- bzw. Bachelorarbeiten zum Aufbau, den Messungen und der Auswertung der experimentellen Daten beigetragen. Vielen Dank an alle für die hervorragende Mitarbeit. Ich wünsche Euch alles Gute für Eure weitere Laufbahn.

Vielen Dank an

Monika Hejjas für die positive Arbeitsatmosphäre, die Zusammenarbeit im Labor, die vielen und konstruktiven Gespräche über Physik und viel mehr, die Kaffee- und Zigarettenpausen und die generelle Unterstützung,

Falk Königsmann für die unvergleichliche UP II Atmosphäre, die Zusammenarbeit beim Experiment, die unendlichen Diskussionen (auch die über Physik), das Aushalten von Tastaturgeräuschen und die Ausflüge in die späte römische Republik,

Ralph Püttner für die Einführung in die Welt der Elementarteilchen, die physikalischen Einsichten und die kulinarischen Abende,

und auch die früheren Mitglieder und Gäste der AG Schwentner Heide Ibrahim, Markus Gühr, Mizuho Fushitani, Toni Kiljunen, David Anderson, Lisa-Marie Krocker, Oli Hübner, Ingeborg Twesten und Vadim Alexeev für die gute Zusammenarbeit.